Índice

Presentación

Las Jornadas de Trabajo en Mecánica Celeste son ya una actividad consolidada en el mapa español de reuniones científicas de carácter periódico, en este caso, en el ámbito de la astrodinámica. Distintos lugares de la geografía peninsular han sido sedes de este evento en los últimos años: San Fernando (1998 y 2004), Logroño (1999), Valladolid (2000), La Manga (2001), Albarracín (2002), Señorío de Bértiz (2003), Rianxo (2005), Jaca (2006), Barcelona (2007), Ezcaray (2008) y Lalín (2009).

En efecto, esta ha sido la segunda vez que tienen lugar en Galicia, organizadas por el Observatorio Astronómico Ramón María Aller (OARMA) de la Universidade de Santiago de Compostela. Aunque la edición de 2009 le correspondía a los compañeros de Madrid, dado que se trataba del Año Internacional de la Astronomía, el OARMA solicitó de nuevo ser anfitrión con objeto de poder rendir un homenaje al añorado Ramón María Aller, iniciador de la investigación astronómica en Galicia desde su observatorio particular de Lalín y luego ya tanto en su cátedra de astronomía como, y sobre todo, en el Observatorio Astronómico universitario que el fundó en Compostela.

La sede de estas XII JTMC fué la actual Casa Museo que la villa de Lalín dedica a sus hijos ilustres, entre los que hay que citar al matemático Rodríguez, al aviador Loriga, al pintor Laxeiro y sobre todo al matemático y astrónomo Aller. De hecho, ésta fue su casa familiar y su Observatorio anexo, actualmente fuera de uso desde su traslado al Campus, el lugar emblemático cuna de la astronomía gallega.

La organización de las Jornadas en esta localidad, capital de la comarca del Deza, estaba encuadrada dentro de un amplio convenio con el Alma Mater santiaguesa, en el que se contempla la recuperación del observatorio original para fines didácticos y que se espera que esté en funcionamiento en unos meses. De esta forma, la Reunión Científica se desarrolló en un clima de colaboración total por parte del ayuntamiento lalinense, al que la organización quiso corresponder con dos conferencias de divulgación abiertas al público, así como con una sesión de observación astronómica con un telescopio portátil.

En el acto inaugural estuvieron presentes el Vicerrector Adjunto de Investigación y Proyección Exterior, Dr. D. Jesús A. Casabiell Pintos, así como la Concejala de Cultura, Dña. Nuria Rodriguez Carral, quien representó al Alcalde, ausente esos días.

Dos conferencias invitadas a cargo de los doctores Mortari y Trigo-Rodríguez, además de 21 comunicaciones orales y las ya comentadas charlas de divulgación impartidas por los doctores José Angel Docobo e Iván Fernández, completaron el programa de las Jornadas,

en las que se trataton temas tan diversoso como órbitas periódicas, variedades invariantes en sistemas hamiltonianos, métodos analíticos y numéricos para resolver EDOs, automatización de métodos de perturbaciones, movimientos estelares, de asteroides, de amarras espaciales, etc.

Los asistentes tuvieron la oportunidad de conocer una de las construcciones de mayor solera de la zona, el Pazo de Bendoiro, donde tuvo lugar la cena oficial; en el transcurso de la misma, los organizadores de las Jornadas hicieron entrega de un recuerdo a los Drs. Elipe, Lanchares y Palacios, que junto con el Dr. Docobo han participado en todas las ediciones de las Jornadas. Ya en la jornada de clausura, pudimos disfrutar de la visita a dos enclaves de excepcional belleza como son el Monasterio benedictino de Oseira y los Cañones del Sil.

Es obligado mostrar nuestro agradecimiento tanto al Ministerio de Ciencia e Innovación como a la Xunta de Galicia por las ayudas económicas que han permitido la celebración de estas Jornadas. Otros patrocinadores como La Caixa y Compostela Monumental, no pueden tampoco ser olvidados y, por supuesto, el Concello de Lalín, garante de la memoria de Ramón María Aller, por todas las atenciones recibidas. Nuestro agradecimiento así mismo a la Real Academia de Ciencias Exactas, Físicas, Químicas y Naturales de Zaragoza, que una vez más ha aceptado con entusiasmo la publicación de las presentes Actas en su serie de Monografías.

Entendemos que, fiel a su filosofía inicial, las Jornadas de Trabajo en Mecánica Celeste han cumplido nuevamente su misión actuando como nexo de todos aquellos grupos españoles que tienen algo que transmitir en este amplio campo científico que abarca desde las Matemáticas a la Física, pasando por la Astronomía, las Ingenierías, la Geodesia, y demás áreas afines.

Por último sólo unas palabras de reconocimiento tanto al Comité Científico por su labor vigilante de la calidad de los trabajos presentados, como al Comité Organizador por sus múltiples desvelos y por acordarse de nuevo de los jóvenes investigadores y becarios al ofrecerles alojamiento gratuito.

Santiago de Compostela, 2010, Año Santo Xacobeo.

The Editors

José Ángel Docobo
Antonio Elipe
Roberto Barrio

USC
UNIVERSIDADE DE SANTIAGO DE COMPOSTELA

Observatorio Astronómico
Ramón Mª Aller / Dpto. Matemática Aplicada

XII JORNADAS
DE TRABAJO EN MECÁNICA CELESTE

COMITÉ CIENTÍFICO:
J. A. Docobo Durántez. Universidade de Santiago de Compostela
A. C. Elipe Sánchez (Coord.). Universidad de Zaragoza
M. Ollé Torner. Universitat Politècnica de Catalunya
A. I. Pascual Leria. Universidad de La Rioja
J. Peláez Álvarez. Universidad Politécnica de Madrid
P. Yanguas Sayas. Universidad Pública de Navarra

COMITÉ LOCAL:
Manuel Andrade Baliño (Secretario)
Pedro Pablo Campo Díaz
José Ángel Docobo Durántez (Coordinador)

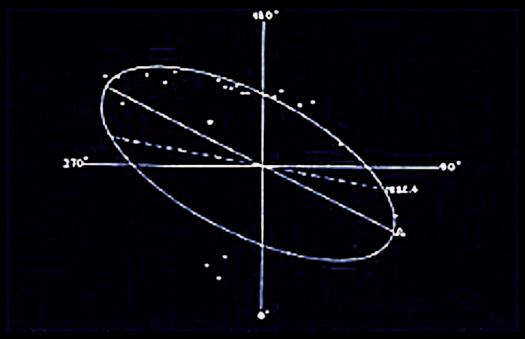

Órbita del sistema STT 77. Primera órbita de una estrella doble calculada en España (Aller, 1935)

EL UNIVERSO PARA QUE LO DESCUBRAS
AÑO INTERNACIONAL DE LA ASTRONOMÍA 2009

GOBIERNO DE ESPAÑA
MINISTERIO DE CIENCIA E INNOVACIÓN
XUNTA DE GALICIA
CONSELLERÍA DE EDUCACIÓN E ORDENACIÓN UNIVERSITARIA
"la Caixa"
Compostela Monumental
CENTRO COMERCIAL ABERTO
Concello de Lalín

Lalín, 1-3 de julio de 2009

Vista de los participantes

Direcciones de los participantes

1. Abad Medina, Alberto
   Universidad de Zaragoza — abad@unizar.es
   Grupo de Mecánica Espacial - IUMA — 976 762 204
   C/ Pedro Cerbuna, 12
   50009 Zaragoza

2. Andrade Baliño, Manuel
   Universidade de Santiago de Compostela — manuel.andrade@usc.es
   Departamento de Matemática Aplicada — 981 594 488 ext 23319
   Escola Politécnica Superior
   Campus Universitário
   27002 Lugo

3. Arribas Jiménez, Mercedes
   Universidad de Zaragoza — marribas@unizar.es
   Grupo de Mecánica Espacial - IUMA — 976 761 979
   María de Luna, 3
   50018 Zaragoza

4. Baeza Richer, Federico
   Real Instituto y Observatorio de la Armada — fbaeza@roa.es
   Pl. de las Tres Marinas, s/n — 956 599 367
   11110 San Fernando (Cádiz)

5. Barrio Gil, Roberto
   Universidad de Zaragoza — rbarrio@unizar.es
   Grupo de Mecánica Espacial - IUMA — 976 762 480
   C/ Pedro Cerbuna, 12
   50009 Zaragoza

6. Bombardelli, Claudio
   Universidad Politécnica de Madrid — claudio.bombardelli@upm.es
   Departamento de Física Aplicada a la Ingeniería — 913 363 939
   Aeronáutica
   Pl. Cardenal Cisneros, 3
   28040 Madrid

7. Calvo Pinilla, Manuel
   Universidad de Zaragoza — calvo@unizar.es
   Departamento de Matemática Aplicada - IUMA — 976 761 126
   C/ Pedro Cerbuna, 12
   50009 Zaragoza

8. Campo Díaz, Pedro Pablo
   Universidade de Santiago de Compostela — pedropablo.campo@usc.es
   Observatorio Astronómico R.M. Aller — 981 592 747
   Av. das Ciencias, s/n
   15782 Santiago de Compostela

9. Concepción (de la) Sáenz, Daniel
   Universidad de La Rioja — daniel-de-la.concepcion@alum.unirioja.es
   C/ Luis de Ulloa, s/n — 941 299 439
   26004 Logroño

10. Corbera Subirana, Montserrat
    Universitat de Vic — montserrat.corbera@uvic.cat
    Departament de Tecnologies Digitals i de la Informació — 938 815 519
    C/ Laura, 13
    08500 Vic (Barcelona)

11. Crespo Cutillas, Francisco
    Universidad de Murcia — pacocrespocutillas@gmail.com
    Departamento de Matemática Aplicada — 696 036 104
    Campus Universitario de Espinardo
    30100 Espinardo (Murcia)

12. Dena Arto, Ángeles
    Universidad de Zaragoza — adena@unizar.es
    Grupo de Mecánica Espacial - IUMA
    C/ Pedro Cerbuna, 12
    50009 Zaragoza

13. Docobo Durántez, José Ángel
    Universidade de Santiago de Compostela — joseangel.docobo@usc.es
    Observatorio Astronómico R.M. Aller — 981 592 747
    Av. das Ciencias, s/n
    15782 Santiago de Compostela

14. Elipe Sánchez, Antonio
    Universidad de Zaragoza — elipe@unizar.es
    Grupo de Mecánica Espacial - IUMA — 976 761 138
    C/ Pedro Cerbuna, 12
    50009 Zaragoza

15. Farrelly, David
Utah State University
Department of Chemistry and Biochemistry
0300 Old Main Hill
84322-0300 Logan (Utah, USA)
david.farrelly@gmail.com
+1-435-797-1608

16. Fernández Pérez, Iván
Universidade de Santiago de Compostela
Observatorio Astronómico R.M. Aller
Av. das Ciencias, s/n
15782 Santiago de Compostela
ivan.fernandez@usc.es
981 592 747

17. Gamboa Suárez, Antonio
Utah State University
Department of Chemistry and Biochemistry
0300 Old Main Hill
84322-0300 Logan (Utah, USA)
angamboa@yahoo.com

18. Kalvouridis, Tilemachos
National Technical University of Athens
Department of Mechanics
5, Heroes of Politechnion Ave.
Zografou Campus, 15773
Atenas (Grecia)
tkalvouridis@gmail.com
+30 210 7721691

19. Lanchares Barrasa, Víctor
Universidad de La Rioja
Departamento de Matemáticas y Computación
C/ Luis de Ulloa, s/n
26004 Logroño
vlancha@unirioja.es
941 299 467

20. Lara Coira, Martín
Real Instituto y Observatorio de la Armada
Pl. de las Tres Marinas, s/n
11110 San Fernando (Cádiz)
mlara@roa.es
956 545 612

21. Llibre Saló, Jaume
Universitat Autónoma de Barcelona
Departament de Matemàtiques
Edificio C (Campus UAB)
08193 Cerdanyola del Vallés (Barcelona)
jllibre@mat.uab.cat
935 811 303

22. Molero Madrid, Francisco Javier
Universidad de Murcia
Departamento de Matemática Aplicada
Facultad de Informática
30071 Espinardo (Murcia)
javier.moleromadrid@gmail.com
696 384 687

23. Mortari, Daniele
Texas A&M University
Department of Aerospace Engineering
Ross Street - 3141 Tamu
77843-3141 College Station (Texas, USA)
mortari@aero.tamu.edu
+1-979-845-0734

24. Ollé Torner, Mercé
Universitat Politécnica de Catalunya
Departament de Matemàtica Aplicada I
C/ Diagonal, 647
08028 (Barcelona)
merce.olle@upc.edu
934 011 780

25. Palacián Subiela, Jesús Francisco
Universidad Pública de Navarra
Departamento de Ingeniería Matemática e Informática
Campus de Arrosadia
31006 Pamplona
palacian@unavarra.es
948 169 554

26. Palacios Latasa, Manuel
Universidad de Zaragoza
Grupo de Mecánica Espacial - IUMA
C/ María de Luna 3
50018 Zaragoza
mpala@unizar.es
976 761 981

27. Pascual Lería, Ana Isabel
Universidad de La Rioja
Departamento de Matemáticas y Computación
C/ Luis de Ulloa, s/n
26004 Logroño
aipasc@unirioja.es
941 299 439

28. Peláez Álvarez, Jesús
Universidad Politécnica de Madrid
Departamento de Física Aplicada a la Ingeniería Aeronáutica
Pl. Cardenal Cisneros, 3
28040 Madrid
j.pelaez@upm.es
913 366 306

29. Piasecki, Sławomir Stanisław
Universidad de Zaragoza — piasek@unizar.es
Grupo de Mecánica Espacial - IUMA
C/ Pedro Cerbuna, 12
50009 Zaragoza

30. Rández García, Luis
Universidad de Zaragoza — randez@unizar.es
Departamento de Matemática Aplicada - IUMA — 976 761 122
C/ Pedro Cerbuna, 12
50009 Zaragoza

31. Riaguas Guedán, Andrés
Universidad de Valladolid — andresrg@mac.uva.es
Departamento de Matemática Aplicada — 975 129 419
Campus Universitario Duques de Soria
42004 Soria

32. Rodríguez Rodríguez, Marcos
Universidad de Zaragoza — marcos@unizar.es
Grupo de Mecánica Espacial - IUMA — 976 761 000 ext 3284
C/ Pedro Cerbuna, 12
50009 Zaragoza

33. San Juan Díaz, Félix
Universidad de La Rioja — juanfelix.sanjuan@unirioja.es
Departamento de Matemáticas y Computación — 941 299 440
C/ Luis de Ulloa, s/n
26004 Logroño

34. Sanjurjo Rivo, Manuel
Universidad Politécnica de Madrid — m.sanjurjo@upm.es
Departamento de Física Aplicada a la Ingeniería — 913 666 306
Aeroespacial
Pl. Cardenal Cisneros, 3
28040 Madrid

35. Sayas Bordonaba, Flora
Universidad de Zaragoza — fsayas@unizar.es
Grupo de Mecánica Espacial - IUMA
C/ Pedro Cerbuna, 12
50009 Zaragoza

36. Tresaco Vidaller, Eva
Universidad de Zaragoza — etresaco@unizar.es
Grupo de Mecánica Espacial - IUMA — 976 761 137
C/ Pedro Cerbuna, 12
50009 Zaragoza

37. Trigo Rodríguez, Josep Maria
Institut de Ciéncies de l'Espai — trigo@ieec.uab.es
Campus UAB — 935 814 778
Facultat de Ciencies, Torre C5-parell, 2a
08193 Bellaterra (Barcelona)

38. Vilhena de Moraes, Rodolpho
Universidade Estadual Paulista — rodolpho@feg.unesp.br
Departamento de Matemática — (55)12-3123 2848
Campus de Guaratinguetá
12516-410 Guaratinguetá (São Paulo, Brasil)

39. Yanguas Sayas, Patricia
Universidad Pública de Navarra — yanguas@unavarra.es
Departamento de Ingeniería Matemática e Informática — 948 169 546
Campus de Arrosadia
31006 Pamplona

Monografías de la Real Academia de Ciencias de Zaragoza **35**, 1–12, (2011).

Detecting variations of the orbital elements due to periastron effect in eclipsing binaries.

Manuel Andrade and José Á. Docobo

Astronomical Observatory R.M. Aller

Universidade de Santiago de Compostela

15782 Santiago de Compostela, Galiza (Spain)

Abstract

In this study we examine the relation between the dynamical evolution of the eclipsing binaries and their observed light curves. More precisely, we focus our attention in the influence of mass loss along with what is known as the periastron effect (PE) in the light curves of non-circular eclipsing binaries. The enhanced mass loss during periastron passages gives rises to secular trends in the orbital elements of the binary system. This secular behavior can be detected by carefully examining its light curve.

After analysing some remarkable mass-loss laws with the PE, simulations are presented for actual eclipsing binaries with unexplained variations in their light curves. They allow us to hypothesise that peristron effect could play a significant role in the evolution of these systems.

1 Introduction

It is well known that mass loss is one of the keys to the stellar evolution in binary systems. Undoubtedly, this is still more noteworthy in the case of eccentric binary systems undergoing mass loss by means of the PE. This effect has been analysed in the past in the general context of double and triple stars [2, 3, 1, 4]. Now we focuse our attention on eclipsing binaries (thereafter, EB) with moderate eccentricities. In this way, we present here the very onset of an investigation that we hope to develop later.

In the next section we will describe EB. Some notes about its importance in the study of stellar evolution will be also given. The third section is dedicated to defining the PE and to review some mass-loss laws that have been used to model this phenomenon in the

last years. In the fourth section, we will show how we can detect this additional mass loss by analysing light curves of eccentric eclipsing binaries (thereafter, EEB). In fact, they are the secular variations in the orbital elements caused by the PE that lead to slight alterations in the light curve of an EEB. Finally, main results and some ideas to develop in future works will be presented in the last section.

2 Eclipsing binaries

An EB is a binary star with its orbital plane so close to the line of sight of the observer that the components undergo mutual eclipses. Actually, the most distinctive feature of this type of system is its light curve from which it is possible to obtain meaningful data about the orbit and about the morphology of the components. In Figure 1, we can see an example of the light curve obtained for the RXJ 0529.4+0041 system, a low-mass pre-main sequence EB.

In spite of the fact that only 0.3% of all binary stars are eclipsing binaries, they provide fundamental information about stellar masses, radii, and luminosities. Yet, by analysing its light curves one can obtain essential data about stellar atmospheres, stellar interiors, magnetic activity and so on. Furthermore, EB can be considered *standard candles* since they allow us to determine accurate distances within and outside our galaxy.

3 Mass loss and the periastron effect

The two-body problem with variable mass is one of the most investigated since its origin in the middle of the 19^{th} century. The case in which mass is ejected isotropically from the two-body system and is lost to the system is called Gyldén-Meščerskij's problem [GMP]. In 1924, Jeans [8] was the first to consider this as an astrophysical problem by taking into account the relationship between luminosity and stellar mass developed by Eddington [7]. From this study, he obtained the Jeans' law for mass loss:

$$\dot{\mu}(t) = -\alpha\mu^n(t), \tag{1}$$

where α and n are real numbers, the first one is approximate to zero and n varies between 1.4 and 4.4. This mass-loss law, which only depends on time, gives rise to periodic variations in some orbital elements but not in semimajor axis that increases secularly. This expression can be extended to separately take into account a different mass-loss rate for each component:

$$\dot{\mu}(t) = -\alpha_1\mu^n(t) - \alpha_2\mu^q(t), \tag{2}$$

where α_i $(i = 1, 2)$, n and q are defined in a similar way to the previous case.

These well-known expressions were used to integrate the mass-loss two-body problem in its Hamiltonian formulation a few years ago [10, 11].

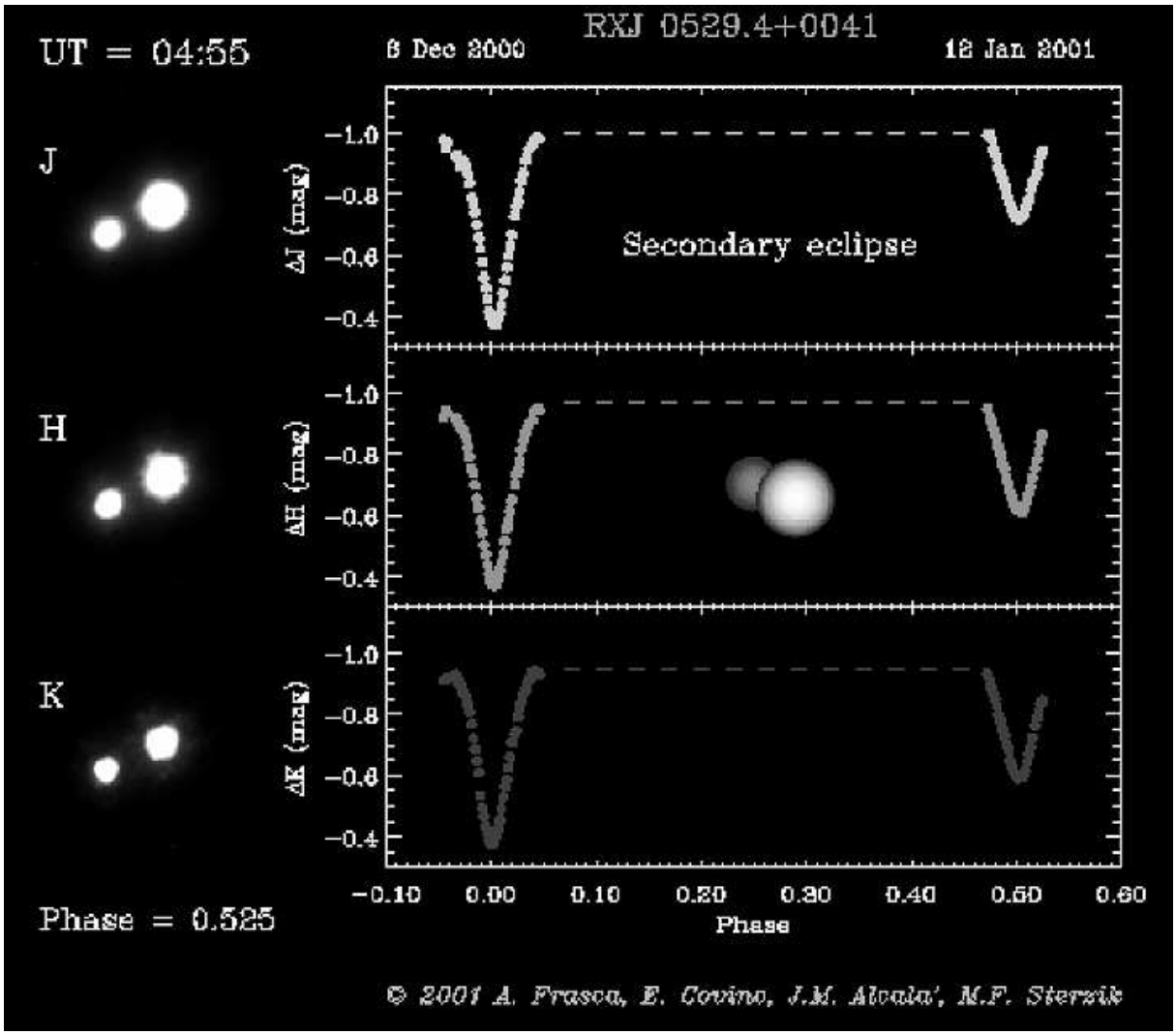

Figure 1.— Light curve of RXJ 0529.4+0041 system obtained by a team of astronomers from Italy and ESO using the ADaptive Optics Near Infrared System (ADONIS) on the 3.6-metre telescope at the ESO La Silla Observatory

On the other hand, in order to explain eccentric binary systems abundance, other laws depending on distance between components were subsequently suggested. These laws describe an enhanced mass-loss rate during periastron passages which, in turn, leads to secular increments in eccentricity. For this reason such effect is known as the PE. The first law of this type was considered by [9, 5]; it is called Martin's law:

$$\dot{\mu}(r;t) = -\frac{k(t)}{r^2}, \tag{3}$$

with $k(t)$ a function depending on time and r the distance between the two components of the system.

Recently, another time-dependent mass-loss law with PE has been suggested by the authors [2]:

$$\dot{\mu}(r, p_\theta; t) = -\dot{\mu}(t) - \beta\frac{p_\theta}{r^2}, \tag{4}$$

where $\dot{\mu}(t)$, which represents time-dependent mass loss, is given by Jeans' law as a rule. The last term introduces the PE, r being the distance between the two components; p_θ the total angular momentum; and β, a small parameter close to zero.

4 The periastron effect in EEB

In general, as we mentioned above, the main source of information for an EB is its light curve. On the hypothesis that every perturbation in this two-body system must generate changes in its light curve, our purpose is to investigate the way in which we can determine them. Indeed, in the future we would want to define a model so that from these changes in the light curve, we would be able to calculate the corresponding alterations in the orbital elements.

In this way we are mainly analysing secular variations due to the PE but the same procedure could be applied to another type of secular perturbation as, for example, those due to the existence of accretion disks, mass transfer, and so on (see Figure 2).

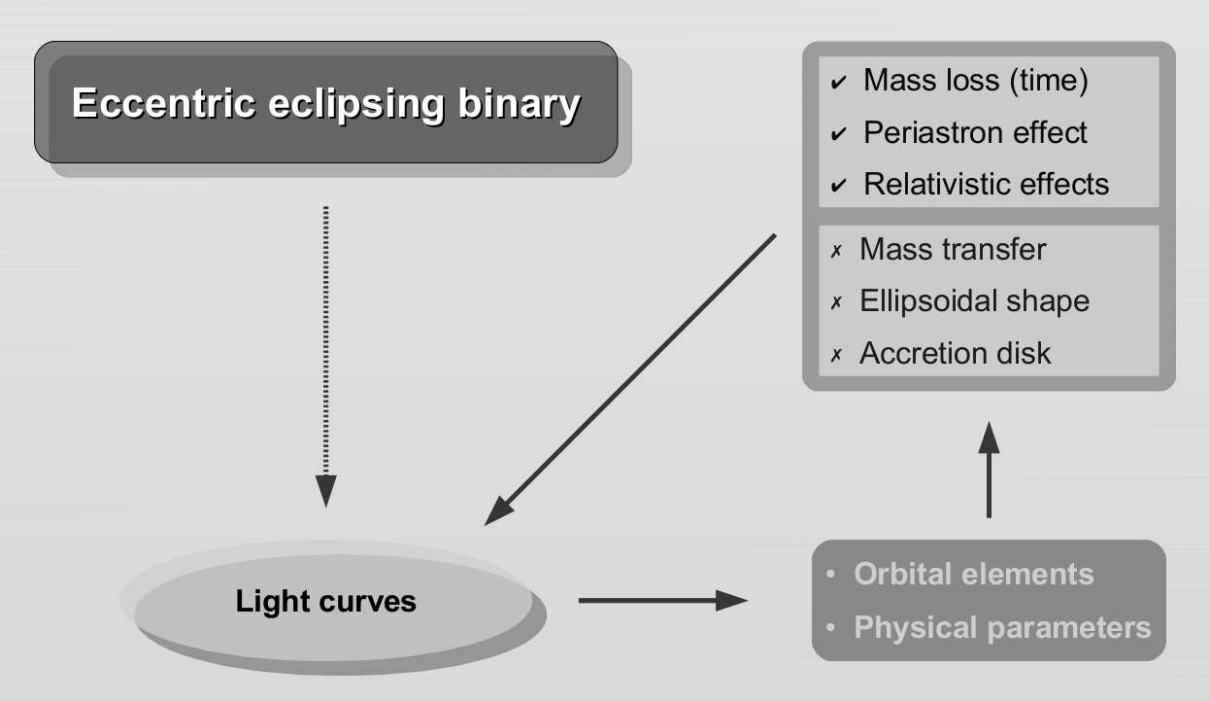

Figure 2.— Diagram of changes in the light curve and variations in the orbital elements

We will consider the Hamiltonian of the problem given by:

$$H(r,\theta;p_r,p_\theta;t)=\frac{1}{2}\left(p_r^2+\frac{p_\theta^2}{r^2}\right)-\frac{\mu(r;p_\theta;t)}{r}+V_r; \tag{5}$$

here the first and second terms of the right-hand side correspond to the two-body problem with mass depending on time and distance (PE), whereas the last term is the relativistic

potential correction. The equations of motion are numerically integrated along with mass-loss laws given in Equations (3) and (4).

In the last part of this section, we will use this model to analyse the influence of the PE in a couple of EEBs. In the first case, we will show that mass loss by the PE causes secular variations in orbital elements, namely, in eccentricity and in semimajor axis, which eventually could give rise to serious changes in the orbital stability. In the second one, we will see the way in that the PE modifies the light curve.

4.1 Example: OX Cas

The first example is the detached and double-lined (B2V+B2V) eclipsing binary OX Cassiopeiae. Its light curve is shown in Figure 3 and the spectroscopic and physical parameters are listed in Table 1.

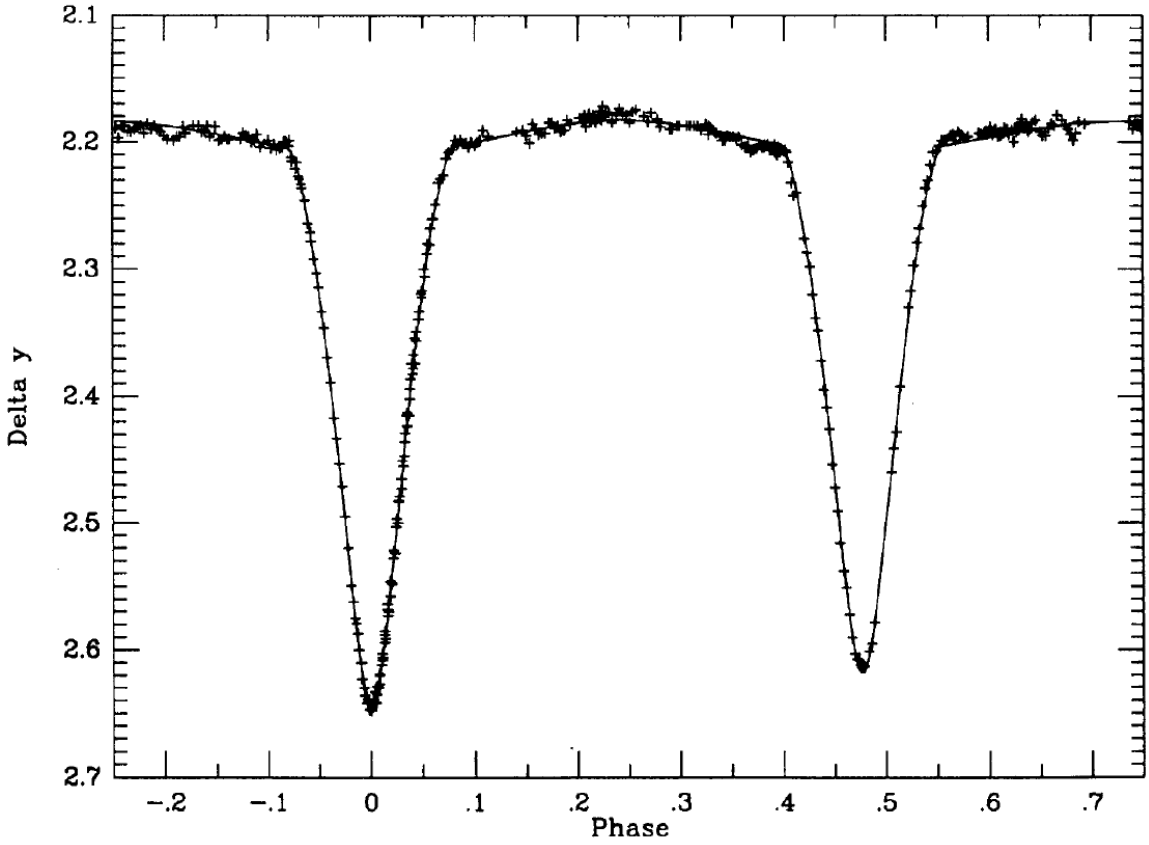

Figure 3.— Differential observations of OX Cas and light curve given by [6]

We integrate the Hamiltonian (5) over 1000 orbital periods considering three general situations (note that, in all of them, we also apply the relativistic corrections):

a. Time-dependent mass loss by means of Jeans' law given in (2),

b. Mass loss by the PE according to Martin's law given in (3), and

Parameter	Value
M_1 [$M_\odot$]	7.2 ± 0.5
M_2 [$M_\odot$]	6.3 ± 0.5
P [d]	2.4893467 ± 0.0000004
e	0.04147 ± 0.00005
i [°]	84.15 ± 0.25
ω [°]	31.9 ± 0.1

Table 1.— Physical and orbital parameters for the OX Cas (taken from [12])

c. Time-dependent mass loss plus mass loss by the PE according to the authors' law given in (4).

Values for the mass-loss coefficients in different cases are shown in Table 2. In this integration, exponents in Jeans' law are $n = q = 3$. Our aim is to show secular trends in orbital elements, mainly in eccentricity and in semimajor axis considering its strong relation with orbital stability.

Coefficients	Jeans	Martin	This paper	
			[PE]	[TML+PE]
α_1	10^{-5}	10^{-5}	0	10^{-5}
α_2	10^{-5}	10^{-5}	0	10^{-5}
β	—	—	10^{-5}	10^{-5}

Table 2.— Mass-loss coefficients for mass loss by means of Jeans' law, mass loss by means of Martin's law, and mass loss by means of the authors' law (PE: exclusively mass loss by the periastron effect. TML+PE: time-dependent mass loss plus the PE)

4.1.1 Jeans' law

As is well known this time-dependent mass-loss law gives rise to periodic variations in eccentricity and secular increase in the semimajor axis as well as in periastron and apoastron distances so that orbital stability is not significantly disturbed, at least during short time intervals. Variations for some orbital elements and parameters can be seen in Figure 4.

4.1.2 Martin's law

In this case, eccentricity as semimajor axis as well as the periastron and apoastron distances increase secularly. Now, such increments are much larger than in the case of Jeans' law. Moreover, the most remarkable feature is the secular increase in eccentricity taking into account that it may lead to the disruption of the system eventually.

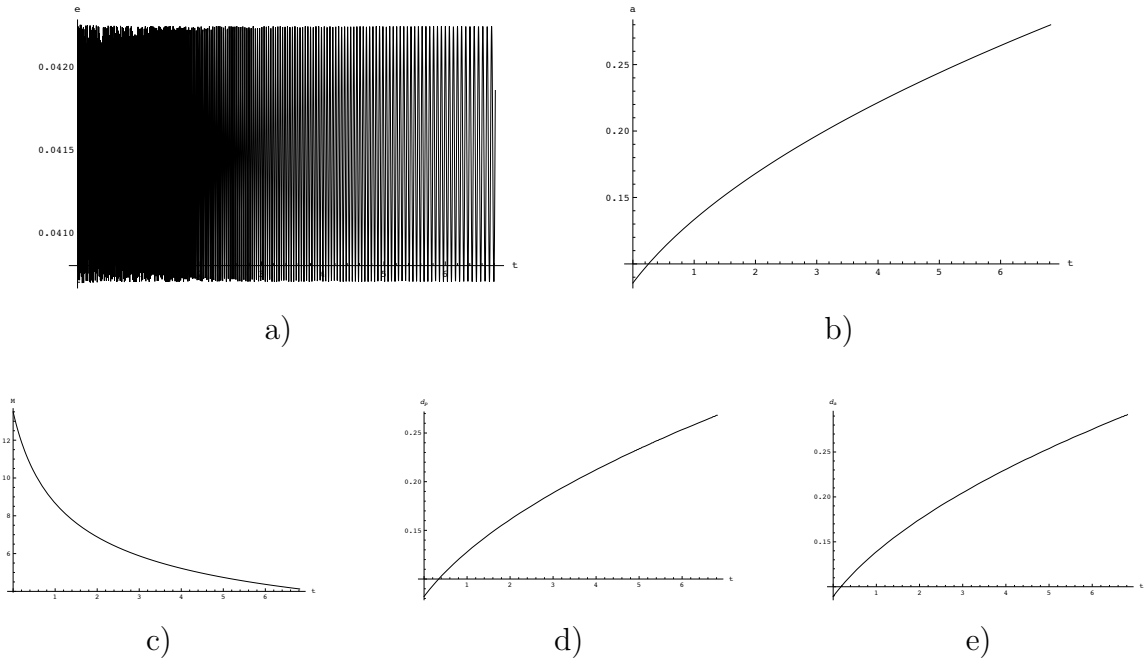

Figure 4.— Time-dependent variations for mass loss by means of Jeans' law: a) eccentricity; b) semimajor axis; c) total mass; d) periastron distance; and e) apoastron distance

Variations for some orbital elements and parameters can be seen in Figure 5. There we can note some oscillations in every curve which are characteristic of the mass-loss laws with the PE.

4.1.3 Authors' law

We must basically distinguish between two cases in Equation 4 depending upon the values of the small parameters (note that $\beta = 0$ corresponds simply to the Jeans' law):

i. *Pure* periastron effect ($\alpha_i = 0$ and $\beta \neq 0$), and

ii. Time-dependent mass loss plus the periastron effect ($\alpha_i \neq 0$ and $\beta \neq 0$).

Behavior exhibited by the orbital elements in the first case is utterly different to that shown with the previous mass-loss laws. In this case all of them undergo secular decreases with the notable exclusion of eccentricity which increases secularly. This last behavior along with the decrease in semimajor axis will result, at some future time, in a collision of both components. Time-dependent evolution for some orbital elements can be seen in Figure 6.

When we consider that mass loss by the PE is superimposed to time-dependent mass loss (second case) the evolution of some orbital elements will depend on the fine adjustment of the small parameters (α_i and β). Invariably, since $\beta \neq 0$ eccentricity increases secularly. But the most noticeable difference with the first case is that the semimajor axis,

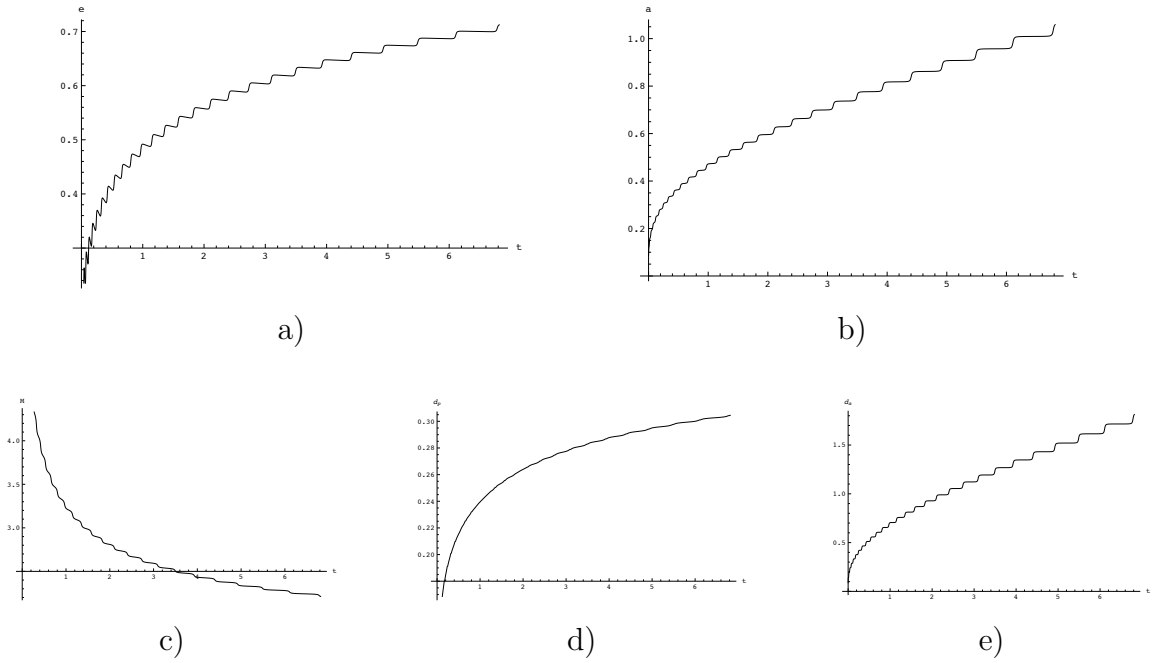

Figure 5.— Time-dependent variations for mass loss by means of Martin's law: a) eccentricity; b) semimajor axis; c) total mass; d) periastron distance; and e) apoastron distance

and, therefore the periastron and apoastron distances as well, may increase or decrease depending on whether the first term in the right-hand side of Equation 4 is dominant, or not. Indeed, if this adjustment between parameters is made in certain appropriate ways then the semimajor axis and periastron-apoastron distances may show very different and even opposite trends in the interplay. This peculiar behavior is related with angular momentum loss. In fact, among the mass-loss laws analysed in this paper, the last one is the only one that possesses this feature.

4.2 Fictitious example

Now, we will consider a highly eccentric EB, the parameters of which are shown in Table 3. The equations of motion will be integrated over 100 orbital periods.

Parameter	**Value**	**Parameter**	**Value**
M_1 [$M_\odot$]	8	P [d]	2.72241
M_2 [$M_\odot$]	10	e	0.8
R_1 [$R_\odot$]	1.5	a [AU]	0.1
R_2 [$R_\odot$]	1.0	i [°]	87
T_1 [K]	25000	Ω [°]	20
T_2 [K]	20000	ω [°]	31.9

Table 3.— Physical and orbital parameters for the fictitious example

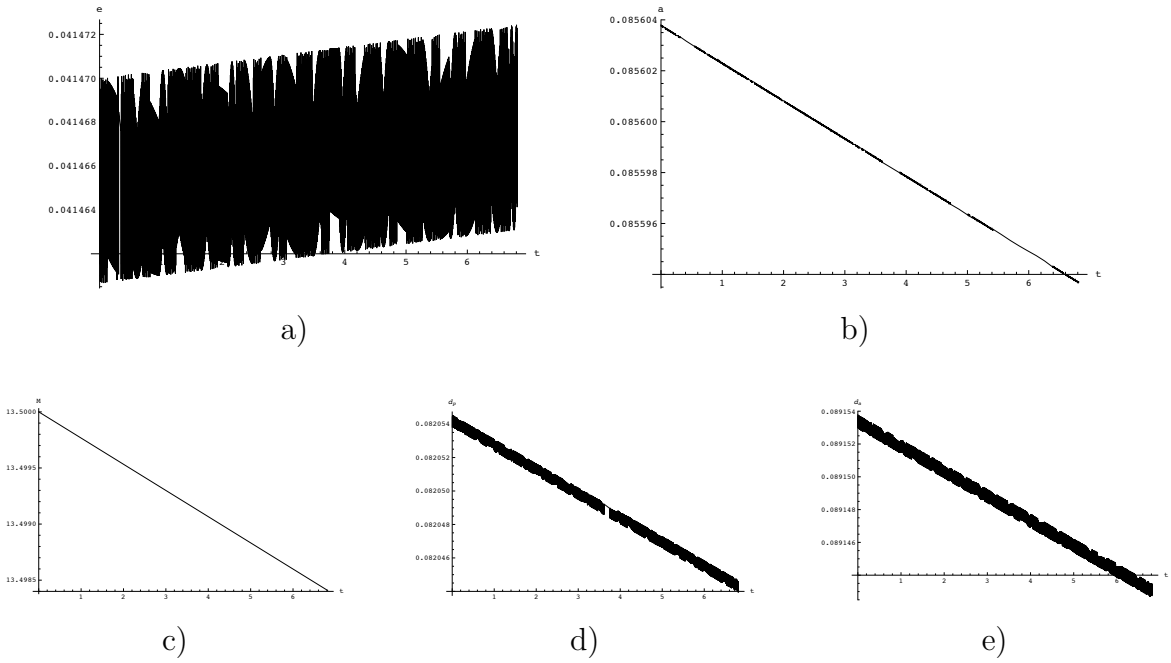

Figure 6.— Time-dependent variations for mass loss by means of authors' law: a) eccentricity; b) semimajor axis; c) total mass; d) periastron distance; and e) apoastron distance

We have defined a photometric model in order to obtain the light curve from the physical and orbital parameters listed in Table 3. It is applied to the current system at the beginning and, subsequently, at the end of the integration time. We observe that secular variations in orbital elements due to mass loss by the PE give rise to a slight advance over time in the light curve. In this particular example, we notice that eclipses happen 0.024 days (about 35 minutes) earlier than in the Keplerian case (see Figure 7).

5 Conclusions

It is well known that time-dependent mass loss tends to increase the semimajor axis and to induce periodic variations in eccentricity. However, we have demonstrated that such behavior changes drastically when we consider an additional mass loss during periastron passages according to the law given in Equation (4). In that case, not only the eccentricity begins to undergo a secular increase but also the semimajor axis can eventually begin to show a secular decrease. Depending upon which term is dominant in this expression (time-dependent mass loss or the PE), such a situation could lead in the future to a disruption or to a collision between both components of the system. This equilibrium is summarised in Table 4.

Another noteworthy consequence is that angular momentum of the system is no longer a constant of motion. In this way, this law could explain not only an increase in the mass loss close to the periastron but also the evolution of some systems in which an angular

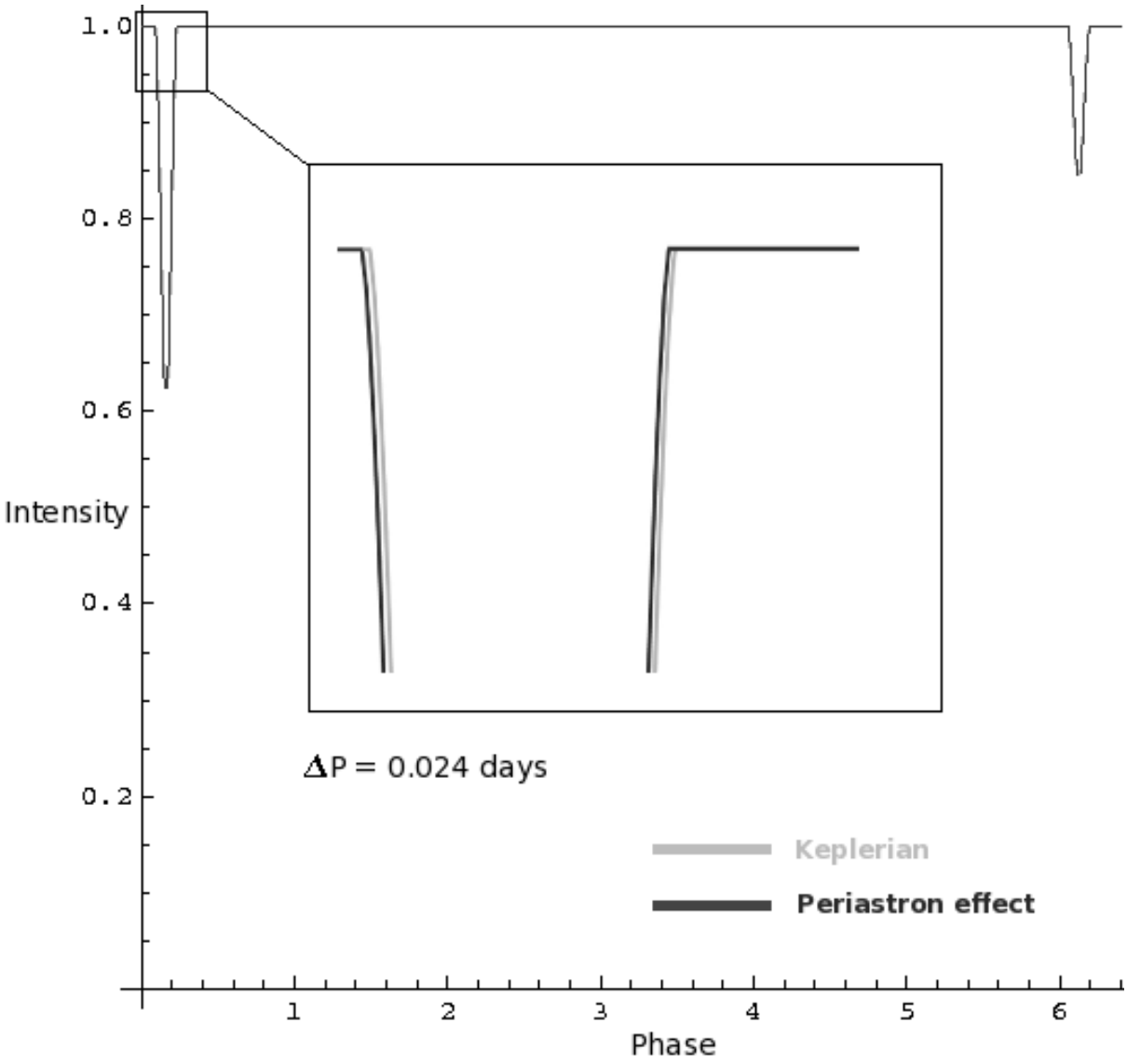

Figure 7.— Alterations in the light curve by the PE

momentum loss has been observed.

Moreover, and this is the main suggestion of this contribution, in the case of EEB, we are able to indirectly detect the PE by measuring a certain advance in the light curve. After this preliminary study, our intention is to obtain a more complete model including another perturbations such as mass transfer between components, accretion disks, and so on.

Dominant term	Δe	Δa	Δd_p	Δd_a
TML	0	$\uparrow$	$\uparrow$	$\uparrow$
PE	$\uparrow$	$\downarrow$	$\downarrow$	$\downarrow$
TML+PE	$\uparrow$	$\updownarrow$	$\updownarrow$	$\updownarrow$

Table 4.— Secular trends in eccentricity (e), semimajor axis (a), periastron distance (d_p), and apoastron distance (d_a) according to the dominant term in the mass-loss law given in (4): first term (TML, time-dependent mass loss), second term (PE, mass loss by the periastron effect); or no clear dominance (TML+PE, time-dependent mass loss plus the PE). Secular increase is indicated by $\uparrow$, secular decrease by $\downarrow$, whereas $\updownarrow$ indicates increase as much as decrease or even non-secular variation

References

[1] Andrade, M. *O Problema de Gyldén-Meščerskij em Cenários Perturbados. Métodos e Aplicações*. Ph.D. dissertation, ISBN: 978-84-9750-851-3, Universidade de Santiago de Compostela, 2007.

[2] Andrade, M. & Docobo, J. A. Orbital dynamics analysis of binary systems in mass-loss scenarios. *Rev. Mex. Astron. Astrofis. (SC)*, **15**, 223–225, 2003.

[3] Andrade, M. & Docobo, J. A. Estudio de la estabilidad en sistemas estelares triples con pérdida de masa. *Mon. Acad. Cienc. Zaragoza*, **25**, 13–22, 2004.

[4] Andrade, M. & Docobo, J. A. Modelización de vientos estelares en el marco del problema restringido elíptico de tres cuerpos con masa variable. *Boletín ROA*, **1**, 107–120, 2009.

[5] Chiara, L. Casi in cui nel problema dei due corpi di massa decrescente leccentricitá varia in ragione inversa della massa. *Pubblicazioni dell'Osservatorio Astronomico di Palermo*, **10**, 3–16, 1957.

[6] Crinklaw, G. & Etzel, P. B. A photometric analysis of the eclipsing binary OX Cassiopeiae. *The Astronomical Journal*, **98**, 1418–1426, 1989.

[7] Eddington, A. S. On the Relation between the Masses and Luminosities of the Stars. *Mon. Not. R. Astron. Soc.*, **84**, 308–332, 1924.

[8] Jeans, J. H. Cosmogonic problems associated with a secular decrease of mass. *Mon. Not. R. Astron. Soc.*, **85**, 2–11, 1924.

[9] Martin, E. L. Sulle variazioni secolari del periastro e della eccentricità secondo una nuova legge di irraggiamento della massa per i sistemi binari. *Reale Stazione Astron. e Geof. di Carloforte* (Cagliari), **30**, 1934.

[10] Prieto, C. and Docobo, J. A. Analytic solution of the two-body problem with slowly decreasing mass. *Astronomy & Astrophysics* **318**, 657–661 (1997).

[11] Prieto, C. and Docobo, J. A. On the two-body problem with slowly decreasing mass. *Cel. Mech. Dyn. Astron.* **68**, 53–62 (1997).

[12] Švaříček, P. et al. Rapid apsidal motion in eccentric eclipsing binaries: OX Cassiopeia, PV Cassiopeia, and CO Lacertae. *Astronomy & Astrophysics*, **477**, 615–620, 2008.

Monografías de la Real Academia de Ciencias de Zaragoza **35**, 13–20, (2011).

On the stability of the planar $n+1$ ring body problem with quasi-homogeneous potentials

M. Arribas, A. Elipe* and M. Palacios

Grupo de Mecánica Espacial - IUMA. Universidad de Zaragoza

*Centro Universitario de la Defensa de Zaragoza

Abstract

In a previous work we analyzed the linear stability of the planar $n+1$ ring body problem where the potential of the central body is a Manev's type potential. By introducing a perturbation parameter (ϵ_0) to the Newtonian potential associated with the central primary, we showed that unstable cases for the unperturbed problem, as $n \leq 6$, may become stable for some values of the perturbation.

The purpose of this paper is to study the possibility of increasing the range of values of the mass parameter ($\mu = m/m_0$) and the parameter ϵ_0 that let stable the configuration. For that, we introduce a second perturbation term (with parameter ϵ_1) to the Newtonian potential of the bodies in the ring. We show some results for different values of the parameters.

1 Introduction

The n-ring configuration consists of n bodies of equal masses placed at the vertices of a regular n-gon which is rotating about its center of masses with constant angular velocity. Another body of mass m_0 is placed at the center of the n-gon.

For Newtonian forces, the stability of this configuration depends essentially of two parameters, the mass relation between the central body and the peripheral ones ($\mu = m_0/m$) and their number (n). It is known since Maxwell that the configuration is unstable for $n \leq 6$, whereas for $n \geq 7$ the configuration is stable when the mass ratio is within certain values [8, 10, 9]. Generally speaking, the greater the number of bodies the smaller the mass parameter to have stability.

Recently, the authors analyzed the stability when the central body is a spheroid or a radiating body [2](see also [7]), which may be considered as bodies attracted by a Manev's

type force, and that belongs to a more general class of quasi-homogeneous potentials [5, 4, 1, 6]. In this case a new parameter ϵ representing the oblateness (prolateness) or the radiation coefficient must be considered in the force function, which takes the form:

$$U = k^2\, m_0 \sum_{1\le j\le n} m_j \left(\frac{1}{r_{j0}} + \frac{\epsilon}{r_{j0}^2}\right) + k^2 \sum_{1\le i<j\le n} \frac{m_i\, m_j}{r_{ij}}.$$

Note that the parameter ϵ may be positive, negative or null.

In the above mentioned work [2] we proved that the stability depends also on ϵ, in such a way that for values $n \le 6$, unstable for Newtonian forces, we found regions for $\epsilon < 0$ in which the configuration is stable. Besides, for $n > 6$ the influence of ϵ increases the stability bound.

Thus, the "non Newtonian" part of the potential due to the central primary modifies the region of stability. Hence, we decided to investigate the effect on the stability of the n bodies placed on the ring when these bodies are of the same type as the central one, i.e., spheroids or even radiating bodies. The procedure we will follow along the paper is analogous to the one described in [2, 3].

2 The problem

We assume that bodies on the ring are identical and when all bodies are spheroids or radiating sources, we have a new parameter ϵ_1, whereas ϵ_0 is the same as in [2]. Then, the force function is

$$U = k^2\, m_0 \sum_{1\le j\le n} m_j \left(\frac{1}{r_{j0}} + \frac{\epsilon_0}{r_{j0}^2}\right) + k^2 \sum_{1\le i<j\le n} m_i\, m_j \left(\frac{1}{r_{ij}} + \frac{\epsilon_1}{r_{ij}^2}\right), \tag{1}$$

Both parameters are independent each other and may take positive, negative or null values.

In order to perform a stability analysis, we need a synodic frame in wich all primaries remain in rest. With respect such a frame, the equations of motion are:

$$\frac{d^2\boldsymbol{r}_i}{dt^2} + 2\boldsymbol{\Omega} \times \frac{d\boldsymbol{r}_i}{dt} + \boldsymbol{\Omega} \times (\boldsymbol{\Omega} \times \boldsymbol{r}_i) = \frac{\partial U_i}{\partial \boldsymbol{r}_i} \qquad i = 1, \ldots, n$$

with $\boldsymbol{\Omega}$ a vector perpendicular to the plane containing the primaries, and its norm, $\tilde{\omega} = \|\boldsymbol{\Omega}\|$ is

$$\begin{aligned}\tilde{\omega}^2 &= 1 + \frac{\mu}{4} \sum_{k=1}^{n-1} |\csc\, k\theta| + \frac{2\epsilon_0}{\alpha} + \frac{\mu\epsilon_1}{4\alpha} \sum_{k=1}^{n-1} \frac{1}{\sin^2\, k\theta} \\ &= \omega^2 + \frac{2\epsilon_0}{\alpha} + \frac{\mu\epsilon_1}{12\alpha}\,(n^2 - 1)\end{aligned}$$

where ω^2 is the angular velocity corresponding to the Newtonian atraction, α is the radius of the ring and $\theta = \pi/n$.

Because of the geometry of the problem, it is convenient the use of cylindric coordinates (r, λ, z). The correspondig equations are

$$\left.\begin{aligned} \ddot{r}_j - r_j(\dot{\lambda}_j + \tilde{\omega})^2 &= \frac{\partial U_j}{\partial r_j}, \\ r_j\ddot{\lambda}_j + 2\dot{r}_j(\dot{\lambda}_j + \tilde{\omega}) &= \frac{1}{r_j}\frac{\partial U_j}{\partial \lambda_j}, \\ \ddot{z}_j &= \frac{\partial U_j}{\partial z_j}, \end{aligned}\right\} \qquad j = 1, \ldots, n \tag{2}$$

It is easy to prove that

$$r_j = 1, \quad \lambda_j = 2\theta j, \quad z_j = 0, \tag{3}$$

is an equilibrium solution of equations (2).

3 Linear stability of the equilibrium solution

As usual, in order to determine the linear stability, we slightly perturb the equilibrium. Let us introduce a new set of variables $\boldsymbol{\rho} = (\rho_1, \ldots, \rho_n)$, $\boldsymbol{\sigma} = (\sigma_1, \ldots, \sigma_n)$, $\boldsymbol{z} = (z_1, \ldots, z_n)$ in such way that

$$r_j = 1 + \rho_j, \quad \lambda_j = 2\theta j + \sigma_j, \quad z_j = z_j, \qquad j = 1, \ldots, n,$$

and the variational equations of (2) become

$$\begin{aligned} \ddot{\boldsymbol{\rho}} - 2\tilde{\omega}\dot{\boldsymbol{\sigma}} &= \tilde{\omega}^2\boldsymbol{\rho} + A\boldsymbol{\rho} + B\boldsymbol{\sigma}, \\ \ddot{\boldsymbol{\sigma}} + 2\tilde{\omega}\dot{\boldsymbol{\rho}} &= C\boldsymbol{\rho} + D\boldsymbol{\sigma}, \\ \ddot{\boldsymbol{z}} &= E\boldsymbol{z}, \end{aligned} \tag{4}$$

where A, B, C, D, E are the matrices which elements are the second partial derivatives of the force function evaluated at the equilibrium (3) (see [3]).

After some transformations, it is possible to reduce the complexity of the system (4). Indeed, the first $2n$ equations are linear in ρ_j, σ_j, but the system is coupled in those $2n$ variables. To uncouple the system, let us introduce the $n \times n$ complex matrix $\mathcal{F}$ with elements $\mathcal{F}_{lk} = \exp(2\theta lk\sqrt{-1})$. Its inverse matrix is simply $\mathcal{F}^{-1} = \bar{\mathcal{F}}/n$, with $\bar{\mathcal{F}}$ its conjugate matrix.

As proven by Pendse ([8]), this transformation uncouples the system (4) due to the fact that matrices A, B, C, D, and E are periodic of period n and, besides, matrices B and C are odd functions, whereas the remaining matrices A, D, and E are even.

If we use the matrix $\mathcal{F}$ to define the complex transformation

$$\boldsymbol{\rho} = \mathcal{F}\,\boldsymbol{\xi}, \quad \boldsymbol{\sigma} = \mathcal{F}\,\boldsymbol{\eta}, \quad \boldsymbol{z} = \mathcal{F}\,\boldsymbol{\zeta},$$

the system (4) is transformed into

$$\begin{aligned}
\ddot{\boldsymbol{\xi}} - 2\tilde{\omega}\,\dot{\boldsymbol{\eta}} &= \tilde{\omega}^2\boldsymbol{\xi} + \Lambda^A\,\boldsymbol{\xi} + \Lambda^B\,\boldsymbol{\eta},\\
\ddot{\boldsymbol{\eta}} + 2\tilde{\omega}\dot{\boldsymbol{\xi}} &= \Lambda^C\,\boldsymbol{\xi} + \Lambda^D\,\boldsymbol{\eta},\\
\ddot{\boldsymbol{\zeta}} &= \Lambda^E\,\boldsymbol{\zeta},
\end{aligned} \tag{5}$$

an uncoupled system with respect to their indices, where Λ^X is the diagonal matrix of eigenvalues of matrix X. Note also that the new complex variables satisfy $\bar{\xi}_j = \xi_{n-j}$, $\bar{\eta}_j = \eta_{n-j}$, $\bar{\zeta}_j = \zeta_{n-j}$, so we only deal with equations with scripts $j = 1, 2, \ldots, [n/2], n$, where $[a]$ denotes the integer part of a.

To compute the eigenvalues, we follow the procedure given by [9], based on the results provided by [8]. By proceeding in such way, we find

$$\begin{aligned}
\Lambda^A_j &= 2\tilde{\omega}^2 + \mu(2J_j - \frac{1}{4}\,L_j) + 2\epsilon_0 + 3\mu\epsilon_0(2 + S^A_j) + \frac{\mu\epsilon_1}{4}(\frac{1}{3}(n^2-1) - (P_j + 2Q_j)),\\
\Lambda^B_j &= \mathrm{i}\;\mu\left(J_j + \frac{1}{8}\,M_j + \epsilon_0\,S^B_j + \frac{\epsilon_1}{8}(P_{j+1} - P_{j-1})\right),\\
\Lambda^C_j &= \mathrm{i}\;\mu\left(2\,J_j - \frac{1}{8}\,M_j + 3\,\epsilon_0\,S^B_j - \frac{\epsilon_1}{8}(P_{j+1} - P_{j-1})\right),\\
\Lambda^D_j &= \mu\left(-J_j + \frac{1}{4}\,N_j - \epsilon_0\,(2 + S^A_j) + \frac{\epsilon_1}{4}(3P_j - 2Q_j)\right),\\
\Lambda^E_j &= -1 - 2\,\epsilon_0 - \mu\left(S_j + \frac{1}{12}\,(L_j + N_j) + \epsilon_0\,(2 + S^E_j) + \frac{\epsilon_1}{4}P_j\right),
\end{aligned}$$

where $L_j, M_j, N_j, J_j, S_j, P_j, Q_j, S^A_j, S^B_j, S^E_j$ are given in [3].

4 Stability analysis

The roots of the characteristic equation determine the linear stability of the system (5). In this system, the last n equations, those corresponding to variable $\boldsymbol{\zeta}$, depend only on $\boldsymbol{\zeta}$, whereas those corresponding to $\boldsymbol{\xi}$ and $\boldsymbol{\eta}$ are coupled. As a result, we split our analysis in two parts, one for the out-of-plane motion ($\boldsymbol{\zeta}$) and the other for the on-plane motion ($\boldsymbol{\xi}$ and $\boldsymbol{\eta}$).

4.1 Out-of-plane stability

The out-of-plane variations are determined by the equation:

$$\ddot{\boldsymbol{\zeta}} = \Lambda^E\,\boldsymbol{\zeta} = -\left[1 + 2\,\epsilon_0 + \mu\left(S + \frac{1}{12}\,(L + N) + \epsilon_0\,(2 + S^E) + \frac{\epsilon_1}{4}P_j\right)\right]\,\boldsymbol{\zeta},$$

therefore, the out-of-plane motion is stable when

$$1 + 2\,\epsilon_0 + \mu\left(S_j + \frac{1}{12}\,(L_j + N_j) + \epsilon_0\,(2 + S^E_j) + \frac{\epsilon_1}{4}P_j\right) > 0, \quad \forall\, j = 1, \ldots, [n/2], n \tag{6}$$

Note that $S, L, N, (2+S^E), P$ are non-negative quantities, so if ϵ_0 and ϵ_1 are positive, the stability condition (6) is always satisfied, hence vertical motions are linearly stable. For any values of ϵ_0 and ϵ_1 we have two different situations depending on the value of j:

a) $j = n$: $S_n = n$, $L_n = 0$, $N_n = 0$, $2 + S_n^E = 2\,n$, $P_n = 0$ and the stability condition is: $(1 + 2\,\epsilon_0)\,(1 + \mu\,n) > 0 \Longleftrightarrow 1 + 2\epsilon_0 > 0$.

b) $j \neq n$: $S_j = 0$, $2 + S_j^E = 0$, hence, the stability condition is

$$1 + 2\,\epsilon_0 + \mu\,\Big(\frac{1}{12}(L_j + N_j) + \frac{\epsilon_1 P_j}{4}\Big) > 0,$$

Now, for $\epsilon_0 > -1/2$ and $\epsilon_1 > 0$ all the conditions are satisfied. If $\epsilon_1 < 0$, the value is restricted to:

$$\epsilon_1 > -\frac{4\,(1 + 2\epsilon_0)}{\mu P_j} - \frac{N_j + L_j}{3P_j}$$

4.2 In-plane stability

Let us now consider the variational displacements on the plane containing the bodies. As it is known [3], the stability of this linear system is determined by the purely imaginary roots, $(\,\mathrm{i}\,\tilde{\omega}\,x)$, of its characteristic equation, where x must be a real root of the quartic equation

$$x^4 - q\,x^2 + r\,x + s = 0, \tag{7}$$

whose coefficients q, r, s (for each script j) are functions of the eigenvalues of the matrices A, B, C, D, and E (see [3]).

For $j = n$, we have

$$2 + S_n^A = 0,\ S_n^B = 0,\ S_n = n,\ L_n = M_n = N_n = C_n = J_n = 0,$$
$$P_n^- - P_n^+ = 0, \quad P_n = 0, \quad Q_n = 0$$

and the polynomial equation (7) is reduced to

$$x^4 - \Big(1 - \frac{2\epsilon_0}{\tilde{\omega}^2} - \frac{\mu\,\epsilon_1}{12\tilde{\omega}^2}(n^2 - 1)\Big)\,x^2 = 0.$$

Their four roots, namely

$$0, 0, +\sqrt{1 - 2\epsilon_0/\tilde{\omega}^2 - \frac{\mu\,\epsilon_1}{12\tilde{\omega}^2}(n^2-1)}, -\sqrt{1 - 2\epsilon_0/\tilde{\omega}^2 - \frac{\mu\,\epsilon_1}{12\tilde{\omega}^2}(n^2-1)}$$

are real because we recall $\tilde{\omega}^2 = \omega^2 + 2\epsilon_0 + \frac{\mu\,\epsilon_1}{12}(n^2 - 1)$. Consequently, we only need to analyze the cases for the scripts $j = 1, \ldots, [n/2]$. The following three conditions must be fulfilled (see [2]):

$$q > 0, \tag{8}$$

$$\Gamma = 2q(q^2 - 4s) - 9r^2 > 0, \tag{9}$$

$$\Delta = 4q^3r^2 - 27r^4 + 16q^4s - 144qr^2s - 128q^2s^2 + 256s^3 > 0. \tag{10}$$

5 Stability domains

In this section we analyze the stability for two cases, namely a) $\epsilon_0 = 0, \epsilon_1 \neq 0$ and b) $\epsilon_0 \neq 0, \epsilon_1 \neq 0$, in order to complete the work done in [2] where we considered the case c) $\epsilon_0 \neq 0, \epsilon_1 = 0$. The procedure we follow is the same that the one described in [2].

5.1 Stability regions for $\epsilon_0 = 0, \epsilon_1 \neq 0$

In this case, the central body is a point whereas the surrounding bodies are spheroids or radiating bodies (i.e. under Manev's type force). In Fig. (1) we present the stability region on the parametric plane (ϵ_1, μ) for $n = 6$ (left) and $n = 7$ (right). Note that when $\epsilon_1 = 0$ we recover the classical result, that is, for $n = 6$ the system is unstable whereas for $n = 7$ we have stability for $\mu < 0.007150403074$. Besides, it is shown that there are values of ϵ_1 where we get stability, but the upper bound of μ for stability decreases when ϵ_1 increases.

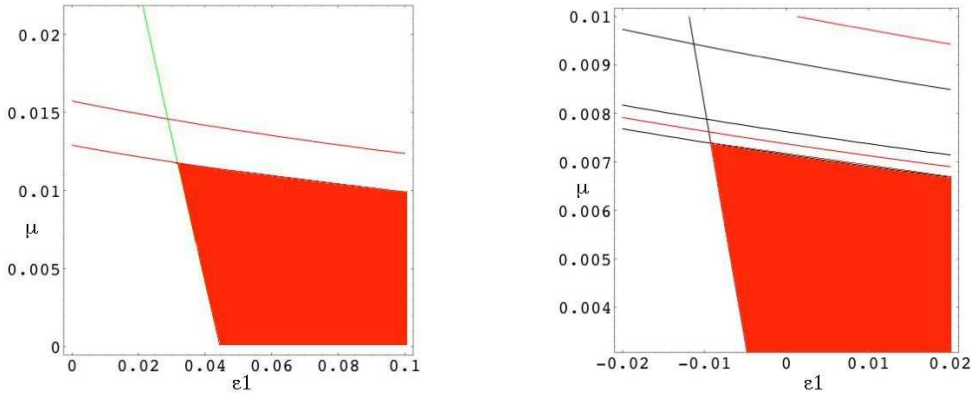

Figure 1.— Stability regions for $n = 6$ (left) and $n = 7$ (right) when $\epsilon_0 = 0$

5.2 Stability regions for $\epsilon_0 \neq 0, \epsilon_1 \neq 0$

The results presented in this section correspond to the case $n = 7$, since this is the first case of possible stability for the classical problem (Newtonian forces). For another different number of bodies the procedure is the same. Besides, as illustration of the behavior when every body acts Manev's forces, we take only three cases ($\epsilon_1 = -0.05$, 0, 0.05) for bodies on the circle and make the 2-D plot on the plane (ϵ_0, μ). The corresponding stability regions are represented in Fig. (2) and show a similar aspect, although we can conclude that the size of the stability area decreases with ϵ_1. Besides, for a certain value of ϵ_0 given, the stability value of the mass factor μ also decreases with ϵ_1.

The aim of this paper is to analize the possibility of increasing the interval of values of μ and ϵ_0 having a stable configuration. In fact, the upper bound for these two parameters

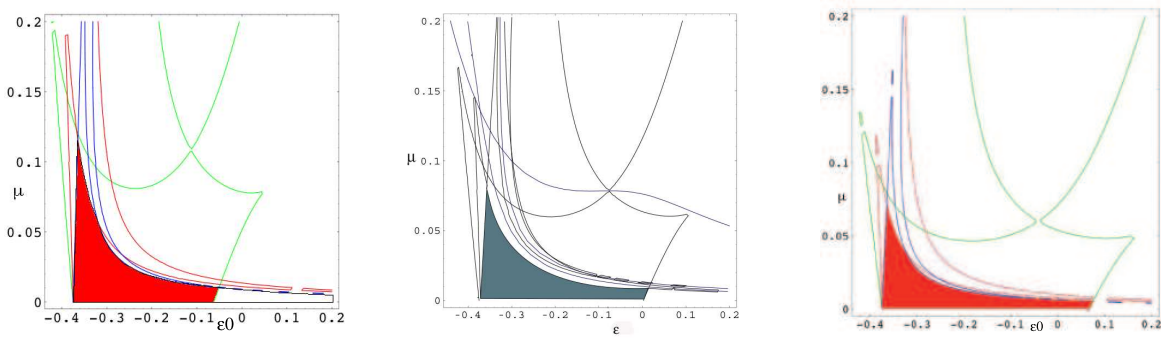

Figure 2.— Stability region: $n = 7$, $\epsilon_1 = -0.05$(l), $\epsilon_1 = 0$(c) and $\epsilon_1 = 0.05$(r)

can be increased as it can see in Fig.(2): in the graphic on the left the bound for μ is increased having negative values of ϵ_1 and in the graphic on the right the interval of possible values of ϵ_0 is bigger when we take positive values for ϵ_1 than if we do not take into account this parameter.

In Fig.(3) we show the stability region for two values of ϵ_0: one that corresponds to stability (l) and another that corresponds to unstability (r) when $\epsilon_1 = 0$. We get stability for values of $\epsilon_1 > 0$ but the value of μ has to decrease when ϵ_1 increases. The value of μ is increased only if we consider negative values of the parameters.

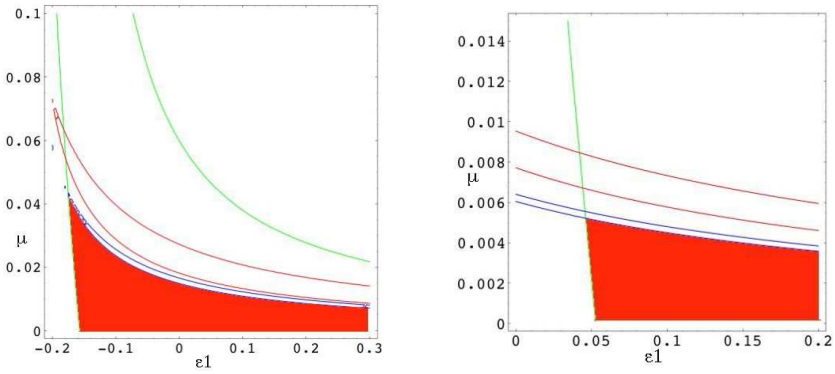

Figure 3.— Stability region for $\epsilon_0 = -0.2$ (l) and $\epsilon_0 = 0.07$ (r)

Finally, we may have values of μ for which the system is unstable, however, we could adjust the values either of the parameter ϵ_0 or ϵ_1 or both in order to have stability. For instance, in the Newtonian case ($\epsilon_0 = \epsilon_1 = 0$, and again $n = 7$) the system is stable for $0 < \mu < 0.007150403074$. Is it possible to find values of ϵ_0 and ϵ_1 in order to have stability for a grater value of μ, let say $\mu = 0.04$. The answer is positive as we can see in Fig. (4), where we plot for $\mu = 0.04$ the stability region on the plane (ϵ_0, ϵ_1).

Acknowledgments

Supported by the Spanish Ministry of Science and Technology (Projects # MTM2009-10767 and # AYA2008-05572).

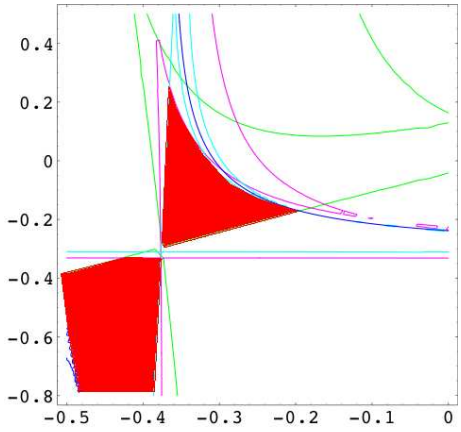

Figure 4.— Stability region in the plane (ϵ_0, ϵ_1) for $\mu = 0.04$

References

[1] M. Arribas, A. Elipe, T. Kalvouridis, and M. Palacios, *Homographic solutions in the planar n + 1 body problem with quasi-homogeneous potentials*, Celest. Mech. Dyn. Astr., 99 (2007), pp. 1–12.

[2] M. Arribas, A. Elipe, and M. Palacios, *Linear stability of ring systems with generalized central forces*, Astron. Astrophys., 489 (2008), pp. 819–824.

[3] M. Arribas, A. Elipe, and M. Palacios, *Linear stability in a extended ring system*, AIP Conf. Proc. 1283, pp. 128–136 (2010), DOI:10.1063/1.3506047

[4] R. Cid and A. Elipe, *On the motion of three rigid bodies. central configurations*, Celest. Mech. Dyn. Astr., 37 (1985), pp. 113–126.

[5] R. Cid, S. Ferrer, and A. Elipe, *Regularization and linearization of the equations of motion in central force field*, Celest. Mech. Dyn. Astr., 31 (1983), pp. 73–80.

[6] F. Diacu, E. Pérez-Chavela, and M. Santoprete, *The Kepler problem with anisotropic perturbations*, J. Math. Phys. 46 (2005), no. 7, 072701, 21 pp.

[7] R. J. Vanderbei, *Linear stability of ring systems around oblate central masses*, J. Adv. Space Res. 42 (2008), no. 7, pp. 1370–1377.

[8] C. G. Pendse, *The theory of Saturn's rings*, Phil. Trans. Roy. Soc., CCXXXIV–A (1935), pp. 145–177.

[9] D. J. Scheeres and N. X. Vinh, *Linear stability of a self-gravitating ring*, Celest. Mech. Dyn. Astr., 51 (1991), pp. 83–103.

[10] A. Wintner, *The Analytical Foundations of Celestial Mechanics.*, Princeton University Press, Princeton, (1947).

Monografías de la Real Academia de Ciencias de Zaragoza **35**, 21–26, (2011).

Cascade of n-round homoclinic orbits to a center×saddle

E. Barrabés[1], J. M. Mondelo[2] and M. Ollé[3]

[1] Dept. Informàtica i Matemàtica Aplicada Universitat de Girona
Avd. Lluís Santaló s/n, 17071 Girona, Spain.
[2] Dept. Matemàtiques, Universitat Autònoma de Barcelona,
08193 Bellaterra, Barcelona, Spain.
[3] Dept. Matemàtica Aplicada I. Universitat Politècnica de Catalunya,
Diagonal 647, 08028 Barcelona, Spain.

Abstract

We consider a Hamiltonian system with two degrees of freedom depending on a parameter, having an equilibrium point, p, of center×saddle type. We assume there is a homoclinic orbit to p. We explore the phenomenon of cascade of n-round homoclinic orbits when varying the parameter. Explicit computations are shown for the collinear equilibrium point L_3 of the planar restricted three-body problem.
Key words and expressions: equilibrium point, homoclinic orbits

1 Preliminaries and setting of the problem

In this work, we consider the existence of homoclinic orbits to a center×saddle equilibrium point of a given Hamiltonian system. We recall that homoclinic and heteroclinic connections of hyperbolic objects (equilibrium points being the simplest ones) play an important role when studying a dynamical system from a global point of view. In particular they are relevant in applications to Celestial Mechanics and Astrodynamics, more particularly in the design of libration point missions (see [4], [5], [7], [14] and references therein).

The general setting considered from now on is the following: we assume that we have a real analytic Hamiltonian $H(x;\mu)$ of two degrees of freedom, depending on a parameter μ, such that for all values of the parameter the origin is an equilibrium point of center×saddle type, i.e., the eigenvalues of the Jacobian matrix of the Hamiltonian vector field, X_H, at the origin are $\pm i\omega$, $\pm\lambda$ with $\omega\lambda \neq 0$, $\omega, \lambda \in R$. Let us denote by $H_0 = H(0)$ and let us consider the one-dimensional manifolds, stable W^s and unstable

W^u, and the corresponding branches W^s_+, W^s_-, W^u_+, W^u_-, associated with the origin. Due to the Lyapunov theorem (see [12]), we know that for each value of H close to H_0, there is an unstable periodic orbit. When varying H, we obtain the so called Lyapunov family of periodic orbits associated with the equilibrium point.

Let us assume now that, for a particular value of the parameter, say μ_1, one branch of W^s coincides with one branch of W^u, giving rise to a homoclinic orbit, Γ, to the origin. Two natural questions appear in this context:

1. How is the dynamics close to the homoclinic orbit Γ?

2. What happens to the homoclinic orbit when we consider values of the parameter in a neighborhood of μ_1?

Several authors have studied question 1. Maybe the first one was Conley ([2]) in the context of the planar RTBP taking the mass parameter as a natural parameter. We also mention the paper by Llibre et al. (see [11]) where they consider the same problem and prove the existence of homoclinic orbits to the collinear equilibrium point L_2 as well as the transversal intersection of the stable and unstable manifolds of the Lyapunov periodic orbits.

In a general analytic Hamiltonian, in the paper by Koltsova and Lerman [8], the authors prove, under generic conditions, two important results for $\mu = \mu_1$:

- the existence of countable families of periodic orbits accumulating to the homoclinic orbit and lying on the same energy level as the center×saddle, and

- the existence of homoclinic orbits to each hyperbolic Lyapunov periodic orbit.

In the 3 degree-of-freedom Hamiltonian case, given an equilibrium point of center×-center×saddle type, we can regard a homoclinic orbit to the equilibrium point not only as the skeleton of homoclinic orbits to periodic orbits closeby, but also of 2d-invariant tori (see [10]).

In order to answer the second question, we must introduce n-round homoclinic orbits. We define a homoclinic orbit to the origin to be n-round if it enters and also leaves some small neighborhood of the origin n times; in each path outside this neighborhood, it more or less follows the homoclinic orbit Γ (see [6]). In this context, we consider the set of values of the parameter μ in a neighborhood of μ_1, and we define the set

$$\Lambda_n = \{\mu > 0 \,/\, \text{ there exists an } n\text{-round homoclinic orbit to the origin}\}.$$

The most complete investigation of n-round homoclinic orbits to a center×saddle in a one-parameter unfolding of reversible two-degree-of-freedom Hamiltonian systems was accomplished in [6] and [13]. An alternative proof for 2-round and 3-round homoclinic

orbits was carried out in [8], and revisited in [9] for n-round homoclinic orbits, for $n = 2, 3$, and $n = m2^k$, $m = 2, 3$ and $k \in N$. Roughly speaking, the main result may be stated as follows: given $\mu_1 \in \Lambda_1$, there exist values of $\mu \in \Lambda_n$, close enough to μ_1, for all $n > 1$ (see [13]).

The purpose of this work is to show numerical evidence of this result in the context of the restricted three-body problem. For the details of the computations done, the reader is referred to [1].

2 Example: the planar RTBP. Homoclinic orbits to L_3.

Now we consider the planar circular RTBP, whose well known Hamiltonian function, depending on the mass parameter $\mu \in (0, 1/2]$, is

$$H(x, y, p_x, p_y) = \frac{1}{2}(p_x^2 + p_y^2) - xp_y + yp_x - \frac{1-\mu}{r_1} - \frac{\mu}{r_2} + \frac{1}{2}\mu(1-\mu)$$

with $r_1 = \sqrt{(x-\mu)^2 + y^2}$ and $r_2 = \sqrt{(x-\mu+1)^2 + y^2}$. We may also consider the equations of motion in the rotating (non canonical) coordinates $x, y, x' = p_x + y, y' = p_y - x$ (see [15])

$$\begin{aligned} x'' - 2y' &= D_x\Omega(x, y), \\ y'' + 2x' &= D_y\Omega(x, y), \end{aligned} \tag{1}$$

where

$$\Omega(x, y) = \frac{1}{2}(x^2 + y^2) + \frac{1-\mu}{r_1} + \frac{\mu}{r_2} + \frac{1}{2}\mu(1-\mu).$$

The system of equations (1) has a first integral, called the Jacobi integral, which is given by

$$\mathcal{C} = 2\Omega(x, y) - x'^2 - y'^2. \tag{2}$$

This C value is related to H by $C = -2H + \mu(1-\mu)$ Furthermore, we recall that equations (1) satisfy the well known symmetry

$$(t, x, y, x', y') \longrightarrow (-t, x, -y, -x', y'). \tag{3}$$

This implies that, for each solution of equations (1), there also exists another one, which is seen as symmetric with respect to $y = 0$ in configuration space.

We also recall that the RTBP has five equilibrium points: the collinear points, L_1, L_2 and L_3, situated on the line containing the primaries, and the equilateral ones, L_4 and L_5, both forming equilateral triangles with the two primaries. We will consider that $x_{L_2} \leq \mu - 1 \leq x_{L_1} \leq \mu \leq x_{L_3}$, that is, L_1 is between both primaries, L_2 is on the left hand side of the small one and L_3 is on the right hand side of the large one.

We will concentrate on the collinear equilibrium point L_3. It is well known that, if we write the differential equations (1) as

$$\mathbf{x}' = \mathbf{X}(\mathbf{x})$$

then Spec $DX(L_i) = \{\pm i\omega, \pm\lambda\}$, so the equilibrium point L_i, $i = 1, 2, 3$ is a center×saddle point. In this case W^u_+, W^u_- are the two branches of the unstable manifold of L_3, whose (x, y) projection lies (when $t \to -\infty$) on the $y > 0$ and $y < 0$ region respectively and, similarly, W^s_+ and W^s_-. If, for a given value of μ, the unstable and stable manifolds intersect, they give rise to a homoclinic connection to L_3.

So, our setting now is the RTBP with one parameter, μ, and L_3 (instead of the origin in the previous Section) being the associated equilibrium point for a given $\mu \in (0, \mu/2]$. We say that a value μ belongs to Λ_n if for that μ there exists an n-round *symmetric* homoclinic orbit (SHO from now on) to L_3.

Our aim in this Section is, on the one hand, to numerically illustrate the existence of values of $\mu \in \Lambda_1$; and, on the other hand, given a fixed value of $\mu = \mu_1 \in \Lambda_1$, to display sequences of values in Λ_n tending to μ_1, for any $n > 1$. Of course we cannot explore *all* the values of n; we will only take the cases $n = 2, 3, 4$.

An easy strategy to detect SHO is simply the following: we consider $\Sigma = \{y = 0\}$ as surface of section and, for a given μ, denote by $x'_j(\mu)$ the x' coordinate of the j–th intersection of a branch of a manifold of L_3 (we will take from now on W^u_-) with Σ. If this j–th cut is orthogonal, that is,

$$x'_j(\mu) = 0, \tag{4}$$

the application of symmetry (3) to a trajectory following W^u_- up to its j–th cut with $y = 0$ forward in time will give rise to a symmetric trajectory following W^s_+ backward in time and therefore becoming a SHO.

Let us start analyzing the set Λ_1. We vary the μ parameter and we consider the function $x'_1(\mu)$ given in Fig. 1 left. Its behavior provides numerical evidence of the existence of a decreasing sequence of values of $\mu^1_n \in \Lambda_1$, with $\mu^1_1 < 0.01$ and $\mu^1_n \to 0$ when $n \to \infty$ (see [3] for an expression of such values). For any given value of μ^1_n, the corresponding (x, y) projection of the SHO typically surrounds once L_4 and L_5 describing a horseshoe–shaped orbit. See Fig. 1 right.

We plot the functions $x'_2(\mu)$ in Fig. 2. We can see that there are sequences of values in Λ_2 tending (on each side) to each value in Λ_1, and therefore providing the values of μ for 2-round SHO.

In a similar way, we plot in Fig. 3 the functions $x'_3(\mu)$ and $x'_4(\mu)$ in the neighborhood of a fixed value of $\mu \in \Lambda_1$, denoted by μ_1. We see again the existence of sequences of values of $\mu \in \Lambda_3$ and Λ_4 tending to μ_1.

As a final remark, we note that the jumps observed in the curves $x'_j(\mu)$, $j = 1, 2, 3, 4$, in the different figures can also be analysed graphically in detail. This has been done in [1].

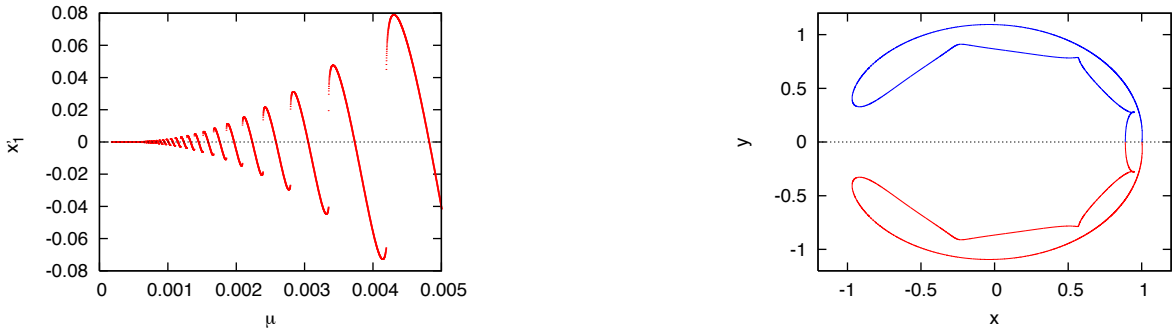

Figure 1.— Left. Function $x_1'(\mu)$. Right. Homoclinic invariant manifold –(x, y) projection– for $\mu = 0.0037257851523$.

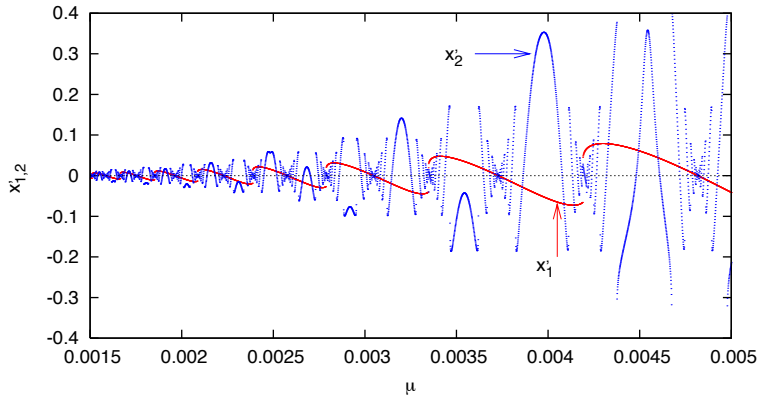

Figure 2.— Functions $x_1'(\mu)$ (in red) and $x_2'(\mu)$ (blue).

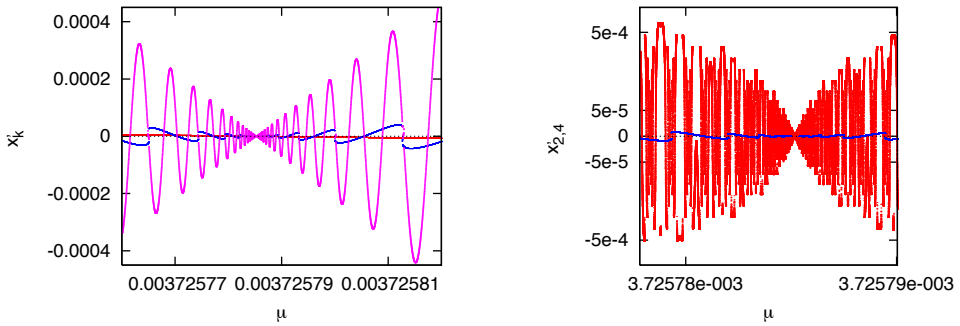

Figure 3.— Left: functions $x_k'(\mu)$, for $k = 1$ (in red), $k = 2$ (in blue), $k = 3$ (in magenta). Right. Functions $x_2'(\mu)$ and $x_4'(\mu)$. For display purposes, the function x_4' has been rescaled using the arcsinh(x) function, and the y axis has been labeled accordingly.

Acknowledgments

E. Barrabés and J.M. Mondelo are partially supported by the MCyT/FEDER grant MTM2006-05849/Consolider. J.M. Mondelo is also supported by the MCyT/FEDER grant MTM2008-01486 M. Ollé is partially supported by MICINN-FEDER grant MTM2009-06973 and CUR-DIUE grant 2009SGR859.

References

[1] E. Barrabés, J. M. Mondelo, and M. Ollé. Dynamical aspects of multi-round horseshoe-shaped homoclinic orbits in the RTBP. *Celest. Mech. Dyn. Astr.*, 105:197–210, 2009.

[2] C. Conley. Low energy transit orbits in the restricted three-body problem. SIAM J. Appl. Math., 16:732–746, 1968.

[3] J. Font. The role of homoclinic and heteroclinic orbits in two-degrees of freedom Hamiltonian systems. *Ph. D. Thesis*, Barcelona University, 1999.

[4] G. Gómez, J. J. Masdemont, and J. M. Mondelo. Libration Point Orbits: A survey from tye dynamical point of view. In G. Gómez, M. W. Lo, and J. J. Masdemont (Eds.), *Libration Point Orbits and Applications*. World Scientific, 2003.

[5] G. Gómez, W. S. Koon, M. W. Lo, J. E. Marsden, J. Masdemont, S.D. Ross. Connecting orbits and invariant manifolds in the spatial restricted three-body problem. *Nonlinearity*, 17:1571–1606, 2004.

[6] C. Grotta Ragazzo. Irregular dynamics and homoclinic orbits to Hamiltonian saddle centers. *Comm. Pure Appl. Math. 50*(2), 105–147, 1997.

[7] K. C. Howell, B. T. Barden, R. S. Wilson, and M. W. Lo. Trajectory design using a dynamical systems approach with application to GENESIS. *Advances in the Astronautical Sciences 97*, 1665–1684, 1998.

[8] O. Y. Koltsova and L. M. Lerman. Periodic and homoclinic orbits in a two-parameter unfolding of a hamiltonian system with a homoclinic orbit to a saddle-center. *Int. J. Bifurcation and Chaos 5*(2), 397–408, 1995.

[9] O. Y. Koltsova. Families of multi-round homoclinic and periodic orbits near a saddle-center equilibrium. *Regul. Chaotic Dyn. 8*(2), 191–200, 2003.

[10] O. Y. Koltsova, L. Lerman, A. Delshams, and P. Gutiérrez. Homoclinic orbits to invariant tori near a homoclinic orbit to center-center-saddle equilibrium. *Phys. D 201*(3-4), 268–290, 2005.

[11] J. Llibre, R. Martínez, and C. Simó. Transversality of the invariant manifolds associated to the Lyapunov family of periodic orbits near L_2 in the restricted three-body problem. *J. Differential Equations 58*(1), 104–156, 1985.

[12] K. Meyer, G. Hall. Introduction to Hamiltonian Dynamical systems and the N-Body Problem, Ed Springer-Verlag, 1991.

[13] A. Mielke, P. Holmes, and O. O'Reilly. Cascades of homoclinic orbits to, and chaos near, a Hamiltonian saddle-center. *J. Dynam. Differential Equations 4*(1), 95–126, 1992.

[14] J. S. Parker and M. W. Lo. Shoot the moon 3D. *Advances in the Astronautical Sciences 123*, 2067–2086, 2006.

[15] V. Szebehely. *Theory of orbits.* Academic Press, 1967.

Monografías de la Real Academia de Ciencias de Zaragoza **35**, 27–39, (2011).

A note on some exact analytical solutions of the rotation of a rigid body with a external torque

M. Calvo, J.M. Franco, J.I. Montijano and L. Rández

Departamento Matemática Aplicada

Universidad de Zaragoza. 50009-Zaragoza, Spain.

Abstract

In two recent papers of M. Romano (Cel. Mech. 100: 181–189, 2008 and Cel. Mech. 101: 375–390, 2008) this author has derived new exact analytical solutions that describe both the dynamic and kinematic behavior a rigid body around a fixed point with spherical and symmetric ellipsoids of inertia self excited by some special torques in the fixed body reference frame. The aim of this note is to give an alternative simplified derivation of these solutions by using the symmetries of the system and suitable matrix transformations and to show that a wider class of analytical solutions may be derived.

1 Introduction and basic notations.

The motion of a rigid body around a fixed point is a classical problem of Mechanics that has been studied by many relevant mathematicians for more than two centuries. It is worth to mention the earlier contributions of Euler, during his stay in Berlin (1741–1766), in which he made a precise formulation of the differential equations of this problem and obtained some particular analytical solutions. They were published in several papers of the Royal Academie of Berlin (1751–1767). Later all these researches were published together in 1765 in Chapters 10th and 15th of the treatise: "Theoria Motus Corporum Solidorum seu Rigidorum". Many well known mathematicians like Poinsot, Lagrange, Jacobi, T. Levi-Civita, F. Klein, Kovalevskaya among others have studied for about two centuries some aspects and particular cases of the problem mainly concerned with the existence of first integrals, the integrability of these equations and the stability of some particular solutions.

Although the classical studies about the motion of the rigid body have been almost closed by more than a century, recent practical applications have open new problems in

some fields such as robotics, spatial dynamics and molecular dynamics. Further actual computers have led to a substantial revision of classical algorithms used in the practical computation of solutions of these problems. Finally, since rigid body problems usually possess first integrals and sometimes periodic solutions (both stable and instable) their differential equations are excellent test problems for new numerical integrators of ODEs.

We will consider the rotational motion of a rigid body around a fixed point that will be taken as the origin O of two coordinates systems: A body fixed frame $\mathcal{B}$ with the axes directed along the principal axes of the ellipsoid of inertia of the body and an inertial fixed frame $\mathcal{I}$. In the remainder we will assume that the transformation from the inertial to the body frame is sufficiently smooth (of class $\mathcal{C}^p, p \geq 2$ in some interval of $\mathbb{R}$ but for simplicity we will take all $\mathbb{R}$) so that the coordinates $\mathbf{x}_\mathcal{I}$ and $\mathbf{x}_\mathcal{B}$ of a given vector in the corresponding systems satisfy

$$\mathbf{x}_\mathcal{I} = R(t)\, \mathbf{x}_\mathcal{B}, \tag{1}$$

where $R(t) = R_{\mathcal{I}\mathcal{B}}(t) \in \mathcal{C}^p$ is an orthogonal matrix of determinant $+1$. Clearly the columns of $R(t)$ give us the components of the unit vectors of the moving frame in the inertial frame.

Since $R(t)^T\, R(t) = I$ for all t, $R(t)^T\, R'(t) = \Sigma_R$ is a skew symmetric matrix that will be denoted by

$$R^{-1}R' = \begin{pmatrix} 0 & -w_3(t) & w_2(t) \\ w_3(t) & 0 & -w_1(t) \\ -w_2(t) & w_1(t) & 0 \end{pmatrix} = \Sigma(\mathbf{w}(t)). \tag{2}$$

It is important to note that $\mathbf{w} = (w_1(t), w_2(t), w_3(t))^T$ behaves as a vector under linear time independent transformations. In fact under a change of coordinates $\mathbf{x} \to P\mathbf{x}$ it is easy to show that $R \to PRP^{-1}$, $\Sigma \to P\Sigma P^{-1}$ and $\mathbf{w} \to P\mathbf{w}$.

The vector with components in the body frame $\mathbf{w}_\mathcal{B} = (w_1, w_2, w_3)^T$, is usually referred to as the instant angular velocity, and for all vector $\mathbf{v}_\mathcal{B}$ we have

$$\Sigma(\mathbf{w}_\mathcal{B})\, \mathbf{v}_\mathcal{B} = \mathbf{w}_\mathcal{B} \times \mathbf{v}_\mathcal{B}, \tag{3}$$

where $\times$ denotes the cross product and the signs in (2) have been chosen so that (3) holds.

Note that when R is a time dependent rotation around the x_3-axis, with angle $\phi = \phi(t)$

$$R(t) = \begin{pmatrix} \cos\phi & -\sin\phi & 0 \\ \sin\phi & \cos\phi & 0 \\ 0 & 0 & 1 \end{pmatrix}, \quad \text{and} \quad \mathbf{w} = (0, 0, \phi')^T,$$

and similarly for the rotations around the other axes.

Recall that in the inertial frame the basic equation of the dynamics of a rigid body with a fixed point O is

$$\frac{\mathrm{d}}{\mathrm{d}t}\mathbf{L}_{\mathcal{I}} = \mathbf{M}_{\mathcal{I}}, \tag{4}$$

where the vectors $\mathbf{L}_{\mathcal{I}} = \mathbf{L}_{\mathcal{I}}(t)$ and $\mathbf{M}_{\mathcal{I}} = \mathbf{M}_{\mathcal{I}}(t)$ are the angular momentum and the total external torque with respect to O. By using (1), this basic equation with respect to the body frame becomes

$$\frac{\mathrm{d}}{\mathrm{d}t}\mathbf{L}_{\mathcal{B}} + \mathbf{w}_{\mathcal{B}} \times \mathbf{L}_{\mathcal{B}} = \mathbf{M}_{\mathcal{B}}, \tag{5}$$

where $\mathbf{w}_{\mathcal{B}} = \mathbf{w}_{\mathcal{B}}(t)$ is the angular velocity of the body in the body frame with the components defined by (2).

Since the body frame has the axes directed along the principal axes of the ellipsoid of inertia $\mathbf{L}_{\mathcal{B}} = \mathbf{I}\ \mathbf{w}_{\mathcal{B}}(t) = (I_1 w_1, I_2 w_2, I_3 w_3)^T$ where $\mathbf{I} = \mathrm{diag}\ (I_i)$, and putting $\mathbf{M}_{\mathcal{B}} = (M_1, M_2, M_3)^T$, equation (5) can be written as

$$\begin{aligned} I_1 w_1' - (I_2 - I_3) w_2 w_3 &= M_1, \\ I_2 w_2' - (I_3 - I_1) w_3 w_1 &= M_2, \\ I_3 w_3' - (I_1 - I_2) w_1 w_2 &= M_3, \end{aligned} \tag{6}$$

which are the well known Euler's equations that describe the dynamics of the rigid body around O with respect to $\mathcal{B}$.

In addition to (6) we have the kinematic equations that describe the orientation of the body frame $\mathcal{B}$ with respect to the inertial frame $\mathcal{I}$ that according to (2) are

$$R'(t) = R(t)\ \Sigma(\mathbf{w}_{\mathcal{B}}(t)). \tag{7}$$

This is a linear matrix equation with the components of Σ given after solving (6) and the unknown matrix function $R(t)$ which is orthogonal for all t and therefore depends on three free parameters.

Several analytical solutions have been obtained for special mass distributions and/or torques. In the Euler-Poinsot case of a free body $\mathbf{M} = 0$ and equations (6) can be solved in terms of elliptic functions and when the kinematic equations are written in terms of Euler angles the integration can be reduced to quadratures. For a symmetric rigid body with fixed point which is different from its center of mass under the gravity force the Lagrange-Poisson and Kovalevskaya heavy top cases are two well known examples of integrable problems.

Concerning the integration of (7) it is worth to mention that some authors say that the solution of the linear kinematic equations (7) can be written in the matrix form

$$R(t) = R(0)\ \exp\left(\int_0^t \Sigma(\mathbf{w}_{\mathcal{B}}(s))\,\mathrm{d}s\right), \tag{8}$$

and therefore the solution reduces to quadratures. However, as follows from the theory of matrix functions, (8) is the solution of (7) only when

$$\Sigma(\mathbf{w}_{\mathcal{B}}(t)) \quad \text{and} \quad \int_0^t \Sigma(\mathbf{w}_{\mathcal{B}}(s))\,\mathrm{d}s \qquad \text{commute.} \tag{9}$$

In this note we will consider some cases of the motion of a rigid body around a fixed point under some prescribed torques studied recently by Romano in [2], [3]. We will show that taking into account the assumed symmetries of these problems it is possible to simplify the derivation of the analytical solution of the corresponding kinematic equations.

2 Rigid body with a spherical ellipsoid of inertia under a constant torque in $\mathcal{B}$

Suppose a rigid body with $I_1 = I_2 = I_3 = I$ under a constant torque $\mathbf{M}_{\mathcal{B}} = \mu\ \mathbf{u}_{\mathcal{B}}$ in the body frame $\mathcal{B}$ with $\mu = \|\mathbf{M}_{\mathcal{B}}\|_2$ and $\mathbf{u}_{\mathcal{B}}$ a unit vector in the direction of the torque. Note that we are considering bodies with spherical dynamic symmetry and this class of bodies contain the class of bodies with geometric axial symmetry.

By the spherical symmetry, Euler equations (5) in the body frame are

$$I\ \frac{\mathrm{d}\mathbf{w}_{\mathcal{B}}}{\mathrm{d}t} = \mu\ \mathbf{u}_{\mathcal{B}},$$

with the solution

$$\mathbf{w}_{\mathcal{B}}(t) = \mathbf{w}^0_{\mathcal{B}} + t\, I^{-1}\, \mu\ \mathbf{u}_{\mathcal{B}}, \tag{10}$$

where $\mathbf{w}^0_{\mathcal{B}}$ is the initial angular velocity of the body at the initial time $t = 0$ in the body frame $\mathcal{B}$.

To obtain a complete analytical solution we must solve the linear matrix system (7) with a given $R(0)$ where $\mathbf{w}_{\mathcal{B}}(t)$ is the affine function (10).

More generally, for given constant vectors $\mathbf{a}$ and $\mathbf{b} \in \mathbb{R}^3$ we will obtain the solution of

$$R'(t) = R(t)\ \Sigma(\mathbf{a} + t\ \mathbf{b}), \qquad \text{with a given } R(0). \tag{11}$$

First of all if $\mathbf{a}$ and have the same direction $\mathbf{b} = \nu\ \mathbf{a}$ and this implies that $\Sigma(\mathbf{a} + t\ \mathbf{b}) = (1 + \nu\ t)\ \Sigma(\mathbf{a})$. Hence

$$\exp\left(\int_0^t \Sigma(\mathbf{a} + s\ \mathbf{b})\ \mathrm{d}s\right) \quad \text{and} \quad \Sigma(\mathbf{a} + t\ \mathbf{b}),$$

commute and the solution of (11) is

$$R(t) = R(0)\ \exp\left[(t + \nu t^2/2)\Sigma(\mathbf{a})\right]. \tag{12}$$

For the explicit computation of the exponential in (12) we may use the well known formula

$$\exp(S) = I + \left(\frac{\sin\delta}{\delta}\right)\ S + \left(\frac{1 - \cos\delta}{\delta^2}\right)\ S^2, \tag{13}$$

where

$$S = \begin{pmatrix} 0 & -s_3 & s_2 \\ s_3 & 0 & -s_1 \\ -s_2 & s_1 & 0 \end{pmatrix}, \qquad \delta^2 = s_1^2 + s_2^2 + s_3^2. \tag{14}$$

If $\mathbf{a}$ and $\mathbf{b}$ do not have the same direction we will make some time independent transformations to simplify the vector $\mathbf{a} + t\mathbf{b}$ as much as possible. Let $\beta \in [-\pi, \pi]$ and $\alpha \in [0, 2\pi)$ be the polar coordinates of the unit vector $\mathbf{b}$ so that

$$\mathbf{b} = \|\mathbf{b}\| \, (\sin\beta\cos\alpha, \sin\beta\sin\alpha, \cos\beta). \tag{15}$$

We will make the orthogonal transformation $\mathbf{x} \to S_1\mathbf{x}$ with

$$S_1 = \begin{pmatrix} \cos\beta & 0 & -\sin\beta \\ 0 & 1 & 0 \\ \sin\beta & 0 & \cos\beta \end{pmatrix} \begin{pmatrix} \cos\alpha & \sin\alpha & 0 \\ -\sin\alpha & \cos\alpha & 0 \\ 0 & 0 & 1 \end{pmatrix}, \tag{16}$$

that maps

$$\mathbf{b} \quad \to \quad S_1 \, \mathbf{b} = \begin{pmatrix} 0 \\ 0 \\ \mu \end{pmatrix} = \mu \, \mathbf{e}_3,$$

where $\mathbf{e}_3$ is the unit vector along the third axis and $\mu = \|\mathbf{b}\|$.

It must be observed that, by the assumed spherical ellipsoid of inertia, the principal axes of inertia of the rigid body could be chosen with arbitrary orientation, in particular with the x_3-axis in the direction of the torque, however we will consider here the kinematic equations independently of the rigid body because they will be used in other problems without such a spherical symmetry.

As remarked above the argument $\mathbf{w}$ of $\Sigma(\mathbf{w})$ behaves as a vector in changes of coordinates and therefore

$$\mathbf{a} + t \, \mathbf{b} \quad \to \quad S_1 \, (\mathbf{a} + t \, \mathbf{b}) = S_1 \, \mathbf{a} + \, \mu \, t \, \mathbf{e}_3 = \widetilde{\mathbf{a}} + t\mu \, \mathbf{e}_3. \tag{17}$$

This implies that in the transformed system the dependence on t only appears in the third component of the angular velocity and the corresponding $\Sigma(S_1(\mathbf{a} + t \, \mathbf{b}))$ matrix will be

$$\Sigma(\widetilde{\mathbf{a}} + t\mu \, \mathbf{e}_3) = \begin{pmatrix} 0 & -\widetilde{a}_3 - t\mu & \widetilde{a}_2 \\ \widetilde{a}_3 + t\mu & 0 & -\widetilde{a}_1 \\ -\widetilde{a}_2 & \widetilde{a}_1 & 0 \end{pmatrix}.$$

Next we will make another time independent transformation in the (1,2) plane

$$\mathbf{y} \to S_2\mathbf{y} \equiv \begin{pmatrix} \cos\theta & \sin\theta & 0 \\ -\sin\theta & \cos\theta & 0 \\ 0 & 0 & 1 \end{pmatrix} \mathbf{y}, \tag{18}$$

with the purpose of vanishing the second component of the $\widetilde{\mathbf{a}}$ vector. In fact, defining θ by

$$\widetilde{a}_1 = \sqrt{\widetilde{a}_1^2 + \widetilde{a}_2^2}\,\cos\theta, \quad \widetilde{a}_2 = \sqrt{\widetilde{a}_1^2 + \widetilde{a}_2^2}\,\sin\theta,$$

for the transformed angular velocity we have

$$S_2 S_1\,(\widetilde{\mathbf{a}} + t\mu\ \mathbf{e}_3) = \begin{pmatrix} \sqrt{\widetilde{a}_1^2 + \widetilde{a}_2^2} \\ 0 \\ \widetilde{a}_3 + t\mu \end{pmatrix} \equiv \begin{pmatrix} \widetilde{w}_1 \\ 0 \\ \widetilde{a}_3 + t\mu \end{pmatrix} = \widetilde{\mathbf{w}}, \tag{19}$$

with $\widetilde{w}_3(t) = \widetilde{a}_3 + t\mu$, which is the simplest form of the angular velocity under time independent rotations.

In conclusion with the time independent transformation

$$\mathbf{x} \quad \rightarrow \quad S\mathbf{x}, \qquad S = S_2 S_1,$$

the kinematic equations are

$$\widetilde{R}'(t) = \widetilde{R}(t)\ \Sigma(\widetilde{\mathbf{w}}), \qquad \widetilde{\mathbf{w}} = (\widetilde{w}_1, 0, \widetilde{a}_3 + t\mu)^T. \tag{20}$$

with $\widetilde{R}(t) = S\ R(t)\ S^{-1}$, $\Sigma(\widetilde{\mathbf{w}}_{\mathcal{B}})$ the skew symmetric associated to (19) and the initial conditions

$$\widetilde{R}(0) = S\ R(0)\ S^{-1}. \tag{21}$$

After this simplification, to write the solution of (20) in terms of elementary functions we observe that for the orthogonality of $\widetilde{R}(t)$ each row $\mathbf{v}^T = \mathbf{v}_k^T = (\widetilde{r}_{k1}, \widetilde{r}_{k2}, \widetilde{r}_{k3})$ can be considered as a point of $\mathcal{S}^2 \subset \mathbb{R}^3$ that satisfies the linear system

$$\frac{\mathrm{d}}{\mathrm{d}t}\mathbf{v}^T = \mathbf{v}^T\ \Sigma(\widetilde{\mathbf{w}}_{\mathcal{B}}). \tag{22}$$

Now we will map

$$\begin{array}{ccc} \mathcal{S}^2 & \rightarrow & \mathcal{C}\bigcup\{\infty\} \\ \mathbf{v} = (v_1, v_2, v_3)^T & \mapsto & \omega \end{array}$$

by means of the stereographic projection from the south pole on the complex equatorial plane given by

$$\omega = \omega(\mathbf{v}) = \frac{v_2 - iv_1}{1 + v_3}, \qquad \omega(-1) = \infty, \tag{23}$$

with the inverse

$$v_1 = \frac{i(\omega - \overline{\omega})}{1 + |\omega|^2}, \quad v_2 = \frac{\omega + \overline{\omega}}{1 + |\omega|^2}, \quad v_3 = \frac{1 - |\omega|^2}{1 + |\omega|^2}. \tag{24}$$

With the transformation (23),(24), the linear equation (22) in the new stereographic variables is transformed into the Riccati equation

$$\omega' = \left(\frac{\widetilde{w}_1}{2}\right)\ \omega^2 - i\widetilde{w}_3(t)\ \omega + \left(\frac{\widetilde{w}_1}{2}\right). \tag{25}$$

Next we introduce the standard change of variables

$$\omega \ \rightarrow \ \zeta, \qquad \omega = -\frac{2\zeta'}{\zeta \widetilde{w}_1},$$

that transforms a Riccati equation into a linear equation and (25) becomes

$$\zeta'' + i\widetilde{w}_3(t)\ \zeta' + \frac{1}{4}\widetilde{w}_1^2\ \zeta = 0, \tag{26}$$

with $\widehat{w}_1$ a real constant and $\widehat{w}_3$ an affine function of t defined by (19)

Finally with the linear change of time

$$t \ \rightarrow \ z, \qquad t = (z - z_0)/\gamma,$$

with

$$z_0 = \frac{\widetilde{a}_3\gamma}{\mu}, \quad \gamma^2 = \frac{\mu}{2i}, \quad \widetilde{w}_3(t) = \widetilde{a}_3 + \mu t,$$

we arrive to the Hermite equation for the unknown function $\zeta = \zeta(z)$

$$\frac{d^2\zeta}{dz^2} - 2z\ \frac{d\zeta}{dz} + 2\nu\ \zeta = 0, \quad \text{with the complex constant } \nu = \frac{i\widetilde{w}_1^2}{4\mu}. \tag{27}$$

It must be remarked that this transformed equation was obtained by Romano in ([2]).

Let $\langle \varphi_1(z), \varphi_2(z) \rangle$ be a basis of solutions of Hermite's equation (27), then any solution of this equation can be written as $\zeta(z) = c_1\ \varphi_1(z) + c_2\ \varphi_2(z)$, with arbitrary constants c_1, c_2. Since $z = z_0 + \gamma t$

$$\zeta(\gamma t + z_0) = c_1\ \varphi_1(\gamma t + z_0) + c_2\ \varphi_2(\gamma t + z_0),$$

and in the complex variable of the stereographic projection the solution becomes

$$\omega(t) = -\frac{2\gamma(c_1\ \varphi_1'(\gamma t + z_0) + c_2\ \varphi_2'(\gamma t + z_0))}{\widehat{w}_1\ (c_1\ \varphi_1(\gamma t + z_0) + c_2\ \varphi_2(\gamma t + z_0))}. \tag{28}$$

For the choice of the arbitrary constants c_1, c_2 observe that for a given unit vector $\mathbf{v}$ at $t = 0$, we have a unique $\omega(0) \in \mathbb{C}$ and we must select these constants so that

$$\omega(0) = -\frac{2\gamma(c_1\ \varphi_1'(z_0) + c_2\ \varphi_2'(z_0))}{\widetilde{w}_1\ (c_1\ \varphi_1(z_0) + c_2\ \varphi_2(z_0))}. \tag{29}$$

This equation shows that c_1, c_2 are not uniquely determined because for homogeneity if c_1, c_2 is a solution Kc_1, Kc_2 is also solution for any $K \in \mathbb{C}$. Nevertheless the same homogeneity appears in (28) and therefore we can take any solution $K\zeta(t)$ because it leads to the same $\omega(t)$.

Concerning the choice of the basis solutions, for Hermite's equation there are several possibilities: In many classical references on the subject it is remarked that if $\zeta(z) = \zeta_\nu(z)$ is a solution of (27), $\zeta_\nu(-z)$ is also solution and denoting by $W(z) = W(\zeta_\nu(z), \zeta_\nu(-z))$

the Wronskian of these solutions, it is easy to show that $W'(z) = 2zW(z)$ which implies $W(z) = W(0)\exp(z^2)$. Hence taking a solution with $W(0) \neq 0$ we have two independent solutions. The standard choice for φ_1 is the so called Hermite's function $H_\nu(z)$ given by

$$H_\nu(z) = \frac{1}{2\Gamma(-\nu)} \sum_{m\geq 0} \frac{(-1)^m \Gamma((m-\nu)/2)}{m!} (2z)^m.$$

Hermite's symmetric basis $\langle H_\nu(z), H_\nu(-z)\rangle$ is relevant for theoretical studies because it has an integral representation in the complex plane and allows further developments.

Next we will present another basis essentially equivalent to te given by Romano in [2] using hypergeometric functions. Observe that

$$\zeta(z) = \sum_{n\geq 0} a_n \frac{z^n}{n!},$$

is a solution of (27) if the coefficients satisfy the two-term recurrence $a_{n+2} = 2(n-\nu)a_n$. Hence for $a_0 = 1, a_1 = 0$ we have the even solution

$$\varphi_1(z) = \sum_{j\geq 0} a_{2j} \frac{z^{2j}}{2j!}, \qquad (a_0 = 1, a_{2j} = 2(2j-2-\nu)a_{2j-2}).$$

For $a_0 = 0, a_1 = 1$ the odd solution

$$\varphi_2(z) = \sum_{j\geq 0} a_{2j+1} \frac{z^{2j+1}}{2j+1!}, \qquad (a_1 = 1, a_{2j+1} = 2(2j-1-\nu)a_{2j-1}).$$

In the general solution $\zeta(z) = c_1\varphi_1(z) + c_2\varphi_2(z)$ for the computation of c_1, c_2 we can proceed as above.

Finally, another alternative is to transform Hermite's equation

$$\zeta \quad \to \quad \eta, \qquad \zeta(z) = e^{z^2/2}\,\eta(z),$$

arriving to the normal form

$$\eta''(z) + (1 - 2\nu - z^2)\eta(z) = 0.$$

This is (with a constant scale of independent variable) Weber's equation (see e.g. [6]) that has been extensively used because it appears in the solution of some wave equations by separation of variables. Taking the basis of Weber-Hermite functions (also called the parabolic cylinder functions) $D_\nu(z)$ and $D_{-\nu}(z)$ for the last equation we obtain immediately the corresponding basis in the original equation.

Remarks.

- The above analytical solution of a body with a spherical ellipsoid of inertia excited by a constant torque can be easily extended to the case of a piecewise constant torque. In fact, if the torque $\mathbf{M}$ is given by $\mu_0\mathbf{u}_{\mathcal{B},0}$ for $t \in [t_0, t_1)$, $\mu_1\mathbf{u}_{\mathcal{B},1}$ for $t \in [t_1, t_2)$, ... then it enough to match the corresponding solutions in the intervals $[t_0, t_1], [t_1, t_2], \ldots$.

- In this derivation, for any time dependent skew symmetric matrix $\Sigma(\mathbf{w}_{\mathcal{B}}(t))$ with an affine function $\mathbf{w}_{\mathcal{B}}(t)$, each row of the kinematic equations $R' = R\ \Sigma(\mathbf{w}_{\mathcal{B}}(t))$ is transformed into the linear second order equation (26) and conversely. This shows that any second order equation with time dependent coefficients that admit a basis analytical solutions and can be transformed into the form (26) leads to some torque with a integrable problem.

3 Axially symmetric rigid body under a constant torque in the direction of the symmetry axis

Here we consider the first problem of Romano in [3] of a rigid body with $I_1 = I_2 = I \neq I_3$ under a constant torque $\mathbf{M} = \mu \mathbf{e}_{\mathcal{B},3}$ ($\mu > 0$ constant) along the third axis of the body frame.

Now Euler's equations can be written as

$$\begin{aligned} I\ \frac{\mathrm{d}w_1}{\mathrm{d}t} &= (I - I_3) w_2 w_3, \\ I\ \frac{\mathrm{d}w_2}{\mathrm{d}t} &= (I_3 - I) w_3 w_1, \\ I_3\ \frac{\mathrm{d}w_3}{\mathrm{d}t} &= \mu. \end{aligned} \tag{30}$$

¿From the last equation $w_3(t) = w_3^0 + (\mu/I_3)t$ and putting

$$\alpha(t) = \left(\frac{I - I_3}{I}\right)\ w_3(t),$$

the first two equations of (33) are

$$\frac{\mathrm{d}w_1}{\mathrm{d}t} = \alpha(t)\ w_2, \quad \frac{\mathrm{d}w_2}{\mathrm{d}t} = -\alpha(t)\ w_1.$$

By introducing the complex function $\zeta(t) = w_1(t) + i w_2(t)$ we have

$$\frac{\mathrm{d}}{\mathrm{d}t}\zeta = -i\alpha(t)\ \zeta, \quad \Rightarrow \quad \zeta(t) = \zeta(0)\ e^{-i\widehat{\alpha}(t)}$$

with $\widehat{\alpha}(t) = \int_0^t \alpha(s)\mathrm{d}s$. Hence with the initial conditions $w_1(0) = w_1^0, w_2(0) = w_2^0$ the solution is

$$\begin{aligned} w_1 &= \cos\left(\widehat{\alpha}(t)\right)\ w_1^0 + \sin\left(\widehat{\alpha}(t)\right)\ w_2^0, \\ w_2 &= -\sin\left(\widehat{\alpha}(t)\right)\ w_1^0 + \cos\left(\widehat{\alpha}(t)\right)\ w_2^0. \end{aligned}$$

Thus the solution of the dynamic equations (33) is

$$\mathbf{w}(t) = \begin{pmatrix} \cos\left(\widehat{\alpha}(t)\right)\ w_1^0 + \sin\left(\widehat{\alpha}(t)\right)\ w_2^0 \\ -\sin\left(\widehat{\alpha}(t)\right)\ w_1^0 + \cos\left(\widehat{\alpha}(t)\right)\ w_2^0 \\ w_3^0 + (\mu/I_3)t \end{pmatrix}, \tag{31}$$

with

$$\widehat{\alpha}(t) = \int_0^t \alpha(s)\, \mathrm{d}s = \left(\frac{I - I_3}{I}\right) \left[w_3^0 t + \left(\frac{\mu}{2I_3}\right) t^2\right].$$

For the solution of the kinematic equations

$$R'(t) = R(t)\ \Sigma(\mathbf{w}(t)), \tag{32}$$

observe that under a non singular time dependent change of variable

$$R \longrightarrow \widetilde{R}, \qquad R = \widetilde{R}\ S(t),$$

we have,

$$R'(t) = R(t)\ \Sigma_R \quad \longrightarrow \quad \widetilde{R}'(t) = \widetilde{R}(t)\ \Sigma_{\widetilde{R}},$$

with

$$\Sigma_{\widetilde{R}} = -S'\ S^{-1} + S\ \Sigma_R\ S^{-1}.$$

In particular taking for S a rotation around the third axis

$$S = \begin{pmatrix} \cos\phi & -\sin\phi & 0 \\ \sin\phi & \cos\phi & 0 \\ 0 & 0 & 1 \end{pmatrix}, \qquad \phi = \phi(t),$$

we get

$$S'\ S^{-1} = \begin{pmatrix} 0 & -\phi' & 0 \\ \phi' & 0 & 0 \\ 0 & 0 & 0 \end{pmatrix},$$

and

$$S\ \Sigma_R\ S^{-1} = \begin{pmatrix} 0 & -w_3 & (w_1 \sin\phi + w_2 \cos\phi) \\ w_3 & 0 & -(w_1 \cos\phi - w_2 \sin\phi) \\ -(w_1 \sin\phi + w_2 \cos\phi) & (w_1 \cos\phi - w_2 \sin\phi) & 0 \end{pmatrix},$$

and then the components of the angular velocity $\widetilde{\mathbf{w}} = (\widetilde{w}_1, \widetilde{w}_2, \widetilde{w}_3)$ associated to $\Sigma_{\widetilde{R}}$ are

$$\begin{aligned} \widetilde{w}_1 &= (w_1 \cos\phi - w_2 \sin\phi), \\ \widetilde{w}_2 &= (w_1 \sin\phi + w_2 \cos\phi), \\ \widetilde{w}_3 &= w_3 - \phi', \end{aligned}$$

Hence taking into account (34) and choosing $\phi(t) = \widehat{\alpha}(t) + \pi/2$ we have

$$\widetilde{w}(t) = \left(w_1^0, w_2^0, \left(\frac{2I - I_3}{I}\right) w_3^0 + \left(\frac{\mu(I - I_3)}{II_3}\right) t\right).$$

These are the same kinematic equations studied in section 2 with a different set of constants in the angular velocity. Hence we may apply the transformations used there to get the analytical solution.

4 Axially symmetric rigid body under a rotating external torque constant in magnitude and perpendicular to the symmetry axis

This is the second case considered by Romano in [3]. Now the components of the torque in the body frame are

$$\mathbf{M}_{\mathcal{B}} = (\beta_0 I_1 \cos(\alpha t), \beta_0 I_1 \sin(\alpha t), 0)\,, \tag{33}$$

with non zero constants β_0 and α. Hence Euler's equations are

$$\begin{aligned} I_1 w_1' &= (I_1 - I_3) w_2 w_3 + \beta_0 I_1 \cos(\alpha t), \\ I_1 w_2' &= (I_3 - I_1) w_3 w_1 + \beta_0 I_1 \sin(\alpha t), \\ w_3' &= 0. \end{aligned} \tag{34}$$

For the derivation of analytic solutions Romano assumes that the angular velocity of rotation of the torque is a function of the initial condition given by

$$\alpha = \frac{I_3 - I_1}{I_1}\, w_3^0, \tag{35}$$

and then equations (34) can be written as

$$w_1' = -\alpha w_2 + \beta_0 \cos(\alpha t), \quad w_2' = \alpha w_1 + \beta_0 \sin(\alpha t), \quad w_3' = 0.$$

These dynamic equations have the general solution

$$\begin{pmatrix} w_1(t) \\ w_2(t) \end{pmatrix} = \begin{pmatrix} \cos(\alpha t) & -\sin(\alpha t) \\ \sin(\alpha t) & \cos(\alpha t) \end{pmatrix} \begin{pmatrix} w_1^0 + t\beta_0 \\ w_2^0 \end{pmatrix}, \qquad w_3(t) = w_3^0. \tag{36}$$

As in the previous case for solving the kinematic equations

$$R'(t) = R(t)\, \Sigma(\mathbf{w}(t)) \tag{37}$$

we introduce the time dependent transformation

$$R = \widetilde{R}\, S(t),$$

where $S = S(t)$ is a rotation around the third axis with angle $-\alpha t$. Now the transformed system is

$$\widetilde{R}'(t) = \widetilde{R}(t)\, \Sigma(\widetilde{\mathbf{w}}(t)), \tag{38}$$

where

$$\begin{pmatrix} \widetilde{w}_1(t) \\ \widetilde{w}_2(t) \end{pmatrix} = \begin{pmatrix} \cos(-\alpha t) & -\sin(-\alpha t) \\ \sin(-\alpha t) & \cos(-\alpha t) \end{pmatrix} \begin{pmatrix} w_1 \\ w_2 \end{pmatrix} = \begin{pmatrix} w_1^0 + t\beta_0 \\ w_2^0 \end{pmatrix},$$

and $\widetilde{w}_3(t) = w_3^0 + \alpha$. Since the transformed angular velocity $\widetilde{\mathbf{w}}(t)$ is an affine function the analytical solution of (38) can be written in terms of Hermite's functions as in the section 2 and we have the desired analytical solution.

Finally, we consider the motion of an axially symmetric rigid body ($I_1 = I_2 \neq I_3$) where the initial angular velocity in the body frame $\mathbf{w}(0) = (w_1^0, w_2^0, w_3^0)$ is contained in the 1-2 plane subjected to a fixed torque perpendicular to its axis of symmetry. By the assumed rotational symmetry we can take the torque $\mathbf{M} = (I_1\mu, 0, 0)$ where μ an arbitrary constant directed along the first axis. In this case the dynamic equations have the solution

$$\mathbf{w}(t) = (w_1^0 + \mu t, w_2^0, 0), \tag{39}$$

and taking into account that (39) is an affine function, the solution of the kinematic equation

$$R'(t) = R(t)\ \Sigma(\mathbf{w}(t)), \tag{40}$$

for arbitrary $R(0)$ can be written in terms of Hermite's functions.

More generally, as it has been proved in section 2, for all affine angular velocity function $\mathbf{w}(t) = \mathbf{a} + t\ \mathbf{b}$ ($\mathbf{a}$, $\mathbf{b}$ constant vectors) after suitable change of variables the general solution of the kinematic equations (40) can be expressed in terms of Hermite's functions. In view of this, for all external torque $\mathbf{M}$ that satisfies Euler's equations

$$\mathbf{I}\,\frac{d\mathbf{w}}{dt} + \mathbf{w} \times \mathbf{I}\,\mathbf{w} = \mathbf{M}, \quad \text{with} \quad \mathbf{w}(t) = \mathbf{a} + t\ \mathbf{b}, \tag{41}$$

the corresponding rigid body problem is completely integrable because both (40) and (41) are completely integrable.

In particular with the values

$$\mathbf{a} = (w_1^0, w_2^0, 0)^T, \quad \mathbf{b} = (\mu, 0, 0)^T, \quad I_1 = I_2 \neq I_3,$$

by substituting in the left hand side of (41) we get

$$M_1 = I_1\mu, \quad M_2 = 0, \quad M_3 = 0,$$

and we have the above particular solutions derived by Romano in [3].

5 Final Remarks

It has been stated that with the present possibilities of machine computation the derivation of analytic solutions in problems of rigid body motion only possess an academic interest. However it must be noticed that numerical methods enable us to obtain very accurate solutions in short time intervals of integration but cannot capture the long time

behavior of solutions. Thus, even in the simplest case of the torque free motion of a general rigid body with a well known analytical solution in terms of Jacobian elliptic functions many numerical integrators do not preserve the existing invariants of the problem.

Recent applications such as the attitude evolution of a spinning spacecraft have open new requirements such as computer algorithms for onboard computations. Now the main task is not the accuracy but the simplicity and reliability of the algorithms for usual spinning-up and spinning-down maneuvers. It must be noticed that very often thruster misalignment or thruster mismatch do not allow an exact knowledge of the torque.

Although Euler's angles, typically the 3-1-2 angle sequence, are used to describe the orientation of the body-fixed reference frame, in practical computations other (complex) variables are more convenient and sometimes avoid singularities. Analytical solution are very frequently a source of inspiration for this purpose.

Acknowledgements

This work was supported by project MTM2007-67530-C02-01.

References

[1] E. Leimanis, *The General Problem of the Motion of Coupled Rigid Bodies about a Fixed Point*, Springer Tracts in Natural Philosphy, vol 7, Springer-Verlag, Berlin (1965).

[2] M. Romano, *Exact analytical solution for the rotation of a rigid body having spherical ellipsoid of inertia and subjected to a constant torque*, Celest. Mech. Dyn. Astron. **100**, 181–189 (2008).

[3] M. Romano, *Exact analytical solution for the rotation of an axially symmetric rigid body subjected to a constant torque*, Celest. Mech. Dyn. Astron. **101**, 375–390 (2008).

[4] P. Tsiotras and J.M. Longuski, *A complex analytical solution of a near symmetric rigid body under body fixed torques*, Celest. Mech. Dyn. Astron. **51**, 281–301 (1991).

[5] A. Wintner, *The Analytical Foundations of Celestial Mechanics*, Princeton University Press, Princeton (1941).

[6] E. T. Whittaker and G.N. Watson, *A course in modern analysis*, Cambridge University Press, Cambridge (1962).

Monografías de la Real Academia de Ciencias de Zaragoza **35**, 41–52, (2011).

Three families of isochrone-type canonical transformations

Sebastián Ferrer

Departamento de Matemática Aplicada, Universidad de Murcia, 30100 Murcia

and

Martín Lara

Real Observatorio de la Armada, 11110 San Fernando.

Abstract

Hénon's isochrone Hamiltonian is formulated in extended phase space including a time transformation. Then, the Hamilton-Jacobi equation *a la Poincaré* is used to find suitable canonical transformations that reduces the original Hamiltonian to a function of only the momenta. We focus on three different time transformations, for each of which we build a family of canonical transformations where the new Hamiltonian remains unspecified. Materialization of particular transformations based on specific requirements lead to a partial differential equation which the new Hamiltonian ought to satisfy. Specifically, we show how different canonical transformations in the Literature may be recovered from our families.

Introduction

Hénon isochrone model [10] is a particular case of a central potential that has been successfully used in some fields of astronomy. Specifically, it is suitable for representing the mean potential of a stellar system, and may be used to understand the evolution of our galaxy [6]. The isochronal potential is studied in textbooks as an interesting example of an integrable problem depending on two parameters, which comprises the Keplerian potential as a limit case [3]. Besides, it may be used as a zero order to apply perturbation theory to systems that slightly depart from the spherical symmetry [8, 19]. To make tractable the perturbation approach it is necessary to find a suitable set of variables or elements, so that the integrable Hamiltonian in the new variables is usually expressed as a function of momenta only. The Hamilton-Jacobi equation provides a convenient way of finding the required transformation.

The Hamilton-Jacobi equation is commonly used for finding a single canonical transformation tailored to a specific problem; for instance, it is usually applied in the search for efficient numerical integrators or when dealing with perturbation methods. However, as far as the new Hamiltonian may remain formal in the procedure of computing the transformation [18], the Hamilton-Jacobi equation of a particular Hamiltonian may give rise to a whole family of transformations. General applications of this procedure have been discussed in Ref. [7]; we present here details on its application to finding canonical transformations useful in orbital problems.

We form the Hamilton-Jacobi equation of the isochronal potential in the extended phase space. Besides, we scale the Hamiltonian by a regularizing function, which further extends the powerful of this technique [15]. We deal with three specific regularizing functions for which we are able to compute the quadratures involved in the procedure. For each of them, the transformation equations are left as function of the (undefined) new Hamiltonian, thus providing three different families of canonical transformations.

Because of the super-integrability of the isochronal Hamiltonian, the possible solutions are constrained to planar, quasi periodic ellipses. Therefore, the closure of a trajectory is a two-torus and two actions (three in the extended phase space formulation) are required in the new Hamiltonian if one wants to retain the topology of the reduced problem. Resonances between the frequencies of the angle variables result in periodic motion that, of course, can be studied with a reduced Hamiltonian that may depend on less momenta.

With an aim on perturbation theory, we discuss several transformation equations derived from the three computed families of isochronal canonical transformations. We show that simple requirements on the transformation, as for instance "simplification", result in elementary partial differential equations from whose solution the new Hamiltonian may be determined. We further show that a variety of canonical transformations in the literature, ranging from historic ones like Delaunay's, Levi-Civita's or Hill's, to the recent transformation due to Yanguas [19], can be recovered from our family.

1 Hamilton-Jacobi reduction of the isochrone

Given the Hamiltonian

$$\mathcal{H} = \left[\frac{1}{2}\left(R^2 + \frac{\Theta^2}{r^2}\right) - \frac{\mu}{b + \sqrt{b^2 + r^2}} + T\right] \chi(r, R, \Theta, N, T) \tag{1}$$

where $(r, \theta, \nu, t, R, \Theta, N, T)$ are Hill or polar-nodal variables in the extended phase space, μ and b are parameters, and χ is a regularizing function that only depends on distance and momenta, we look for a canonical transformation

$$(r, \theta, \nu, t, R, \Theta, N, T) \xrightarrow{\mathcal{T}_\Phi} (f, g, h, u, F, G, H, U)$$

that converts Eq. (1) in a certain function $\Phi = \Phi(F, G, H, U)$ depending only on the momenta.

The transformation will be defined through a generating function $\mathcal{S} = \mathcal{S}(r, \theta, \nu, t, F, G, H, U)$ in mixed variables such that

$$f = \mathcal{S}_F, \quad g = \mathcal{S}_G, \quad h = \mathcal{S}_H, \quad u = \mathcal{S}_U, \quad R = \mathcal{S}_r, \quad \Theta = \mathcal{S}_\theta, \quad N = \mathcal{S}_\nu, \quad T = \mathcal{S}_t, \quad (2)$$

where we use the notation $\mathcal{S}_x = \partial\mathcal{S}/\partial x$. Then, from Eq. (1) we set the Hamilton-Jacobi equation

$$\left[\frac{1}{2}\left(\mathcal{S}_r^2 + \frac{1}{r^2}\,\mathcal{S}_\theta^2\right) - \frac{\mu}{b + \sqrt{b^2 + r^2}} + \mathcal{S}_t\right] \chi(r, \mathcal{S}_r, \mathcal{S}_\theta, \mathcal{S}_\nu, \mathcal{S}_t) = \Phi(F, G, H, U). \quad (3)$$

Because t, θ, and ν are not present in Eq. (1), the generating function may be chosen in separate variables

$$\mathcal{S} = U\,t + H\,\nu + G\,\theta + \mathcal{W}(r, F, G, H, U). \quad (4)$$

Then,

$$\frac{1}{2}\left(\mathcal{W}_r^2 + \frac{G^2}{r^2}\right) - \frac{\mu}{b + \sqrt{b^2 + r^2}} + U = \frac{1}{\chi(r, \mathcal{W}_r, G, H, U)}\,\Phi(F, G, H, U). \quad (5)$$

We limit ourselves to the cases in which $\mathcal{W}_r$ can be solved from a quadratic equation. Specifically, we request that $\chi = \chi^\star(r)\,\mathcal{W}_r^{-n}\,\Xi(G, H, U)$ and $n = 0, 1, 2$. Because Ξ can be subsumed in Φ, there is no ambiguity in dropping the star from χ, and writing Eq. (5) like

$$\frac{1}{2}\left(\mathcal{W}_r^2 + \frac{G^2}{r^2}\right) - \frac{\mu}{b + \sqrt{b^2 + r^2}} + U = \frac{\mathcal{W}_r^n}{\chi(r)}\,\Phi(F, G, H, U). \quad (6)$$

Therefore,

$$n = 0 \;\Rightarrow\; \mathcal{W}_r = \sqrt{\frac{2\,\Phi}{\chi(r)} - \frac{G^2}{r^2} + \frac{2\mu}{b + \sqrt{b^2 + r^2}} - 2U}, \quad (7)$$

$$n = 1 \;\Rightarrow\; \mathcal{W}_r = \frac{\Phi}{\chi(r)} \pm \sqrt{\frac{\Phi^2}{\chi^2(r)} - \frac{G^2}{r^2} + \frac{2\mu}{b + \sqrt{b^2 + r^2}} - 2U} \quad (8)$$

$$n = 2 \;\Rightarrow\; \mathcal{W}_r = \sqrt{\left(-\frac{G^2}{r^2} + \frac{2\mu}{b + \sqrt{b^2 + r^2}} - 2U\right)\frac{\chi(r)}{\chi(r) - 2\Phi}}. \quad (9)$$

that can be solved for $\mathcal{W}$ by quadrature.

We only discuss here the case $n = 0$. Then, $\mathcal{W} = \int_{r_0}^{r} \sqrt{Q(r, F, G, H, U)}\,\mathrm{d}r$, where $Q \geq 0$ is

$$Q = \frac{2\,\Phi}{\chi(r)} + \frac{2\mu}{b + \sqrt{b^2 + r^2}} - 2U - \frac{G^2}{r^2} = \frac{s^2}{s^2 - b^2}\,\mathcal{Q}, \quad (10)$$

with $s = \sqrt{r^2 + b^2}$ and

$$\mathcal{Q} = 2\left(\frac{\Phi}{\chi(s)} - U\right)\frac{s^2 - b^2}{s^2} + 2\mu\,\frac{s - b}{s^2} - \frac{G^2}{s^2}. \quad (11)$$

Therefore, the transformation is: $\Theta = G$, $N = H$, $T = U$, $R = \sqrt{Q}$, and

$$f = \Phi_F \, \mathcal{I}_3, \tag{12}$$

$$g = \theta + G \, \mathcal{I}_1 + \Phi_G \, \mathcal{I}_3, \tag{13}$$

$$h = \nu + \Phi_H \, \mathcal{I}_3, \tag{14}$$

$$u = t - \mathcal{I}_2 + \Phi_U \, \mathcal{I}_3, \tag{15}$$

where

$$\mathcal{I}_1 = \int_{s_0}^{s} \frac{s^2}{(s^2 - b^2)\sqrt{\mathcal{Q}}} \, \mathrm{d}\Big(\frac{1}{s}\Big), \qquad \mathcal{I}_2 = \int_{s_0}^{s} \frac{\mathrm{d}s}{\sqrt{\mathcal{Q}}}, \qquad \mathcal{I}_3 = \int_{s_0}^{s} \frac{\mathrm{d}s}{\chi\sqrt{\mathcal{Q}}} = -\int_{r_0}^{r} \frac{s^2}{\chi\sqrt{\mathcal{Q}}} \, \mathrm{d}\Big(\frac{1}{s}\Big). \tag{16}$$

Note that $\mathcal{I}_3 = \mathcal{I}_2$ for $\chi = 1$, and $\mathcal{I}_3 = -\mathcal{I}_1$ for $\chi = r^2 = s^2 - b^2$.

In order to avoid dealing with elliptic integrals we require for $\mathcal{Q}$ to be at most quadratic in s, what limits the possible choices of the regularizing function to $\chi = 1$, $\chi = s \pm b$, and $\chi = s^2 - b^2$. Then, we find convenient to write Eq. (11) as

$$\mathcal{Q} = -\alpha \left(\frac{p}{s^2} - \frac{2}{s} + \frac{1}{a} \right), \tag{17}$$

where α, p, and a, are certain functions of the momenta and parameters that will be specified after χ has been chosen. Therefore,

$$\mathcal{Q} = \alpha \, p \left(\frac{1}{s} - \frac{1}{s_1} \right) \left(\frac{1}{s_2} - \frac{1}{s} \right), \tag{18}$$

where $s_1 \geq s \geq s_2$ are the two possible roots of the conic $\mathcal{Q} = 0$:

$$s_{1,2} = \frac{p}{1 \pm \sqrt{1 - p/a}} = \frac{a\,(1 - e^2)}{1 \pm e} = a\,(1 \pm e), \qquad e^2 = 1 - \frac{p}{a} < 1. \tag{19}$$

These roots, the extreme values of s, make natural the introduction of the auxiliary variables ψ and ϕ, defined by

$$s = a\,(1 - e\cos\psi), \qquad \mathrm{d}s = a\,e\sin\psi\,\mathrm{d}\psi, \tag{20}$$

$$s = \frac{p}{1 + e\cos\phi}, \qquad \mathrm{d}\Big(\frac{1}{s}\Big) = -\frac{e}{p}\sin\phi\,\mathrm{d}\phi. \tag{21}$$

Then,

$$\mathcal{I}_1 = -\frac{1}{\sqrt{\alpha}} \left(\frac{1}{\sqrt{p - 2b + b^2/a}} \, \frac{\phi_1}{2} + \frac{1}{\sqrt{p + 2b + b^2/a}} \, \frac{\phi_2}{2} \right), \tag{22}$$

$$\mathcal{I}_2 = \sqrt{\frac{a^3}{\alpha}} \, (\psi - e\sin\psi), \tag{23}$$

where the two new auxiliary variables ϕ_1, ϕ_2, are defined by means of the trigonometric relations (see [19] for details)

$$\tan\frac{\phi_1}{2} = \sqrt{\frac{1 + e - b/a}{1 - e - b/a}} \sqrt{\frac{1 - e}{1 + e}} \tan\frac{\phi}{2} = \sqrt{\frac{1 + e - b/a}{1 - e - b/a}} \tan\frac{\psi}{2}, \tag{24}$$

$$\tan\frac{\phi_2}{2} = \sqrt{\frac{1 + e + b/a}{1 - e + b/a}} \sqrt{\frac{1 - e}{1 + e}} \tan\frac{\phi}{2} = \sqrt{\frac{1 + e + b/a}{1 - e + b/a}} \tan\frac{\psi}{2}. \tag{25}$$

The integration of $\mathcal{I}_3$ needs the previous specification of the regularizing function χ.

2 Discussion

Details on the families of canonical transformations generated by the cases $\chi = 1$, $\chi = b + \sqrt{b^2 + r^2}$, and $\chi = r^2$ are given below.

2.1 $\chi = 1$

From Eq. (11) and Eq. (17) we obtain

$$\alpha = \mu, \qquad a = \frac{\mu}{2(U-\Phi)}, \qquad p = \frac{G^2}{\mu} + 2b - \frac{1}{a}\, b^2, \tag{26}$$

that replaced in Eqs. (22) and (23) give

$$\mathcal{I}_1 = -\frac{\phi_1}{2G} - \frac{\phi_2}{2\sqrt{G^2 + 4b\,\mu}}, \tag{27}$$

$$\mathcal{I}_3 = \mathcal{I}_2 = \frac{\mu}{\sqrt{8(U-\Phi)^3}}\,(\psi - e\sin\psi). \tag{28}$$

Therefore, the transformation is ($\Theta = G$, $N = H$, $T = U$, $R = \sqrt{Q}$)

$$f = \Phi_F \frac{\mu}{\sqrt{8(U-\Phi)^3}}\,(\psi - e\sin\psi), \tag{29}$$

$$g = \theta - \frac{\phi_1}{2} - \frac{G}{\sqrt{G^2 + 4b\,\mu}}\,\frac{\phi_2}{2} + \frac{\Phi_G}{\Phi_F}\, f, \tag{30}$$

$$h = \nu + \frac{\Phi_H}{\Phi_F}\, f, \tag{31}$$

$$u = t + \frac{\Phi_U - 1}{\Phi_F}\, f, \tag{32}$$

where ψ is an implicit function of f and the new momenta. Note that Φ remains undefined and different choices may be done depending on a variety of criteria. Thus, for instance, the topology of the problem is maintained if we choose $\Phi = U + \Psi(F, G)$. Then, $h = \nu$, $u = t$, and

$$f = \Psi_F \frac{\mu}{\sqrt{-8\Psi^3}}\,(\psi - e\sin\psi), \tag{33}$$

$$g = \theta - \frac{\phi_1}{2} - \frac{G}{\sqrt{G^2 + 4b\,\mu}}\,\frac{\phi_2}{2} + \frac{\Psi_G}{\Psi_F}\, f, \tag{34}$$

Among the variety of possible choices of Ψ a simplifying option is to take $\Psi_F = \Psi_G = \mu^{-1}\,(-2\Psi)^{3/2}$, which may be solved for Ψ, to give

$$\Phi = U - \frac{\mu^2}{2(F+G)^2} \tag{35}$$

that maximally simplifies the remaining transformation equations:

$$f = \psi - e\sin\psi, \tag{36}$$

$$g = \theta - \frac{\phi_1}{2} - \frac{G}{\sqrt{G^2+4b\,\mu}}\,\frac{\phi_2}{2} + f. \tag{37}$$

Yanguas' selection

$$\Phi = U - \frac{\mu^2}{2F^2} \tag{38}$$

depends on fewer momenta and, therefore, constrains the topology of the original system to periodic solutions only —which may be adequate for a perturbation study like [19].

In the Keplerian case $b = 0$, the selection of the new Hamiltonian $\Phi = \Phi(U, F)$ does not constrain the range of solutions and the specific selection Eq. (38) provides the popular Delaunay transformation that, taking into account that $\phi_1 = \phi_2 = \phi$ and $\Phi_G = 0$ in Eq. (30), is

$$f = \psi - e\sin\psi, \qquad g = \theta - \phi, \qquad h = \nu, \qquad u = t, \tag{39}$$

where the most extended notation writes $L \equiv F$, $\ell \equiv f$.

2.2 $\chi = b + \sqrt{b^2 + r^2}$

Now, we write

$$\alpha = \Phi + \mu, \qquad a = \frac{\Phi+\mu}{2U}, \qquad p = \frac{G^2}{\Phi+\mu} + 2b - \frac{1}{a}\,b^2, \tag{40}$$

that are repalced in $\mathcal{I}_1$, Eq. (22), and $\mathcal{I}_2$, Eq. (23). To integrate $\mathcal{I}_3$ we use the change of Eq. (20). We get

$$\mathcal{I}_1 = -\frac{\phi_1}{2G} - \frac{\phi_2}{2\sqrt{G^2+4b\,(\mu+\Phi)}}, \tag{41}$$

$$\mathcal{I}_2 = \frac{\mu+\Phi}{\sqrt{8U^3}}\,(\psi - e\sin\psi), \tag{42}$$

$$\mathcal{I}_3 = \frac{\psi}{\sqrt{2U}} - \frac{b\,\phi_2}{\sqrt{G^2+4b\,(\mu+\Phi)}}. \tag{43}$$

where ϕ_1, ϕ_2, are the same auxiliary variables defined in (24) and (25) respectively.

Therefore, the transformation is $\Theta = G$, $N = H$, $T = U$, $R = \sqrt{Q}$,

$$f = \Phi_F\left(\frac{\psi}{\sqrt{2U}} - \frac{b\,\phi_2}{\sqrt{G^2+4b\,(\mu+\Phi)}}\right), \tag{44}$$

$$g = \theta - \frac{\phi_1}{2} - \frac{G\,\phi_2}{2\sqrt{G^2+4b\,(\mu+\Phi)}} + \frac{\Phi_G}{\Phi_F}\,f, \tag{45}$$

$$h = \nu + \frac{\Phi_H}{\Phi_F}\,f, \tag{46}$$

$$u = t - \frac{\mu+\Phi}{\sqrt{8U^3}}\,(\psi - e\sin\psi) + \frac{\Phi_U}{\Phi_F}\,f, \tag{47}$$

2.2.1 Family 1

Assuming $b \neq 0$, Eq. (44) clearly simplifies if we require that $-2b\,\Phi_F = \sqrt{G^2 + 4b\,(\mu + \Phi)}$. Then,

$$\Phi = \frac{1}{4b}\left[F - 2b\,\Psi(G,H,U)\right]^2 - \frac{G^2}{4b} - \mu,$$

where Ψ is an arbitrary function. As the topology of the isochrone requires only three momenta (in the extended phase space formulation), we find great simplification by choosing $\Psi = \Psi(H)$. Thus,

$$f = \frac{F - 2b\,\Psi}{2b\,\sqrt{2U}}\,\psi - \frac{\phi_2}{2}, \tag{48}$$

$$g = \theta - \frac{\phi_1}{2} - \frac{G}{2b\,\sqrt{2U}}\,\psi, \tag{49}$$

$$h = \nu - \Psi_H\left(\frac{F - 2b\,\Psi}{\sqrt{2U}}\,\psi - b\,\phi_2\right), \tag{50}$$

$$u = t - \frac{(F - 2b\,\Psi)^2 - G^2}{4b\,\sqrt{8U^3}}\,(\psi - e\sin\psi), \tag{51}$$

Finally, if we select $\Psi = H/(2b)$, we get

$$\Phi = \frac{1}{4b}\left[(F-H)^2 - G^2\right] - \mu,$$

and

$$f = \frac{F - H}{2b\,\sqrt{2U}}\,\psi - \frac{\phi_2}{2}, \tag{52}$$

$$g = \theta - \frac{G}{2b\,\sqrt{2U}}\,\psi - \frac{\phi_1}{2}, \tag{53}$$

$$h = \nu - f, \tag{54}$$

$$u = t - \frac{(F-H)^2 - G^2}{4b\,\sqrt{8U^3}}\,(\psi - e\sin\psi), \tag{55}$$

2.2.2 Family 2:

A transformation that doest not need the non-vanishing of the parameter b is found as follows. First, in Eqs. (44)–(47) we require that $\Phi_F = \sqrt{2U}$; therefore, $\Phi = \sqrt{2U}\,(F + \Psi)$ with $\Psi = \Psi(G,H,U)$ an arbitrary function. Thus,

$$f = \psi - \frac{\sqrt{2U}\,b\,\phi_2}{\sqrt{G^2 + 4b\,(\mu + \sqrt{2U}\,(F+\Psi))}}, \tag{56}$$

$$g = \theta - \frac{\phi_1}{2} - \frac{G\,\phi_2}{2\sqrt{G^2 + 4b\,(\mu + \sqrt{2U}\,(F+\Psi))}} + \Psi_G\,f, \tag{57}$$

$$h = \nu + \Psi_H\,f, \tag{58}$$

$$u = t - \left(\frac{\mu}{\sqrt{8U^3}} + \frac{F+\Psi}{2U}\right)(\psi - e\sin\psi) + \left(\frac{F+\Psi}{2U} + \Psi_U\right)f. \tag{59}$$

Then, we avoid secular terms in ψ in the u (time) transformation by requiring that $\Psi_U = \frac{\mu}{\sqrt{8U^3}}$; therefore, $\Psi = -\frac{\mu}{\sqrt{2U}} + \Psi'$, where $\Psi' = \Psi'(G, H)$, and

$$f = \psi - \frac{\sqrt{2U}\, b\, \phi_2}{\sqrt{G^2 + 4b\sqrt{2U}\,(F + \Psi')}}, \tag{60}$$

$$g = \theta - \frac{\phi_1}{2} - \frac{G\,\phi_2}{2\sqrt{G^2 + 4b\sqrt{2U}\,(F + \Psi')}} + \Psi'_G\, f, \tag{61}$$

$$h = \nu + \Psi'_H\, f, \tag{62}$$

$$u = t - \frac{F + \Psi'}{2U}\left[\frac{\sqrt{2U}\, b\, \phi_2}{\sqrt{G^2 + 4b\sqrt{2U}\,(F + \Psi')}} - e\sin\psi\right]. \tag{63}$$

Finally, as it is enough for the new Hamiltonian to depend on three momenta, we may choose $\Psi' = G$ giving the transformation

$$f = \psi - \frac{\sqrt{2U}\, b\, \phi_2}{\sqrt{G^2 + 4b\sqrt{2U}\,(F + G)}}, \tag{64}$$

$$g = \theta - \frac{\phi_1}{2} - \frac{G\,\phi_2}{2\sqrt{G^2 + 4b\sqrt{2U}\,(F + G)}} + f, \tag{65}$$

$$h = \nu, \tag{66}$$

$$u = t + \frac{F + G}{2U}\left[e\sin\psi - \frac{\sqrt{2U}\, b\, \phi_2}{\sqrt{G^2 + 4b\sqrt{2U}\,(F + G)}}\right], \tag{67}$$

that completely reduces the Hamiltonian, Eq. (1), to a function of only the momenta $\Phi = \sqrt{2U}\,(F + G) - \mu$.

In the Keplerian case $b = 0$ and $\phi_1 = \phi_2 = \phi$. Furthermore, it is enough for the new Hamiltonian to depend only on two momenta. Now, Eqs. (44)-(47), are written

$$f = \frac{\Phi_F}{\sqrt{2U}}\,\psi, \quad g = \theta - \phi + \frac{\Phi_G}{\sqrt{2U}}\,\psi, \quad h = \nu + \frac{\Phi_H}{\sqrt{2U}}\,\psi, \quad u = t - \frac{\mu + \Phi}{\sqrt{8U^3}}\,(\psi - e\sin\psi) + \frac{\Phi_U}{\sqrt{2U}}\,\psi.$$

The choice $\Phi = 2U\,\Phi_U$, gives $\Phi = \sqrt{2U}\,\Psi(F, G, H)$, that reduces the time transformation to

$$u = t - \frac{\mu}{\sqrt{8U^3}}\,(\psi - e\sin\psi) + \frac{\Phi}{\sqrt{8U^3}}\,e\sin\psi$$

The simple option $\Phi = \sqrt{2U}\,(F + \mu)$ produces $\Phi_F = \sqrt{2U}$, $\Phi_G = \Phi_H \equiv 0$, and leads to the well known "first" Levi-Civita transformation [12],

$$f = \psi, \qquad g = \theta - \phi, \qquad h = \nu, \qquad u = t - \frac{\mu}{\sqrt{8T^3}}\,(\psi - e\sin\psi). \tag{68}$$

where u plays the role of the epoch of pericenter passage in the Keplerian motion, where the mean anomaly $\phi = n\,(t - u) = \psi - e\sin\psi$, and $n = (2T)^{3/2}/\mu$, from the energy equation $-T = -\mu/(2a)$. Note that we make use of the fact that $\Phi = 0$ to drop the corresponding term from the time transformation.

Other choice is to make $\Phi = 2U\,\Phi_U - \mu$, that produces $\Phi = \sqrt{2U}\,\Psi(F,G,H) - \mu$, and reduces the time transformation to

$$u = t + \frac{\mu + \Phi}{\sqrt{8U^3}}\, e \sin\psi.$$

The option $\Phi = \sqrt{2U}\,F - \mu$: $\Phi_F = \sqrt{2U}$, $\Phi_G = \Phi_H \equiv 0$, leads to the famous "second" Levi-Civita [13] transformation

$$f = \psi, \qquad g = \theta - \phi, \qquad h = \nu, \qquad u = t + \frac{\mu}{\sqrt{8T^3}}\, e \sin\psi, \tag{69}$$

where, again, we make $\Phi = 0$.

2.3 $\chi = s - b = -b + \sqrt{b^2 + r^2}$

This case is analogous to the previous one, and provides similar transformations that embrace also those of Levi-Civita for the Keplerian case.

2.4 $\chi = r^2$

We get now

$$\alpha = \mu, \qquad a = \frac{\mu}{2U}, \qquad p = \frac{G^2 - 2\Phi}{\mu} + 2b - \frac{b^2}{a}, \tag{70}$$

that replaced in Eqs. (22) and (23) give

$$-\mathcal{I}_3 = \mathcal{I}_1 = -\frac{\phi_1}{2\sqrt{G^2 - 2\Phi}} - \frac{\phi_2}{2\sqrt{G^2 - 2\Phi + 4b\,\mu}}, \tag{71}$$

$$\mathcal{I}_2 = \frac{\mu}{\sqrt{8U^3}}\,(\psi - e\sin\psi), \tag{72}$$

Therefore, the family of transformations is $\Theta = G$, $N = H$, $T = U$, $R = \sqrt{Q}$,

$$f = \Phi_F \left(\frac{\phi_1}{2\sqrt{G^2 - 2\Phi}} + \frac{\phi_2}{2\sqrt{G^2 - 2\Phi + 4b\,\mu}} \right), \tag{73}$$

$$g = \theta - \frac{G - \Phi_G}{\Phi_F}\, f, \tag{74}$$

$$h = \nu + \frac{\Phi_H}{\Phi_F}\, f, \tag{75}$$

$$u = t - \frac{\mu}{\sqrt{8U^3}}\,(\psi - e\sin\psi) + \frac{\Phi_U}{\Phi_F}\, f, \tag{76}$$

In view of Eqs. (73)–(76), a straightforward simplification requirement is $\Phi_H = 0$ and $\Phi_F = \Phi_U = G - \Phi_G$. Then, we might choose

$$\Phi = \frac{1}{2}\left[G^2 - (G - F - U)^2\right]$$

and the transformation is

$$f = \frac{\phi_1}{2} + \frac{G-F-U}{\sqrt{(G-F-U)^2+4b\,\mu}}\,\frac{\phi_2}{2}, \tag{77}$$

$$g = \theta - f, \tag{78}$$

$$h = \nu, \tag{79}$$

$$u = t - \frac{\mu}{\sqrt{8U^3}}\,(\psi - e\sin\psi) + f. \tag{80}$$

In the Keplerian case $b = 0$, $\phi_1 = \phi_2 = \phi$, further simplifies to $f = \phi$; besides, the reduced Hamiltonian only needs to depend on two momenta (in the extended phase space formulation) and if we choose $\Phi = \frac{1}{2}\left[G^2 - (G-F)^2\right] = F\left(G - \frac{1}{2}F\right)$, then, taking into account that $\Phi_U = 0$ in Eq. (76), we recover the well known TR-mapping [15, 5].

$$f = \phi, \qquad g = \theta - f, \qquad h = \nu, \qquad u = t - \frac{\mu}{\sqrt{8U^3}}\,(\psi - e\sin\psi), \tag{81}$$

3 Conclusions

Normally, the Hamilton-Jacobi equation is used for dealing with a specific class of problems. That is why the new Hamiltonian is commonly chosen before solving the quadratures introduced by the method. The success in that pre-selection strongly depends on the intuition and experience of the user, and may require a tedious sequence of trials. However, the new Hamiltonian can be hold formal to a large extent in the solution of the Hamilton-Jacobi equation, a fact that may help in the selection procedure.

In the case of Henon's isochronal potential, we solve the Hamilton-Jacobi equation keeping formal the new Hamiltonian, thus obtaining whole families of canonical transformations, contrary to single ones, from which we recover classical transformations in the literature as well as come up with new ones. This way of proceeding provides a great insight that is conveniently used in the search for the new Hamiltonian that defines the canonical transformation.

Acknowledgements

We thank financial support from the Government of Spain in the form of research projects MTM 2009-10767 (S.F.), ESP 2007-64068 and AYA 2009-11896 (M.L), and also a grant from Fundación Séneca of the Autonomous Region of Murcia.

References

[1] Andoyer, M.H., 1913, "Sur l'Anomalie Excentrique et l'Anomalie Vraie comme Éléments Canoniques du Mouvement Elliptique d'après MM. T. Levi-Civita et G.-W. Hill," *Bulletin astronomique*, Vol. 30, pp. 425–429.

[2] Benettin, G., 2004, "The elements of Hamiltonian perturbation theory," in *Hamiltonian Systems and Fourier Analysis: New Prospects for Gravitational Dynamics*, D. Benest and C. Froeschle (ed.), pp. 1–98. Cambridge Scientific Publ., Cambridge, UK.

[3] Bocaletti, D., Pucaco, G., 2001, *Theory of Orbits. 1: Integrable Systems and Non-perturbative Methods*, Springer-Verlag, Berlin Heidelberg, pp. 316 and ff.

[4] Delaunay, Ch.E., 1867, "Théorie du Mouvement de la Lune," *Mémoires de l'Academie des Sciences de l'Institut Impérial de France*, Vol. 28, See Chap. 1, para. 5, pp. 9–11.

[5] Deprit, A., 1981, "A Note Concerning the TR-Transformation," *Celestial Mechanics*, Vol. 23, pp. 299–305.

[6] Eggen, O.J., Lynden-Bell, D., Sandage, A.R., "Evidence from the motions of old stars that the galaxy collapsed," *Astrophysical Journal*, Vol. 136, 1962, pp. 748-766

[7] Ferrer, S., Lara, M., `arXiv:0906.5312v2 [nlin.SI]` 18 Nov. 2009.

[8] Gerhard, O.E., Saha, P., 1991, "Recovering galactic orbits by perturbation theory," *Monthly Notices of the Royal Astronomical Society*, Vol. 251, pp. 449–467.

[9] Goldstein, H., 1980, *Classical Mechanics, 2nd edition*, Addison-Wesley series in physics.

[10] Hénon, M., 1959, "L'amas isochrone I," *Annales d'Astrophysique*, Vol. 22, pp. 126–39.

[11] Hill, G.W., 1913, "Motion of a system of material points under the action of gravitation," *Astronomical Journal*, Vol. 27, iss. 646–647, pp. 171–182.

[12] Levi-Civita, T., 1913, "Nouvo sistema canonico di elementi ellittici," *Annali di Matematica*, serie III, Vol. XX, pp. 153–170.

[13] Levi-Civita, T., "Sur la régularization du problème des trois corps," *Acta mathematica*, Vol. 42, 1918, pp. 99–144.

[14] Poincaré, H., 1893, *Les méthodes mouvelles de la mécanique céleste*, Vol. 2, Gauthier-Villars et Fils, Paris, pp. 315–342.

[15] Scheifele, G., "On Nonclassical Canonical Systems," *Celestial Mechanics*, Vol. 2, 1970, pp. 296–310. (see Theorem 4 on p. 30–301)

[16] Sitter, W. de, "On canonical elements," Koninklijke Nederlandsche Akademie van Wetenschappen Proceedings, Vol. 16, No. 1, 1913, pp. 279–291 (`http://www.digitallibrary.nl`).

[17] Struckmeier, J., 2005, "Hamiltonian Dynamics on the symplectic extended phase space for autonomous and non-autonomous systems," *Journal of Physics A: Mathematical and General*, Vol. 38, No. 6, pp. 1257–1278.

[18] Sussman, G.J., Wisdom, J., 2001, *Structure and Interpretation of Classical Mechanics*, The MIT Press, Cambridge, Sec. 5.8, pp. 403 and ff. (`http://mitpress.mit.edu/SICM/`).

[19] Yanguas, P., 2001, "Perturbations of the isochrone model," *Nonlinearity*, Vol. 14, pp. 1–34.

Monografías de la Real Academia de Ciencias de Zaragoza **35**, 53–71, (2011).

Formation and evolution of Newton's regions of convergence in some problems of Celestial Mechanics

Tilemahos J. Kalvouridis and Irene T. Kalvouridis

National Technical University of Athens

Faculty of Applied Sciences, Department of Mechanics

Abstract

In nonlinear dynamical problems, chaos appears in many aspects of their investigation. In this paper we show the chaotic character of the regions of convergence as it is resulted from the numerical investigation of the equilibrium points in some known problems of Celestial Dynamics.

Keywords: chaos; regions of convergence; equilibrium points; Celestial Mechanics; Newton's algorithm.

1 Introduction

One of the most important steps in the study of a dynamical problem is the determination of the equilibrium states of the system. In nonlinear problems this is achieved by using numerical methods. During this process, the nonlinearity of a problem reveals some chaotic aspects of the problem that, beyond the very impressive pictures it provides, it also has some practical benefits. This is exactly the aim of this paper; to give information about the way that the regions of convergence are formed and evolve, in various problems of Celestial Mechanics. Furthermore, we investigate their parametric variation and we establish various general rules and remarks. This issue has been discussed in various papers that have been appeared the last few years ([1]-[6]). For our purposes we have selected the well known Newton's method, which is simple, popular, efficient, fast and accurate. For applications we have selected some known problems of Celestial Mechanics, such as the restricted three-body problem, the gravitational regular-polygon problem of $(N + 1)$ bodies, the photo-gravitational Copenhagen problem, the restricted five-body problem of Ollöngren, the Maranhao-Llibre problem of $3 + 1$ bodies and the ring problem of $N + 1$ bodies with radiation pressure. In all these problems or versions, we study the planar

motion of a very small body in the force field created by $N > 1$ big bodies (primaries) of the dynamical system.

2 Description of the considered cases, equations of planar motion of the small particle and potential functions

2.1 General characteristics and equations of motion

In all the above cases, a small body (or a particle) moves in the force field created by two or more, much bigger bodies, the primaries. This force field can be either purely gravitational or a combination of a gravitational one and a field coming from one or more radiating primaries. If we consider that the primaries, in all these cases, rotate with constant angular velocity around their center of mass, then the motion of the small body in a synodic coordinate system, which is rigidly attached to the rotating primaries, is described in normalized quantities by the following set of second order differential equations,

$$\ddot{x} - 2\dot{y} = \frac{\partial U}{\partial x}, \qquad \ddot{y} + 2\dot{x} = \frac{\partial U}{\partial y} \tag{1}$$

where $U(x, y)$ is the potential function, that has a different form in each of the considered cases. From the above equations we obtain a Jacobian-type integral of motion

$$\dot{x}^2 + \dot{y}^2 = 2\Omega(x, y) - C \tag{2}$$

where C is the so-called Jacobian constant.

2.2 Case 1: The restricted three-body problem

The well-known restricted three-body problem deals with the motion of a small particle in the gravitational field produced by two major bodies called the primaries, P_1 and P_2 that rotate around their center of mass in circular orbits with constant angular velocity (here considered as 1)(Figure 1a). It is characterized by one parameter μ which is the reduced mass $m_2/(m_1 + m_2)$ of primary P_2. The potential function U in this case has the form,

$$U = \frac{1}{2}\left(x^2 + y^2\right) + \frac{1-\mu}{r_1} + \frac{\mu}{r_2} + \frac{1}{2}\mu(1-\mu) \tag{3}$$

r_1 and r_2 are the distances of the small body from the two primaries, with

$$r_1^2 = (x-\mu)^2 + y^2, \qquad r_2^2 = (x-\mu+1)^2 + y^2.$$

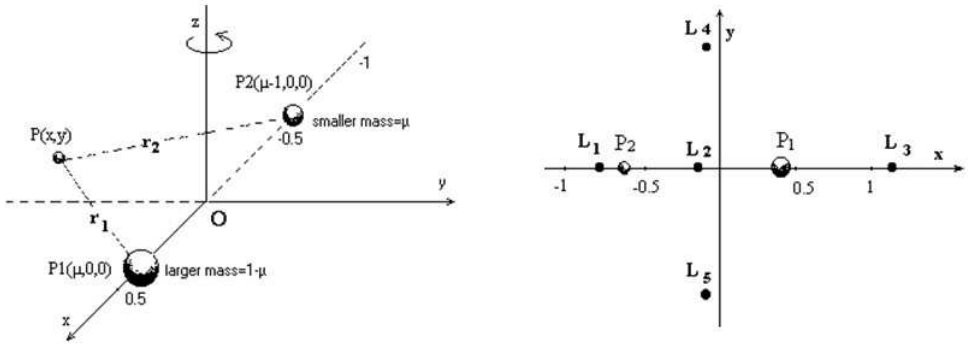

(a) (b)

Figure 1.— (a) The configuration of the restricted three-body problem and the synodic coordinate system (b) The distribution of the equilibrium points

2.3 Case 2: The photo-gravitational Copenhagen problem

The Copenhagen problem is a particular case of the restricted three-body problem with $\mu = 0.5$ (Figure 2a). Here, we consider that in addition to their gravitational character, the primaries are also radiating sources with radiation coefficients q_1 and q_2 respectively. Therefore the problem depends on two parameters namely q_1 and q_2. In this case the potential function has the form

$$U(x,y) = \frac{1}{2}\left[\left(x^2+y^2\right) + \sum_{i=1}^{2}\frac{q_i}{r_i}\right] \tag{4}$$

$$r_1 = \left[\left(x-\frac{1}{2}\right)^2 + y^2\right]^{1/2}, \qquad r_2 = \left[\left(x+\frac{1}{2}\right)^2 + y^2\right]^{1/2}$$

r_1 and r_2 are the distances of the particle from the primaries

$$q_i = 1 - b_i, \quad i = 1,2, \quad \text{where } b = \frac{F_r}{F_g} \tag{5}$$

are, for each radiating source, the ratios of force F_r caused by radiation, to force F_g caused by gravitation.

2.4 Case 3: The gravitational regular polygon problem of $N+1$ bodies

The regular polygon problem of $(N+1)$ bodies, deals with the motion of a small body in the combined Newtonian field created by N much bigger bodies called the primaries. $\nu = N-1$ of these have equal masses m and are arranged at the vertices of a regular ν-gon while the Nth primary is located at the center of mass of the configuration (Figure 3). The peripheral primaries rotate about their center of mass with the same constant angular velocity. The system is characterized by two parameters: the mass parameter $\beta = m_0/m$, that is the ratio of the central mass m_0 to a peripheral one, and the number ν of the peripheral primaries.

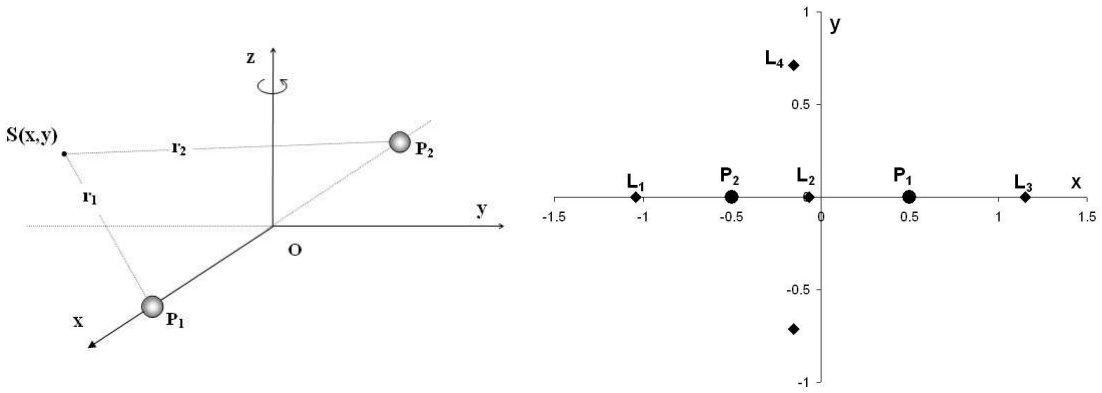

(a) (b)

Figure 2.— The photogravitational Copenhagen case. (a) The configuration of the system. (b) Distribution of the equilibria of the small body when $b_1 = 0.1$, $b_2 = 0.5$

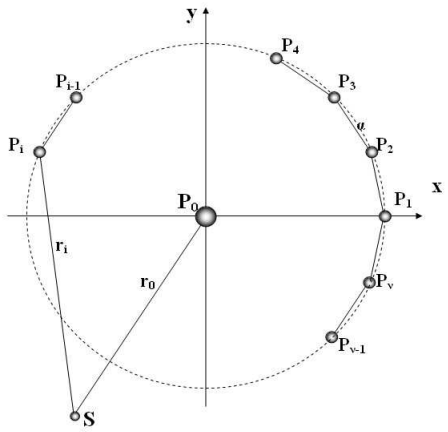

Figure 3.— The planar ring problem of $(N + 1)$ bodies

$$U(x,y) = \frac{1}{2}\left(x^2 + y^2\right) + \frac{1}{\Delta}\left[\frac{\beta}{r_0} + \sum_{i=1}^{\nu}\frac{1}{r_i}\right] \tag{6}$$

$$\Delta = 2\sin\theta\left[\sum_{i=2}^{\nu}\frac{\sin^2\theta}{\sin(i-1)\theta} + 4\beta\sin^2\theta\right], \quad \theta = \pi/\nu \tag{7}$$

and

$$r_0 = \left(x^2 + y^2\right)^{1/2}, \quad r_i = \left[(x_i - x)^2 + (y_i - y)^2\right]^{1/2}, \quad i = 1, 2, 3, \ldots, \nu$$

are respectively the distances of the particle from the central primary and the peripheral ones, where x_i and y_i are their coordinates. The equilibrium locations are arranged on either five or three circular zones depending on the value of the mass parameter β. If this parameter is less than a critical value l_ν (different for each configuration) then five zones exist (Figure 4a). Otherwise, three equilibrium zones are formed (Figure 4b).

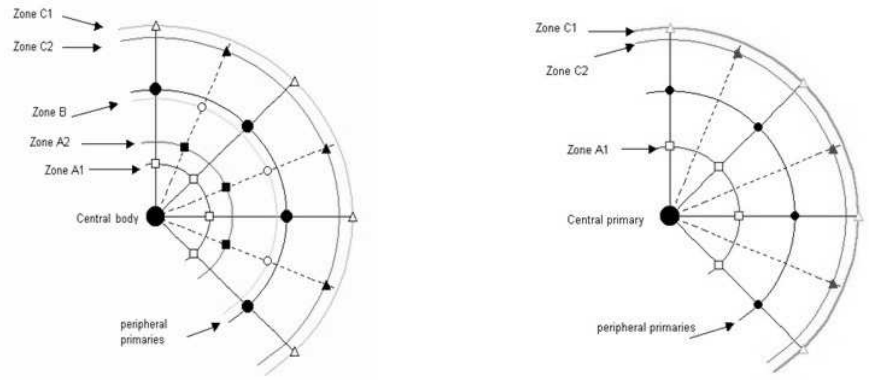

(a) (b)

Figure 4.— General distribution of the equilibrium positions in the ring problem of $N+1$ bodies for two cases: (a) $\beta < l_\nu$, (b) $\beta > l_\nu$, (l_ν is the critical value of the mass parameter)

2.5 Case 4: The restricted five-body problem of Ollöngren

Three big bodies P_1, P_2, P_3 with equal masses m are located at the vertices of an imaginary equilateral triangle. A fourth body P_0 with mass m_0 is located at the mass center of the system. A small particle S with negligible mass moves in the resultant force field of the big bodies (Figure 5). The system is characterized by one parameter which is the ratio $\beta = m_0/m$ of the central mass to a peripheral one. The configuration has three axes of symmetry since it is identified after a rotation of 120^o around the perpendicular axis Oz. The potential function has the form,

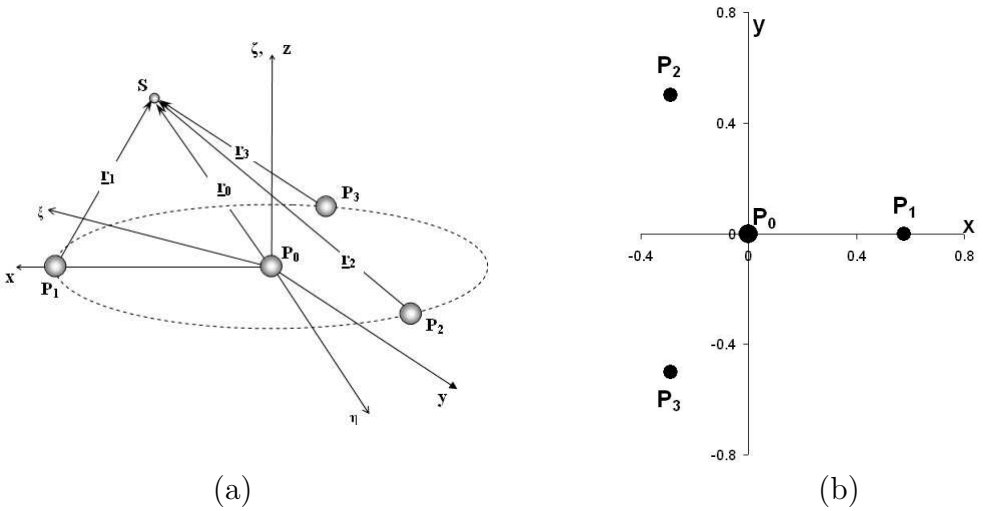

(a) (b)

Figure 5.— The five-body problem of Ollöngren. (a) The three-dimensional case, (b) the planar configuration of the primaries

$$U = \frac{1}{2}\left(x^2 + y^2\right) + \frac{1}{3(1+\beta\sqrt{3})}\left[\frac{\beta}{r_0} + \sum_{i=1}^{3}\frac{1}{r_i}\right] \tag{8}$$

where

$$r_0 = \left(x^2 + y^2\right)^{1/2}, \qquad r_i = \left[(x_i - x)^2 + (y_i - y)^2\right]^{1/2}.$$

The small body S has fifteen equilibrium locations when $\beta < 0.014$. They are grouped in five groups, A_1, A_2, B, C_2 and C_1 by order of appearance from the origin outwards. More specifically, the equilibria of groups A_1 and C_1 are located on the radii that join the central primary and the peripheral ones. Those of A_2, B and C_2 are located on the bisectors of the angles formed by two consecutive primaries and the central one (Figure 6a). The equilibria of each group have the same Jacobian constant C and are characterized by the same state of stability. When $\beta > 0.014$ six of these positions (groups A_2 and B) disappear and the system possesses only nine locations that belong to groups A_1, C_2 and C_1 (Figure 6b).

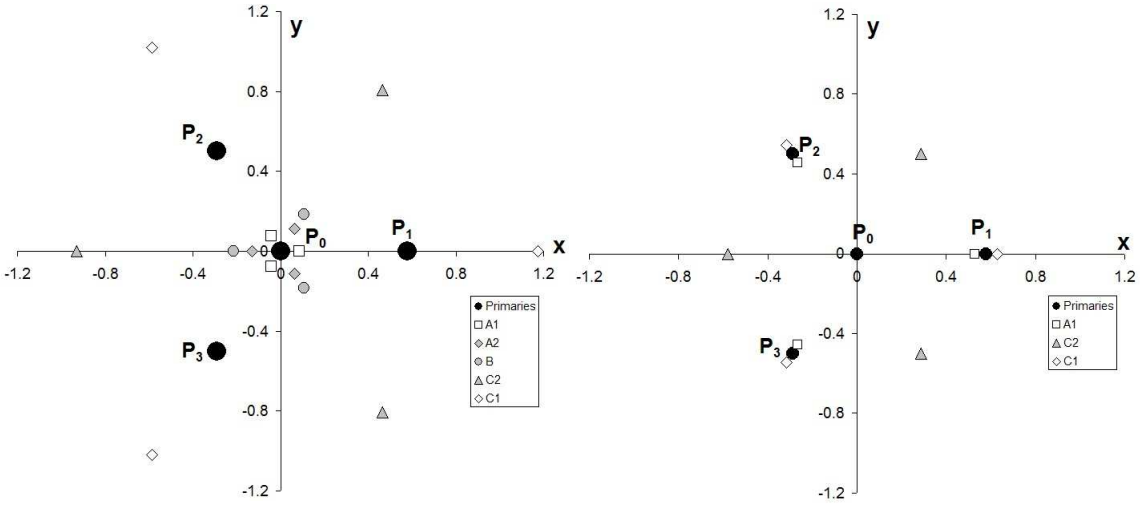

Figure 6.— Distribution of the equilibrium positions (a) for $\beta = 0.01$, (b) for $\beta = 500$

2.6 Case 5: The Maranhao-Llibre problem of $3 + 1$ *bodies*

The configuration is shown in Figure 7a. The problem is characterized by one parameter which is the mass ratio $\beta = m_0/m_1$. In this case the potential function has the form,

$$U = \frac{1}{2}\left(x^2 + y^2\right) + \frac{1}{2(1+4\beta)}\left[\frac{\beta}{r_0} + \sum_{i=1}^{2}\frac{1}{r_i}\right] \tag{9}$$

There are 6 equilibrium points for every value of parameter β ($\beta \neq 0$). Two of them are disposed along the syzygies' axis (x-axis of the synodic coordinate system) in symmetric positions with respect to the origin O (group A_1). Two points lie on the same axis but beyond the peripheral primaries (group C_1). Finally, the remaining two points lie on the y-axis. They form a group which is symbolized by C_2. As the mass parameter decreases

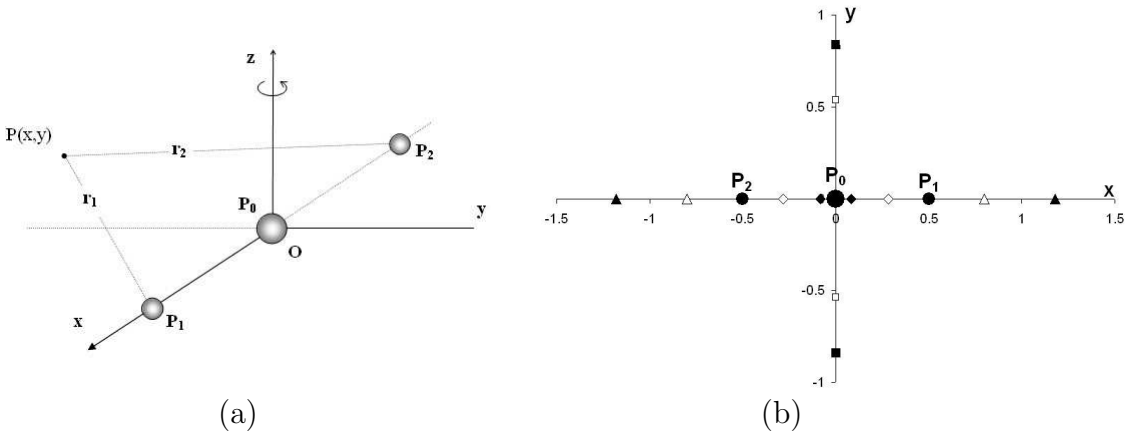

(a) (b)

Figure 7.— The Marañhao-Llibre problem. (a) The configuration. (b) Distribution of the equilibrium positions (for $\beta = 0.2$ (full black) and for $\beta = 2$ (framed black))

the inner collinear points approach each other by moving towards the origin, where they coincide when $\beta = 0$. On the contrary, the outer collinear points go away from each other and from the origin. As a consequence, for the limit value $\beta = 0$, we obtain the five Lagrange equilibrium positions of the Copenhagen case of the restricted three-body problem. Figure 7b shows the distribution of the equilibrium points for $\beta = 0.2$ and $\beta = 2$.

2.7 Case 6: The photo-gravitational ring problem of $N + 1$ bodies

The arrangement of the primaries is the same as in the gravitational version. However, one or more primaries are radiation sources and therefore the system in the general case is characterized by $N + 2$ parameters, that is the number ν of the peripheral bodies, the mass parameter β and the $N = \nu + 1$ radiation coefficients b_i, $i = 0, \ldots, \nu$. The symmetries that appear in the gravitational case are generally destroyed and only in the three following cases is preserved:
(a) The central body is a radiation source (whatever the value of the radiation coefficient b_0 is).
(b) All peripheral bodies are radiation sources and have the same radiation coefficients.
(c) All the primaries are radiation sources and the peripheral bodies have the same radiation coefficients.
The potential has the form,

$$U = \frac{1}{2}\left(x^2 + y^2\right) + \frac{1}{\Delta}\left[\frac{\beta q_0}{r_0} + \sum_{i=1}^{\nu} \frac{q_i}{r_i}\right] \tag{10}$$

where Δ is the same as in the gravitational case (relation (7)) and q_i are the radiation parameters that are given by relations (5). The number of the existing equilibrium points depends on the values of the N radiation coefficients. In all cases where the symmetry that

exists in the gravitational case, is preserved, the configuration has 2ν axes of symmetry and the equilibria are located along them. The equilibrium positions are assembled either in five or three groups of ν points each. Figure 8 shows the distribution of the equilibrium locations for two cases where symmetry is preserved. In Figure 8a all primaries radiate with the same radiation coefficients $b = 0.5$, while in Figure 8b all peripheral primaries radiate with the same radiation coefficients $b = 0.9$.

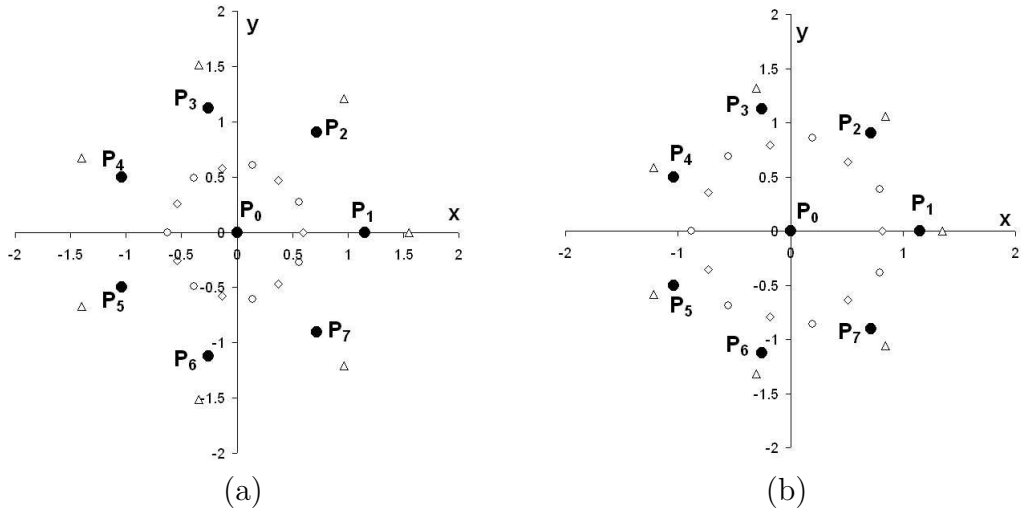

Figure 8.— Distribution of the equilibrium locations in the photo-gravitational ring problem when $\nu = 7$, $\beta = 2$. We mark with small triangles the equilibria of group C_1, with small circles the equilibria of group A_2 and with small rhomboids the equilibria of group A_1. (a) All primaries radiate with radiation coefficients $b = 0.5$ (b) All peripheral primaries radiate with radiation coefficients $b = 0.9$

3 The numerical method and some preliminary notes

3.1 Conditions for equilibrium

The conditions for an equilibrium position of the small body, are $\dot{x} = \dot{y} = \ddot{x} = \ddot{y} = 0$. Under these conditions, these locations are the solutions of the nonlinear system of algebraic equations

$$\frac{\partial U}{\partial x} = 0, \qquad \frac{\partial U}{\partial y} = 0. \tag{11}$$

To locate the equilibrium points on the plane (x, y) we apply a numerical method to solve equations (11).

3.2 The equivalence principle of the equilibrium points

In any dynamical system if two or more equilibrium positions have exactly the same dynamical properties, which means, the same energy (here the value of the Jacobian

constant C) and the same state of stability, then are dynamically equivalent. This property is usually dictated by the symmetry of the force field created by the members of the system. For example the triangular equilibrium points L_4 and L_5 in the restricted three-body problem are dynamically equivalent for any value of the mass parameter μ. When $\mu = 0.5$ (Copenhagen gravitational case) equilibrium points L_1 and L_3 are also dynamically equivalent. Furthermore, in the ring gravitational problem of $N + 1$ bodies, the equilibrium points that belong to some particular equilibrium zone (A_1, A_2, B, C_2, C_1) are dynamically equivalent.

3.3 The crooked path described by the consecutive iterations of the numerical method

We can describe the consecutive iterations of the numerical algorithm as the "motion" of a "point" on a crooked path, just like the Brownian motion of an atom of a gas.

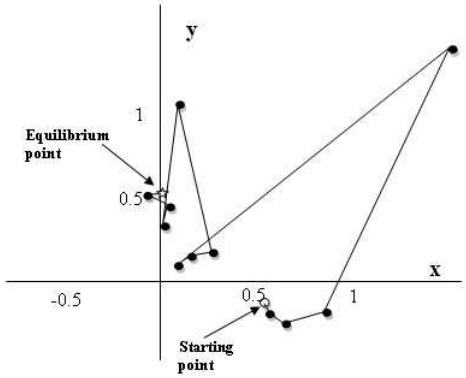

Figure 9.— The crooked path formed by the consecutive approximations of the numerical method

3.4 Sensitivity to small changes in the initial values

The term sensitivity at this point is used to describe the way that the path followed by the method during the iterative process, is affected by small perturbations to the initial values. This sensitivity is evinced by various ways. Here we show five of them:
(1) A small change of the initial values leads to the same equilibrium position with the same or almost the same number of steps.
(2) A small change of the initial values leads to the same equilibrium position but the number of steps significantly differs from the one in the unperturbed case (Figure 10a).
(3) A small change of the initial values leads to a different equilibrium position (dynamically equivalent or not) of the system after a number of steps (Figure 10b).
(4) A small change of the initial values leads to a non-convergent state (Figure 10c).
(5) A small change of the initial values leads to a state in which the "point" oscillates between two values and never reaches the target (Figure 10d).

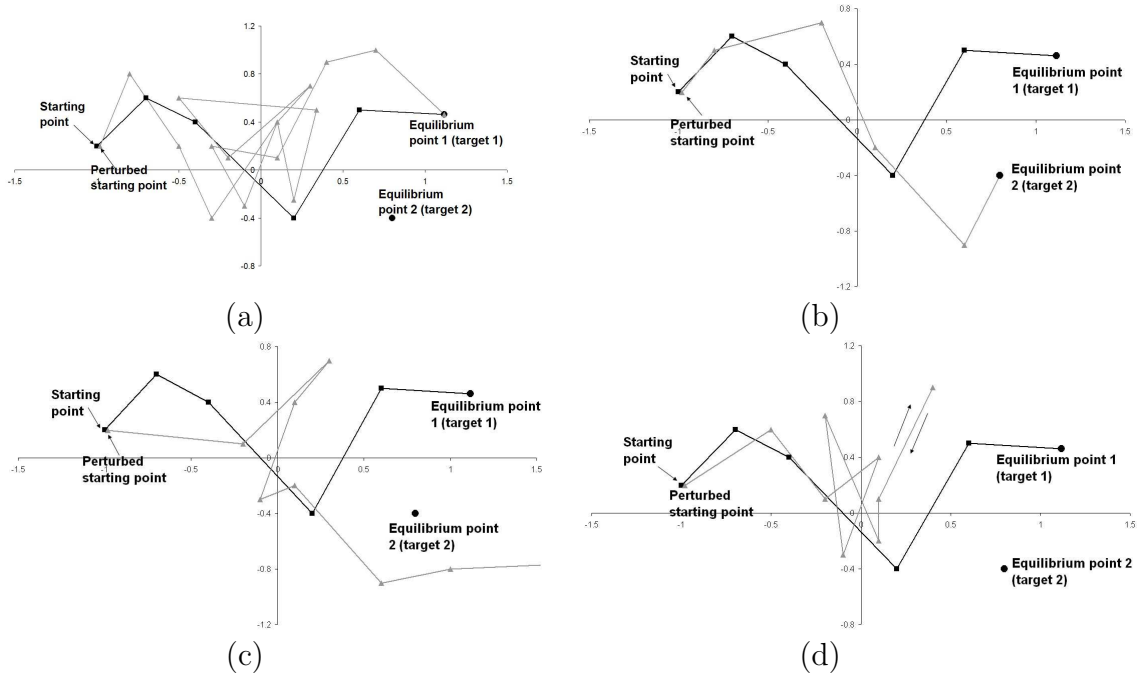

Figure 10.— The black lines show the "unperturbed" paths and the gray lines the "perturbed" ones; (a) the "perturbed" path reaches the same target as the "unperturbed" one but in a very different number of steps; (b) the "perturbed" path reaches a different target (equilibrium point); (c) the "perturbed" path dos not converge at all; (d) the "perturbed" path after some steps "oscillates" between two values

3.5 The numerical method

Several methods for solving algebraic systems of non linear equations are known. However, Newton's method still remains a fast (it converges quadratically), simple and accurate method. In the past (see [3] and [4]), we have used and compared post Newtonian methods like the Broyden's method and an improved version of it. Although the obtained results are qualitatively similar, however, those obtained from Newton's method seem to be much better. The Newton's algorithm for the general case of equations (11) takes the form,

$$\begin{aligned} x_n &= x_{n-1} - \left.\frac{U_x U_{yy} - U_y U_{xy}}{U_{yy} U_{xx} - U_{xy}^2}\right|_{(x_{n-1}, y_{n-1})} \\ y_n &= y_{n-1} + \left.\frac{U_x U_{yx} - U_y U_{xx}}{U_{yy} U_{xx} - U_{xy}^2}\right|_{(x_{n-1}, y_{n-1})} \end{aligned} \tag{12}$$

where we symbolize with U_x, U_y, U_{xx}, U_{yy}, U_{xy} the first and second derivatives of U calculated at the $(n-1)$th step of the iteration process. The process terminates when some predetermined accuracy is reached.

4 The regions of convergence

4.1 General remarks and comments

The regions of convergence (or basins of convergence, or attracting domains) are formed by the launching points of the applied particular numerical method that lead to dynamically equivalent equilibrium positions of the system. As it is shown in the figures obtained from the various case-problems, each region has a fractal structure and generally consists of a "compact" area which evolves around an equilibrium location and of randomly dispersed points that are mixed with the dispersed points that belong to basins of other equilibrium points or equilibrium groups. Next we shall expose the results concerning these regions for each of the considered cases. In Cases 4, 5 and 6 (Figures 14 to 16) we also give the attracting sub-domains which are formed by considering the number of the steps that are needed to reach the equilibrium positions.

4.2 Case 1: The restricted three-body problem

Figure 11 shows the evolution of the regions of convergence for the five Lagrangian points.

The basin of convergence of L_1, occupies the smallest area of all the basins for every value of μ ($0 < \mu < 0.5$). It consists of two "compact" areas of limited extent and of dispersed points (Figure 11a). Both "compact" areas are developed on the left of primary P_2 and are symmetrically arranged with respect to the x-axis. As μ increases, the attracting region expands, while the "compact" regions widen and the dispersed points increase and become denser around the "compact" areas, thus forming fine fractal structures.

The region of convergence of point L_2 consists of two "compact" areas. The first one extends between the two primaries P_1 P_2, while the second one is extended beyond the "compact" regions of L_1 (Figure 11b). The dispersed points which belong to this basin form fractal boundaries. As μ augments the dispersed points become denser, thus forming fractal protrusions near the boundaries of the "compact" areas corresponding to the collinear Lagrangian points.

The region of convergence of L_3 is homothetic of $R(L_1)$ with homothetic ratio > 1. Its center of homothety is a point lying on the x-axis, close to L_2. As μ increases for $0 < \mu < 0.5$, the homothetic ratio approaches 1 and the center of homothety approaches equilibrium position L_2. The region of convergence of L_3 consists of two "compact" areas which extend on the right of primary P_1, as well as of numerous dispersed points (Figure 11c). It shrinks as μ augments.

The region of L_4 holds numerous "compact" areas that extend on the semi-plane $y > 0$. The dispersed points spread all over the plane (Figure 11d). As μ increases, this region

expands, the "compact" areas tend to unite, thus forming a great "compact" area, while the dispersed points become denser inside the area of the basin boundaries. Finally the basin of convergence of L_5 is symmetric with the one of L_4 as regards the x-axis and therefore presents exactly the same characteristics (Figure 11e).

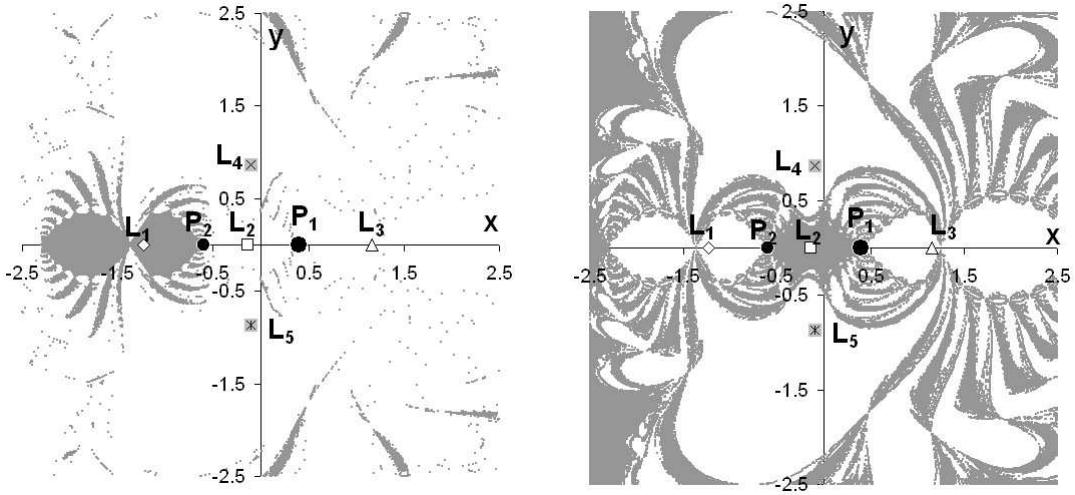

(a) (b)

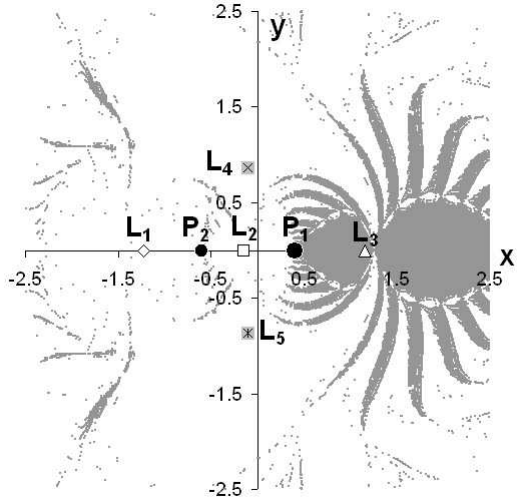

(c)

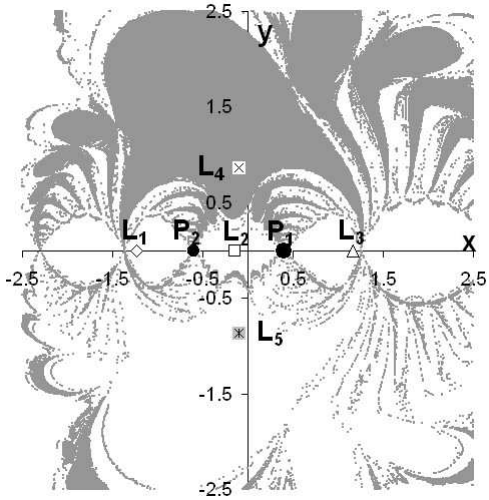

(d)

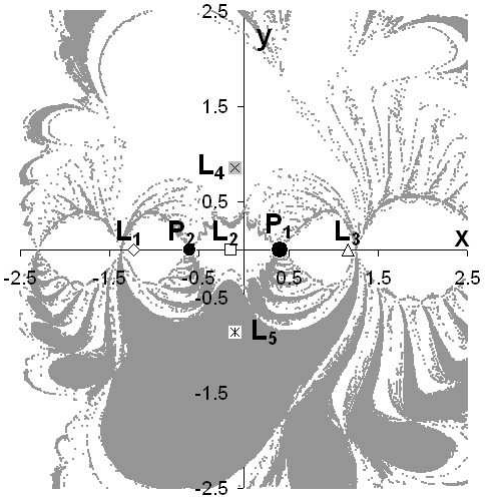

(e)

Figure 11.— Restricted three-body problem; regions of convergence for $\mu = 0.4$. (a) L_1, (b) L_2, (c) L_3, (d) L_4, (e) L_5

4.3 Case 2: The photo-gravitational Copenhagen problem

In this problem the two primaries have equal masses and are both radiation sources. The primaries occupy the same relative distances in the synodic coordinate system. The radiation forces influence the small particle but they do not influence the motion of the primaries. In Figure 12 we can see the regions of convergence of the equilibria that evolve on the upper half of the xy-plane. The picture on the other half of the plane is symmetric with respect to the x-axis. We mark with D some sub-domains which consist of dispersed points and with S the "compact" regions.

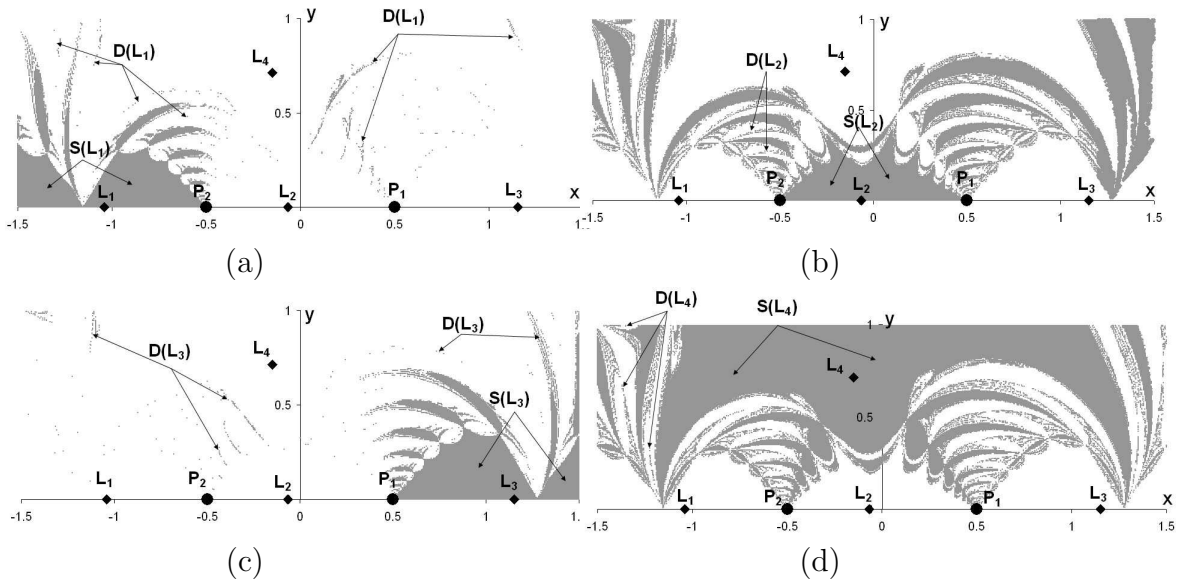

Figure 12.— Regions of convergence in the photo-gravitational Copenhagen problem for $b_1 = 0.1$, $b_2 = 0.5$; (a) L_1, (b) L_2, (c) L_3, (d) L_4

4.4 Case 3: The gravitational regular polygon problem of $N + 1$ bodies

As in the previous case, we mark with D the sub-domains which consist of the dispersed points and with S the "compact" regions. The boundaries of the latter regions are not clearly defined. Figure 13 shows a case with $N = 11$ (regular decagon) and $\beta = 12.5$ ($\beta > l_\nu$). As we have mentioned before, there are three equilibrium zones, A_1, C_2, C_1. The attracting domain of A_1 presents diamond-shaped "compact" parts, whose wavy sides have vague boundaries. These areas develop between the central primary and each of the peripheral ones (Figure 13a). The attracting area of C_1 generally consists of two basic "compact" regions, the biggest of which contains the equilibrium point (Figure 13b). As regards the dispersed points, on the one hand they are organized in a dense way around the two basic "compact" regions, and on the other hand, they are diffused at the boundaries of the "compact" regions of the other zones. In the plane areas that lie between the "compact" regions of A_1 and C_1 stretch the "compact" regions of the attracting area of C_2, (Figure 13c). The dispersed points surround densely the "compact" regions, but also diffuse at the boundaries of the compact regions of the other zones.

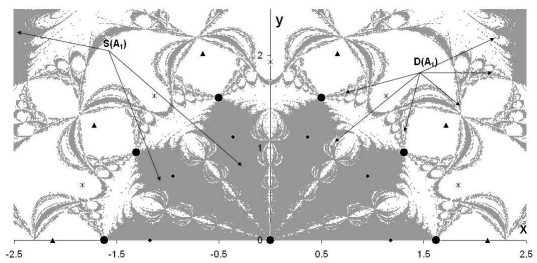

(a)

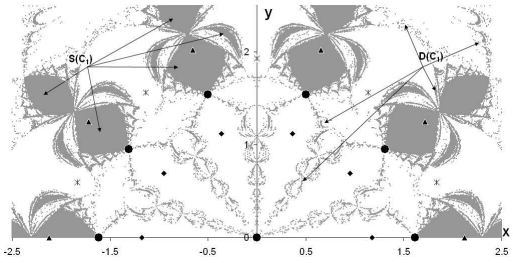

(b)

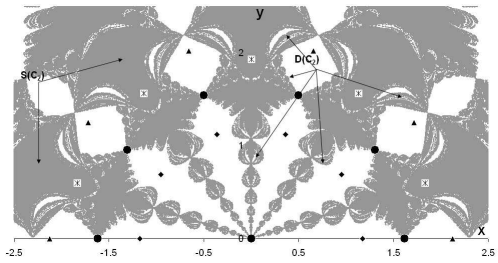

(c)

Figure 13.— Regions of convergence in the gravitational regular polygon problem of $N+1$ bodies for $N = 11$ and $\beta = 12.5$; (a) zone A_1, (b) zone C_1, (c) zone C_2

4.5 Case 4: The restricted five-body problem of Ollöngren

The basins develop in the xy-plane in a way which is consistent with the symmetry of the primaries' configuration. In any case, the basin of group C_2 concentrates the majority of the considered launching points of the xy-plane, while that of group C_2 concentrates the minority of the points. Figure 14 shows two different cases for $\beta = 2$ and $\beta = 500$. As we can see, when β increases, the shape and size of these basins change; the basin of C_2 enlarges (Figures 14e and f) while those of A_1 and C_1 shrink (Figures 14a,b and 14c,d).

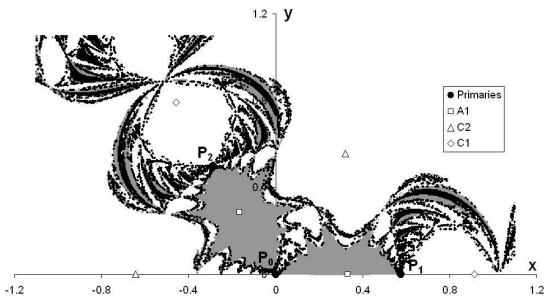

(a)

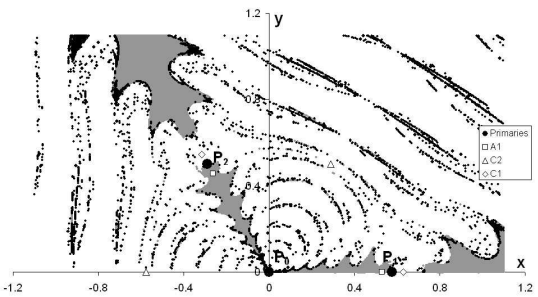

(b)

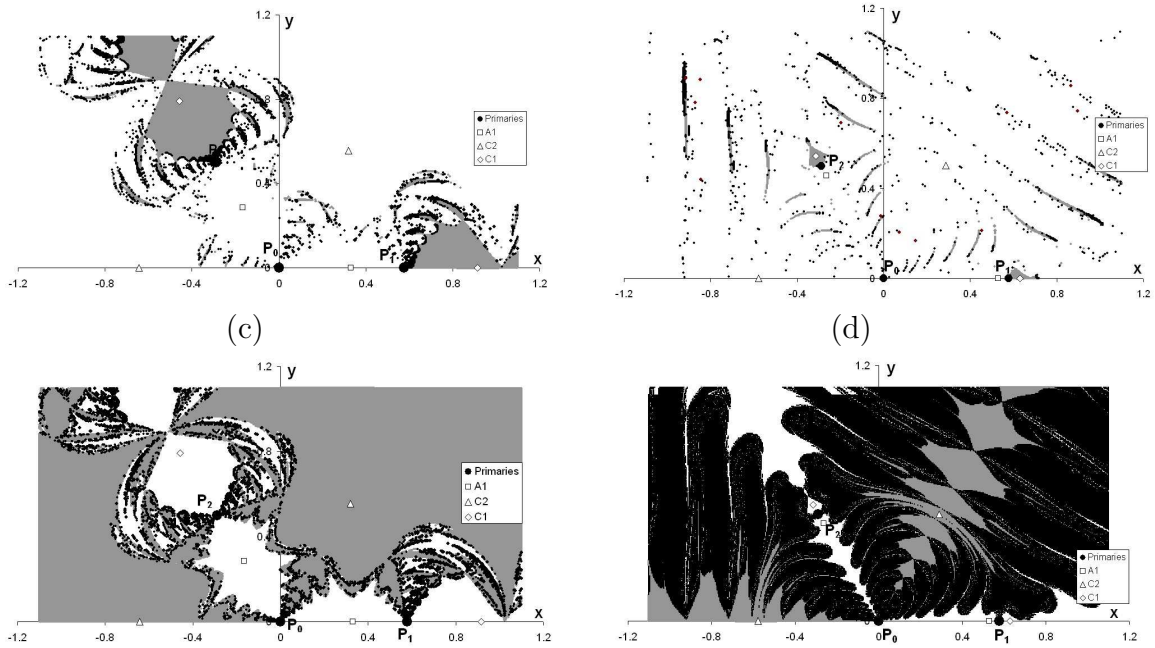

Figure 14.— Regions of convergence in the restricted five-body problem of Ollöngren. The gray regions consist of points where convergence occurs up to 9 iterations, while black regions consist of points where convergence occurs in more than 9 steps; (a) A_1 ($\beta = 2$), (b) A_1 ($\beta = 500$), (c) C_1 ($\beta = 2$), (d) C_1 ($\beta = 500$), (e) C_2 ($\beta = 2$), (f) C_2 ($\beta = 500$)

4.6 Case 5: The Maranhao-Llibre problem of $3 + 1$ *bodies*

Figure 15 shows the attracting domains of the three equilibrium groups for the value of the mass parameter, $\beta = 2$. A "deterministic" region with a fractal structure surrounds each equilibrium position of zone A_1. From its boundaries leap tentacles formed by dispersed points that terminate to the boundaries of the "compact" region of the symmetric equilibrium position of that group. Several other dispersed points also accumulate rather a long way from the x-axis in strip-like areas. Between these two concentrations no other points of this class exist (Figure 15a). When the mass parameter augments, then the "deterministic" regions shrink, while other similar areas are formed in a distance from the first ones. Regarding the attracting domain of zone C_2, it is the biggest one in comparison to the respective regions of the other two groups, as is evident in Figure 15c. It covers most of the surface of the xy plane but presents considerable gaps near the x-axis. As mass parameter β increases, the attracting domain extends and comes closer to the x-axis. The attracting domain of zone C_1 consists of four "deterministic" regions that are symmetrically disposed with respect to the origin. These regions are also symmetric with respect to the x-axis. Two of them, those that are closer to the origin, are wider than the other two. The dispersed points either form tentacles that come out from the boundaries

of the "deterministic" regions, or they form shapes that surround the origin and resemble the wings of a windmill (Figure 15b).

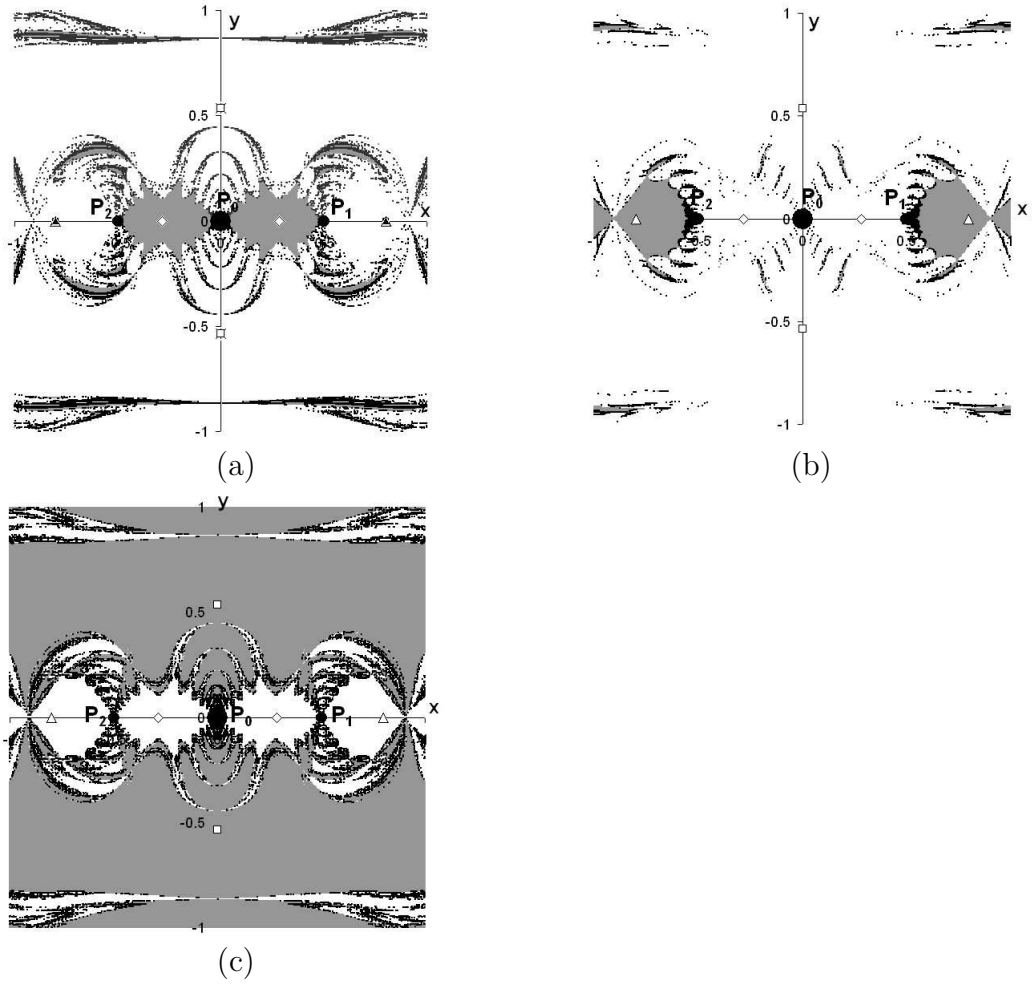

Figure 15.— Regions of convergence in the Marañhao-Llibre problem of $3+1$ bodies for $\beta = 2$; (a) zone A_1, (b) zone C_1, (c) zone C_2. The gray regions consist of points where convergence occurs up to 9 iterations, while black regions consist of points where convergence occur in more than 9 steps

4.7 Case 6: The photo-gravitational ring problem of $N+1$ bodies

The domain of each basin presents, as it is expected, all the symmetry elements of the force field. The very dense parts mainly evolve around the equilibrium points of a given group, while the dispersed points lie on the boundaries of the dense regions of this group or other ones showing a chaotic aspect. The boundaries of the dense parts are not clear and in some cases present a fractal structure. Figure 16 shows a case in a configuration with $\nu = 7$ and $\beta = 2$, where all peripheral primaries are radiation sources with radiation coefficients 0.9. The points of each attracting region have been classified in three classes according to the number of iterations that are needed to achieve convergence with a

predetermined accuracy. The light gray regions consist of points characterized by very fast convergence ($1-5$ iterations) while the gray and the black regions are characterized by fast ($6-10$ iterations) or moderate convergence (more than 10 iterations) respectively. The sub-region of the first class is a very small one and evolves around each equilibrium position of this particular group. The sub-region of class interval $6-10$ iterations of each group consists of areas or points that mainly surround and complement the central regions of the first class interval. Regarding the region of class interval > 10 iterations, it merely consists of dispersed points lying either on the boundaries of the dense regions of the previously mentioned class interval, or between the dense regions of the other equilibrium groups.

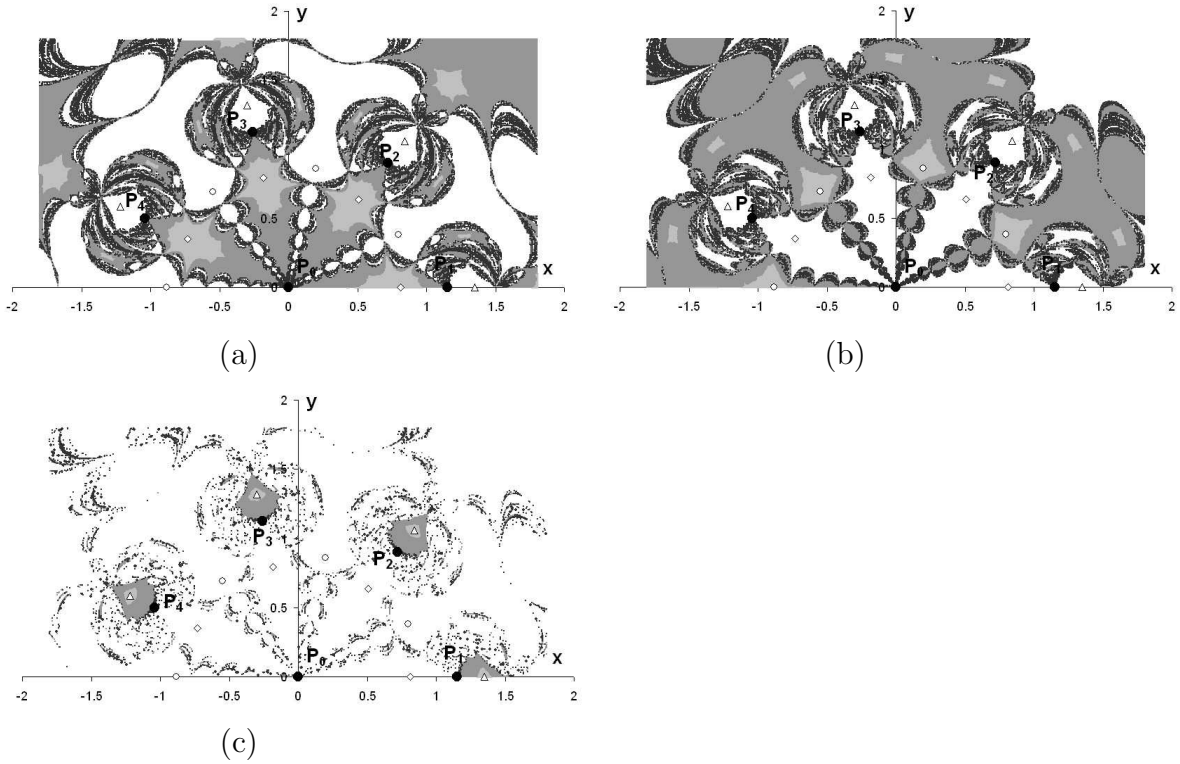

Figure 16.— Regions of convergence in the photo-gravitational ring problem of $(N+1)$-bodies with $\nu = 7$ and $\beta = 2$, when all peripheral primaries are radiation sources with radiation coefficients 0.9; (a) A_1, (b) A_2, (c) C_1. (class $1-5$ steps (light gray), class $6-10$ steps (gray), class > 11 steps (black))

5 Conclusions and remarks

An attracting domain consists of "compact" parts and of dispersed points. These points are distributed on the boundaries of the compact parts of the same or other equilibrium points or zones. The central parts of the "compact" areas show a deterministic aspect, while in the areas where isolated points of different classes of iterations are mixed,

the chaotic character is obvious. The regions that consist of points which converge very fast to an equilibrium position, have "compact" parts which surround these positions and dispersed points. The "compact" parts do not have well defined boundaries. Regarding the regions of moderate or slow convergence, they merely consist of dispersed points lying either on the boundaries of the dense regions of the previously mentioned class interval, or between the dense regions of the other equilibrium points or groups. In all the examined cases the attracting domains present similar properties. The parameters that characterize each case (mass parameter, radiation coefficients, reduced mass, etc.) play an important role on the formation of these domains and they influence in a very definitive way their form and evolution, the distribution of their points on the working plane, as well as, their density and fractal structure.

References

[1] Croustalloudi, M., Kalvouridis, T.: 2007, *Attracting Domains in Ring-Type N-Body Formations*, Planet. Space Sci., **55**, 1-2, 53-69.

[2] Croustalloudi M., Kalvouridis T.: 2004, *Structure and parametric evolution of the Basins of attraction in the restricted three-body problem*, 7th National Congress on Mechanics, HSTAM, June 24-26, Technical Univ. of Crete, Chania, Crete, Greece, Vol. II, pp. **144-150**.

[3] Gousidou-Koutita, M., Kalvouridis, T.J.: 2008, *Numerical study of the attracting domains in a non-linear problem of Celestial Mechanics*, In: G. Akrivis, E. Gallopoulos, A. Hadjidimos, I. Kotsireas, D. Noutsos, M. Vrahatis (eds.) "Recent Approaches to Numerical Analysis: Theory, Methods and Applications", Proceedings, vol. 1, pp.**84-87**, (Conference in Numerical Analysis (NumAn2008), Kalamata, Greece, 1-5 September 2008).

[4] Gousidou-Koutita,M., Kalvouridis, T.J.: 2008, *On the efficiency of Newton and Broyden numerical methods in the investigation of the regular polygon problem of* $(N + 1)$ *bodies*, Appl.Math.Comp., 212 (2009), **100-112**.

[5] Kalvouridis, T.J., Paraskevopoulou, M.: 2009, *Basins of convergence in the restricted five-body problem of Ollöngren*, 2nd Chaotic Modeling and Simulation International Conference (CHAOS2009), 1-5 June 2009, Chania, Crete, Greece. ook of abstracts p. **31**.

[6] Douskos, Ch.: 2010, *Collinear equilibrium points of Hill's problem with radiation and oblateness and their fractal basins of attraction*, Astrophys. Sp. Sci., DOI: 10.1007/s10509-009-0213-5 (in press).

Monografías de la Real Academia de Ciencias de Zaragoza **35**, 73–81, (2011).

Frozen orbits around a prolate body

V. Lanchares, A. I. Pascual and J. F. San Juan

Departamento de Matemáticas y Computación, CIME

Universidad de la Rioja, 26004 Logroño, Spain

Abstract

For a satellite orbiting a prolate body we determine the class of the so called frozen orbits, a kind of trajectories for which either the eccentricity and the argument of the perigee are close to be stationary. This is done after an averaging procedure that produces a one degree of freedom Hamiltonian system retaining the main qualitative features of the original one. This reduced system can be studied in a systematic way in order to calculate the equilibrium solutions, directly related to the frozen orbits.

1 Introduction

In the problem of mission design for artificial satellites there is a set of orbits of special interest for which the eccentricity and the argument of the perigee remain almost stationary [10]. These orbits are called *frozen orbits* and, according to [5], they are in correspondence with equilibrium solutions of an averaged system resulting from the original one.

For the main problem of the artificial satellite, when only the effect of the oblateness coefficient is taken into account, frozen orbits has been studied from the very beginning of the spacial era, pointing out a singularity at the so called critical inclination [3]. This singularity can be resolved when the problem is brought to normal form and the frozen orbits are viewed as relative equilibria [3, 5]. Under this point of view, the critical inclination is just a value for which a parametric bifurcation of the family of frozen orbits occurs. Numerical continuation of periodic orbits [9] and Poincaré surfaces of section [2] have confirmed the appearance of this bifurcation. In this way, the class of frozen orbits can be grouped into families in terms of the inclination, acting the critical inclination as a value that separates different families.

The main problem of the artificial satellite is linked to the Earth and the body around the satellite orbits is supposed oblate. In this way, no much is known for prolate bodies. However, recent missions to objects of the solar system with different shapes could find of interest an extension of the main problem for prolate bodies. This is, for instance, the point of view adopted in [8], where a special kind of halo orbits are derived. Nevertheless, the family of frozen orbits remains unexplored, at least from an analytical point of view, because they were presented in [4] as an application of the *paint by number* technique. The aim of this contribution is to determine the families of frozen orbits for the main problem of an artificial satellite around a prolate body analytically by means of the identification of critical inclinations, when frozen orbits suffer a bifurcation.

2 Problem formulation

The main problem of the artificial satellite is described by the Hamiltonian

$$\mathcal{H} = -\frac{1}{2a} - J_2 \frac{\mu}{2r}\left(\frac{\alpha}{r}\right)^2 (3\sin^2 I \sin^2(\omega+\nu) - 1), \tag{1}$$

where a is the semimajor axis of the orbit, r the distance of the satellite to the origin, that is supposed at the center of the attracting body, α is the equatorial radius of the attracting body, I the inclination of the orbit, ω the argument of perigee, ν the true anomaly, μ the mass parameter of the system and J_2 the oblateness coefficient (see for instance [1]).

Frozen orbits are referred as equilibrium solutions of an averaged system. This averaged system is obtained by performing a Delaunay normalisation [6] up to second order, due to the fact that at first order it exhibits a degeneration. Indeed, there is a set of non-isolated equilibria which corresponds to the critical inclination. Once the normalisation is carried out, we arrive to the new Hamiltonian function

$$\begin{aligned}\mathcal{H} = &-\tfrac{\mu}{2L^2} - J_2\,\alpha^2\mu^4\tfrac{G^2-3H^2}{4G^5L^3} + 3\,J_2^2\,\alpha^4\,\mu^6\left(\tfrac{-5G^4+18G^2H^2-5H^4}{128G^9L^5} - \tfrac{\left(G^2-3H^2\right)^2}{32G^{10}L^4}\right.\\ &\left. + \tfrac{5\left(G^4-2G^2H^2-7H^4\right)}{128G^{11}L^3} + \tfrac{\left(G^2-15H^2\right)\left(G^2-H^2\right)\left(G^2-L^2\right)\cos(2g)}{64G^{11}L^5}\right),\end{aligned} \tag{2}$$

where (L, G, H, ℓ, g, h) are the Delaunay elements describing the orbit of the satellite. L is related with the semimajor axis, G is the total angular momentum, H the third component of the angular momentum, ℓ the mean anomaly, g the argument of perigee and h the argument of the node.

It is worth noting that ℓ and h are cyclic coordinates and then H and L are conserved quantities in this averaged model. Thus, the dynamics is reduced to that of the pair of variables (g, G), described by the canonical differential equations

$$\dot{g} = \frac{\partial \mathcal{H}}{\partial G}, \quad \dot{G} = -\frac{\partial \mathcal{H}}{\partial g}.$$

The equilibrium solutions of this system give rise to the families of frozen orbits and. They are obtained by setting to zero the right hand sides of the two equations. As it happens for a wide class of perturbed Keplerian systems [7], equilibria appear as the solutions of a nonlinear system of the form

$$\begin{aligned} &P_1(G, J_2)\sin 2g = 0, \\ &P_2(G, J_2) + P_3(G, J_2)\cos 2g = 0, \end{aligned} \tag{3}$$

such that $g \in [0, 2\pi)$, $G \in [|H|, L]$ and P_1, P_2 and P_3 are real polynomials in G whose coefficients are polynomial functions of J_2, as well as of α and μ. Nevertheless, a proper choice of units yields $\alpha = \mu = 1$.

For the case considered here, polynomials P_1, P_2 and P_3 are given by

$$\begin{aligned} P_1 \equiv{}& (G-H)\,(G+H)\,(G^2-15\,H^2)\,(G-L)\,(G+L)\,, \\ P_2 \equiv{}& -32\,L^2\,G^8 + (160\,H^2\,L^2 - 25\,J_2)\,G^6 - 24\,J_2\,L\,G^5 \\ &+ (126\,H^2\,J_2 + 35\,J_2\,L^2)\,G^4 + 192\,H^2\,J_2\,L\;\;G^3 \\ &- (45\,H^4\,J_2 + 90\,H^2\,J_2\,L^2)\,G^2 - 360\,H^4\,J_2\,L\,G \\ &- 385\,H^4\,J_2\,L^2, \\ P_3 \equiv{}& 10\,J_2\,G^6 - (224\,H^2\,J_2 + 14\,J_2\,L^2)\,G^4 \\ &+ (270\,H^4\,J_2 + 288\,H^2\,J_2\,L^2)\,G^2 - 330\,H^4\,J_2\,L^2. \end{aligned} \tag{4}$$

3 Bifurcations and families of frozen orbits

In order to establish the solutions of system (3) we observe that they can be divided into different classes, attending to the structure of the first equation in (3). On the one hand we have the solutions for which $P_1(G, J_2) = 0$. They are

$$G = |H|, \quad G = L, \quad G = \sqrt{15}|H|.$$

The two first correspond with equatorial and circular orbits, respectively, and they constitute equilibrium solutions that must be studied in a different way, as Delaunay variables are singular for these kind of orbits. Thus, we are left with the third case $G = \sqrt{15}|H|$. A direct substitution of G into the second equation of (3) yields

$$54000H^4L^2 + J_2\left(2835H^2 - 307L^2 + 144\sqrt{15}L|H| + 42(15H^2 - L^2)\cos 2g\right) = 0.$$

Thus, if g_0 is a solution of the last equation we have the equilibrium point $(g_0, \sqrt{15}|H|)$. This point exists whenever $-1 \leq \cos 2g_0 \leq 1$. As a consequence, we obtain two bifurcation surfaces when $\cos 2g$ reaches the extremum values, namely:

$$\begin{aligned} B_1 &\equiv 54000H^4L^2 + J_2(3465H^2 + 144\sqrt{15}L|H| - 349L^2) = 0, \\ B_2 &\equiv 54000H^4L^2 + J_2(3465H^2 + 144\sqrt{15}L|H| - 265L^2) = 0. \end{aligned} \tag{5}$$

The other solutions of system (3) come from $\sin 2g = 0$. In this case, $\cos 2g = \pm 1$ and G must be a root of one of the two following polynomials

$$\begin{aligned}
\mathcal{P}_+ &= 32L^2G^8 + (15J_2 - 160H^2L^2)G^6 + 24J_2LG^5 + (98H^2 - 21L^2)J_2G^4 \\
&\quad - 192J_2H^2LG^3 - (225H^4 + 198H^2L^2)J_2G^2 + 360J_2H^4LG \\
&\quad + 715J_2H^4L^2, \\
\mathcal{P}_- &= 32L^2G^8 + (35J_2 - 160H^2L^2)G^6 + 24J_2LG^5 - (350H^2 + 49L^2)J_2G^4 \\
&\quad - 192J_2H^2LG^3 + (315H^4 + 378H^2L^2)J_2G^2 + 360J_2H^4LG \\
&\quad + 55J_2H^4L^2,
\end{aligned} \tag{6}$$

where $\mathcal{P}_+$ and $\mathcal{P}_-$ are obtained from $\cos 2g = 1$ and $\cos 2g = -1$ respectively.

An explicit calculation of the roots of $\mathcal{P}_+$ and $\mathcal{P}_-$ is not possible, and even the task of counting the number of roots in the interval $[|H|, L]$ is very difficult. Nevertheless, we satisfy ourselves by determining a change in the number of roots in the interval $[|H|, L]$. In this way we consider the following two situations:

1. one of the roots reaches the extrema of the interval,

2. two or more roots join to produce a multiple root.

We emphasize that the first item is straightforward to compute, but not the second one. Indeed, there is a multiple root if and only if the polynomial's discriminant vanishes. However, a vanishing discriminant is not enough to ensures that the multiple root lies inside the interval $[|H|, L]$. Thus, the second item must be followed by a numerical process in order to discard those situations accounting for multiple roots outside the interval $[|H|, L]$.

By considering all the above, we arrive to six new bifurcation surfaces. Four of then obtained by application of the first item

$$\begin{aligned}
&L_1 : \ \mathcal{P}_+(|H|) = 0 \longrightarrow 8\,H^4\,L^2 + J_2\,(7\,H^2 - 12\,L\,|H| - 31\,L^2) = 0, \\
&L_2 : \ \mathcal{P}_+(L) = 0 \longrightarrow 16\,L^8 - 80\,H^2\,L^6 + J_2\,(425\,H^4 - 146\,H^2\,L^2 + 9\,L^4) = 0, \\
&L_3 : \ \mathcal{P}_-(H) = 0 \longrightarrow 2\,H^4\,L - 3\,J_2\,(|H| + 2\,L) = 0, \\
&L_4 : \ \mathcal{P}_-(L) = 0 \longrightarrow 16\,L^8 - 80\,H^2\,L^6 + J_2\,(365\,H^4 - 82\,H^2\,L^2 + 5\,L^4) = 0,
\end{aligned} \tag{7}$$

and two more derived from the second one

$$\begin{aligned}
L_5 : \ \mathrm{disc}(\mathcal{P}_+) = 0, \\
L_6 : \ \mathrm{disc}(\mathcal{P}_-) = 0.
\end{aligned} \tag{8}$$

The expression of the equations defining L_5 and L_6 are too involved and they are given in Appendix 1.

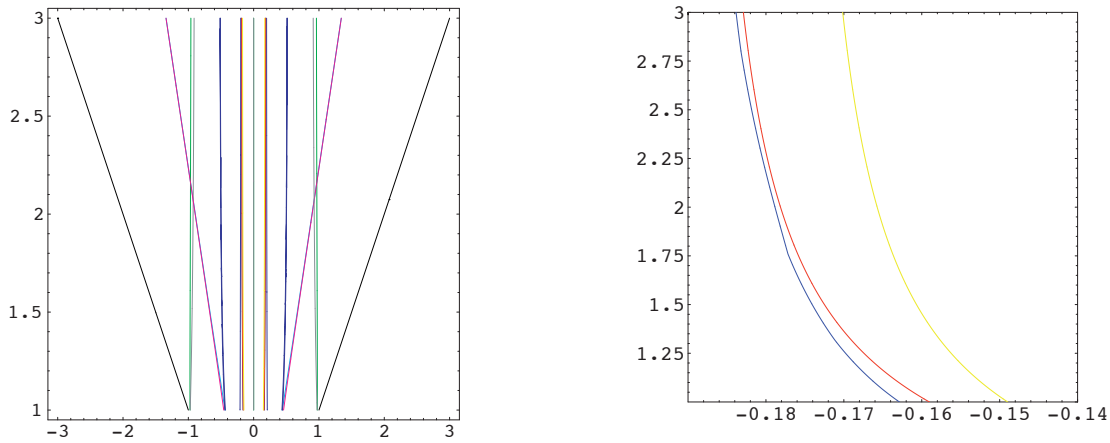

Figure 1.— The plane (H, L) divided in different regions where the number and stability of frozen orbits change, for $J_2 = -0.2$. The right figure gives an enlarged view of the lines when H is close to 0.

Now, we can depict the bifurcation surfaces in the parameter space (H, L, J_2) once we have discarded those branches of the surfaces L_5 and L_6 related with multiple roots outside the interval $[|H|, L]$. However, for the sake of simplicity, we will plot on the plane (H, L) a contour level of the surfaces of bifurcation for a fixed value of J_2. In this way, we choose $J_2 = -0.2$, a large negative value of the oblateness coefficient, in order highlight the many different regions where families of frozen orbits live, as Figure 1 shows.

Once the regions are established, we can determine the frozen orbits by solving the corresponding equations in (3). Nevertheless, they can also be visualized by depicting the phase flow on the reduced space, after normalisation. This is what we do by the technique of paint by number on the spheres defined in [5], although these spheres do not constitute the fully reduced space (see for instance [7]). As an example, we show in Figura 2 the phase flow in the regions enlarged in Figure 1, where frozen orbits correspond to the equilibrium points. It can be seen how the number of frozen orbits changes as the bifurcation lines are crossed. Indeed, if one of the lines is crossed the number of frozen orbits changes in two, and the region with the largest number of frozen orbits (14 in total) is that in between the red and yellow lines.

4 Conclusions

We have presented an analytical study of the families of frozen orbits in the main problem of artificial satellite for a prolate body. Despite the general treatment, an example is considered to see how the families of frozen orbits can be localized in the phase space. A more detailed study, by considering bifurcations surfaces in the general parameter space (H, L, J_2) is left for further development, as well as the evolution of the families in terms of physical parameters, inclination and eccentricity.

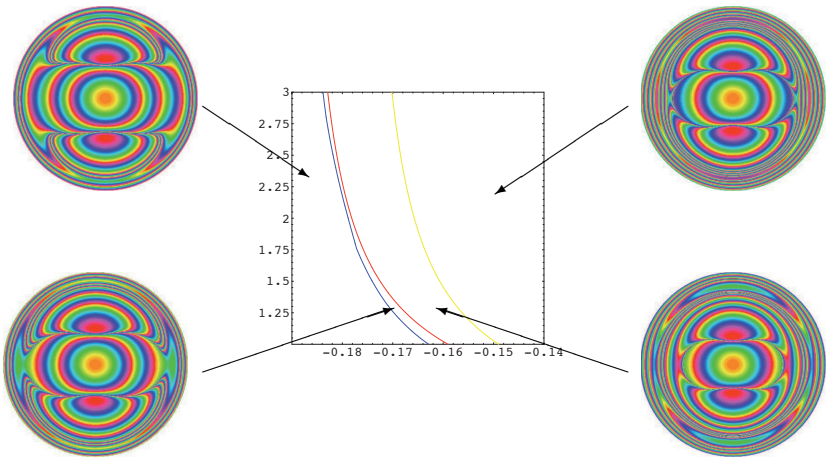

Figure 2.— Phase flow in four different regions. Frozen orbits correspond with equilibrium points.

Acknowledgments

We acknowledge financial support from the Spanish Ministry of Science and Technology (Project MTM2008-03818/MTM).

References

[1] Beletsky, V. V., *Essays on the Motion of Celestial Bodies*, Birkhäuser Verlag, Boston, 2001.

[2] Broucke, R. A., Numerical Integration of Periodic Orbits in the Main Problem of Artificial Satellite Theory. *Cel. Mech. Dyn. Astron.*, **58**, 99–123, 1994.

[3] Coffey, S. L., Deprit, A and Miller, B. R., The Critical Inclination in Artificial Satellite Theory. *Cel. Mech Dyn. Astron..*, **39**, 365–406, 1986.

[4] Coffey, S., Deprit, A., Deprit, E. and Healy, L., Painting the Phase Space Portrait of an Integrable Dynamical System, *Science*, **247**, 833–836, 1990.

[5] Coffey, S. L., Deprit, A. and Deprit, E., Frozen Orbits for Satellites Close to an Earth-Like Planet. *Cel. Mech. Dyn. Astron.*, **59**, 37–72, 1994.

[6] Deprit, A., Delaunay Normalisations. *Cel. Mech. Dyn. Astron.*, **26**, 9–21, 1982.

[7] Iñarrea, M., Lanchares, V., Palacián, J. F., Pascual, A. I., Salas, J. P. and Yanguas, P., Reduction of Some Perturbed Keplerian Problems. *Chaos, Solitons & Fractals*, **27**, 527–536, 2006.

[8] Langbort, C., Bifurcation of Relative Equilibria in the Main Problem of Artificial Satellite Theory for a Prolate Body. *Cel. Mech. Dyn. Astron.*, **84**, 369–385, 2002.

[9] Lara, M., Deprit, A. and Elipe, A., Numerical Continuation of Families of Frozen Orbits in the Zonal Problem of Artificial Satellite Theory. *Cel. Mech. Dyn. Astron.*, **62**, 167–181, 1995.

[10] Parke, M. E., Stewart, R. H., Farless, D. L. and Cartwright, D. E., On the Choice of Orbits for an Altimetric Satellite to Study Ocean Circulation and Tides. *J. Geophys. Res.*, **92** (C11), 693–707, 1987.

Appendix 1

$$L_5 : \operatorname{disc}(\mathcal{P}_+) = 0$$

$$
\begin{aligned}
&146082502080000000000000000000H^{28}J_2^2L^{12} - 151781748584760000000000000000H^{26}J_2^3L^{10} - \\
&651428568000000000000000000000H^{26}J_2^2L^{14} + 553073913243648000000000000000H^{26}J_2L^{18} + \\
&754300195115261737500000000H^{24}J_2^4L^8 + 790518168094307040000000000H^{24}J_2^3L^{12} - \\
&644925648175376256000000000000H^{24}J_2^2L^{16} - 102578155408163635200000000000H^{24}J_2L^{20} + \\
&285685136880087859200000000000000H^{24}L^{24} - 191164215583205221500000000H^{22}J_2^5L^6 - \\
&446425782920880798312000000H^{22}J_2^4L^{10} + 354476508197652213926400000000H^{22}J_2^3L^{14} + \\
&146205776159207750246400000000H^{22}J_2^2L^{18} - 335752314072357371904000000000H^{22}J_2L^{22} + \\
&243247624016593525425000000H^{20}J_2^6L^4 + 127457976773382706398960000H^{20}J_2^5L^8 - \\
&104057827780680328527064000000H^{20}J_2^4L^{12} - 968782905228030331599360000000H^{20}J_2^3L^{16} + \\
&142585680987595489628160000000H^{20}J_2^2L^{20} + 118020956505645868646400000000H^{20}J_2L^{24} - \\
&507715241019510093750000H^{18}J_2^7L^2 - 178141991565371073324192000H^{18}J_2^6L^6 + \\
&164563104716244294414742400000H^{18}J_2^5L^{10} + 330941450135594277969136000000H^{18}J_2^4L^{14} + \\
&147285560834429978055680000000H^{18}J_2^3L^{18} - 138455914098893864140800000000000H^{18}J_2^2L^{22} + \\
&290490993554194335937 5H^{16}J_2^8 + 403898701014657793935000 0H^{16}J_2^7L^4 - \\
&100189960463972667436380400 0H^{16}J_2^6L^8 - 592799262885792837319039360 00H^{16}J_2^5L^{12} - \\
&183551232581881119270540960000H^{16}J_2^4L^{16} + 491205909716027481181184000000H^{16}J_2^3L^{20} + \\
&247154224515915654299648000000H^{16}J_2^2L^{24} - 225160112747177465625 00H^{14}J_2^8L^2 + \\
&153698475676255849106100 00H^{14}J_2^7L^6 + 366491086913341939429151616 0H^{14}J_2^6L^{10} + \\
&536342827835716747720423488 00H^{14}J_2^5L^{14} - 198126344363197270628966400 00H^{14}J_2^4L^{18} - \\
&212498960185413325797457920000H^{14}J_2^3L^{22} - 860272075246056350625 00H^{12}J_2^8L^4 - \\
&691004743635995361455220 00H^{12}J_2^7L^8 - 276235910276238786237899472 0H^{12}J_2^6L^{12} - \\
&248007105786811569415103347 20H^{12}J_2^5L^{16} + 460667581753053391653371904 00H^{12}J_2^4L^{20} + \\
&257998257349104136444968960 00H^{12}J_2^3L^{24} + 343781101823937430162500H^{10}J_2^8L^6 + \\
&680915168260673451959052 00H^{10}J_2^7L^{10} + 863920550586708072958874112H^{10}J_2^6L^{14} + \\
&737584504885012144280640307 2H^{10}J_2^5L^{18} - 140266654976573419257357926 40H^{10}J_2^4L^{22} - \\
&265033862085859013913750H^8J_2^8L^8 - 310585585367865288650680 80H^8J_2^7L^{12} - \\
&120425013704246647334202144H^8J_2^6L^{16} - 136993374877404738465858355 2H^8J_2^5L^{20} + \\
&135774601378398089594221363 2H^8J_2^4L^{24} + 883369999414375180425 00H^6J_2^8L^{10} + \\
&765626859355888381330008 0H^6J_2^7L^{14} + 689652575224080127006924 8H^6J_2^6L^{18} + \\
&119829067487105599404638208H^6J_2^5L^{22} - 141666757637744035665 00H^4J_2^8L^{12} - \\
&100468097090673546470385 6H^4J_2^7L^{16} - 638150376927829591959552H^4J_2^6L^{20} - \\
&162940267302265622731161 6H^4J_2^5L^{24} + 888475280639647189500H^2J_2^8L^{14} + \\
&542343720359120438119 68H^2J_2^7L^{18} + 100213085349883223359488H^2J_2^6L^{22} + \\
&49351911676991673 75J_2^8L^{16} + 304473296707603575552J_2^7L^{20} + \\
&483387416599791255552J_2^6L^{24} = 0.
\end{aligned}
$$

$$L_6:\ \mathrm{disc}(\mathcal{P}_-)=0$$

$$-769433134694400000000000\,H^{24}\,L^{24}-381684012746342400000000000\,H^{26}\,J_2\,L^{18}+$$
$$887487457362739200000000000\,H^{24}\,J_2\,L^{20}-488617568046710784000000000\,H^{22}\,J_2\,L^{22}+$$
$$270609416796635136000000000\,H^{20}\,J_2\,L^{24}+612801777079296000000000000\,H^{28}\,{J_2}^2\,L^{12}-$$
$$182075567772672000000000000\,H^{26}\,{J_2}^2\,L^{14}-573979526215764480000000000\,H^{24}\,{J_2}^2\,L^{16}+$$
$$353306225595777085440000000000\,H^{22}\,{J_2}^2\,L^{18}-319132097261414443008000000000\,H^{20}\,{J_2}^2\,L^{20}-$$
$$121250892527857778680000000000\,H^{18}\,{J_2}^2\,L^{22}-247949445628221056614400000\,H^{16}\,{J_2}^2\,L^{24}+$$
$$170184415744292544000000000\,H^{26}\,{J_2}^3\,L^{10}-160962402989376172800000000\,H^{24}\,{J_2}^3\,L^{12}+$$
$$274038014466435260160000000\,H^{22}\,{J_2}^3\,L^{14}+433393829094073715942400000\,H^{20}\,{J_2}^3\,L^{16}-$$
$$657596619027193979130880000\,H^{18}\,{J_2}^3\,L^{18}-145405931119868839294976000\,H^{16}\,{J_2}^3\,L^{20}+$$
$$724331089819077530877952000\,H^{14}\,{J_2}^3\,L^{22}+176203135034840680339865600\,H^{12}\,{J_2}^3\,L^{24}+$$
$$180713878806532354290000000\,H^{24}\,{J_2}^4\,L^{8}-283442373848366148024000000\,H^{22}\,{J_2}^4\,L^{10}+$$
$$106217747013076277062960000\,H^{20}\,{J_2}^4\,L^{12}+178691171327803981254688000\,H^{18}\,{J_2}^4\,L^{14}-$$
$$532980638553687786923896000\,H^{16}\,{J_2}^4\,L^{16}+227109073322779502288076800\,H^{14}\,{J_2}^4\,L^{18}+$$
$$838977832055864994849259520\,H^{12}\,{J_2}^4\,L^{20}-752249718608159703372922880\,H^{10}\,{J_2}^4\,L^{22}-$$
$$337673902665735363327688704\,H^{8}\,{J_2}^4\,L^{24}+891456806222842860000000000\,H^{22}\,{J_2}^5\,L^{6}-$$
$$192140825488563319956000000\,H^{20}\,{J_2}^5\,L^{8}+775321442637895178188800000\,H^{18}\,{J_2}^5\,L^{10}-$$
$$147380295287094731220800000\,H^{16}\,{J_2}^5\,L^{12}-162711765209304920829171200\,H^{14}\,{J_2}^5\,L^{14}+$$
$$505969041951600945496774400\,H^{12}\,{J_2}^5\,L^{16}+925277536558038956232192000\,H^{10}\,{J_2}^5\,L^{18}-$$
$$269379630516921325893345280\,H^{8}\,{J_2}^5\,L^{20}-572298085672817367724851 2\,H^{6}\,{J_2}^5\,L^{22}+$$
$$433020913753001140866252 8\,H^{4}\,{J_2}^5\,L^{24}+191319806832557661562500000\,H^{20}\,{J_2}^6\,L^{4}-$$
$$511336919905960445325000000\,H^{18}\,{J_2}^6\,L^{6}+209183712423654347446550000 0\,H^{16}\,{J_2}^6\,L^{8}-$$
$$214071225033376335869720000 0\,H^{14}\,{J_2}^6\,L^{10}-933696982390801376336260000\,H^{12}\,{J_2}^6\,L^{12}+$$
$$489513903070900926026808000\,H^{10}\,{J_2}^6\,L^{14}-254406294997384315708312 00\,H^{8}\,{J_2}^6\,L^{16}-$$
$$158827569619862579337216 00\,H^{6}\,{J_2}^6\,L^{18}+285339225304881837489971 2\,H^{4}\,{J_2}^6\,L^{20}+$$
$$145109853157362994102272\,H^{2}\,{J_2}^6\,L^{22}-143804814012208252682 24\,{J_2}^6\,L^{24}+$$
$$116411669327027812500000 00\,H^{18}\,{J_2}^7\,L^{2}-337810493363599580625000 00\,H^{16}\,{J_2}^7\,L^{4}+$$
$$137618205999304226595000000\,H^{14}\,{J_2}^7\,L^{6}-174070961394917201398700000\,H^{12}\,{J_2}^7\,L^{8}+$$
$$700523391381873580315200 0\,H^{10}\,{J_2}^7\,L^{10}+108757109198457373773288 00\,H^{8}\,{J_2}^7\,L^{12}-$$
$$355555975307521747269152 0\,H^{6}\,{J_2}^7\,L^{14}+796436721714524933019 84\,H^{4}\,{J_2}^7\,L^{16}+$$
$$109582034737133950975872\,H^{2}\,{J_2}^7\,L^{18}-787351991019014818073 6\,{J_2}^7\,L^{20}+$$
$$212208772210727783203125\,H^{16}\,{J_2}^8-659890079247464296875000\,H^{14}\,{J_2}^8\,L^{2}+$$
$$266340373142819680468750 0\,H^{12}\,{J_2}^8\,L^{4}-381768133580455762612500 0\,H^{10}\,{J_2}^8\,L^{6}+$$
$$109310917779206558401875 0\,H^{8}\,{J_2}^8\,L^{8}-148700459548578550445000\,H^{6}\,{J_2}^8\,L^{10}-$$
$$245969165239815258885 00\,H^{4}\,{J_2}^8\,L^{12}+946071284037834731700 0\,H^{2}\,{J_2}^8\,L^{14}-$$
$$594632672565549492875\,{J_2}^8\,L^{16}=0.$$

Monografías de la Real Academia de Ciencias de Zaragoza **35**, 83–95, (2011).

TIDES: A free software based on the Taylor series method

M. Rodríguez[1,2], A. Abad[1], R. Barrio[1] and F. Blesa[3]

[1] GME and IUMA, Universidad de Zaragoza, 50009 Zaragoza, Spain

[2] Centro Universitario de la Defensa de Zaragoza, 50090 Zaragoza, Spain

[3] GME and Depto. Física Aplicada, Universidad de Zaragoza, 50009 Zaragoza, Spain

Abstract

In many branches of the science, the numerical solution of differential equations is a natural request. However, the way to solve those equations is not always the same. Sometimes it is needed to solve the equation as fast as possible. In other cases good precision is required, even 100 digits or more to guarantee the final results. Sensitivity analysis also may be wanted in some integrators. In this paper, a new integration software based on the Taylor series method is introduced, with all these features. It can provide fast integrations that compete with well established codes and it is ready for high precision integrations with as many digits as desired. Besides it can compute the partial derivatives of the variables with respect to initial conditions or parameters of the system up to any order. This software has been written focusing in the philosophy *easy-to-use*, so with very simple commands the necessary code is generated automatically. At the end, we also present some numerical results to illustrate its competitiveness and high performance with chaotic problems.

1 INTRODUCTION

The Taylor Series Method (TSM) is an integration method with a long history. Classical authors like Newton or Euler already used power series expansions as integration methods. However, nowadays it has been rediscovered with the implementation of automatic differentiation [11] techniques which allow us to transform a theoretical method into a practical one. Afterwards, it has reached a good position as an integration method and many research groups [5, 6, 15, 19, 20] have adopted this method as their main integrator algorithm.

This method is widely used in the study of Dynamical Systems because, apart from being a competitive integration method, it is very flexible, that is, it can be easily adapted

for many purposes like the study of partial derivatives [8], high precision calculations [1, 9, 15] or detection of events. It also may be implemented by using interval arithmetic in order to attain a rigorous method of integration [10,17,23] which guarantees the results, a needful step in Computer Aided Proofs [13, 16].

Here we present an implementation of the Taylor Series Method adapted to integrate ODEs, partial derivatives up to any order and ready to use multiple precision if needed. A piece of the software has been written in MATHEMATICA under the *easy-to-use* philosophy, so with very simple commands we will have all the necessary code for our purposes.

The main idea of the Taylor Method is very simple. Let is consider the initial value problem:

$$\frac{d\boldsymbol{y}(t)}{dt} = \boldsymbol{f}(t, \boldsymbol{y}(t); \boldsymbol{p}), \qquad \boldsymbol{y}(t_0) = \boldsymbol{y}_0, \qquad t \in \mathbb{R},\, \boldsymbol{y} \in \mathbb{R}^s,\, \boldsymbol{p} \in \mathbb{R}^k. \tag{1}$$

where $\boldsymbol{p}$ represents a vector of $k \geq 0$ parameters.

Now, the value of the solution at $t_{i+1} = t_i + h_{i+1}$ (that is, $\boldsymbol{y}(t_{i+1})$) is approximated from the n-th degree Taylor series of $\boldsymbol{y}(t)$ developed at t_i and evaluated at $t = t_{i+1}$ (the function $\boldsymbol{f}$ has to be a smooth function, in this paper we will consider $\boldsymbol{f}$ to be analytic).

$$\begin{aligned}
\boldsymbol{y}(t_0) &\stackrel{\text{def}}{=} \boldsymbol{y}_0, \\
\boldsymbol{y}(t_{i+1}) &\simeq \boldsymbol{y}(t_i) + \frac{d\boldsymbol{y}(t_i)}{dt}\, h_{i+1} + \frac{1}{2!}\, \frac{d^2\boldsymbol{y}(t_i)}{dt^2}\, h_{i+1}^2 + \ldots + \frac{1}{n!}\, \frac{d^n\boldsymbol{y}(t_i)}{dt^n}\, h_{i+1}^n \\
&\simeq \boldsymbol{y}_i + \boldsymbol{f}(t_i, \boldsymbol{y}_i)\, h_{i+1} + \frac{1}{2!}\, \frac{d\boldsymbol{f}(t_i, \boldsymbol{y}_i)}{dt}\, h_{i+1}^2 + \ldots + \frac{1}{n!}\, \frac{d^{n-1}\boldsymbol{f}(t_i, \boldsymbol{y}_i)}{dt^{n-1}}\, h_{i+1}^n \stackrel{\text{def}}{=} \boldsymbol{y}_{i+1}.
\end{aligned} \tag{2}$$

The practical way of computing the coefficients $\{d^j\boldsymbol{y}(t_j)/dt^j\}_j$ is using the automatic differentiation techniques [12,21]. In the literature we can find many software implementations of the TSM which compute these coefficients automatically, for example ATOMFT (Corliss et al.), COSY INFINITY (Berz et al.), DAETS (Nedialkov et al.), TAYLOR (Jorba and Zou) and, of course, TIDES.

2 AUTOMATIC DIFFERENTIATION WITH PARTIAL DERIVATIVES

The practical calculation of the coefficients of a Taylor series expansion of a function is done with the classical rules of automatic differentiation. Automatic differentiation gives us a recursive procedure to obtain the numerical value of reiterated derivatives with no error (but the round off one).

The technique is based on the decomposition of the function into a sequence of arithmetic operations and calls to standard unary functions. For example, if we consider $f(x) = \log(x^2 + 1)/(x^2 - 1) + x$, we evaluate the function starting from the value of the

variable x and obtain the value of $f(x)$ as follows:

$$\begin{aligned} l_1 &= x, \\ l_2 &= l_1\, l_1, \\ l_3 &= l_2 + 1, \\ l_4 &= l_2 - 1, \\ l_5 &= \log l_3, \\ l_6 &= l_5/l_4, \\ l_7 &= l_6 + l_1 \\ f(x) &= l_7. \end{aligned} \tag{3}$$

and by applying differentiation rules at each step we can obtain the value of the derivatives of f for any order. Once we have these values, from equation (1) we obtain the coefficients of the Taylor series of the solution y:

$$\boldsymbol{y}^{[j]}(t) \stackrel{\text{def}}{=} \frac{1}{j!}\frac{d^j \boldsymbol{y}(t)}{dt^j} = \frac{1}{j!}\frac{d^{j-1}\boldsymbol{f}(t)}{dt^{j-1}} = \frac{1}{j}\boldsymbol{f}^{[j-1]} \tag{4}$$

If we also want to calculate the Taylor coefficients of the partial derivatives of the solution with respect to some parameter or initial condition we can use also automatic differentiation. First we introduce some notation. We will call $\mathbb{N}_0$ the set of the natural numbers with zero, $\mathbf{i} = (i_1, \ldots, i_s) \in \mathbb{N}_0^s$ a multi-index with the partial derivative orders, $\mathbf{i}^* = \mathbf{i} - (0, \ldots, 0, 1, 0, \ldots, 0)$, that is $\mathbf{i}^* = (0, \ldots, 0, i_k - 1, i_{k+1}, \ldots, i_s)$ (we subtract 1 to de first non-zero element of $\mathbf{i}$), $|\mathbf{i}| = \sum i_j$ the total order of partial derivation, and $\mathbf{i} - \mathbf{j} = (i_1 - j_1, \ldots, i_s - j_s)$. For $\mathbf{v} \in \mathbb{N}_0^s$, we define the multi-combinatorial number $\binom{\mathbf{i}}{\mathbf{v}} = \binom{i_1}{v_1} \cdots \binom{i_s}{i_s}$. Finally we define the the Taylor j-th coefficient of the partial derivative of $\boldsymbol{f}$ as:

$$\boldsymbol{f}_{\mathbf{i}}^{[j]}(t) = \frac{\partial^{i_1+\ldots+i_s}\boldsymbol{f}^{[j]}(t)}{\partial y_1^{i_1} \cdots \partial y_s^{i_s}} \tag{5}$$

and

$$\tilde{h}_{\mathbf{v},\mathbf{i}}^{[j,n]} = h_{\mathbf{v}}^{[j]} \text{ if } (j \neq n \text{ or } \mathbf{v} \neq \mathbf{i}); \quad \tilde{h}_{\mathbf{v},\mathbf{v}}^{[n,n]} = 0. \tag{6}$$

The basic rules of automatic differentiation extended with partial derivatives can be found in [8] (with the same notation). We show as an example the rule of the logarithm.

Proposition 1. *Let f be a function of class $\mathcal{C}^n$. Then, if we define $h(t) = \log f(t)$, the automatic differentiation rule for h is:*

$$\begin{aligned} h_{\mathbf{0}}^{[0]} &= \log\left(f^{[0]}(t)\right), \\ h_{\mathbf{i}}^{[0]} &= \frac{1}{f^{[0]}}\left(f_{\mathbf{i}}^{[0]} - \sum_{\mathbf{0}<\mathbf{v}\leq\mathbf{i}^*} \binom{\mathbf{i}^*}{\mathbf{v}} h_{\mathbf{i}-\mathbf{v}}^{[0]} \cdot f_{\mathbf{v}}^{[0]}\right), \qquad \mathbf{i} > \mathbf{0}, \\ h_{\mathbf{i}}^{[n]} &= \frac{1}{f^{[0]}}\left(f_{\mathbf{i}}^{[n]} - \frac{1}{n}\sum_{j=0}^{n-1}(n-j)\left\{\sum_{\mathbf{v}\leq\mathbf{i}} \binom{\mathbf{i}}{\mathbf{v}} \tilde{h}_{\mathbf{i}-\mathbf{v},\mathbf{i}}^{[n-j,n]} \cdot f_{\mathbf{v}}^{[j]}\right\}\right), \quad n > 0. \end{aligned} \tag{7}$$

Proof. For $h^0_{\mathbf{i}}$, first we derive with respect $\mathbf{e_k}$ (k is the first non-zero component of $\mathbf{i}$) and we have the relation $f^{[0]}_{\mathbf{e_k}} = h^{[0]}_{\mathbf{e_k}} \cdot f$. Now we perform $\mathbf{i} - \mathbf{e_k} = \mathbf{i}^*$ derivatives by applying the Leibniz rule for partial derivation of the product (see [8]) and we have $f^{[0]}_{\mathbf{i}} = \sum_{\mathbf{v}\leq\mathbf{i}^*} \binom{\mathbf{i}^*}{\mathbf{v}} h^{[0]}_{\mathbf{i}-\mathbf{v}} \cdot f^{[0]}_{\mathbf{v}}$. Finally we just have to work out the value of $h^{[0]}_{\mathbf{i}}$.

For $h^{[n]}_{\mathbf{i}}$, we first derive once with respect to time to reach the expression $f^{[1]} = h^{[1]} \cdot f$. Then we apply the well known automatic differentiation rule of the product [21] to reach

$$nf^{[n]} = \sum_{j=0}^{n-1} (n-j) h^{[n-j]} \cdot f^{[j]}$$

. At this point we derive with respect to $\mathbf{i}$ applying the Leibniz rule again:

$$nf^{[n]}_{\mathbf{i}} = \sum_{j=0}^{n-j} (n-j) \sum_{\mathbf{v}\leq\mathbf{i}} \binom{\mathbf{i}}{\mathbf{v}} h^{[n-j]}_{\mathbf{i}-\mathbf{v}} \cdot f^{[j]}_{\mathbf{v}}$$

. Finally, considering the definition of $\tilde{h}$ (6), we work out the value of $h^{[n]}_{\mathbf{i}}$. □

2.1 Dealing with partial derivatives

Here we are going to explain briefly how MATHEMATICA deals with the partial derivatives and how it transforms expressions of the form $\mathbf{v} \leq \mathbf{i}$ into sums with natural indexes which can be traduced into C or Fortran codes. We call $\mathcal{D}^m_s = \{\mathbf{i}, |\mathbf{i}| \leq m\}$, the set of all partial derivatives of the function f of order less or equal to m. We may easily define a total order relationship in this set by considering $\mathbf{i} < \mathbf{j}$ if $\sum i_k < \sum j_k$ or $\sum i_k = \sum j_k$ and there exists an index p such as $i_k = j_k$, $\forall k < p$, and $i_p < j_p$, and $\mathbf{i} = \mathbf{j}$ if $i_k = j_k$, $\forall k$.

This order relationship is the one used in the extended formulas of automatic differentiation (see equation (7) for example). MATHEMATICA, for each index $\mathbf{i}$ computes the set $\mathcal{V}(\mathbf{i}) = \{\mathbf{v}, \mathbf{v} \leq \mathbf{i}\}$, the set of all partial derivatives needed to perform the calculation of the $\mathbf{i}$ partial derivative. If instead of one partial derivative we have a set of partial derivatives $\mathcal{D}$, we define $\mathcal{V}(\mathcal{D}) = \bigcup_{\mathbf{i}\in\mathcal{D}} \mathcal{V}(\mathbf{i}) \subset \mathcal{D}^m_s$. Then we order this set and identify each element of the set $\mathcal{V}(\mathcal{D})$ with an integer number between 0 and $N-1$, with $N = \sharp\mathcal{D}$ the number of elements of $\mathcal{V}(\mathcal{D})$. This index will represent the position in the ordered set $\mathcal{V}(\mathcal{D})$.

We notice that in the process of computing partial derivatives in the Taylor series method only two kind of expressions are involved (see equation (7)):

$$\sum_{\mathbf{v},\mathbf{w}\in\mathcal{V}(\mathbf{i})} C_{\mathbf{i},\mathbf{v}} f^{[-]}_{\mathbf{v}} g^{[-]}_{\mathbf{w}}, \qquad \sum_{\mathbf{v},\mathbf{w}\in\mathcal{V}(\mathbf{i}^*)} C_{\mathbf{i}^*,\mathbf{v}} f^{[-]}_{\mathbf{v}} g^{[-]}_{\mathbf{w}}, \quad \mathbf{w} = \mathbf{i} - \mathbf{v}, \quad C_{\mathbf{i},\mathbf{v}} = \binom{\mathbf{i}}{\mathbf{v}},$$

where $\mathbf{i}$ goes over the set $\mathcal{V}(\mathcal{D})$.

In order to write the code to compute the Taylor series of the partial derivatives of the solution of an ODE we need to know the sets $\mathcal{V}(\mathbf{i}), \mathcal{V}(\mathbf{i}^*)$ of every derivative that appears

in the process. The MATHEMATICA package MathTIDES computes automatically these sets and uses them to write the final C code. The way to perform this is by building two lists of integers that represent the indexes for $\mathbf{v}$, and another two lists for the indexes of $\mathbf{w} = \mathbf{i} - \mathbf{v}$. MATHEMATICA also computes the lists with the integer value of the multi-combinatorial numbers $C_{\mathbf{i},\mathbf{v}}$ and $C_{\mathbf{i}^*,\mathbf{v}}$. Finally, MATHEMATICA also writes two lists with the initial and final position in each list for each value of $\mathbf{i}$ and $\mathbf{i}^*$.

We show the process with an example. If we want to compute the partial derivative

$$\frac{\partial^4 f}{\partial y_1^3 \partial y_2}$$

first we construct the set of all derivatives we want to compute: $\mathcal{D} = \{(3,1)\}$. Now we need to calculate the set of all necessary derivatives for the elements of $\mathcal{D}$, to order that set, and to identify each element with an integer:

$$\mathcal{V}(\mathcal{D}) = \{(0,0),(1,0),(0,1),(2,0),(1,1),(3,0),(2,1),(3,1)\} = \{0,1,2,3,4,5,6,7\}$$

And for each element we will have:

$$\begin{array}{rcccl}
\mathcal{V}(0) & = & \mathcal{V}((0,0)) & = & \{(0,0)\} = \{0\} \\
\mathcal{V}(1) & = & \mathcal{V}((1,0)) & = & \{(0,0),(1,0)\} = \{0,1\} \\
\mathcal{V}(2) & = & \mathcal{V}((0,1)) & = & \{(0,0),(0,1)\} = \{0,2\} \\
\mathcal{V}(3) & = & \mathcal{V}((2,0)) & = & \{(0,0),(1,0),(2,0)\} = \{0,1,3\} \\
\mathcal{V}(4) & = & \mathcal{V}((1,1)) & = & \{(0,0),(1,0),(0,1),(1,1)\} = \{0,1,2,4\} \\
\mathcal{V}(5) & = & \mathcal{V}((3,0)) & = & \{(0,0),(1,0),(2,0),(3,0)\} = \{0,1,3,5\} \\
\mathcal{V}(6) & = & \mathcal{V}((2,1)) & = & \{(0,0),(1,0),(0,1),(2,0),(1,1),(2,1)\} = \{0,1,2,3,4,6\} \\
\mathcal{V}(7) & = & \mathcal{V}((3,1)) & = & \{(0,0),(1,0),(0,1),(2,0),(1,1),(3,0),(2,1),(3,1)\} = \{0,1,2,3,4,5,6,7\}
\end{array}$$

3 MULTIPLE PRECISION LIBRARIES

In this section we are going to comment briefly the high precision libraries used and the reason for choosing them. In the scientific community there are many libraries which implement arbitrary precision. Different libraries have different ways to represent arbitrary-precision numbers so the election of one or other library will determine the program. There are libraries for C (GMP, MPFR, IMSL, decNUMBER), Fortran (FMLIB, ARPREC, MPFUN), java (APFLOAT), C++ (APFLOAT), etc. Also these libraries are designed to manage only integer numbers (LiDIA), real numbers (almost all of them) or even complex arithmetic (MPFR).

Another important aspect when choosing one of them is the kind of license it has. We have avoided commercial or proprietary licenses in order to be able to distribute it within our software, so good options are GPL (GNU Public License) and LGPL (Lesser GNU Public License).

Finally we wanted an *easy-to-use* library which fits properly in the global philosophy of TIDES. The library having all these features is MPFR[1]. To compile and use this library it is necessary to have compiled and installed the high precision library of the GNU project GMP[2] both with LGPL license.

The use of the libraries is internal and the program can be used easily with the interface in MATHEMATICA as it is described in the next section.

4 USE OF TIDES

In this section we are going to explain in the first place the structure of TIDES. Afterwards we will comment the basic commands in MATHEMATICA necessary to use the library.

4.1 Structure of TIDES

TIDES has two different parts (pieces of software): The MATHEMATICA package MathTIDES and the C library libTIDES. The structure is shown in this table:

TIDES		
Product		Language
MathTIDES	preprocessor	MATHEMATICA
libTIDES	library (objects or source code)	C

MATHEMATICA builds automatically the necessary code to integrate the differential equation. The files generated by MATHEMATICA usually are enough to solve the equation, therefore the user just has to compile and execute them. If the user wants additional features, such as high precision or partial derivatives of the solution, the use of the library libTIDES is required.

Depending on the demands of the user one engine or other engine is used. This table illustrates the features of the different engines of TIDES:

[1] `http://www.mpfr.org`
[2] `http://gmplib.org`

Engine	Contents	mathTIDES generates	linked with
minf-tides	basic TSM	Fortran files	
minc-tides	basic TSM	C files	
dp-tides	complete TSM with partial derivatives	C files	libTIDES
mp-tides	complete TSM with partial derivatives with arbitrary precision	C files	libTIDES GMP library MPFR library

The two first engines (minf-tides and minc-tides) are minimal versions thought to be fast and simple. They are developed to integrate ordinary differential equations in which only simple functions appear: $x \pm y$, $x \times y$, x/y, $1/x$, $x^\alpha\,(\alpha \in \mathbb{R})$, $\alpha^x\,(\alpha > 0)$, e^x, $\log x$, $\sin x$ and $\cos x$. In these cases MATHEMATICA generates files (C or Fortran) with the integration engine, the implementation of the automatic differentiation (without partial derivatives) and the driver (main program).

If we want to integrate hyperbolic functions or inverse of trigonometric or inverse of hyperbolic functions, we have to use the next engine (dp-tides). It is also necessary to use this engine if we want to integrate with partial derivatives. MathTIDES generates files with the implementation of the automatic differentiation for the function, and with the driver (main program). In this case, the engine is included in the library libTIDES, so it is needed to link with this library when compiling.

The last engine, mp-tides, is the complete integrator with all the features: all the functions, partial derivatives and arbitrary precision. MathTIDES builds, like in the case of dp-tides, files with automatic differentiation and with the driver (main program). The engine is also in library libTIDES, but when compiling it is also required to link with high precision libraries GMP and MPFR (GMP needed by MPFR).

4.2 The MATHEMATICA *interface*

Along this subsection we are going to see the easy-to-use concept underlying in TIDES. We are going to explain the basic commands taking the example of the Lorenz equations [18]:

$$\dot{x} = -\sigma(x+y), \quad \dot{y} = -xz + rx - y, \quad \dot{z} = xy - bz \tag{8}$$

First we load the package with the command `<<MathTIDES`` , and then we can use the basic commands: `FirstOrderODE` and `CodeFiles`. The first one generates the internal expression that represents the differential equation. The second one generates the codes. To generate the differential equation other commands can be used, `NthOrderODE`, `PotentialToODE` or `HamiltonianToODE`, which creates the differential system from a n-th

order differential equation, a potential or a Hamiltonian, respectively. In our case we have to use `FirstOrderODE`. The arguments are: a list with the symbolic expression of the ODE, the independent variable, a list with the dependent variables and optionally a list with the parameters that appear in the equation. So, the command is:

```
lorenz = FirstOrderODE[{s(y-x), -x z + r x - y, x y - b z},
              t, {x, y, z}, {s, r, b}]
```

Once we have created the differential equation, we just have to execute the command `CodeFiles` according to our needs. The first argument is the equation, in our case `lorenz`. The second one is an string with the desired name for the files in C or Fortran. The next arguments are optional. These are the basic ones:

- `MinTIDES->"Fortran"` or `MinTIDES->"C"`. This generates the appropriated files to use the minimal engines in Fortran or C.

- `Output->Screen`, `Output->"filename"` or `Output->False`. Specifies the output stream, on the screen or in a file called `filename`. If `False` (default value) no output is shown or written (the final result is in an output variable).

- `PrecisionDigits->n`. With this option we control the number of digits of precision we are working with. If greater than 16 the engine mp-tides and all its libraries are required. The default value is 16.

- `AddPartials->{{x, y}, n, Until}` or `AddPartials->{{x, s}, n, Only}`. With this option we add the calculation of partial derivatives. The firs argument is the list of variables or parameters with respect to we want to perform the partial derivative. The next number is the maximum order of partial derivation. The next option may be `Until`, or `Only`, in case we want all partials until that order, or just the ones of order n. For example:
  `AddPartials->{{y,a},2, Until}` computes:

$$\frac{\partial x}{\partial y_0}, \frac{\partial x}{\partial a}, \frac{\partial y}{\partial y_0}, \frac{\partial y}{\partial a}, \frac{\partial z}{\partial y_0}, \frac{\partial z}{\partial a}, \frac{\partial^2 x}{\partial y_0^2}, \frac{\partial^2 x}{\partial a^2}, \frac{\partial^2 x}{\partial y_0 \partial a}, \frac{\partial^2 y}{\partial y_0^2}, \frac{\partial^2 y}{\partial a^2}, \frac{\partial^2 y}{\partial y_0 \partial a}, \frac{\partial^2 z}{\partial y_0^2}, \frac{\partial^2 z}{\partial a^2}, \frac{\partial^2 z}{\partial y_0 \partial a}.$$

Here we have some examples we can execute in our case:

```
CodeFiles[lorenz, "lorenzMinF",
      MinTIDES->"Fortran",
      Output->Screen]
```

to generate a minimal Fortran code with output on the screen. Or we can execute

```
CodeFiles[lorenz, "lorenzMP",
      Output->"lorenzMP.txt",
      PrecisionDigits->500,
      AddPartials->{{x, y, z, s}, 2, Until}]
```

if we want high precision integration (with 500) digits. In this case the output will be written in a file called `lorenzMP.txt`.

There are many other options and combinations which use is carefully described in the user guide within the software.

5 NUMERICAL EXPERIMENTS

In the numerical experiments we have used three kinds of architectures. Fortran integrations both in double and quadruple precision have been performed in a PC Pentium D 3.40 GHz. with Windows XP SP2. The high precision computation has been done in a PC Intel ® Core^{TM} 2 Duo CPU E6750 2.66 GHz with Linux Kernel 2.6.27.7-smp compiled for i686. The compiler for Fortran has been `gcc 4.2` (`gfortran`) for double precision and `Lahey LF95` for quadruple precision. The compiler for C has been also `gcc 4.2`.

5.1 Test Problems

To illustrate the use of the integrator we present two classical problems in dynamical systems.

Arenstorf orbits [2]. These are the particular case of the planar orbits in the restricted three body problem. One considers two bodies of masses $1-\mu$ and μ, in circular rotation in a plane and a third body of negligible mass moving around in the same plane. The interval of integration is $t \in [0, 30]$. and the equations are:

$$
\begin{aligned}
&x'' = x + 2y' - \mu' \frac{x+\mu}{D_1} - \mu \frac{x-\mu'}{D_2},\\
&y'' = y - 2x' - \mu' \frac{y}{D_1} - \mu \frac{y}{D_2},\\
&\begin{cases}
D_1 = ((x+\mu)^2 + y^2)^{3/2}, \qquad D_2 = ((x-\mu')^2 + y^2)^{3/2},\\
x(0) = 0.994, \quad y(0) = 0,\\
x'(0) = 0, \quad y'(0) = -2.00158510637908252240537862224,\\
\mu = 0.012277471, \qquad \mu' = 1-\mu.
\end{cases}
\end{aligned}
$$

Lorenz Model [18]. The classical system given by equations (8) and the classical Salztman values of the paramenters: $r = 28$, $\sigma = 10$ and $b = 8/3$. We use the initial

conditions of an unstable periodic orbit up to 500 digits thanks to professor Divakar Viswanath [22].

$$\begin{aligned} x(0) &= -13.763610682134200\ldots \\ y(0) &= -19.578751942451795\ldots \\ z(0) &= 27, \\ T &= 1.5586522107161747\ldots \end{aligned}$$

5.2 Numerical tests

In the first test we are going to compare TIDES with `dop853` and `odex`. Since we have used the implementation of `dop853` and `odex` made by Hairer and Wanner [14] and it has been written in Fortran, we have compared them with the minf-tides engine, also in Fortran. We present in the figures relative error vs CPU time diagrams, a standard in numerical ODE community.

In the Figure 1 we have compiled all the programs using `gfortran` and the optimization option `-O2`, and allowing dense output. We can observe the same behavior for both for Arenstorf and Lorenz problems: For low precision demands `dop853` is the fastest integrator. However, when we achieve 10^{-10} precision level minf-tides becomes the fastest option. The reason is the variable order formulation of the Taylor series method which guarantees a softer growing slope. `odex` also has variable order formulation, but the extrapolation method needs more precision in order to beat the Runge-Kutta code.

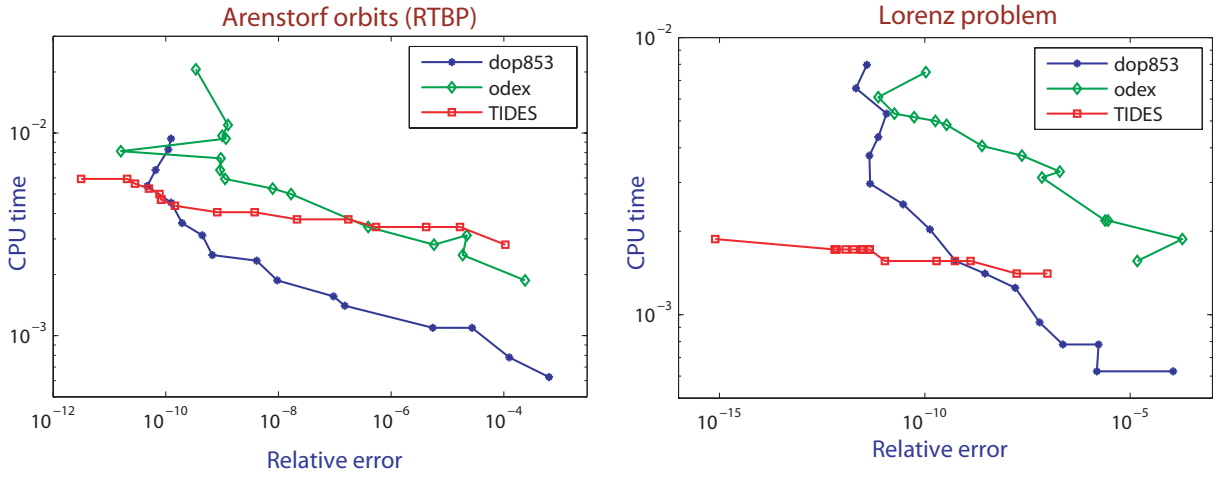

Figure 1.— Computational relative error vs CPU time diagrams in double precision

In Figure 2 we present the same tests, but we have used `Lahey LF95` Fortran compiler to have native quadruple precision. Since we can go farther than double precision we can appreciate that minf-tides and `odex` have almost the same slope, due to their variable

order formulation. We also can see that the difference between the variable order methods and Runge-Kutta is quite big for more accurate demands.

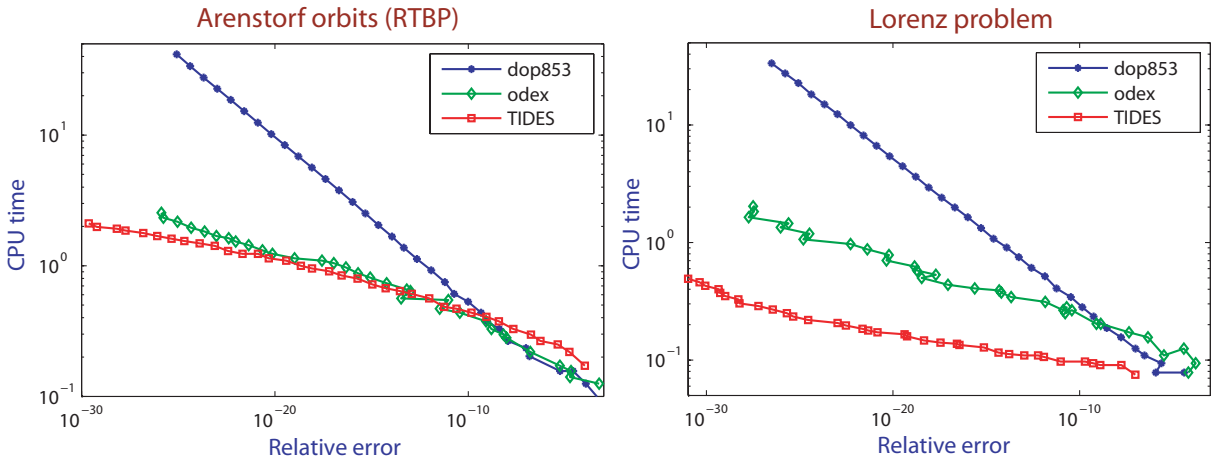

Figure 2.— Computational relative error vs CPU time diagrams in quadruple precision

High precision has become very useful both in theoretical and practical applications [3]. Our software includes a high precision engine, mp-tides, which can integrate differential equations (with partial derivatives if needed) with all the desired precision in a very easy way.

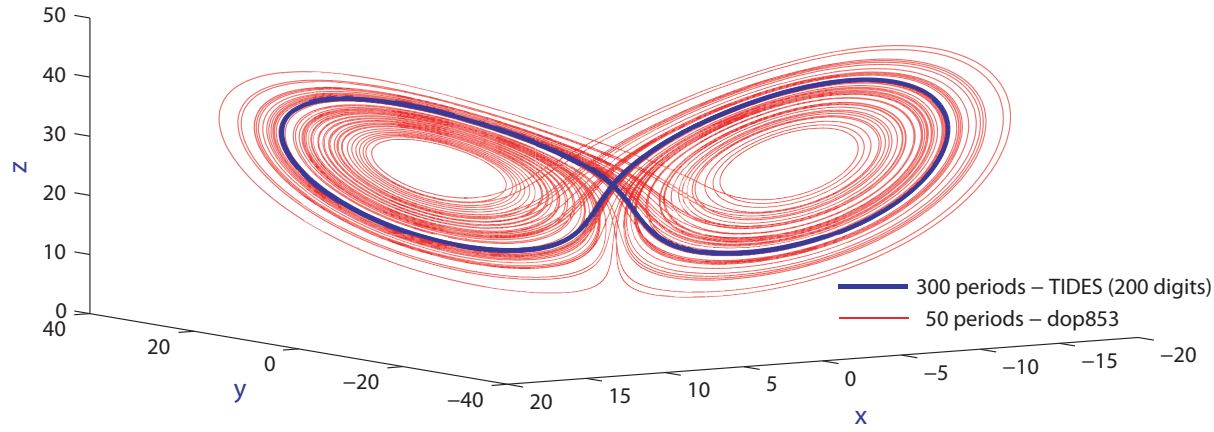

Figure 3.— 300 periods using mp-tides and 50 periods using `dopri853` in double precision

There are many problems in which, even if we are interested in results in double precision, the operations must be performed with enough digits of precision due to the unstable nature of the underlying system. The Lorenz system is a good example of system

of this nature. In Figure 3 we present integrations of the same orbit. We have drawn in red 300 revolutions using mp-tides with high precision arithmetic, and we can appreciate that the structure of the periodic orbit is preserved. In blue we have plotted only 50 periods performed with `dopri853` compiled and executed in double precision. In this case the loss of digits of precision is too fast, so with only a small number of periods, compared to the high precision computation, we have fallen into the famous chaotic attractor.

Acknowledgements

We thank Prof. Divarak Viswanath for providing us periodic initial conditions of the Lorenz system up to 500 digits. Also we thank the free software community for providing us arbitrary precision libraries of such an excellent quality. Finally we would like to remark that this work has been supported by the Spanish Research projects MTM2009-10767 and AYA2008-05572.

References

[1] R. Abad, R. Barrio, F. Blesa, and M. Rodríguez. TIDES: a Taylor series Integrator of Differential EquationS. *preprint*, 2010.

[2] R.F. Arenstorf. Periodic solutions of the restricted three body problems representing analytic continuations of keplerian elliptic motions. *Amer. J. Math.*, LXXXV:27–35, 1963.

[3] D.H. Bailey, J.M. Borwein, and R. Barrio. A High-Precision Computation: Mathematical Physics and Dynamics. *preprint*, 2009.

[4] R. Barrio, F. Blesa, and M. Lara. VSVO formulation of the Taylor method for the numerical solution of ODEs. *Comput. Math. Appl.*, 50(1-2):93–111, 2005.

[5] R. Barrio, F. Blesa, and S. Serrano. Bifurcations and safe regions in open Hamiltonians. *New J. Phys.*, 11:053004 (15pp.), 2009.

[6] R. Barrio and S. Serrano. A three-parametric study of the Lorenz model. *Phys. D*, 229(1):43–51, 2007.

[7] Roberto Barrio. Performance of the Taylor series method for ODEs/DAEs. *Appl. Math. Comput.*, 163(2):525–545, 2005.

[8] Roberto Barrio. Sensitivity analysis of ODEs/DAEs using the Taylor series method. *SIAM J. Sci. Comput.*, 27(6):1929–1947, 2006.

[9] M. Berz. COSY INFINITY version 8 reference manual. *Technical Report MSUCL—1088, National Superconducting Cyclotron Lab., Michigan State University, East Lansing, Mich.*, 1997.

[10] Martin Berz. Algorithms for higher derivatives in many variables with applications to beam physics. In *Automatic differentiation of algorithms (Breckenridge, CO, 1991)*, pages 147–156. SIAM, Philadelphia, PA, 1991.

[11] Y. F. Chang and G. Corliss. ATOMFT: solving ODEs and DAEs using Taylor series. *Comput. Math. Appl.*, 28(10-12):209–233, 1994.

[12] G. F. Corliss, A. Griewank, P. Henneberger, G. Kirlinger, F. A. Potra, and H. J. Stetter. High-order stiff ODE solvers via automatic differentiation and rational prediction. In *Numerical analysis and its applications (Rousse, 1996)*, volume 1196 of *Lecture Notes in Comput. Sci.*, pages 114–125. Springer, Berlin, 1997.

[13] Z. Galias and P. Zgliczyński. Computer assisted proof of chaos in the Lorenz equations. *Phys. D*, 115(3-4):165–188, 1998.

[14] E. Hairer, S. P. Nørsett, and G. Wanner. *Solving ordinary differential equations. I*, volume 8 of *Springer Series in Computational Mathematics*. Springer-Verlag, Berlin, second edition, 1993.

[15] Àngel Jorba and Maorong Zou. A software package for the numerical integration of ODEs by means of high-order Taylor methods. *Experiment. Math.*, 14(1):99–117, 2005.

[16] Tomasz Kapela and Piotr Zgliczyński. The existence of simple choreographies for the N-body problem—a computer-assisted proof. *Nonlinearity*, 16(6):1899–1918, 2003.

[17] Tomasz Kapela and Piotr Zgliczyński. A Lohner-type algorithm for control systems and ordinary differential inclusions. *Discrete Contin. Dyn. Syst. Ser. B*, 11(2):365–385, 2009.

[18] E.N. Lorenz. Deterministic nonperiodic flow. *Journal of Atmospheric Sciences*, 20:130–141, 1963.

[19] N. S. Nedialkov, K. R. Jackson, and G. F. Corliss. Validated solutions of initial value problems for ordinary differential equations. *Appl. Math. Comput.*, 105(1):21–68, 1999.

[20] Nedialko S. Nedialkov and John D. Pryce. Solving differential algebraic equations by Taylor series. III. The DAETS code. *JNAIAM J. Numer. Anal. Ind. Appl. Math.*, 3(1-2):61–80, 2008.

[21] Louis B. Rall and George F. Corliss. An introduction to automatic differentiation. In *Computational differentiation (Santa Fe, NM, 1996)*, pages 1–18. SIAM, Philadelphia, PA, 1996.

[22] Divakar Viswanath. The fractal property of the Lorenz attractor. *Phys. D*, 190(1-2):115–128, 2004.

[23] Piotr Zgliczyński. C^1 Lohner algorithm. *Found. Comput. Math.*, 2(4):429–465, 2002.

Monografías de la Real Academia de Ciencias de Zaragoza **35**, 97–117, (2011).

Deflexión de asteroides por medio de fuerzas electromagnéticas durante un fly-by a la Tierra

M. Sanjurjo-Rivo[1], J. Peláez[1], D. Izzo[2], O. Purcell[2], and D.J. Scheeres[3]

[1] Universidad Politécnica de Madrid, Pza. Cardenal Cisneros 3, 28040 Madrid, Spain.

[2] Advanced Concepts Team, ESA

[3] Colorado University at Boulder

Resumen

En los últimos años, se han dirigido muchos esfuerzos a tratar de evitar un posible impacto sobre la superficie terrestre de un asteroide. Se han propusto nuevas estrategias y tecnologías en este campo, investigando la utilización de aplicaciones innovadoras para ese propósito. En este contexto, este trabajo explora la posibilidad de utilizar las fuerzas que actuarían sobre el asteroide durante un fly-by a la Tierra debido a la interacción con el campo magnético terrestre. Entre estas interacciones, este artículo se centra en la fuerza de Lorentz, valorando bajo qué hipótesis y condiciones podría proporcionar una deflexión efectiva de la órbita del asteroide.

1. INTRODUCCIÓN

Existen asteroides próximos a la órbita terreste (NEO en su acrónimo en inglés) que representan un peligro potencial para la Tierra, debido al riego de que dichos objetos puedan entrar en trajectoria de colisión con la misma. Reducir este riego requiere de la consideración y el análisis de aquellas técnicas que permitan modificar la trajectoria de asteroides. El objetivo de cualquier misión de deflexión de asteroides es la de alterar su órbita para evitar posibles encuentros en el futuro. Habitualemente estas misiones se caracterizan en la literatura por la actuación continua sobre la trajectoria heliocéntrica del asteroide a lo largo de su órbita.

No obstante, es posible explorar las oportunidades de modificar la órbita de un asteroide en unas escalas de espacio y tiempo más corta, esto es, durante un fly-by a la Tierra. En esta situación, existen condiciones particulares que dejan abiertas algunas cuestiones. En particular, nos centraremos en responder a la pregunta de si es factible aprovechar

la interación entre el campo geomagnético y el asteroide. En trabajos previos, se ha considerado el uso de fuerzas electrostáticas para la deflexión de asteroides [1], donde se proporciona la estimación de la carga necesaria para obtener una fuerza significativa, o en el diseño del Electrostatic Tractor [2]. Asimismo, en [3] se pueden encontrar estimaciones de las perturbaciones electromagnéticas en las órbitas de los asteroides.

En el presente artículo, se desarrolla un método general para el análisis del efecto de aceleraciones de perturbación durante un fly-by de un asteroide. Este método nos permitirá estimar la fuerza necesaria para obtener la deflexión deseada. Además, se han considerado tres escenarios diferentes en este estudio. En primer lugar, se supondrá que un asteroide cargado electrostáticamente evoluciona bajo los efectos de las fuerzas gravitatoria y de Lorentz, asumiendo una carga eléctrica fija durante el fly-by. El efecto de esta fuerza de perturbación en la órbita es analizado en términos de las condiciones iniciales necesarias de un fly-by puramente gravitatorio para obtener unas condiciones de salida iguales a las de la trajectoria perturbada. En segundo lugar, se estudiará la posibilidad de utilizar amarras electrodinámicas en fly-bys que crucen la ionosfera terrestre. La operación de estos dispositivos está fuertemente condicionada por la capacidad de colectar electrones en un ambiente plasmático muy rarificado. Finalmente, se analizará la importancia del uso de amarras electrodinámicas en el movimiento de actitud del asteroide durante el fly-by, estudiando el efecto de estos dispositivos en el cambio de momento angular que sufre el asteroide en este proceso. La viabilidad de estas estrategias se discutirá a la luz de los resultados obtenidos.

En resumen, este artículo está dedicado a evaluar la viabilidad de utilizar la fuerza de Lorentz para la deflexión de órbita de asteroides, proporcionado estimaciones de los efectos de las interaciones electromagnéticas con el campo geomagnético.

2. Análisis de la deflexión de asteroides durante un fly-by

El propósito de este artículo es el de analizar la deflexión de ateroides durante un fly-by terrestre. Por lo tanto, y en primer lugar, nos centraremos en establecer las herramientas necesarias para el estudio del efecto de las fuerzas de perturbación que actúan durante el swing-by en la subsiguiente trajectoria heliocéntrica del asteroide. Para ello, usaremos la aproximación de las "patched conic", es decir, durante el fly-by únicamente consideraremos la fuerza gravitatoria terrestre, despreciando la fuerza atractiva del resto de cuerpos celestes. Además, analizaremos las ecuaciones planetarias de Gauss para determinar el efecto de las fuerzas de perturbación en la trayectoria hiperbólica del fly-by, por una parte; y por otra parte, la modificación que resulta en el "b-plane" (plano perpendicular a la asíntota de llegada que contiene al foco atractor).

Dentro de la validez de la aproximación de "patched-conic", la órbita inicial será una

hipérbola. Para analizar el problema, se usarán tres sistemas de referencia:

- Sistema de referencia osculador polar local $(\vec{\boldsymbol{i}}_r, \vec{\boldsymbol{i}}_\theta, \vec{\boldsymbol{i}}_h)$. El vector unitario $\vec{\boldsymbol{i}}_r$ apunta en la dirección del vector de posición y $\vec{\boldsymbol{i}}_h$ apunta en la dirección perpendicular a los vectores de posición y velocidad, simultáneamente.

- Sistema de referencia del plano orbital osculador $(\vec{\boldsymbol{i}}_e, \vec{\boldsymbol{i}}_p, \vec{\boldsymbol{i}}_h)$. El vector unitario $\vec{\boldsymbol{i}}_e$ se encuentra en la dirección del vector excentricidad y $\vec{\boldsymbol{i}}_h$ se define de la misma forma que en el caso anterior.

- Sistema de referencia pseudo-inercial $(\vec{\boldsymbol{i}}_x, \vec{\boldsymbol{i}}_y, \vec{\boldsymbol{i}}_z)$. El origen de este sistema de referencia sería el centro de masas de la Tierra, los ejes $\vec{\boldsymbol{i}}_x$ y $\vec{\boldsymbol{i}}_y$ definen el plano ecuatorial y $\vec{\boldsymbol{i}}_z$ coincide con el eje de rotación de la Tierra. Además, la proyección de $\vec{\boldsymbol{i}}_x$ en la eclíptica tiene el mismo sentido que el vector de posición de la Tierra respecto del Sol[1].

La hipérbola inicial se puede caracterizar bien por los elementos orbitales osculadores iniciales ($\Omega_0, i_0, \omega_0, a_0, e_0, \tau_0$, donde $a_0 < 0$ y $e_0 > 1$) o bien por el vector velocidad de llegada $\vec{\boldsymbol{v}}_\infty$ y el pretendido vector de posición en el periapsis $\vec{\boldsymbol{r}}_p$. Los elementos osculadores usados para describir el cambio de la hipérbola serán: $\Omega, i, \omega, a, e, \lambda$, donde $\lambda = n\,\tau$, y $n = \sqrt{\mu/(-a)^3}$. Otras relaciones que han sido utilizadas para la descripción de la hipérbola son:

$$r = a\,(1 - e\,\cosh H) \qquad\qquad p = a(1 - e^2)$$
$$b = a\sqrt{e^2 - 1} \qquad\qquad h = n\,a\,b$$

donde H es una cantidad relacionada con la anomalía verdadera de la siguiente forma:

$$\tan\left(\frac{1}{2}f\right) = \sqrt{\frac{e+1}{e-1}}\tanh\left(\frac{1}{2}H\right)$$

Si el vector de aceleraciones de perturbación se expresa en el sistema de referencia osculador polar local de la forma: $\vec{\boldsymbol{a}} = \{a_{d,r}, a_{d,\theta}, a_{d\,h}\}^T$, la formulación de las ecuaciones

[1]Se supone que la órbita terrestre es perfectamente circular

planetarias de Gauss para la hipérbola es como sigue:

$$\frac{d\,\Omega}{d\,t} = \frac{r\,\sin\theta}{h\,\sin i}\,a_{d,h} \tag{1}$$

$$\frac{d\,i}{d\,t} = \frac{r\,\cos\theta}{h}\,a_{d,h} \tag{2}$$

$$\frac{d\,\omega}{d\,t} = \frac{1}{h\,e}\left[-p\,\cos f\,a_{d,r} + (p+r)\,\sin f\,a_{d,\theta}\right] - \frac{r\,\cos i\,\sin\theta}{h\,\sin i}\,a_{d,h} \tag{3}$$

$$\frac{d\,a}{d\,t} = -\frac{2\,a^2}{h}\left[e\,\sin f\,a_{d,r} + (1+e\,\cos f)\,a_{d,\theta}\right] \tag{4}$$

$$\frac{d\,e}{d\,t} = -\frac{1}{h}\left[p\,\sin f\,a_{d,r} + \left(p\,\cos f + p\,\frac{(a+r)}{a\,e}\right)a_{d,\theta}\right] \tag{5}$$

$$\frac{d\,\lambda}{d\,t} = a_{d,r}\left[\frac{b}{h\,a\,e}\,(2\,r\,e - p\,\cos f) - \frac{3\,t\,e\,\sin f}{b}\right] - a_{d,\theta}\left[\frac{3\,t\,(1+e\,\cos f)}{b} - \frac{b\,\sin f}{h\,a\,e}\,(p+r)\right] \tag{6}$$

Junto con la ecuación de Kepler:

$$n\,t + \lambda = e\,\sinh H - H \tag{7}$$

las ecuaciones planetarias permiten calcular la evolución de los elementos orbitales osculadores dadas unas condiciones iniciales y la ley de aceleraciones de perturbación $\{a_{d,r}(t), a_{d,\theta}(t), a_{d,h}(t)\}$.

En relación con el "b-plane", es posible establecer la relación entre el vector $\vec{\boldsymbol{B}}$ (vector contenido en el "b-plane" que une el foco de atracción de la trayectoria y la interseción entre el propio plano y la hipérbola, también llamado b-vector) y los elementos osculadores de la hipérbola. De hecho, llamando $\vec{\boldsymbol{s}}$ al vector unitario en la dirección de la asíntota de llegada y $\vec{\boldsymbol{n}}$ al vector unitario en la dirección perpendicular al plano orbital ($\vec{\boldsymbol{n}} = (\vec{\boldsymbol{r}}\times\vec{\boldsymbol{v}})/\,|\vec{\boldsymbol{r}}\times\vec{\boldsymbol{v}}|$), el parámetro de impacto puede ser calculado como:

$$\vec{\boldsymbol{B}} = (-b)\,(\vec{\boldsymbol{s}}\times\vec{\boldsymbol{n}})$$

Las expresiones de dichos vectores en el sistema de referencia inercial será:

$$\vec{\boldsymbol{s}} = \mathcal{R}\,\{\cos\alpha, \sin\alpha, 0\}^T \qquad \vec{\boldsymbol{n}} = \mathcal{R}\,\{0,0,1\}^T$$

donde $\mathcal{R}(\Omega, i, \omega)$ es la matriz de rotación de las coordenadas del plano osculador a las coordenadas del sistema de referencia inercial y α es el ángulo definido como:

$$\alpha = \arccos\,(1/e)$$

Por lo tanto, la veriación del vector $\vec{\boldsymbol{B}}$ debido a las aceleraciones de perturbación puede calcularse a partir de la siguiente expresión:

$$\frac{d\,\vec{\boldsymbol{B}}}{d\,t} = -\frac{d\,b}{d\,t}(\vec{\boldsymbol{s}}\times\vec{\boldsymbol{n}}) - b\left(\frac{d\,\vec{\boldsymbol{s}}}{d\,t}\times\vec{\boldsymbol{n}}\right) - b\left(\vec{\boldsymbol{s}}\times\frac{d\,\vec{\boldsymbol{n}}}{d\,t}\right)$$

donde:

$$\begin{aligned}
\frac{d\,\vec{\boldsymbol{n}}}{d\,t} &= \left(\frac{\partial\,\mathcal{R}}{\partial\,\Omega}\frac{d\,\Omega}{d\,t}+\frac{\partial\,\mathcal{R}}{\partial\,i}\frac{d\,i}{d\,t}+\frac{\partial\,\mathcal{R}}{\partial\,\omega}\frac{d\,\omega}{d\,t}\right)\begin{bmatrix}0\\0\\1\end{bmatrix}\\
\frac{d\,\vec{\boldsymbol{s}}}{d\,t} &= \left(\frac{\partial\,\mathcal{R}}{\partial\,\Omega}\frac{d\,\Omega}{d\,t}+\frac{\partial\,\mathcal{R}}{\partial\,i}\frac{d\,i}{d\,t}+\frac{\partial\,\mathcal{R}}{\partial\,\omega}\frac{d\,\omega}{d\,t}\right)\begin{bmatrix}\cos\alpha\\\sin\alpha\\0\end{bmatrix}+\mathcal{R}\begin{bmatrix}-\sin\alpha\\\cos\alpha\\0\end{bmatrix}\frac{\partial\,\alpha}{\partial\,e}\frac{d\,e}{d\,t}\\
\frac{d\,b}{d\,t} &= \frac{b}{a}\frac{d\,a}{d\,t}+\frac{a^2\,e}{b}\frac{d\,e}{d\,t}
\end{aligned}$$

2.1. Análisis asintótico

En este apartado se intenta sacar partido del hecho de que las variaciones de los elementos orbitales del asteroide serán pequeños como lo es la aceleración de perturbación. Comenzaremos estableciendo la formulación adimensional de las ecuaciones planetarias. La longitud característica será el valor absoluto del semi-eje mayor en el instante inicial, $|a_i|$. Por su parte, el tiempo característico, τ_c, será $\tau_c = \sqrt{|a_i|^3/\mu_{\sun}}$. Las variables adimensionales se designarán con un sombrero, esto es, $a = |a_i|\,\hat{a}$. Las ecuaciones planetarias (1-6) se rescriben teniendo en cuenta lo anterior como:

$$\begin{aligned}
\frac{d\,\Omega}{d\,\tau} &= \frac{\hat{r}\,\sin\theta}{\hat{h}\,\sin i}\,\hat{a}_{d,h}\\
\frac{d\,i}{d\,\tau} &= \frac{\hat{r}\,\cos\theta}{\hat{h}}\,\hat{a}_{d,h}\\
\frac{d\,\omega}{d\,\tau} &= \frac{1}{\hat{h}\,e}\left[-\hat{p}\,\cos f\,\hat{a}_{d,r}+(\hat{p}+\hat{r})\,\sin f\,\hat{a}_{d,\theta}\right]-\frac{\hat{r}\,\cos i\,\sin\theta}{\hat{h}\,\sin i}\,\hat{a}_{d,h}\\
\frac{d\,\hat{a}}{d\,\tau} &= -\frac{2\,\hat{a}^2}{\hat{h}}\left[e\,\sin f\,\hat{a}_{d,r}+(1+e\,\cos f)\,\hat{a}_{d,\theta}\right]\\
\frac{d\,e}{d\,\tau} &= -\frac{1}{\hat{h}}\left[\hat{p}\,\sin f\,\hat{a}_{d,r}+\left(\hat{p}\,\cos f+\hat{p}\,\frac{(\hat{a}+\hat{r})}{\hat{a}\,e}\right)\hat{a}_{d,\theta}\right]\\
\frac{d\,\lambda}{d\,\tau} &= \hat{a}_{d,r}\left[\frac{\hat{b}}{\hat{h}\,\hat{a}\,e}\,(2\,\hat{r}\,e-\hat{p}\,\cos f)-\frac{3\,\tau\,e\,\sin f}{\hat{b}}\right]-\hat{a}_{d,\theta}\left[\frac{3\,\tau\,(1+e\,\cos f)}{\hat{b}}-\frac{\hat{b}\,\sin f}{\hat{h}\,\hat{a}\,e}\,(\hat{p}+\hat{r})\right]
\end{aligned}$$

Mientras que la ecuación de Kepler equation se expresa del siguiente modo:

$$\tau+\lambda = e\,\sinh H - H$$

Las siguientes relaciones se han usado en el sistema (8-8):

$$\begin{aligned}
r &= |a_i|\,\hat{r} & p &= |a_i|\,\hat{p}\\
b &= |a_i|\,\hat{b} & h &= \sqrt{|a_i|\,\mu_{\sun}}\,\hat{h}\\
a_d &= \frac{\mu_{\sun}}{|a_i|^2}\,\hat{a}_d
\end{aligned}$$

Suponiendo que la aceleración de perturbación es pequeña comparada con la aceleración gravitatoria, es posible derivar una formulación más simple para el cálculo de la variación de los elementos orbitales osculadores. Sea $\varepsilon \ll 1$ un parámetro pequño, que satisface la siguiente relación para la aceleración de perturbación adimensional $\hat{a}_d = \varepsilon\, \tilde{a}_d$. Haciendo uso de este parámetro, se considera la expansión asintótica de los elementos orbitales en potencias de ε: $\hat{\vec{\boldsymbol{\alpha}}} = \hat{\vec{\boldsymbol{\alpha}}}_0 + \varepsilon\, \hat{\vec{\boldsymbol{\alpha}}}_1 + \varepsilon^2\, \hat{\vec{\boldsymbol{\alpha}}}_2 + \mathcal{O}(\varepsilon^2)$, donde $\hat{\vec{\boldsymbol{\alpha}}}_0$ se corresponde con la solución del problema no perturbado. Además, se supondrá que la variable H relacionada con la anomalía verdadera puede expandirse en términos del mismo parámetro ε: $H(\tau) = H_0(\tau) + \varepsilon\, H_1(\tau) + \mathcal{O}(\varepsilon)$. El sistema de ecuaciones diferenciales que gobierna la evolución de $\hat{\vec{\boldsymbol{\alpha}}}_1$ se puede calcular haciendo uso de las ecuaciones planetarias adimensionales:

$$
\begin{aligned}
\frac{d\,\Omega_1}{d\,\tau} &= \frac{(1 - e_0\, \cosh H_0(\tau))\, \sin\left(f(\tau) + \omega_0\right) \tilde{a}_{d,h}}{\sqrt{e_0^2 - 1}\, \sin i_0} \\
\frac{d\,i_1}{d\,\tau} &= \frac{(1 - e_0\, \cosh H_0(\tau))\, \cos\left(f(\tau) + \omega_0\right) \tilde{a}_{d,h}}{\sqrt{e_0^2 - 1}} \\
\frac{d\,\omega_1}{d\,\tau} &= -\frac{(1 - e_0^2)\, \cos f(\tau)\, \tilde{a}_{d,r} + (e_0^2 - 2 + e_0\, \cosh H_0(\tau))\, \sin f(\tau)\, \tilde{a}_{d,\theta}}{e_0\, \sqrt{e_0^2 - 1}} - \\
&\quad - \frac{(1 - e_0\, \cosh H_0(\tau))\, \cos i_0\, \sin\left(f(\tau) + \omega_0\right) \tilde{a}_{d,h}}{\sqrt{e_0^2 - 1}\, \sin i_0} \\
\frac{d\,\hat{a}_1}{d\,\tau} &= \frac{2\,(e_0\, \sin f(\tau)\, \tilde{a}_{d,r} + (1 + e_0\, \cos f(\tau))\, \tilde{a}_{d,\theta})}{\sqrt{e_0^2 - 1}} \\
\frac{d\,e_1}{d\,\tau} &= \sqrt{e_0^2 - 1}\, \left[\sin f(\tau)\, \tilde{a}_{d,r} + \left(\cos f(\tau) + \frac{(-2 + e_0\, \cosh H_0(\tau))}{e_0}\right)\, \tilde{a}_{d,\theta}\right] \\
\frac{d\,\lambda_1}{d\,\tau} &= \left[\frac{3\,\tau\, e_0\, \sin f(\tau)}{\sqrt{e_0^2 - 1}} + 2\,(e_0\, \cosh H_0(\tau) - 1) - \frac{e_0^2 - 1}{e_0}\, \cos f(\tau)\right]\, \tilde{a}_{d,r} + \\
&\quad \left[-\frac{3\,\tau\,(1 + e_0\, \cos f(\tau))}{\sqrt{e_0^2 - 1}} + \frac{(e_0^2 - 1 + (e_0\, \cosh H_0(\tau) - 1))\, \sin f(\tau)}{e_0}\right]\, \tilde{a}_{d,\theta}
\end{aligned}
$$

donde se ha utilizado la relación $\hat{a}_0 = -1$. Las condiciones iniciales para este sistema de ecuaciones diferenciales es $\hat{\vec{\boldsymbol{\alpha}}}_1 = \vec{\mathbf{0}}$, dado que inicialmente los valores osculadores se corresponden con los del problema no perturbado.

Por lo tanto, asumiendo, ya sea aceleración constante $\tilde{a}_d = \tilde{A}_d$, ya sea aceleración impulsiva $\tilde{a}_d = \delta(\tau_M)\, \tilde{A}_d$, los elementos orbitales osculadores de la trajectoria perturbada

pueden ser expresados en función de los parámetros de la hipérbola no perturbada:

$$\Omega_1^F = \frac{\tilde{A}_{d,h}}{\sqrt{e_0^2-1}\,\sin i_0}\left[\cos\omega_0\,\mathcal{I}_2+\sin\omega_0\,\mathcal{I}_1\right] \tag{8}$$

$$i_1^F = \frac{\tilde{A}_{d,h}}{\sqrt{e_0^2-1}}\left[\cos\omega_0\,\mathcal{I}_1-\sin\omega_0\,\mathcal{I}_2\right] \tag{9}$$

$$\begin{aligned}\omega_1^F = {} & \frac{\sqrt{e_0^2-1}}{e_0}\,\tilde{A}_{d,r}\mathcal{I}_3-\frac{\tilde{A}_{d,\theta}}{e_0\,\sqrt{e_0^2-1}}\left[(e_0^2-1)\,\mathcal{I}_4-\mathcal{I}_2\right]\\ & -\frac{\cos i_0\,\tilde{A}_{d,h}}{\sqrt{e_0^2-1}\sin i_0}\left[\cos\omega_0\,\mathcal{I}_1+\sin\omega_0\,\mathcal{I}_2\right]\end{aligned} \tag{10}$$

$$\hat{a}_1^F = \frac{2(e_0\,\mathcal{I}_4\,\tilde{A}_{d,r}+(\mathcal{I}_5+e_0\,\mathcal{I}_3)\,\tilde{A}_{d,\theta})}{\sqrt{e_0^2-1}} \tag{11}$$

$$e_1^F = \sqrt{e_0^2-1}\left[\mathcal{I}_4\,\tilde{A}_{d,r}+\left(\mathcal{I}_3-\frac{\mathcal{I}_5+\mathcal{I}_6}{e_0}\right)\tilde{A}_{d,\theta}\right] \tag{12}$$

donde $\mathcal{I}_i$ representa el valor de las integrales que aparecen en las ecuaciones anteriores. Es posible obtener las cuadraturas en una forma sencilla cuando consideramos una maniobra impulsiva. En ese caso:

$$\mathcal{I}_1 = -\hat{r}_M\,\cos f_M \qquad \mathcal{I}_2 = -\hat{r}_M\,\sin f_M$$
$$\mathcal{I}_3 = \cos f_M \qquad \mathcal{I}_4 = \sin f_M$$
$$\mathcal{I}_5 = \tau_M \qquad \mathcal{I}_6 = -\hat{r}_M$$

donde el subíndice M hace referencia al instante en el que el impulso es aplicado y, por tanto, $\hat{r}_M = (e_0\,\cosh(H_0(\tau_M))-1)$. En el caso de empuje continuo, las expresiones resultan más complejas, pero aún es posible encontrar una expresión analítica cerrada para las integrales. No se han incluido las relaciones explícitas para el parámetro λ dado que los términos seculares conducen a cuadraturas más complejas.

El planteamiento asintótico adimensional puede utilizarse del mismo modo para el cálculo de la variación del vector $\vec{\boldsymbol{B}}$ debido a la aceleración de perturbación. Los valores adimensionales serán:

$$\hat{\vec{\boldsymbol{B}}} = \frac{\vec{\boldsymbol{B}}}{|a_i|} \quad \text{and} \quad \hat{b} = \frac{b}{|a_i|}$$

Por otro lado, la expansión asintótica presenta la misma forma que para los elementos orbitales, es decir, $\hat{\vec{\boldsymbol{B}}} = \hat{\vec{\boldsymbol{B}}}_0 + \varepsilon\,\hat{\vec{\boldsymbol{B}}}_1 + \mathcal{O}(\varepsilon)$, donde $\hat{\vec{\boldsymbol{B}}}_0$ es el vector adimensional del problema no perturbado. Por tanto, la variación del vector $\vec{\boldsymbol{B}}$ con respecto al tiempo tiene la siguiente forma:

$$\frac{d\,\hat{\vec{\boldsymbol{B}}}_1}{d\,\tau} = -\frac{d\,\hat{b}_1}{d\,\tau}(\vec{\boldsymbol{s}}_0\times\vec{\boldsymbol{n}}_0)-b_0\left(\frac{d\,\vec{\boldsymbol{s}}_1}{d\,\tau}\times\vec{\boldsymbol{n}}_0\right)-b_0\left(\vec{\boldsymbol{s}}_0\times\frac{d\,\vec{\boldsymbol{n}}_1}{d\,\tau}\right)$$

donde:

$$\begin{aligned}
\frac{d\,\vec{\boldsymbol{n}}_1}{d\,\tau} &= \left(\frac{\partial\,\mathcal{R}_0}{\partial\,\Omega_0}\frac{d\,\Omega_1}{d\,\tau}+\frac{\partial\,\mathcal{R}_0}{\partial\,i_0}\frac{d\,i_1}{d\,\tau}+\frac{\partial\,\mathcal{R}_0}{\partial\,\omega_0}\frac{d\,\omega_1}{d\,\tau}\right)\begin{bmatrix}0\\0\\1\end{bmatrix}\\
\frac{d\,\vec{\boldsymbol{s}}_1}{d\,\tau} &= \left(\frac{\partial\,\mathcal{R}_0}{\partial\,\Omega_0}\frac{d\,\Omega_1}{d\,\tau}+\frac{\partial\,\mathcal{R}_0}{\partial\,i_0}\frac{d\,i_1}{d\,\tau}+\frac{\partial\,\mathcal{R}_0}{\partial\,\omega_0}\frac{d\,\omega_1}{d\,\tau}\right)\begin{bmatrix}\cos\alpha_0\\\sin\alpha_0\\0\end{bmatrix}+\mathcal{R}_0\begin{bmatrix}-\sin\alpha_0\\\cos\alpha_0\\0\end{bmatrix}\frac{\partial\,\alpha_0}{\partial\,e_0}\frac{d\,e_1}{d\,\tau}\\
\frac{d\,\hat{b}_1}{d\,\tau} &= \sqrt{e_0^2-1}\frac{d\,\hat{a}_1}{d\,\tau}+\frac{e_0}{\sqrt{e_0^2-1}}\frac{d\,e_1}{d\,\tau}
\end{aligned}$$

y $\mathcal{R}_0=\mathcal{R}(\Omega_0,i_0,\omega_0)$. El anterior sistema de ecuaciones puede integrarse en función de los valores finales de los elementos orbitales osculadores. Y sustituyendo (8-12) en aquellos resultados, finalmente obtenemos una relación directa entre la variación del vector $\vec{\boldsymbol{B}}$ y las aceleraciones adimensionales aplicadas en dos casos: empuje continuo y maniobras impulsivas [2].

Estos resultados permiten calcular la diferencia vectorial entre los vectores $\vec{\boldsymbol{B}}$ inicial y final: $\vec{\boldsymbol{B}}^F-\vec{\boldsymbol{B}}_0=\varepsilon\;|a_i|\;\hat{\vec{\boldsymbol{B}}}_1$,

$$\begin{aligned}
\hat{\vec{\boldsymbol{B}}}_1 &= -\hat{b}_1^F\,(\vec{\boldsymbol{s}}_0\times\vec{\boldsymbol{n}}_0)-\hat{b}_0\left(\vec{\boldsymbol{s}}_1^F\times\vec{\boldsymbol{n}}_0\right)-\hat{b}_0\left(\vec{\boldsymbol{s}}_0\times\vec{\boldsymbol{n}}_1^F\right)\\
\vec{\boldsymbol{n}}_1^F &= \left(\frac{\partial\,\mathcal{R}_0}{\partial\,\Omega_0}\Omega_1^F+\frac{\partial\,\mathcal{R}_0}{\partial\,i_0}i_1^F+\frac{\partial\,\mathcal{R}_0}{\partial\,\omega_0}\omega_1^F\right)\begin{bmatrix}0\\0\\1\end{bmatrix}\\
\vec{\boldsymbol{s}}_1^F &= \left(\frac{\partial\,\mathcal{R}_0}{\partial\,\Omega_0}\Omega_1^F+\frac{\partial\,\mathcal{R}_0}{\partial\,i_0}i_1^F+\frac{\partial\,\mathcal{R}_0}{\partial\,\omega_0}\omega_1^F\right)\begin{bmatrix}\cos\alpha_0\\\sin\alpha_0\\0\end{bmatrix}+\mathcal{R}_0\begin{bmatrix}-\sin\alpha_0\\\cos\alpha_0\\0\end{bmatrix}\frac{\partial\,\alpha_0}{\partial\,e_0}e_1^F\\
\hat{b}_1^F &= 3\,e_0\,\mathcal{I}_4\,\tilde{A}_{d,r}+(3\,e_0\,\mathcal{I}_3+\mathcal{I}_5-\mathcal{I}_6)\;\tilde{A}_{d,\theta}
\end{aligned}$$

Finalmente, la variación del vector $\vec{\boldsymbol{B}}$ puede ser expresado en términos de las fuerzas aplicadas. Por claridad, derivamos dicha relación para la variación del semi-eje menor b (el semi-eje menor es el módulo del vector $\vec{\boldsymbol{B}}$). La variación del semi-eje menor es: $\Delta\,b=b^F-b_0=\varepsilon\;|a_i|\,\hat{b}_1^F$. Por otra parte, tenemos: $\varepsilon\,\tilde{A}_d=F\;|a_i|^2/(M_a\,\mu_{\odot\!\!\!+})$ para empuje continuo, y $\varepsilon\,\tilde{A}_d=\eta\,m\;|a_i|^{1/2}/(m+M_a)/\mu_{\odot\!\!\!+}^{1/2}\,U$ donde se ha utilizado la misma notación que en [4] (donde *eta* es la eficiencia del impacto, M_a la masa del asteroide, m la masa del vehćulo que impacta contra el asteroide y U la velocidad de impacto). Por consiguiente, la variación $\Delta\,b$ se expresa como:

$$\Delta\,b=\frac{|a_i|^3}{M_a\,\mu_{\odot\!\!\!+}}\left[3\,e_0\,\mathcal{I}_4\,F_r+(3\,e_0\,\mathcal{I}_3+\mathcal{I}_5-\mathcal{I}_6)\;F_\theta\right]$$

[2]Se considera que no hay pérdida de masa en el sistema, de manera que se utiliza indistintamente aceleración y empuje de perturbación continuos.

o

$$\Delta\, b = \frac{\eta\, m}{m + M_a} \frac{|a_i|^{3/2}}{M_a\, \mu_{\overset{+}{\odot}}^{1/2}} \left[3\, e_0\, \mathcal{I}_4\, U_r + (3\, e_0\, \mathcal{I}_3 + \mathcal{I}_5 - \mathcal{I}_6)\; U_\theta\right]$$

Por lo tanto, dada una trayectoria inicial, la masa del asteroide (y la masa del vehiculo espacial) y la fuerza aplicada (o la velocidad relativa respecto al asteroide en caso de impacto), es posible calcular directamente la variación del vector $\vec{\boldsymbol{B}}$. Esto se ha llevado a cabo para los dos casos de empuje conjsiderados: continuo e impulsivo. Para el empuje continuo hemos obtenido que la inclinación de la órbita tiene relativa importancia cuando se aplican aceleraciones normales o tangenciales. Sin embargo, el comportamiento es diferente en sendos casos: mientras que las mayores variaciones en el módulo del b-vector se consiguen para órbitas casi polares cuando el empuje es aplicado en dirección normal a la trayectoria, para empuje tangencial los mejores resultados se obtienen para inclinaciones de alrededor de los 45º. La mayor variación en el módulo del b-vector considerando todas las diferentes estrategias de orientación se obtiene para aceleración de perturbación en dirección normal a la trayectoria, y esta variación es del orden de 60 cm cuando el empuje continuo aplicado es de 1 N, como puede observarse en la Figura 1. La razón por la cual las variaciones en el módulo del b-vector son tan pequeñas las podemos encontrar en el pequeño intervalo de tiempo en el que se ejerce la fuerza de perturbación. Por otra parte, la eficiencia de la aceleración normal a la órbita puede explicarse por el hecho de que el efecto de dicha aceleración es el de cambiar el momento angular de la órbita, y el brazo del momento aplicado es grande. Este resultado es más interesante para una maniobra impulsiva, no sólo para impulsos normales a la órbita sino también para impulsos tangenciales, dado que permite cambiar la orientación de la órbita dentro del plano orbital. De hecho, la estrategia de maniobra impulsiva presenta un grado de libertad adicional: la posición del encuentro. Hay dos ubicaciones extremas privilegiadas, el pericentro y la posición inicial a la distancia de la esfera de influencia. En el perigeo la velocidad relativa es mayor mientras que en la esfera de influencia el brazo del momento para cambiar el momento angular de la órbita es máximo. Para clarificar cuál es el efecto dominante, hemos realizado simulaciones suponiendo que la maniobra impulsiva es producida por un vehículo espacial viajando en la órbita del asteroide en sentido contrario. Los resultados muestran que la deflexión máxima que se obtiene cuando el impacto se produce a la distancia de la esfera de influencia es uno o dos órdenes de magnitud mayor que los obtenidos en el pericentro. Esto es, para la misma velocidad de impacto, la ubicación lejana del impacto es más eficiente. En la Figura 1 se presentan los resultados para una maniobra impusiva a la distancia de la esfera de influencia. La velocidad relativa considerada es de 10 km/s, la masa del vehículo espacial es 1 Tn y $\eta = 1$. De nuevo la influencia de la inclinación sigue el mismo patrón que para el empuje continuo y las mayores variaciones del b-vector se consiguen para inclinaciones de aproximadamente 45º cuando se aplican impulsos radiales

o tangenciales y órbitas casi polares cuando se aplican impulsos normales a la trayectoria.

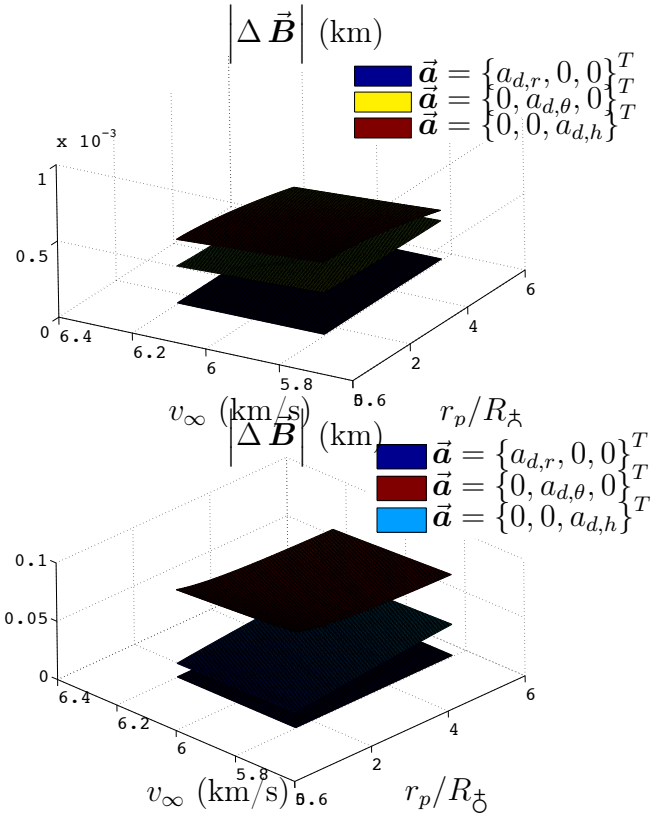

Figura 1.— En el gráfico de la izquierda se muestra la variación de $|\vec{\boldsymbol{B}}|$ cuando se aplica un empuje continuo de 1 N durante el fly-by para diferentes hipérbolas iniciales y diferentes orientaciones de la aceleración de perturbación. En el gráfico de la derecha, se muestra la variación del b-vector para el caso de impacto. La velocidad relativa es 10 km/s, la masa del vehículo espacial que impacta sobre el asteroide es de 1 Tn y $\eta = 1$. Los resultados se presentan para distintas hipérbolas iniciales y distintas orientaciones de impacto.

3. Modelo de la fuerza electrostática

La posibilidad de cargar la superficie de un asteroide para proporcionar la deflexión de su órbita ya ha sido estudiada en trabajos anteriores [3, 1]. No obstante, siempre ha sido considerado en el contexto de la órbita heliocéntrica del asteroide. Aquí, supondremos que el comportamiento del asteroide durante el fly-by terrestre puede ser caracterizado como el de una partícula cargada con una carga eléctrica constante Q durante toda la trayectoria. La fuerza electrostática que actúa sobre el asteroide puede calcularse como:

$$\vec{\boldsymbol{F}} = Q\,\left(\vec{\boldsymbol{v}} \times \vec{\boldsymbol{B}}_{Mg}\right)$$

La velocidad $\vec{\boldsymbol{v}}$ es la velocidad relativa al sistema de referencia pseudo-inercial y puede expresarse en función de los elementos orbitales osculadores como sigue:

$$\vec{\boldsymbol{v}} = -\frac{\sqrt{-\mu\, a}}{r}\, \sinh H\, \vec{\boldsymbol{i}}_e + \frac{\sqrt{\mu\, p}}{r}\, \cosh H\, \vec{\boldsymbol{i}}_p$$

Por otra parte, el campo magnético $\vec{\boldsymbol{B}}_{Mg}$ es el campo geomagnético, es este caso. En este trabajo consideraremos un modelo simple de dipolo:

$$\vec{\boldsymbol{B}}_{Mg} = \frac{\mu_m\, R_{\overset{+}{\circlearrowleft}}^3}{r^3} \left(3\, (\hat{m} \cdot \hat{r})\, \hat{r} - \hat{m}\right)$$

donde $\hat{m}$ es el vector unitario en la dirección del dipolo, μ_m es la intensidad del dipolo, $\hat{r}$ el radio vector, r su módulo y R_{earth} el radio ecuatorial terrestre. Se supondrá que el dipolo está alineado con el eje de rotación terrestre, $\hat{m} = \vec{\boldsymbol{i}}_z$.

Finalmente, la expresión que permite calcular la aceleración de perturbación debida a las fuerzas electrostáticas es como sigue:

$$\vec{\boldsymbol{a}}_d = \frac{Q}{M_a} \left(\vec{\boldsymbol{v}} \times \vec{\boldsymbol{B}}_{Mg}\right)$$

donde M_a es la masa del asteroide. Dado que la aceleración se expresa en coordenadas osculadoras polares en las ecuaciones (1- 6), debemos expresar el vector $\left(\vec{\boldsymbol{v}} \times \vec{\boldsymbol{B}}_{Mg}\right)$ en dichas coordenadas.

$$\vec{\boldsymbol{v}}|_{OPC} = \mathcal{R}_f^T \begin{bmatrix} -\frac{\sqrt{-\mu\, a}}{r}\, \sinh H \\ \frac{\sqrt{\mu\, p}}{r}\, \cosh H \\ 0 \end{bmatrix};$$

$$\vec{\boldsymbol{B}}_{Mg}\Big|_{OPC} = \frac{\mu_m\, R_{\overset{+}{\circlearrowleft}}^3}{r^3} \left\{ 3 \left(\mathcal{R}^T\, \mathcal{R}_f^T \begin{bmatrix} 0 \\ 0 \\ 1 \end{bmatrix} \cdot \begin{bmatrix} 1 \\ 0 \\ 0 \end{bmatrix} \right) \begin{bmatrix} 1 \\ 0 \\ 0 \end{bmatrix} - \mathcal{R}^T\, \mathcal{R}_f^T \begin{bmatrix} 0 \\ 0 \\ 1 \end{bmatrix} \right\}$$

donde:

$$\mathcal{R}_f = \begin{bmatrix} \cos f & \sin f & 0 \\ -\sin f & \cos f & 0 \\ 0 & 0 & 1 \end{bmatrix}$$

En la Figura 2, se muestran los resultados obtenidos para una carga del asteroide de 10^9 C para diferentes hipérbolas iniciales y diferentes inclinaciones. La máxima desviación en el módulo del b-vector corresponde a las inclinaciones más bajas. A pesar de la enorme carga eléctrica, los efectos en el vector $\vec{\boldsymbol{B}}$ son del orden del milímetro. Un cálculo estimativo proporciona una primera aproximación al valor del potencial eléctrico necesario para conseguir dicha carga en el asteroide: $Q = C\, V$ donde C es su capacitancia y V su potencial eléctrico. La capacitancia de una esfera es $C = 4\, \pi\, \varepsilon_0\, r$ y por tanto:

$$V = \frac{Q}{4\, \pi\, \varepsilon_0\, r}$$

Para obtener $Q = 10^9$ C, el potencial eléctrico debe ser del orden de $V \sim 10^{17}$ kV. La potencia necesaria para mantener dicha diferencia de potencial en la superficie del asteroide es inviable, independientemente del método utilizado para estimar la corriente de especies repelidas o de las partículas emitidas [2].

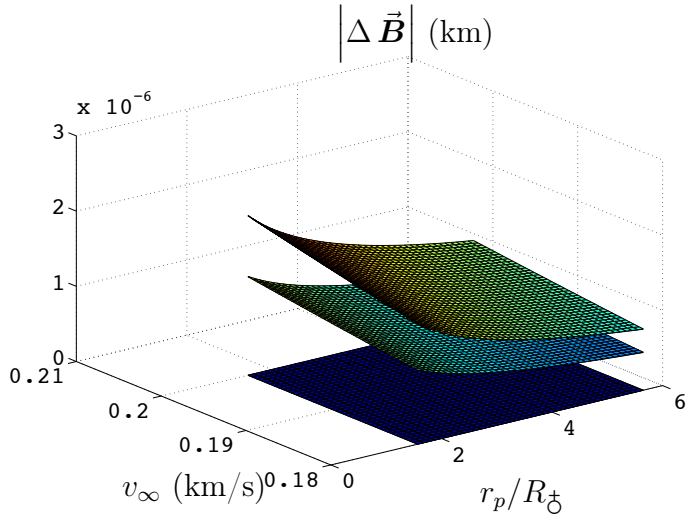

Figura 2.— Variación del b-vector cuando la fuerza electrostática actúa sobre el asteroide. Carga del asteroide: 10^9 C. Los resultados se presentan para distintas hipérbolas e inclinaciones iniciales.

4. Modelo de la fuerza electrodinámica

El modelo de la fuerza electrodinámica es necesario para estimar el efecto de un tether electrodinámico que actúa sobre un asteroide. No se estudia en detalle el modo de unión del cable al asteroide. El objetivo de esta sección es la de proporcionar una primera aproximación de las aceleraciones de perturbación que podrían obtenerse si la totalidad de la fuerza electrodinámica generada en el cable pudiese aplicarse directamente en el centro de masas del asteroide.

La fuerza elecrtodinámica que actúa en un elemento de cable, F_{ed}^{ds}, puede escribirse como:

$$\vec{\boldsymbol{F}}_{ed}^{ds} = I(s, \vec{\boldsymbol{r}}, \vec{\boldsymbol{v}}, \vec{\boldsymbol{q}}, \dot{\vec{\boldsymbol{q}}})\, \vec{\boldsymbol{u}}(\vec{\boldsymbol{q}}) \times \vec{\boldsymbol{B}}_{Mg}(s, \vec{\boldsymbol{r}})$$

donde $I(s, \vec{\boldsymbol{r}}, \vec{\boldsymbol{v}}, \vec{\boldsymbol{q}}, \dot{\vec{\boldsymbol{q}}})$ es la corriente a lo largo del cable, $\vec{\boldsymbol{B}}_{Mg}(s, \vec{\boldsymbol{r}})$ es el campo magnético en el elemento de cable, s es la variable a lo largo del tether y $\vec{\boldsymbol{r}}, \vec{\boldsymbol{v}}, \vec{\boldsymbol{q}}, \dot{\vec{\boldsymbol{q}}}$ es el estado del sistema. Para simplificar esta expresión, se han realizado algunas hipótesis:

- Tanto el campo magnético y la velocidad no varían a lo largo del cable: $\vec{\boldsymbol{B}}_{Mg}(s, \vec{\boldsymbol{r}}) \approx \vec{\boldsymbol{B}}_{Mg}(\vec{\boldsymbol{r}})$, $\vec{\boldsymbol{v}}(s, \vec{\boldsymbol{r}}) \approx \vec{\boldsymbol{v}}(\vec{\boldsymbol{r}})$.
- El vector unitario en la dirección del cátodo al ánodo, $\vec{\boldsymbol{u}}$, apunta siempre al origen del sistema de referencia psedudo-inercial. Por lo tanto, $\vec{\boldsymbol{u}} = \hat{\vec{\boldsymbol{r}}}$.

- La intensidad a lo largo del cable se calcula como la media de la intensidad en un instante dado: $L_t\, I_{av}(\vec{\boldsymbol{r}}, \vec{\boldsymbol{v}}, \vec{\boldsymbol{u}}) = \int_{s_0}^{s_f} I(\xi, \vec{\boldsymbol{r}}, \vec{\boldsymbol{v}}, \vec{\boldsymbol{u}})\, d\,\xi$.

- El campo magnético se define como en el apartado anterior:
$\vec{\boldsymbol{B}}_{Mg} = \frac{\mu_m\, R_\oplus^3}{r^3} \left(3\,(\hat{m}\cdot\hat{r})\;\hat{r} - \hat{m}\right)$

Por consiguiente, la fuerza de Lorentz se escribe como:

$$\vec{\boldsymbol{F}}_{ed}\Big|_{OPC} = L_t\, I_{av} \left(\{1,0,0\}^T \times \vec{\boldsymbol{B}}_{Mg}\Big|_{OPC}\right)$$

El parámetro $L_t\, I_{av}$ puede utilizarse para estimar el efecto de las fuerzas electrodinámicas en la deflexión del asteroide. No obstante, también es posible establecer un modelo que permita estimar la intensidad media a lo largo del cable como función del estado del sistema y de los parámetros ambientales. En este trabajo, usaremos el modelo del régimen OML (orbital-motion-limited) como se define en [5]:

$$I_{av,OML}(\vec{\boldsymbol{r}}, \vec{\boldsymbol{v}}, \phi) = \frac{2}{5}\, e\, N_\infty\, \frac{L_t\, p}{\pi} \sqrt{\frac{2\, e\, E_m\, L_t}{m_e}}$$

donde

$$E_m = \vec{\boldsymbol{u}} \cdot [(\vec{\boldsymbol{v}} - \vec{\boldsymbol{v}}_{pl}) \times \vec{\boldsymbol{B}}_{Mg}] = \{1,0,0\}^T \cdot \left[\left(\vec{\boldsymbol{v}}|_{OPC} - \mathcal{R}^T\, \mathcal{R}_f^T\; \{1,0,0\}^T\right) \times \vec{\boldsymbol{B}}_{Mg}\Big|_{OPC}\right]$$

es el campo electromotriz, e es la carga del electrón, N_∞ es la densidad de plasma, m_e es la masa del electrón y p es el perímetro de la sección transversal del cable. Hay que hacer notar que la utilización del OML en este escenario no se ajusta completamente a las condiciones en las que la expresión de la intensidad OML ha sido obtenida. En particular, la distribución de velocidad del viento solar no sigue una distribución maxwellliana [6].

En la Figura 3, se presentan los resultados obtenidos para una tether de 100 km de longitud con una corriente de 1 A a lo largo del mismo. En tal caso, la variación del módulo del b-vector es del orden de kilómetros, correspondiendo los mejores resultados a órbitas de baja inclinación. Los valores de deflexión son próximos a los obtenidos con estrategias impulsivas óptimas [4]. No obstante, se ha de evaluar si es factible tener una intensidad media de 1 A durante el fly-by. Utilizando los siguientes valores:

- Velocidad del plasma a 1 AU: $v_{pl} = 500$ km/s [3].

- Densidad electrónica de plasma a 1 AU: $N_\infty = 3 \cdot 10^6\,\mathrm{m}^{-3}$ [7].

- Campo magnético terrestre en el pericentro: $B_{Mg} = 2.5\ 10^{-7}$ T.

y la expresión para la intensidad media en el régimen OML, obtenemos una expresión que relaciona la longitud del cable y el perímetro de su sección transversal:

$$L_t^{3/2}\, p \approx 8 \cdot 10^7 \quad \mathrm{m}^{5/2}$$

Suponiendo que p es del orden de centímetros, la longitud necesaria para lograr una corriente de 1 A durante el fly-by resulta ser $L_t \sim 4 \cdot 10^3$ km. Esta longitud es, a priori, inviable desde un punto de vista práctico.

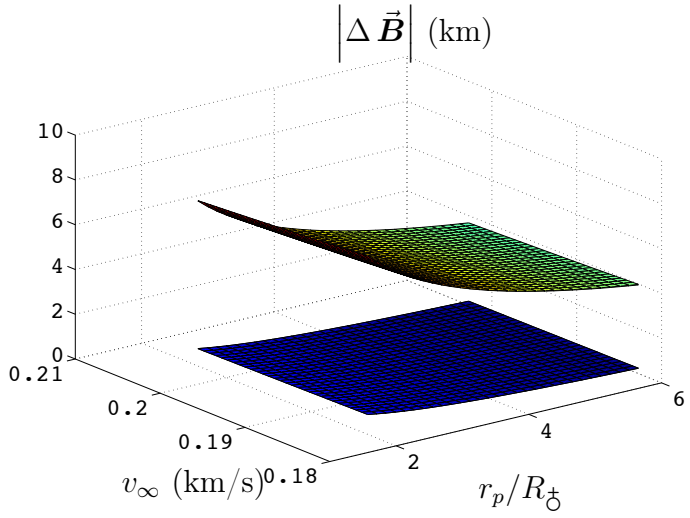

Figura 3.— Variación del b-vector cuando actúan fuerzas electrodinámicas sobre el asteroide. Intensidad en el tether 1 A. Los resultados se presentan para distintas hipérbolas e inclinaciones iniciales.

5. Cambio en momento angular haciendo uso de cables electrodinámicos

En trabajos anteriores se ha señalado la relevancia de la alteración en el estado dinámico de rotación de los asteroides durante un fly-by [8, 9]. Este fenómeno depende del coeficiente gravitatorio C_{22} del asteroide, relacionado con su elipticidad ecuatorial [10]. Este efecto natural puede conducir a la ruptura o reforma del asteroide bajo la acción de momentos gravitatorios. Además, la variación del estado rotacional del asteroide cambiará la subsiguiente aceleración de Yarkovsky que sufrirá durante el movimiento heliocéntrico.

En este apartado se estudia la posibilidad de potenciar este proceso haciendo uso de cables electrodinámicos. La contribución de estos dispositivos al cambio en el momento angular del asteroide presenta una doble vertiente. En primer lugar, modifican la forma del cuerpo y, en consecuencia, su coeficiente C_{22}. Por otra parte, pueden proporcionar un momento debido a la presencia de fuerzas electrodinámicas.

Para estimar la importancia de la primera contribución, es necesario calcular la influencia del tether en el coeficiente C_{22}. Se supondrá que el tether y el asteroide se encuentran rígidamente unidos de manera que ambos constituyen un único sólido rígido. Dentro de la validez de esta aproximación, la expressión del coeficiente recogida en [11] es válida:

$$C_{22} = \frac{A - B}{4\, M_a}$$

donde A y B son los momentos de inercia del cuerpo alrededor de los ejes Ox y Oy en el sistema de refernecia principal del cuerpo. Si la configuración relativa de tether y asteroide es tal que el tether se encuentra en el eje y del sistema de referencia fijado al cuerpo, el nuevo momento de inertia puede calcularse como: $A^{'} = A + A_t$, siendo A_t el momento de inercia del cable respecto al eje Ox. Llamando d a la distancia entre el centro de masas del asteroide [3] y el punto de unión del cable en la superficie del asteroide, asumiendo que la masa del cable se concentra en sus dos extremos y que ambas masas extremas son iguales, el valor de A_t será:

$$A_t = \frac{1}{2}\, m_t\, L_t^2 \left[1 + 2\,\frac{d}{L_t} + 2\,\left(\frac{d}{L_t}\right)^2\right]$$

Por tanto, la variación del coeficiente gravitatorio se puede expresar como:

$$\Delta\, C_{22} = \frac{m_t\, L_t^2}{8\, M_a} \left[1 + 2\,\frac{d}{L_t} + 2\,\left(\frac{d}{L_t}\right)^2\right] \tag{13}$$

Por otra parte, el efecto de las fuerzas electrodinámicas puede medirse por el cambio en el momento angular del asteroide. En este estudio preliminar, la naturaleza de la unión no se discute en detalle. Como anteriormente, se supone que el tether actúa como parte de un sólido rígido compuesto por asteroide y cable. Por consiguiente, la contribución en el cambio de $\vec{\boldsymbol{H}}$ debido a las fuerzas electrodinámicas será:

$$\frac{d\,\vec{\boldsymbol{H}}}{d\,t} = \vec{\boldsymbol{M}}_{ed}$$

A su vez, el momento electrodinámico debido a la fuerza de Lorentz actuando a lo largo del tether puede calcularse como:

$$\vec{\boldsymbol{M}}_{ed} = \int_{\Omega} \left(\left(\vec{\boldsymbol{\rho}}_{G,t} + s\,\vec{\boldsymbol{u}}\right) \times \vec{\boldsymbol{F}}_{ed}^{ds}\right)\, ds$$

donde Ω es el volumen del cable y $\vec{\boldsymbol{\rho}}_{G,t}$ es el radio vector desde el centro de masas del asteroide al centro de masas del tether. Se tendrá en cuenta la anterior definición de las fuerzas electrodinámicas:

$$\vec{\boldsymbol{F}}_{ed}^{ds} = I(s, \vec{\boldsymbol{r}}, \vec{\boldsymbol{v}}, \vec{\boldsymbol{q}}, \dot{\vec{\boldsymbol{q}}})\, \vec{\boldsymbol{u}}(\vec{\boldsymbol{q}}) \times \vec{\boldsymbol{B}}(s, \vec{\boldsymbol{r}})$$

Utilizando las siguientes hipótesis para simplificar la anterior expresión:

- El campo magnético y la velocidad no varían a lo largo del cable: $\vec{\boldsymbol{B}}(s, \vec{\boldsymbol{r}}) \approx \vec{\boldsymbol{B}}(\vec{\boldsymbol{r}})$, $\vec{\boldsymbol{v}}(s, \vec{\boldsymbol{r}}) \approx \vec{\boldsymbol{v}}(\vec{\boldsymbol{r}})$.
- El vector unitario $\vec{\boldsymbol{u}}$ no varía a lo largo del cable.

[3] Se supone de manera implícita que la posición del centro de masas no varía debido a la presencia del tether.

obtenemos:

$$\vec{\boldsymbol{M}}_{ed} = \vec{\boldsymbol{r}}_{G,t} \times \left(\vec{\boldsymbol{u}} \times \vec{\boldsymbol{B}}\right) \int_{\Omega} I\, ds + \vec{\boldsymbol{u}} \times \left(\vec{\boldsymbol{u}} \times \vec{\boldsymbol{B}}\right) \int_{\Omega} s\, I\, ds$$

Además, se tendrá en cuenta el valor medio de las integrales a lo largo del cable en cada instante:

$$L_t\, I_{av} = \int_{\Omega} I\, ds \qquad L_t^2\, I_{m1} = \int_{\Omega} s\, I\, ds$$

Por último, si el tether se despliega de modo que su dirección $\vec{\boldsymbol{u}}$ es coincidente con la dirección del radio vector que conecta los centros de masas de tether y asteroide, tendremos:

$$\vec{\boldsymbol{\rho}}_{G,t} = D\, \vec{\boldsymbol{u}}$$

siendo D la distancia entre ambos centros de masas. Para un tether homogéneo con masas extremas iguales unido a la superficie del asteroide: $D = L_t/2 + d$, donde d es la distancia desde el centro de masas del asteroide al punto de unión. Estas consideraciones conducen a:

$$\vec{\boldsymbol{M}}_{ed} = L_t^2\, I_{av} \left(\frac{1}{2} + \frac{d}{L_t} + \frac{I_{m1}}{I_{av}}\right) \vec{\boldsymbol{u}} \times \left(\vec{\boldsymbol{u}} \times \vec{\boldsymbol{B}}\right)$$

Para una intensidad uniforme a lo largo del cable con su centro de masas localizado en el centro del tether, el valor de I_{m1} sería cero. Con hipótesis menos restrictivas, $I_{m1} \neq 0$ pero $I_{m1} \ll I_{av}$. Además, dada la dependencia del momento con la longitud del cable, cuanto más largo sea el cable mayor será el momento alrededor del centro de masas del sistema. Por tanto, consideraremos cables más largos que la distancia d, $L_t \gg d$. De este modo, la expresión del momento resulta ser:

$$\vec{\boldsymbol{M}}_{ed} \approx \frac{1}{2}\, L_t^2\, I_{av}\, \vec{\boldsymbol{u}} \times \left(\vec{\boldsymbol{u}} \times \vec{\boldsymbol{B}}\right) \quad (L_t \gg d)$$

Finalmente, es necesario establecer un modelo para estimar el producto vectorial $\vec{\boldsymbol{u}} \times \left(\vec{\boldsymbol{u}} \times \vec{\boldsymbol{B}}\right)$. Para el campo magnético, consideraremos la descirpción de dipolo alineado con el eje de rotación terrestre. Por otra parte, para la dirección del cable, la hipótesis tenidas en cuenta son:

- El asteroide se encuentra rotando uniformemente alrededor de su eje de máximo momento de inercia.
- El máximo momento de inercia es perpendicular al plano orbital.
- El tether está contenido en un plano perpendicular a la velocidad angular.

Con estas hipótesis restrictivas, se puede calcular una primera aproximación del cambio en momento angular debido al momento de perturbación de las fuerzas electrodinámicas en función de los parámetros L_t y I_{av}. No obstante, parece más interesante comparar la estimación del cambio en momento angular debido a este efecto con el correspondiente a

la modificación de la interacción gravitatoria entre asteroide y Tierra. Basándonos en [8], se puede estimar dicho cambio en momento angular en función del cambio en el coeficiente gravitatorio ΔC_{22} del asteroide. De hecho, tenemos $\Delta H_g \sim \Delta C_{22}\, \mathcal{F}_g(r_p, v_\infty, i, \Omega, \omega)$ para el cambio debido a la interacción gravitatoria y $\Delta H_{ed} \sim (L_t^2\, I_{av})/2\, \mathcal{F}_{eg}(r_p, v_\infty, i, \Omega, \omega)$ para el caso electrodinámico. En la Figura 4, se presenta el ratio

$$\frac{\Delta H_{ed}}{\Delta H_g} \frac{2\,\Delta C_{22}}{L_t^2\, I_{av}} = \frac{\mathcal{F}_g(r_p, v_\infty, i, \Omega, \omega)}{\mathcal{F}_{eg}(r_p, v_\infty, i, \Omega, \omega)}$$

para diferentes fly-bys caracterizados por el radio de periapsis y el exceso de velocidad hiperbólica. Nótese que el ratio tiene dimensiones de 1/A.

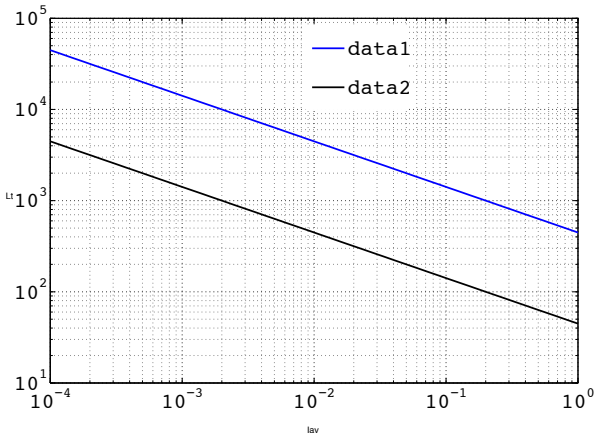

Figura 4.— Ratio entre el cambio en momento angular debido a los efectos gravitatorios y electrodinámicos en función del cambio en el coefficiente ΔC_{22} y los parámetros del tether L_t y I_{av} para distintas inclinaciones.

De estos resultados, podemos deducir el orden de magnitud de los parámetros del tether necesarios para obtener un cambio en momento angular debido a la perturbación electrodinámica del mismo orden que el cambio debido a la perturbación gravitatoria imponiendo $\Delta H_{ed} \sim \Delta H_g$. La condición se expresa

$$\frac{2\,\Delta C_{22}}{L_t^2\, I_{av}} \sim 10^{-7} \quad \frac{1}{\mathrm{A}}$$

para el mejor ratio del momento electrodinámico. Además, teniendo en cuenta (13), puede encontrarse una relación que liga la intensidad en el cable y la masa necesaria para proporcionar un cambio de momento angular del mismo orden para ambas contribuciones.

$$I_{av} \sim \frac{m_t}{4\, M_a}\, 10^7 \text{ A} \tag{14}$$

Nótese que la longitud del cable no aparece de manera explícita en esta relación. De la estimación de la intensidaddel régimen OML, tenemos $I_{av} \sim L_t^{3/2}\, p\, 10^{-7}/8$ A. Considerando

un perímetro del orden de centímetros $p \sim 10^{-2}$ m, y usando una densidad linear para el cable de [4] $\rho_l = m_t/L_t$, la intesidad media OML toma la forma:

$$I_{av} \sim \frac{m_t\sqrt{L_t}}{8\,\rho_l}\,10^{-9}\ \mathrm{A}$$

Y sustituyendo estos resultados en la relación anterior (14), podemos obtener la longitud de tether necesaria para la cual las contribuciones al cambio en momento angular de los efectos electrodinámicos y gravitatorios son del mismo orden de magnitud:

$$L_t \sim \sqrt{\frac{2\,\rho_l}{M_a}}\,10^8\,\mathrm{m}$$

Para un cable de aluminio ($\rho_l \sim 2{,}7 \cdot 10^{-1}$ kg/m) unido a Apophis ($M_a \sim 4{,}6 \cdot 10^{10}$ kg), la longitud de cable que proporcionaría el mismo cambio en momento angular debido al momento electrodinámico y como consecuencia del cambio en la forma del cuerpo será de: $L_t \sim 350$ m. Se puede, por tanto, concluir que la presencia de tethers electrodinámicos largos será más significativa debido al momento electrodinámico, aunque el modelo de colección de corriente acarrea una incertidumbre en las estimaciones anteriores.

Por último, exploramos el cambio en velocidad angular producido por la modificación de la interacción gravitatoria debido a la presencia del cable. El máximo cambio en velocidad angular en un fly-by ecuatorial puede estimarse [8] como:

$$\Delta\,\Omega_z \sim \Omega_H\,\frac{e^2-1}{e^2}$$

donde Ω_H se define como sigue:

$$\Omega_H = 2\,\frac{\nu}{1+\nu}\,\frac{C_{22}}{(I_z/M_a)}\,\frac{v_\infty}{r_p\,(1+r_p\,v_\infty/\mu)}$$

siendo $\nu = M_{\overset{+}{\circlearrowleft}}/M_a$. Cuando el tether es parte del cuerpo, los coeficientes del asteroide varían, así como Ω_H:

$$\Omega_H^{'} = 2\,\frac{\nu}{1+\nu}\,\frac{C_{22}+\Delta\,C_{22}}{((I_z+\Delta\,I_z)/(M_a+m_t))}\,\frac{v_\infty}{r_p\,(1+r_p\,v_\infty/\mu)}$$

Suponiendo $\Delta\,C_{22}/C_{22} \ll 1$, $\Delta\,I_z/I_z \ll 1$ y $m_t/M_a \ll 1$, podemos calcular las variaciones de primer orden en Ω_H, obteniendo:

$$\Omega_H^{'} = \Omega_H\left(1+\frac{m_t}{M_a}+\frac{\Delta\,C_{22}}{C_{22}}-\frac{\Delta\,I_z}{I_z}\right)$$

Modelando el asteroide como un elipsoide triaxial [12], cuyo ancho, longitud y altura serán a,b, c, permite reescribir la relación anterior como una función de los parámetros del asteroide y del tether:

$$\Omega_H^{'} = \Omega_H\left[1+\frac{m_t}{M_a}\left(1+\frac{5}{2}\left(\frac{L_t}{a}\right)^2\left(\frac{1}{(b/a)^4-1}\right)\right)\right]$$

[4] Se supone que el tether es homogéneo y de sección transversal constante.

Por lo tanto, el ratio entre el cambo de velocidad angular debido a la interacción gravitacional con y sin tether se convierte en:

$$\frac{\Delta\,\Omega^{'}}{\Delta\,\Omega} \sim 1 + \frac{m_t}{M_a}\left(1 + \frac{5}{2}\left(\frac{L_t}{a}\right)^2\left(\frac{1}{(b/a)^4 - 1}\right)\right)$$

Utilizando los resultados y el modelo de elipsoide del asteroide recogidos en [12], se puede expresar la anterior relación en términos del cambio del periodo rotacional. Considerando los casos que proporcionan un mayor cambio del periodo, el ratio con y sin tether puede establecerse como:

$$\frac{\Delta\,P'}{\Delta\,P} \sim \frac{1 - \frac{m_t}{M_a}\left[\frac{2}{5} + \left(\frac{L_t}{a}\right)^2\left(\frac{1}{(b/a)^4-1}\right)\right]}{1 + \frac{m_t}{6\,M_a}\left[\frac{2}{5} + \left(\frac{L_t}{a}\right)^2\left(\frac{1}{(b/a)^4-1}\right)\right]}$$

El cambio relativo en el periodo rotacional después de la maniobra se muestra en la Figura 5 en fución del ratio L_t/a. El efecto de la presencia del tether en la interacción gravitacional es perceptible para valores de L_t/a mayores que 10^3. En el caso de Apophis esto se traduce en longitudes de tethers del orden de kilómetros. Además, del análisis anterior se espera que la importancia del momento electrodinámico en esa situación será mayor que la interacción gravitacional. Como conclusión, es posible afirmar que los tethers elctrodinámicos con longitudes del orden de miles de kilómetros alterarán el estado rotacional del asteroide de manera apreciable.

Por lo tanto, el ratio entre el cambio en la velocidad angular debido a la interación gravitacional con y sin tethers pasa a ser:

$$\frac{\Delta\,\Omega^{'}}{\Delta\,\Omega} \sim 1 + \frac{3\,\rho_l}{4\,\pi\,\rho_v\,b\,c}\left(\frac{L_t}{a}\right)\left(1 + \frac{5}{2}\left(\frac{L_t}{a}\right)^2\left(\frac{1}{(b/a)^4 - 1}\right)\right)$$

donde ρ_v es la densidad volumétrica del asteroide. Asumiendo que el cambio de velocidad angular es pequeño con respecto a la velocidad angular inicial $\Delta\Omega/\Omega \ll 1$ y que la contribución del tether a ese cambio es pequeÃśa $\Delta\Omega^{'}/\Delta\Omega = 1 + \mathcal{O}(1)$, el ratio de los periodos rotacionales tiene la misma forma que el correspondiente ratio de velocidades angulares.

6. Conclusiones

En este documento, se desarrolla un método para analizar el efecto de las técnicas de deflexión durante un fly-bys de un asteroide a la Tierra. Dicho método permite estimar la variación de la óbita de un asteroide como función de la estrategia seguida para efectuar la deflexión. Se ha confirmado que pequeñas fuerzas actuando durante el fly-by no provocan grandes cambios en la órbita del asteroide, ya que el lapso de tiempo es pequeño. No obstante, las características específicas de la órbita hiperbólica alrededor del cuerpo principal

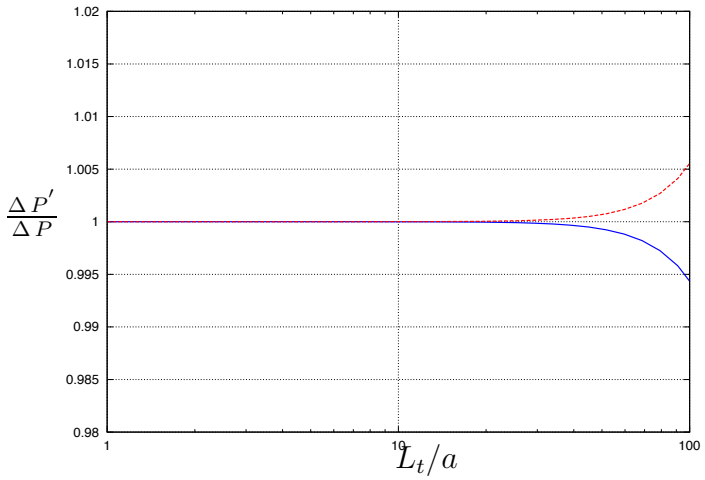

Figura 5.— Ratio entre la cariación del período rotacional debido a la interacción gravitatoria con y sin tether en función de la relación L_t/a.

pueden ser explotadas para producir un cambio significativo en la subsiguiente órbita del asteroide. En particular, la posibilidad de cambiar la orientación del plano orbital por medio de una maniobra impulsiva parece factible incluso con velocidades de impacto no excesivas.

Asimismo, se han estudiado las potenciales interacciones del asteroide con el campo magnético terrestre. Cuando ambas fuerzas, la electroestática y la electrodinámica, son pequeñas, los resultados son similares a los obtenidos para un empuje continuo pequeño. De hecho, para obtener incluso pequeñas fuerzas, es necesario cargar el asteroide o proporcionar una corriente que no es, en principio, viable. Estos resultados establecen la baja importancia del efecto magnético en la trajectoria de los asteroides.

Finalmente, se analiza el efecto de un tether electrodinámico en la dinámica rotacional de un asteriode. En anteriores trabajos se indica la relevancia del estado rotacional del asteroide en la trajectora. A diferencia de lo que ocurre en la dinámica del CM, fuerzas pequeñas actuando a gran distancia del CM pueden provocar un importante momento y jugar un papel significativo en el cambio del momento angular del asteriode. Además, a medida que el tether modifica la forma del cuerpo, puede aumentar la interacción gravitacional entre el primario y el asteroide, siendo ambos efectos simultáneos.

Referencias

[1] D. Fargion. Asteroid Deflection: How, Where and When? *Chinese Journal of Astronomy and Astrophysics Supplement*, 8:399–411, October 2008.

[2] N. Murdoch, D. Izzo, C. Bombardelli, I. Carnelli, A. Hilgers, and D. Rodgers. Electrostatic Tractor for Near Earth Object Deflection. In *Proceedings of the 59th International Astronautical Congress*, number Paper IAC-08-A3.I.5, 2008.

[3] D. Steel. Electromagnetic perturbations of the orbits of asteroids. In B. Warmbein, editor, *Asteroids, Comets, and Meteors: ACM 2002*, volume 500 of *ESA Special Publication*, pages 433–436, November 2002.

[4] D. Izzo, A. Bourdoux, R. Walker, and F. Ongaro. Optimal trajectories for the impulsive deflection of near earth objects. *Acta Astronautica*, 59:294–300, July 2006.

[5] J.R. Sanmartín, M.Martínez-Sánchez, and E. Ahedo. Bare Wire Anodes for Electrodynamic Tethers. *Journal of Propulsion and Power*, 9(3):353–360, MayJune 1993.

[6] W. G. Pilipp, K.-H. Muehlhaeuser, H. Miggenrieder, M. D. Montgomery, and H. Rosenbauer. Characteristics of electron velocity distribution functions in the solar wind derived from the HELIOS plasma experiment. *Journal of Geophysical Research*, 92:1075–1092, February 1987.

[7] N. Meyer-Vernet. *Basics of the Solar Wind*. Cambridge University Press, 2007.

[8] D. J. Scheeres, S. J. Ostro, R. A. Werner, E. Asphaug, and R. S. Hudson. Effects of Gravitational Interactions on Asteroid Spin States. *Icarus*, 147:106–118, September 2000.

[9] D. J. Scheeres. Changes in Rotational Angular Momentum due to Gravitational Interactions between Two Finite Bodies. *Celestial Mechanics and Dynamical Astronomy*, 81:39–44, 2001.

[10] D. J. Scheeres. The Effect of C22 on Orbit Energy and Angular Momentum. *Celestial Mechanics and Dynamical Astronomy*, 73:339–348, January 1999.

[11] A. E. Roy. *Orbital motion*. 2005.

[12] D. J. Scheeres, L. A. M. Benner, S. J. Ostro, A. Rossi, F. Marzari, and P. Washabaugh. Abrupt alteration of Asteroid 2004 MN4's spin state during its 2029 Earth flyby. *Icarus*, 178:281–283, November 2005.

Monografías de la Real Academia de Ciencias de Zaragoza **35**, 119–133, (2011).

Un modelo sencillo para el estudio del movimiento orbital alrededor de planetas con anillos

E. Tresaco[1,2], A. Elipe[1,2] and A. Riaguas[3]

[1]Grupo de Mecánica Espacial-IUMA. Universidad de Zaragoza, 50009 Zaragoza, Spain

[2]Centro Universitario de la Defensa de Zaragoza. 50090 Zaragoza, Spain

[3]Universidad de Valladolid, 42004 Soria Spain

Resumen

En este artículo presentamos el análisis de la dinámica global de una partícula que se encuentra orbitando una corona circular plana, este trabajo se planteó con idea de extender los estudios que encontramos en la literatura donde se aproxima un anillo planetario por una sucesión finita de partículas o por un anillo continuo sin grosor. Además se extiende nuestro modelo del disco anular al caso de tener un planeta achatado rodeado por la corona circular, con objetivo de ir añadiendo cada vez mayor complejidad al sistema para obtener un modelo más preciso de la dinámica alrededor de planetas con anillos tipo Saturno.

1. Introducción

El objetivo de este trabajo es extender los estudios previos sobre la dinámica de una partícula que orbita alrededor de un anillo, donde el anillo se considera o bien formado por una sucesión finita de partículas, o por un cable circular sin grosor, al caso de una corona circular plana. Aproximando así de forma más precisa la realidad de los anillos que podemos encontrar en los planetas de nuestro Sistema, como los de Saturno, que se extienden cientos de kilómetros alrededor del cuerpo. Extender a este nuevo modelo, aunque sencillo en su planteamiento, conlleva bastantes dificultades en el tratamiento de las expresiones que describen este potencial, que incluyen distintas especies de integrales elípticas. Encontramos en la literatura un par de trabajos de Krough, Ng y Snynder [13], y Lass y Blitzer [14], en los que se dan expresiones matemáticamente correctas para estas funciones pero que no sirven para su evaluación numérica por las singularidades existentes.

Por tanto, en una primera parte del trabajo hemos estudiado el potencial creado por la corona circular mediante el análisis de sus propiedades y el trabajo con las funciones elípticas, lo que nos ha permitido reescribir las complejas expresiones de la función potencial de manera que obtenemos una correcta evaluación numérica del mismo, y de sus derivadas sucesivas necesarias para el cómputo de órbitas periódicas.

Posteriormente se presenta el estudio de la dinámica de una partícula orbitando la corona, para ello realizamos un primer análisis de los equilibrios del sistema, para posteriormente calcular las semillas de órbitas periódicas y la continuación de las familias a las que pertenecen. Para estos cómputos numéricos se han desarrollado distintas herramientas, para el cálculo de las condiciones iniciales de las órbitas usamos un programa de representación de Secciones de Poincaré, y el programa *Zeros* basado en el uso de estrategias de evolución para la minimización de funciones [1]. Para el cálculo de las familias periódicas usamos el método de continuación basado en el algoritmos de Henrard y Deprit [8], y el método de continuación de mapas de Poincaré [18]. Además estos métodos nos dan información sobre la estabilidad lineal de las familias de órbitas obteniendo de esta manera una descripción global de la dinámica alrededor de la corona.

Por último, se hace una extensión de estos resultados a un modelo más realista, en que vamos a considerar un planeta circular rodeado por una corona circular plana. Detallando los cambios en la dinámica que se obtienen al incluir un cuerpo central. Además se estudia como afectaría el considerar un coeficiente de achatamiento para el planeta, y una partición de la corona en dos más pequeñas con un hueco entre ambas. Para el modelo de planeta achatado con corona, se presenta un análisis previo de las familias de órbitas periódicas encontradas, incluyendo órbitas en el espacio, que se encuentran por resonancias entre la velocidad orbital de la partícula en el plano meridional y la velocidad de rotación de este plano.

Así encontramos y describimos la evolución de un gran número de órbitas periódicas, que nos sirven para ilustrar estructuras relevantes en el espacio de fases y sus implicaciones. Estos modelos matemáticos relativamente sencillos constituyen una primera aproximación para posteriores estudios de sistemas dinámicos más complejos, ya que las conclusiones que podemos extraer de la estructura de su espacio fásico son genéricas, y por tanto de interés en el contexto de modelos que se ajusten de manera más fiel a la realidad física del problema.

2. Descripción del problema

Consideramos un disco masivo plano, es decir una lámina circular sin grosor y con distribución uniforme de masa sobre el plano ecuatorial de un sistema Cartesiano de coordenadas $Oxyz$, y centrado en el origen. El potencial creado por este cuerpo se puede

obtener directamente de su definición, resolviendo una integral de superficie con integrando el inverso de las distancias al punto donde queremos computar el potencial, o también como una cuadratura sobre anillos circulares de radios incrementales. El desarrollo en detalle de los pasos realizados para obtener la expresión de este potencial se puede encontrar en el artículo [9].

Una vez tenemos la fórmula que describe el potencial de un disco plano, obtenemos la expresión del potencial creado por una corona plana circular de radios a y b como resultado de restar dos discos concéntricos de radios $b < a$,

$$U(x, y, z; a, b) = U(x, y, z; a) - U(x, y, z; b), \tag{1}$$

donde $U(x, y, z; a)$ y $U(x, y, z; b)$ son las funciones potenciales creadas por los discos concéntricos. Teniendo en cuenta que ahora la constante de gravitación es $G\sigma = GM/\pi(a^2 - b^2) \equiv \mu/\pi(a^2 - b^2)$.

Es decir, el potencial gravitatorio creado por la corona circular es

$$\begin{aligned} U = \quad & \frac{2\mu}{\pi(a^2-b^2)}\left(-p_a E(k_a) - \frac{a^2-r^2}{p_a}K(k_a) + |z|\left(\frac{\pi}{2} + \frac{\pi}{2}\operatorname{sign}(a-r)\right)\right. \\ & -|z|\operatorname{sign}(a-r)[E(k_a)F(\phi_a, k'_a) + K(k_a)E(\phi_a, k'_a) - K(k_a)F(\phi_a, k'_a)\,] \\ & +p_b E(k_b) + \frac{b^2-r^2}{p_b}K(k_b) - |z|\left(\frac{\pi}{2} + \frac{\pi}{2}\operatorname{sign}(b-r)\right) \\ & \left. + |z|\operatorname{sign}(b-r)[E(k_b)F(\phi_b, k'_b) + K(k_b)E(\phi_b, k'_b) - K(k_b)F(\phi_b, k'_b)\,]\right), \end{aligned} \tag{2}$$

donde hemos introducido las siguientes cantidades

$$\begin{aligned} & r^2 = x^2 + y^2, && R^2 = x^2 + y^2 + z^2, \\ & p_a^2 = (a+r)^2 + z^2, && q_a^2 = (a-r)^2 + z^2, \\ & k_a^2 = 4ar/p_a^2, && k'_a = \sqrt{1-k_a^2}, && \phi_a = \arcsin\frac{|z|}{q_a}, \\ & p_b^2 = (b+r)^2 + z^2, && q_b^2 = (b-r)^2 + z^2, \\ & k_b^2 = 4br/p_b^2, && k'_b = \sqrt{1-k_b^2}, && \phi_b = \arcsin\frac{|z|}{q_b}. \end{aligned}$$

Este potencial es simétrico respecto a los tre ejes Ox, Oy y Oz gracias a la simetría cilíndrica del problema. Una representación de la función potencial para la sección de corte $y = z = 0$ nos muestra la existencia del origen como único punto de equilibrio inestable con sentido físico ya que encontramos otro punto crítico de carácter estable pero localizado dentro de la corona. Notar además que esta expresión del potencial solventa las dificultades de computación encontradas en formulaciones presentadas en anteriores

trabajos, de esta manera podemos proceder a obtener las ecuaciones del movimiento.
La lagrangiana correspondiente al movimiento de la partícula en el espacio atraída por la fuerza gravitatoria de la corona es

$$\mathcal{L} = T + U = \frac{1}{2}(\dot{x}^2 + \dot{y}^2 + \dot{z}^2) + U(x, y, z), \tag{3}$$

donde $U(x, y, z)$ es el potencial anteriormente hallado.
Con todo esto, las ecuaciones de Euler-Lagrange correspondientes a la lagrangiana son

$$\begin{aligned} \ddot{x} &= -U_x, \\ \ddot{y} &= -U_y, \\ \ddot{z} &= -U_z, \end{aligned} \tag{4}$$

donde U_x, U_y, U_z corresponden a las derivadas parciales de la función potencial,

$$\begin{aligned} \ddot{x} &= -\frac{2\mu}{\pi(a^2-b^2)}\frac{x}{r^2}\left(\sqrt{R^2+a^2+2ar}[(1-\frac{1}{2}k_a^2)K(k_a)-E(k_a)]- \right. \\ &\left. \sqrt{R^2+b^2+2br}[(1-\frac{1}{2}k_b^2)K(k_b)-E(k_b)]\right), \\ \ddot{y} &= -\frac{2\mu}{\pi(a^2-b^2)}\frac{y}{r^2}\left(\sqrt{R^2+a^2+2ar}[(1-\frac{1}{2}k_a^2)K(k_a)-E(k_a)]- \right. \\ &\left. \sqrt{R^2+b^2+2br}[(1-\frac{1}{2}k_b^2)K(k_b)-E(k_b)]\right), \\ \ddot{z} &= \frac{\mu}{\pi(a^2-b^2)}\left(\frac{2z}{\sqrt{R^2+a^2+2ar}}K(k_a) - 2\,\mathrm{sign}(z)\left(\frac{\pi}{2}+\frac{\pi}{2}\,\mathrm{sign}(a-r)\right.\right. \\ &\left. -\mathrm{sign}(a-r)[\,(E(k_a)-K(k_a))F(\phi,k_a')+K(k_a)E(\phi,k_a')]\right) \\ &-\frac{2z}{\sqrt{R^2+b^2+2br}}K(k_b) + 2\,\mathrm{sign}(z)\left(\frac{\pi}{2}+\frac{\pi}{2}\,\mathrm{sign}(b-r)\right. \\ &\left.\left. -\ \mathrm{sign}(b-r)[\,(E(k_b)-K(k_b))F(\phi_b,k_b')+K(k_b)E(\phi_b,k_b')]\right)\right). \end{aligned} \tag{5}$$

Debido a la simetría axial del problema, es de esperar la existencia de ciertas integrales que permitan la reducción del mismo. Se observa que la lagrangiana es invariante a rotaciones alrededor del eje Oz, por lo que la proyección sobre este eje del vector momento angular es una integral. En estas circunstancias el uso de coordenadas cilíndricas (r, λ, z) aparece de forma natural. Por tanto la lagrangiana (3) se transformará en

$$\mathcal{L} = \frac{1}{2}(\dot{r}^2 + r^2\dot{\lambda}^2 + \dot{z}^2) + U(r, -, z),$$

como vemos la variable angular λ es cíclica, por lo que su momento conjugado $\Lambda = \partial\mathcal{L}/\partial\dot{\lambda} = r^2\dot{\lambda}$ es una integral del movimiento, y su correspondiente término de la energía cinética lo podemos añadir al potencial U definiendo un potencial efectivo W como

$$W(r,z) = U(r,z) + \frac{\Lambda^2}{2r^2} \tag{6}$$

Así, las ecuaciones del movimiento en coordenadas cilíndricas son

$$\begin{aligned} &\ddot{r} = -\partial W/\partial r = -\partial U/\partial r + \Lambda^2/r^3, \\ &\ddot{z} = -\partial W/\partial z = -\partial U/\partial z, \\ &\mathrm{d}\Lambda/\mathrm{dt} = 0. \end{aligned} \tag{7}$$

El problema ha quedado por tanto reducido a un sistema de dos grados de libertad, basta con integrar el sistema formado por las dos primeras ecuaciones del sistema anterior (7), y posteriormente, mediante la cuadratura

$$\lambda = \int \frac{\Lambda}{\rho^2}\,\mathrm{d}t,$$

obtendremos λ.
Para buscar las soluciones estacionarias, vamos a analizar las ecuaciones del movimiento (7) reducido a dos grados de libertad (r,z). Debido a la complejidad de las expresiones al contener integrales elípticas, no podemos resolver analíticamente las ecuaciones de forma general, y por tanto nos vamos a centrar en el estudio de los equilibrios cuando el movimiento se da sobre el plano ecuatorial y sobre el eje Oz.

Antes de comenzar con el estudio de los puntos de equilibrios vamos a obtener una formulación para la expresión del potencial que ejerce una corona circular a la cual le añadimos un cuerpo central con un cierto coeficiente de achatamiento $\varepsilon > 0$.
Consideramos ahora una corona de radios $b < a$ localizada en el plano Oxy de un sistema de referencia inercial y centrada en el origen del sistema, por otra parte introducimos un planeta achatado con centro de masas el origen de coordenadas y tal que su plano ecuatorial normal a los polos coincida con el plano Oxy.
La representación del potencial gravitacional de un planeta de radio ecuatorial α, achatamiento ε y coeficiente gravitatorio $\beta = GM_{bod}$, viene expresado en coordenadas cilíndricas (r,λ,z) como

$$U_{bod} = -\frac{\beta}{R} + \frac{\beta}{R}\left(\frac{\alpha}{r}\right)^2 \varepsilon P_2(z/R) = \beta\left(\frac{1}{r^2} + \varepsilon\frac{3\alpha^2}{2R^4}\right), \tag{8}$$

con $R^2 = r^2 + z^2$.
El nuevo potencial gravitario vendrá dado por la composición de este con el potencial de la corona, obteniendo una función que va a depender de varios parámetros propios del problema, el coeficiente gravitatorio β del planeta y μ de la corona circular, los radios

interior b y exterior a de la corona, y el radio ecuatorial y el achatamiento del planeta α, ε. Antes de estudiar los equilibrios del sistema, vamos a introducir una nueva cantidad, el ratio de masas entre los cuerpos, este parámetro adimensional es el cociente entre los coeficientes gravitatorios de ambos cuerpos, $k = \beta/\mu$.

Para ello multiplicamos nuestro lagrangiano por μ, ya que un cambio de escala en la función lagrangiana no modifica formalmente las ecuaciones del movimiento.

Notar que ambos cuerpos tendrán la misma masa si $k = 1$, mientras que valores de $k < 1$ implicarán que el anillo es más masivo que el planeta, y respectivamente para el cuerpo central si $k > 1$.

De esta manera la nueva función potencial queda definida como

$$U(r, z; k; a; b; \varepsilon; \alpha) = U_{ann}(r, z; a; b) + kU_{bod}(r, z; \varepsilon; \alpha). \tag{9}$$

La figura (1) muestra los cortes de la función potencial $U(r, 0)$ en el caso de una corona con un cuerpo central, y en el caso de partir la corona en dos más pequeñas con un hueco entre ambas, esta representación nos da de forma sencilla información sobre la localización de los equilibrios.

Observamos la existencia de un punto de equilibrio de carácter estable sobre la corona,

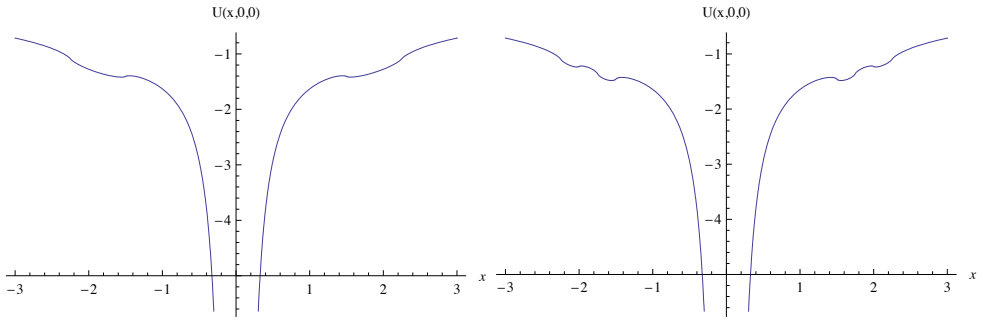

Figura 1.— Representación del corte de la función $U(r, 0)$ para el modelo corona + anillo, y dos coronas + anillo respectivamente.

este punto no es un equilibrio aislado si no una sucesión de puntos, puesto que gracias a la simetría cilíndrica del problema lo que tenemos es toda una circunferencia de equilibrios a una cierta distacia r tal que $b < r < a$. Por otra parte el origen que encontrábamos para la corona simple como punto crítico inestable desaparece ahora al introducir un planeta centrado en el origen de coordenadas.

3. Estudio de los equilibrios

La existencia de las integrales elípticas de primera, segunda y tercera especie, completas e incompletas nos imposibilita obtener expresiones analíticas de los equilibrios. Por

ello nos centramos en la restricción del movimiento al plano ecuatorial Oxy y sobre el eje Oz.

Respecto al movimiento con $r = 0$, si particularizamos las ecuaciones del movimiento para el caso de la corona (Eq. 5) veremos fácilmente que el único punto de equilibrio que aparece corresponde a $z = 0$ o al caso en que ambos radios coinciden $a = b$ y por tanto estaríamos en el problema del anillo circular. La energía en el origen es $E^* = -2\mu/(a+b)$, y por tanto sólo para valores de la energía $E^* < E < 0$ vamos a encontrar órbitas periódicas.

En cuanto al movimiento sobre el plano ecuatorial, las soluciones estacionarias serán los puntos críticos del potencial efectivo que ahora es una función radial

$$W'(r) \equiv \partial W/\partial r = U'(r) - \frac{\Lambda^2}{r^3} = 0. \tag{10}$$

La Figura (2) muestra la derivada del potencial efectivo tanto para la corona como para la corona con un cuerpo central esférico en su interior, para la representación de esta gráfica y posteriores vamos a fijar unos valores de las constates del problema, consideraremos una corona de radios $a = 2.25$ y $b = 1.5$, y un planeta de radio $\alpha = 1$ con un ratio de masas entre los cuerpos de $k = 1$. En ambas gráficas se presenta $W'(r)$ para distintos valores del momento angular. En ellas observamos que en el caso de la corona aislada, obtenemos siempre un punto crítico de carácter estable perteneciente a la corona $b < r < a$, mientras que en la región interior de la corona $r < b$ sólamente encontramos órbitas que parten y mueren en ella para momento angular no nulo, mientras que para $\Lambda = 0$ aparece el orígen como punto crítico estable, este equilibrio corresponde a las oscilaciones periódicas sobre el eje Oz. Respecto a la región exterior a la corona $r > a$ vemos que el comportamiento varía según el valor de Λ, para momento angular nulo y hasta un cierto valor del mismo sólo encontramos órbitas de escape, sin embargo al ir incrementando Λ nos aparece claramente un punto crítico estable, e intuimos la existencia de otro inestable para valores de r cercanos al radio exterior a. Esto también lo podríamos haber observado mediante la representación de sus diagramas de flujo.
En resumen, en el exterior de la corona observamos la existencia de un valor $\widetilde{\Lambda}$ dependiente de las constantes del problema, tal que para valores $\Lambda < \widetilde{\Lambda}$ no existen puntos críticos, mientras que para valores mayores el potencial efectivo tiene al menos un máximo y un mínimo local, que corresponden a soluciones circulares inestable y estable del problema.

La gráfica derecha de la Figura (2) muestra la derivada del potencial efectivo para el caso de un planeta esférico rodeado por una corona. Observamos idéntico comportamiento en cuanto al movimiento dentro y en el exterior de la corona, mientras que en el interior, la existencia de cuerpo central esférico nos permite obtener ningn o un par de equilibrios,

de nuevo dependiendo del valor del momento angular.

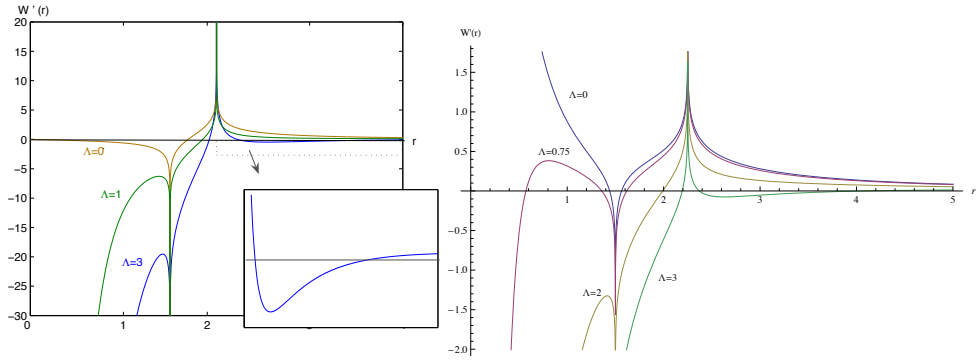

Figura 2.— Puntos críticos del potencial efectivo para distintos valores de Λ en el problema de la corona y de la corona más cuerpo central esférico.

Si consideramos un coeficiente de achatamiento $\varepsilon > 0$ los límites cuando r tiende a 0 cambian modificando únicamente la dinámica en el interior de la corona, ver Figura (3), de manera que ahora obtenemos además del par de equilibrios estable e inestable que veíamos para $\varepsilon = 0$, un nuevo punto crítico de carácter inestable muy próximo a $r = 0$, reseñar que no hemos encontrado ningún set de constantes del problema tal que este punto esté localizado fuera del planeta y por tanto tenga sentido físico. Por último en la gráfica derecha de la Figura (3) está representada la derivada del potencial efectivo en caso de un modelo de planeta esférico más corona, donde hemos partido la corona en dos más pequeñas con un hueco entre ambas. En este caso podemos ver la existencia de un nuevo equilibrio inestable en el agujero comprendido entre las coronas, este punto crítico va a ser único, no va a existir ningún valor del momento angular que modifique el comportamiento en esta región como pasaba en el exterior e interior de la corona.

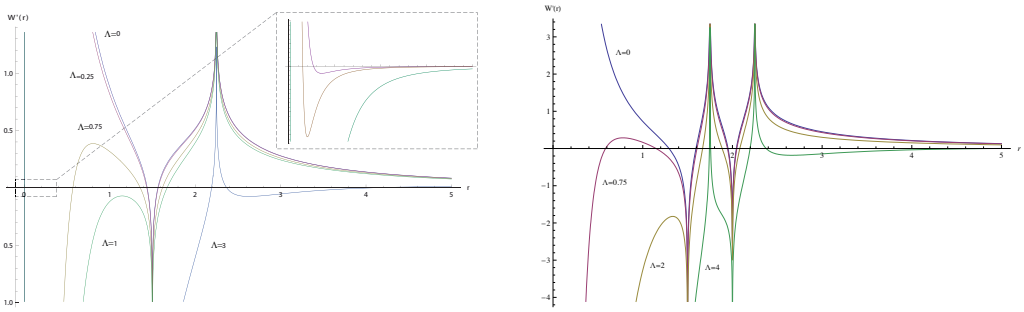

Figura 3.— Derivada del potencial efectivo para distintos valores de Λ en el problema de la corona más cuerpo central achatado y en caso de dos coronas más cuerpo central esférico.

Los puntos estacionarios serán soluciones circulares del problema completo (r, λ, z), es decir, los puntos críticos r_0 del potencial efectivo para valores del momento angular $\Lambda \neq 0$ corresponderán a soluciones circulares en el plano ecuatorial, $(r_0 \cos(\Lambda t/{r_0}^2), r_0 \sin(\Lambda t/{r_0}^2), 0)$

de periodo $T = 2\pi {r_0}^2/\Lambda$.
Por tanto vamos a usar este análisis numérico que hemos hecho de los puntos críticos en el plano para calcular órbitas periódicas cuando restringimos el movimiento al plano ecuatorial.

4. Cómputo de familias de órbitas periódicas

El objetivo es calcular familias de órbitas periódicas, comenzando por las órbitas restringidas al plano ecuatorial que es el caso más sencillo. Para ello partimos de una órbita periódica plana, correspondiente como hemos visto a un punto de equilibrio $W'(r) = 0$ para un cierto valor del momento angular. Estudiaremos la estabilidad de estas soluciones mediante la continuación de las familias de órbitas circulares planas de las cuales hemos probado su existencia, tanto en el interior, exterior como sobre la corona en el apartado anterior.

Consideramos los valores de las constantes del apartado anterior más un coeficiente de achatamiento para el cuerpo central de $\varepsilon = 0.001$. Para el cálculo de las familias usamos el programa de continuación tomando como parámetro de continuación la coordenada x_0 de la órbita.
Comenzaremos calculando la familia exterior a la corona, para ello tomamos un valor del momento angular que satisfaga la condición de existencia de punto crítico, la representación del retrato de fases o la derivada del potencial efectivo para este valor del momento angular nos permite calcular directamente el valor de r_0, y obtener la órbita de arranque del método de continuación.
La siguiente figura (4) representa la evolución de los índices de estabilidad, en el plano k_n y fuera del plano k_b, al continuar la familia exterior de órbitas circulares. Observamos la transición de estabilidad a inestabilidad al aproximarnos a la corona, consecuencia de la coexistencia de dos puntos críticos, uno más exterior estable, y el inestable cercano a la misma.

Por otro lado también encontramos movimiento plano dentro de la propia corona, esto es matemáticamente posible debido a que el potencial creado por la corona tiene discontinuidad esencial en el borde pero es una función definida en el interior. De nuevo tomamos una órbita de arranque para comenzar la continuación, la Figura (5) nos dice que la familia tiene un comportamiento estable con grandes oscilaciones entre los valores límite $Tr = \pm 2$, y que conforme el radio va incrementando, es decir, nos aproximamos al extremo exterior de la corona, ambos índice de estabilidad cruzan la línea $Tr = 2$ y se diparan en magnitud, es decir la familia se vuelve altamente inestable y de muy difícil

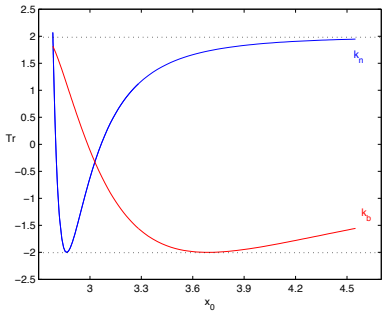

Figura 4.— Evolución de los índices de estabilidad para la familia de órbitas circulares exteriores a la corona.

continuación.

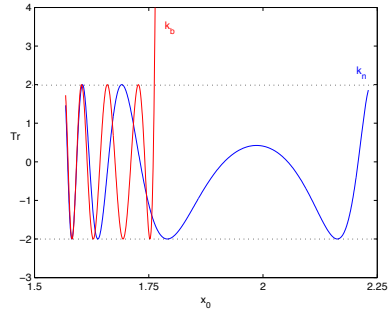

Figura 5.— Evolución de los índices de estabilidad para la familia de órbitas circulares dentro de la corona, $b < r < a$.

Por último si observamos en la Figura (6) el comportamiento de la familia de órbitas circulares planas en la región interior a la corona, vemos que las órbitas se vuelve altamente inestable al aproximarse a la corona, mientras que cuando la distancia hacia el cuerpo central disminuye permanecen estables pero con una tendencia asintótica a $Tr = 2$. Esta tendencia se mantiene hasta $r = 0$ en caso de cuerpo esférico, y se vuelve inestable muy próxima al origen cuando el cuerpo es achatado. Esto es consecuencia de la existencia de dos puntos críticos correspondientes a una órbita circular inestable y otra estable en el caso de $\varepsilon = 0$, y de tres órbitas inestable, estable e inestable para coeficiente de achatamiento no nulo.

En resumen encontramos dos regiones marcadas de inestabilidad, un cambio de estabilidad a inestabilidad cuando el radio de las órbitas circulares se aproxima al borde de la corona desde el interior, y otro al aproximarnos a la corona desde el exterior. Además encontramos varias posiciones donde el índice $k_n = -2$ dando lugar a una bifurcación con una familia de órbitas de doble periodo, hemos continuado a su vez esta nueva familia observando un nuevo punto de bifurcación de periodo doble. Repitiendo este procedi-

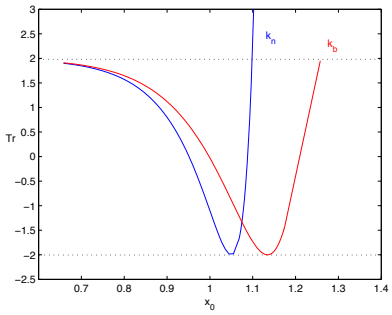

Figura 6.— Evolución de los índices de estabilidad para la familia de órbitas circulares a distancia $0 < r < b$.

miendo podemos encontrar las familias de múltiple periodo cuya evolución del índice de estabilidad en el plano viene dada por la fórmula(11), y están representados en la Figura (4).

$$k_m = 2\cos\left(m \arccos(\frac{k}{2})\right), \qquad |k| \leq 2 \tag{11}$$

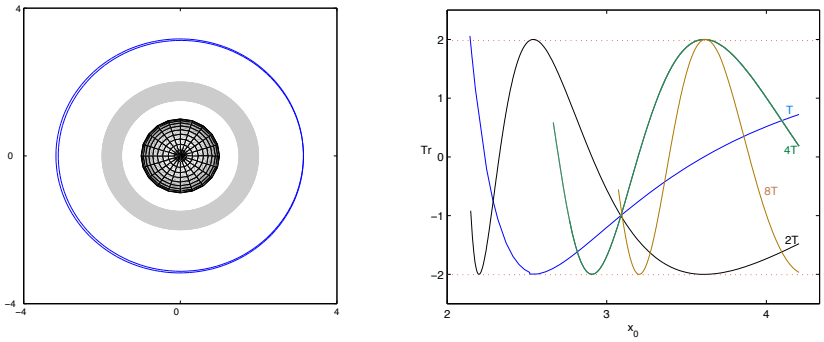

Figura 7.— Evolución del índice de estabilidad en el plano para las familias ecuatoriales de múltiple periodo.

En lo que respecta a la dinámica, fuera del plano podemos restringir el movimiento al plano perpendicular a la corona pasando por el origen. En este caso estamos en un problema no integrable y el procedimiento que vamos a seguir para conseguir órbitas periódicas es la representación de Secciones de Poincaré o del programa *Zeros* que nos servirán para proporcionarnos condiciones iniciales que usaremos para la posterior continuación de sus familias. De este modo encontramos órbitas como las que están representadas en la Figura (8) donde algunas de ellas han sido calculadas directamente de Secciones de Poincaré para distintos niveles de la energía, y otras aparecen como bifurcaciónes de las anteriores.

Por otro lado podemos obtener órbitas periódicas en el espacio $Oxyz$ a partir de órbitas periódicas en el plano meridiano Orz, para ello volvemos a las ecuaciones del movimiento expresadas en coordenadas cilíndricas. Recordar que gracias a la simetría cilíndrica del problema y por tanto a la existencia del momento angular como integral del problema, podemos reducir el estudio a la búsqueda de órbitas en el plano meridiano Orz, que rota

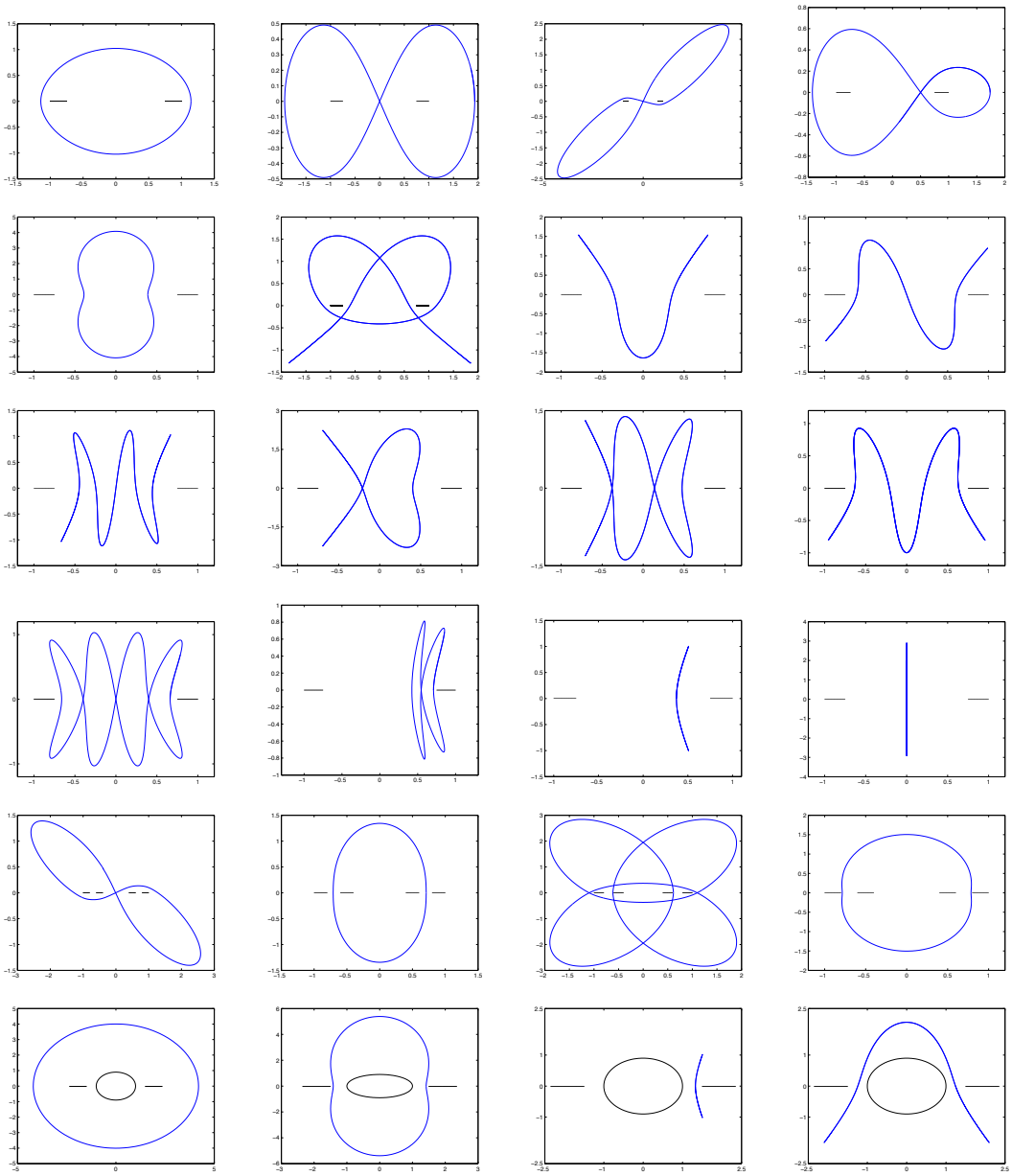

Figura 8.— Representación Oxz de órbitas polares para el problema de la corona, composición de coronas, y planeta + corona.

en torno al eje Oz con velocidad angular λ. Lás órbitas periódicas en este plano no serán necesariamente cerradas en el espacio cartesiano debido a la precesión del ángulo λ. Es decir, si $r(t)$ y $z(t)$ son periódicas, entonces $\dot{\lambda} = \Lambda/r(t)^2$ será también función periódica con el mismo periodo, sin embargo para la longitud se tendrá $\lambda(t_0 + T) - \lambda(t_0) = C$ constante. El ángulo λ mide la posición del meridiano de rotación del satélite, que no es mas que la suma del movimiento del orbitador, y de la precesión de la órbita.
Para conseguir encontrar una órbita periódica en el espacio cartesiano $Oxyz$ a partir de una de las anteriores, es necesario imponer una relación de conmensurabilidad entre la velocidad de rotación de la partícula y la velocidad con la que se mueve el ángulo λ, es decir con la frecuencia de precesión de los nodos, de tal manera que

$$\lambda(t_0 + T) - \lambda(t_0) = 2\pi\frac{m}{n}, \tag{12}$$

es decir, que mientras el orbitador recorre n vueltas en su plano meridiano, este plano describe otro número entero m de rotaciones alrededor del eje polar.

La metodología para conseguir una órbita periódica en el espacio partiendo de una que lo sea en el espacio reducido consiste en aplicar nuevamente el método de continuación de órbitas periódicas, pero ahora el parámetro a variar será la energía. De esta manera, obtendremos una familia de órbitas con variaciones del periodo para las que comprobaremos si satisfacen la condición de periodicidad (12) para un par de enteros (m, n). Notar que la mayoría de las órbitas no la verificarán aunque sí es posible encontrar algunas órbitas que lo hagan.

Hemos realizado este procedimiento para algunas de las familias de órbitas periódicas en el meridiano Orz que hemos encontrado. Aquí presentamos una órbita tipo arco exterior a la corona (E_0), y una de tipo elítico, cuyo uno de los extremos pasaba por la región confinada entre el planeta y la corona (E_1). Las Figuras (9) y (10) muestra su trayectoria en el plano reducido, y para cada una de ellas un par de órbitas periódicas en el espacio que hemos encontrado para relaciones de conmensurabilidad $(m = 9, n = 10)$, $(1, 1)$ y $(3, 4)$, $(5, 7)$ respectivamente.

Destacar que para cada una de estas órbitas periódicas en el espacio podemos calcular a su vez su familia utilizando de nuevo el método de continuación, proporcionándonos además información sobre el carácter estable o inestable de las órbitas mediante el análisis de la evolución de los índices de estabilidad k_1 y k_2.

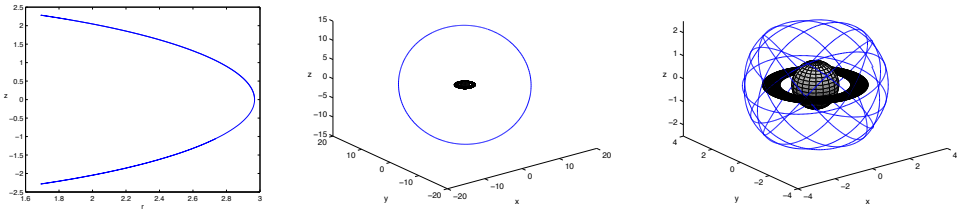

Figura 9.— Órbitas periódicas $1:1$ y $9:10$ en el plano cartesiano para E_0.

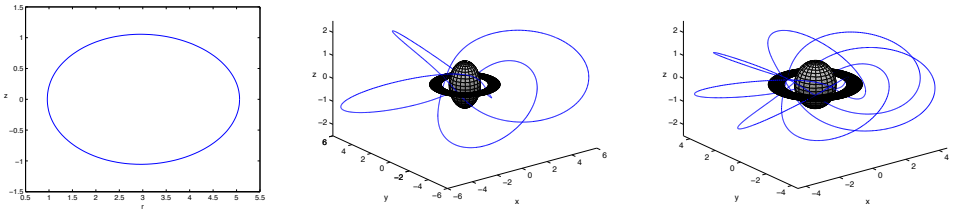

Figura 10.— Órbitas periódicas $3:4$ y $5:7$ en el plano cartesiano para E_1.

Conclusiones

En este artículo se ha hecho una descripción en líneas generales de cómo se estructura la dinámica de una partícula alrededor de una corona circular con o sin planeta en su interior. Posteriores trabajos presentarán una más amplia variedad de familias encontradas, así como el análisis de su evolución a través del estudio de su estabilidad y posibles bifurcaciones, además de completar el estudio analítico de los equilibrios con resultados matemáticos que corroboren los comportamientos observados numéricamente.

Referencias

[1] A. Abad and A. Elipe, "Evolution strategies for computing periodic orbits," *Paper AAS 09-143. February 8-12, 19th AIAA/AAS Space Flight Mechanics Meeting* , 2009.

[2] A. Alberti and C. Vidal, "Dynamics of a particle in a gravitational field of a homogeneous annulus disk," *Celestial Mech. Dynam. Astronom.*, Vol. 98, No. 2, 2007, pp. 75–93.

[3] R. Barrio, R. and Blesa, F., "Systematic search of symmetric periodic orbits in 2DOF Hamiltonian systems" *Chaos, Solitons and Fractals*, (in press) doi:10.1016/j.chaos.2008.02.032

[4] R. Bulirsch, "Numerical calculation of elliptic integrals and elliptic functions," *Numer. Math.*, Vol. 7, 1965, pp. 78–90.

[5] R. A. Broucke and A. Elipe, "The dynamics of orbits in a potential field of a solid circular ring," *Regul. Chaotic Dyn.*, Vol. 10, No. 2, 2005, pp. 129–143.

[6] P. F. Byrd and M. D. Friedman, *Handbook of elliptic integrals for engineers and scientists*. New York: Springer-Verlag, 1971.

[7] B. Carlson, "Computing elliptic integrals by duplication," *Numerische Mathematik*, Vol. 33, 1979, pp. 1–16.

[8] A. Deprit and J. Henrard, "Natural families of periodic orbits," *Astronomical Journal*, Vol. 72, 1967, pp. 158–172.

[9] A. Elipe, E. Tresaco and A. Riaguas, "Description of the dynamocs around an annular disk," *Paper AAS 09-155. February 8-12, 19th AIAA/AAS Space Flight Mechanics Meeting* , 2009.

[10] M. Hénon, "Exploration Numérique du Problème Restreint. II Masses égales, Stabilité des Orbites périodiques," Vol. 28, pp. 992–, 1965.

[11] J. E. Howard and R. S. MacKay, "Linear stability of symplectic maps," *J. Math. Phys.*, Vol. 28, No. 5, 1987, pp. 1036–1051.

[12] O. D. Kellogg, *Foundations of potential theory*. Reprint from the first edition of 1929. Die Grundlehren der Mathematischen Wissenschaften, Band 31, Berlin: Springer-Verlag, 1967.

[13] F. T. Krough, E. W. Ng, and W. V. Snyder, "The gravitational field of a disk," *Celestial Mechanics*, Vol. 26, Apr. 1982, pp. 395–405.

[14] H. Lass and L. Blitzer, "The gravitational potential due to uniform disks and rings," *Celestial Mechanics*, Vol. 30, July 1983, pp. 225–228.

[15] J. Maxwell, *On the Stability of Motions of Saturn's Rings*. Macmillan and Cia. Cambridge, 1859.

[16] W. D. MacMillan, *The theory of the potential*. Reprint. Originally published: New York : McGraw-Hill, 1930. Series MacMillan's Theoretical Mechanics. NewYork: Dover publications, 1958.

[17] D. J. Scheeres, *On symmetric central configurations with application to the satellite motion about rings*. PhD thesis, University of Michigan, 1992.

[18] D. J. Scheeres, "Satellite dynamics about asteroids: computing Poincaré maps for the general case," *Hamiltonian systems with three or more degrees of freedom (S'Agaró, 1995)*, Vol. 533 of *NATO Adv. Sci. Inst. Ser. C Math. Phys. Sci.*, pp. 554–557, Dordrecht: Kluwer Acad. Publ., 1999.

Monografías de la Real Academia de Ciencias de Zaragoza **35**, 135–144, (2011).

Identifying the progenitor bodies of meteorites: Backward integration of NEO and FJC comets

Josep M. Trigo-Rodríguez[1], and José M. Madiedo[2]

[1]Institute of Space Sciences (CSIC-IEEC).
Campus UAB, Facultat de Ciències, Torre C-5 parells, Bellaterra, Barcelona, Spain

[2]Facultad de Ciencias Experimentales Universidad de Huelva 21071 Huelva, Spain

Abstract

A continuous monitoring of fireball activity all over Spain is being completed. This involves recording meteor events over a very large surface area of 500,000 km^2 with new CCD and video cameras operated by the Spanish Meteor and Fireball Network (SPMN). Through the use of these new techniques the SPMN can obtain trajectory and orbital information that provide new clues regarding the dynamical processes that deliver meteorites to the Earth. It transpires that the main asteroid belt is not the only source of these fireballs, Near Earth Objects (NEOs) and Jupiter Family Comets (JFCs) play also a role. To obtain more information in this regard, we are developing new software to compare the orbits of large meteoroids reaching the Earth with those of the members of NEO and JFC populations. By numerically integrating their orbits back in time it may be possible to identify meteoroids delivered by other mechanisms like such as catastrophic disruptions or collisions.

1 Introducción

The SPanish Meteor and Fireball Network (SPMN) is a project to study meteor and fireball events occurring over Spain and the bordering countries [1]. Network operations started in 2004 using high-resolution all-sky CCD cameras from a number of different stations located around the Mediterranean coast [2, 3]. Over the years, these stations have been complemented by using video systems that are the main type of detectors currently operative [4]. The active group working on these projects consists of astrophysicists, chemists, and geologists working together to collect information on meteors and fireballs but with particular emphasis on the recovery of meteorites. Large fireballs can be the

precursors of meteorite falls and modern technology can be applied to track their atmospheric trajectories, and predict probable landing sites. To do this it is necessary to record the luminous trail from at least two different locations. The different SPMN recording stations currently operative are in Fig. 1. From the atmospheric trajectory and the computed initial velocity and geocentric radiant the heliocentric orbit can be determined. Due to the difficulty of recording meteorite-dropping bolides, orbital information has so far only been only computed for nine meteorites, the last one being the Villalbeto de la Peña meteorite in Spain [5]. Meteorites are valuable samples of other solar system bodies, but usually are recovered without information regarding their progenitors. Obtaining orbital information for meteorites that might land at some future date is vital if we are to understand the dynamical processes that deliver meteorites to the Earth. Recent results suggest that the main asteroid belt might not be the only source, Near Earth Objects (NEOs) [6] and Jupiter Family Comets (JFCs) [7] populations may also be significant.

Consequently, the SPMN meteorite recovery program is designed to obtain as much information as possible of the atmospheric transit of the progenitor meteoroid. We are putting all our effort in obtaining records of large fireball events to obtain the heliocentric orbits of new meteorites. It is obviously a big challenge because meteorite-dropping bolides are typically unexpected events that produce a luminous phase (the fireball) for a very short time interval of only a few seconds. Obtaining dynamic information regarding meteorite-dropping bolides is crucial in order to obtain information concerning the physical mechanisms that are placing meteorites on orbits that can lead to collision with the Earth. Similar mechanisms are expected to be playing a role in the delivery of largest bodies, particularly Near Earth Objects (NEOs) to the Earth Environment. We are also setting up portable stations capable to monitor future encounters with NEOs like e.g. 2008TC3. An example of mobile video station appears in Fig. 2.

2 Meteorite recoveries: Villalbeto de la Peña and Puerto Lápice daylight bolides

In 2004 the SPMN had already created the infrastructure necessary to compile the casual records of a remarkable daylight fireball that had been obtained, and promoted the recovery of meteorites associated with the event. The event, on January 4, 2004,, was called Villalbeto de la Peña after the village where the first meteorites were found and resulted in the first recovered meteorite fall in Spain for 56 years. A casual video recording and several photographs allowed a determination of the fireball trajectory, its released energy, and strewnfield reconstruction to be made [8]. From the determination of the radiant position in the sky and the computed initial velocity, the heliocentric orbit of the meteoroid was also obtained. This became only the ninth orbit of a meteorite-producing

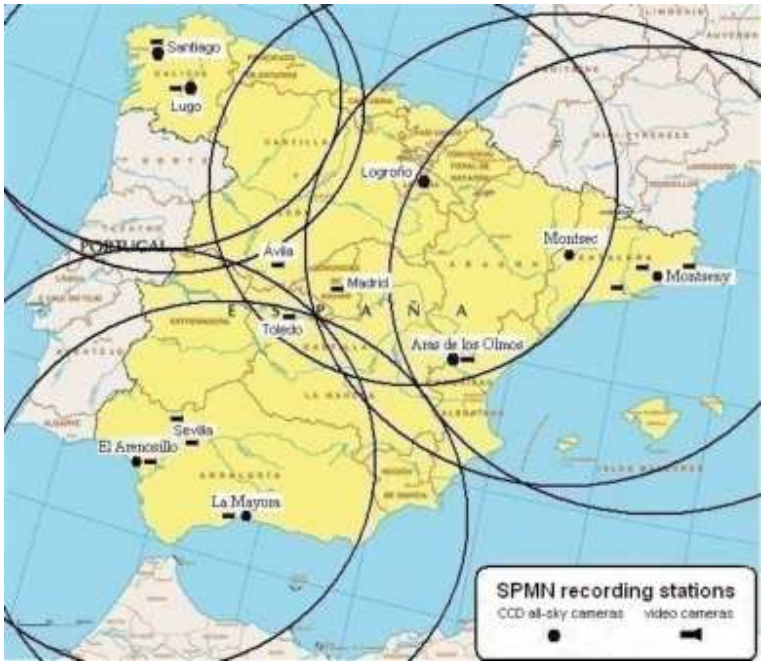

Figure 1.— The SPMN stations currently operating with the different imaging systems that are being used also shown. The circles represent the 400-km wide fireball detection areas optimally covered from each station, although the detection limit for bright bolides is about 550 km.

Figure 2.— A mobile SPMN recording station. a) System control table. b) Different sound and video detectors.

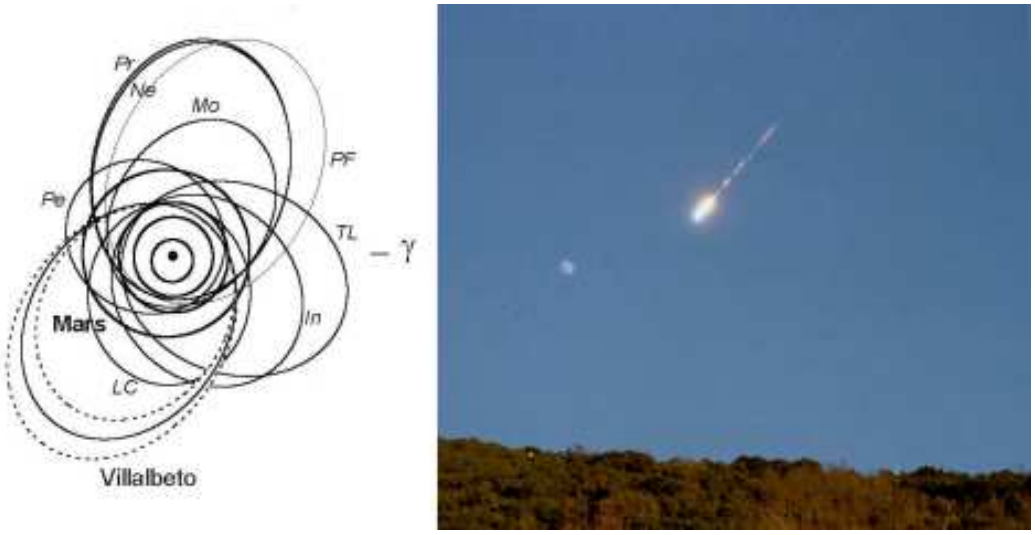

Figure 3.— Left: The heliocentric orbit of Villalbeto de la Peña meteoroid compared with the orbits of previously determined meteoroids dropping meteorites: Pŗibram (Pr, recovered in 1959), Lost City (LC, 1970), Innisfree (IN, 1977), Peeskill (PE, 1992), Tagish Lake (TL, 2000), Morávka (Mo, 2000), Neuschwanstein (Ne, 2002), Park Forest (PF, 2003), and Villalbeto de la Peña (2004). Only in the case of Villalbeto de la Peña orbit the uncertainty in the velocity is shown. Right: The Villalbeto de la Peña bolide after its main fragmentation photographed from Santa Columba de Corueño (León) by María M. Robles.

fireball to be obtained (Fig. 3) [5]. Three years later, on May 10, 2007 SPMN participated in the recovery of Puerto Lápice eucrite type meteorite after giving community data about the impressive daylight bolide that gave rise to the meteorite fall [9]. To date, the SPMN homepage (www.spmn.uji.es) receives thousands of visits every month, and has become an updated reference of the fireball events that have occurred all over Spain, and bordering countries. Our homepage is also playing a role in popularizing astronomy, and meteorite studies among the public.

3 Identifying Earth-impacting debris from NEOs

Halliday was pioneer in suggesting the existence of groups of meteorite-producing bolides [11]. Meter-sized bodies suffer significant gravitational and non-gravitational perturbations (e.g. the Yarkovsky effect) that can produce an extremely fast evolution of the meteoroid orbits. The possible common origin of Pribram and Neuschwanstein meteorites was recently claimed on the basis of their orbital similarity [12], but the fact that they are different meteorite types keeps this result controversial. The association of Pribram and Neuschwanstein meteorites was dynamically investigated recently [13], and the conclusion was that the timescales for orbital decoherence are too short (104 to 105 years) in comparison with the derived age of both meteorites. However it has also been shown

that meteorite streams on high inclination orbits might exists for longer than this [14]

To obtain new information regarding this topic, fireball networks need to modify their mode of operations. First, the "classical" coverage of fireball events during the night should be accompanied by daylight monitoring using the video techniques (see Fig. 4). By doing this, data sampling would be more complete and not biased towards those celestial sources (radiants) detectable during the night. Second, the different networks operating around the world should cooperate to search for paired fireball events. In this way, the chance of recording paired bolides would be significantly increased. Third, the area of coverage of fireball networks should be expanded through the use of new video techniques. Fourth, a wide cooperation with the minor body community should be relevant to identify particular asteroids as source of meteorites.

A particularly interesting research topic that should be explored is the identification of the main mechanisms that are producing large meteoroids from NEOs and other populations. While it is believed that collisions in the main asteroid belt are the main source of meteorites, other processes operating in other populations can also be significant contributors. There is growing evidence that many comets and small asteroids can have a rubble-pile structure. Such weakly-bounded aggregates would suffer disruption during close approaches to any massive bodies. Such scenario would be common for NEOs suffering close approaches with the terrestrial planets and the tidally-induced fragmentation of an NEO could lead to production of debris crossing the orbit of the Earth in much shorter timescales than those measured for delivery from the main asteroid belt. To obtain evidence regarding this we are carrying out a search among the meteoroid orbits obtained by the SPMN network and comparing them with those of currently catalogued NEOs (taken from the NeoDys catalogue). To test the link between the meteoroids and the NEOs, we perform numerical integrations of the orbits backwards in time. Using the Mercury 6 program [15] a hybrid symplectic integrator widely used in Solar System dynamics studies. To confirm a common origin between the meteoroids producing the fireballs and the NEOs, the orbits are usually integrated back in time for at least 100,000 years. Perturbations from the planets Venus, Earth, Mars, Jupiter and Saturn are included. When a good orbital match is found, and the evolution of the main orbital elements occurs in parallel, it is safe affirming that a common origin is likely.

By using that dynamic procedure we have obtained evidence that some NEOs could be a source of meteorites. We found that NEO 2002NY40 was probably the source of at least two of three bright bolides recorded from several stations by the Finish and Spanish Fireball networks in 2006. These meteoroids were forming a complex with other NEO called 2004NL8 that would be a source of LL chondrites to the Earth [6]. We suggested that the origin of this complex would be the disintegration of a progenitor asteroid during a close approach to the Earth or Mars, but several scenarios are open [16].

Figure 4.— A daylight fireball imaged with a color video camera from Sevilla SPMN station. The event took place on Sept. 12, 2008 at 5h41m35.6s UTC.

4 Catastrophic disruptions: A way for delivery of meteorites from comets?

It is generally accepted that amongst the NEO population there are many dormant or extinct comets. The boulders observed during disruption of comet C/1999 S4 LINEAR [17] were tens of meters in size and are far bigger than the cometary meteoroids that reach the Earth during meteor showers. The catastrophic disruption of a comet nucleus could produce dense and tough meteoroids released from the deep interior of the nucleus. These meteoroids could have very different physical properties from those that produce meteor showers which are essentially surface dust grains. Such particles released by sublimation of ices during perihelion passages of their parent comets have maximum sizes of few centimeters. Larger particles cannot be lifted off the cometary surface as gravity is stronger than gas drag for them [18].

On July 11, 2008 a fireball of magnitude −18 was recorded over Salamanca province (Spain), ending with very bright flares at a height of about 22 km over a town called Béjar after which this event was named [7]. Three SPMN video cameras recorded the event together with a professional photographer (see Fig. 5). Fireball deceleration in the atmosphere suggests that the meteoroid approximately had an initial mass of 1.8 metric tons. Assuming a spherical shape, and the typical density of chondrites (2200 kg?m-3) this would correspond roughly to a 1.2 meter-sized meteoroid. After analyzing the observations, we discovered that the fireball followed an orbit more similar to Jupiter Family comets than asteroids. Further, the orbit was quite similar to the mean orbit of the Omicron Draconids, a meteoroid stream possibly produced during the catastrophic

Figure 5.— The Béjar superbolide photographed from Torrelodones (Madrid) by Javier Pérez Vallejo.

disruption of comet C/1919 Q2 Metcalf. The JFCs originate in the trans-Neptunian region and TNOs have been recently suggested a source of meteorites [19]. There is a reasonable probability (about a 10%) of having an Earth-crossing JFC. Fragments of JFCs can reach the Earth provided the geometry is favorable, and some of these fragments could be high-strength materials from the nucleus interior, and it follows that some of the chondritic meteorites, particularly in the CI-class [20] that we find on Earth, could be coming from comets. The parent body of Tagish Lake meteorite has been identified as a D-type dark asteroid formed in the outer part of the main belt [21]. Such a body could be an example of a main belt comet exhibiting sporadic activity like 133P/Elst-Pizarro [22]. We should recognize that cometary nuclei can show significant diversity, depending on their formation location and evolutionary history, and that their decaying products also deliver diverse materials to the Earth.

Although catastrophic disruptions of comets are relatively frequent, it is obviously that having the debris left by the disruptive events crossing the Earths orbit a short time after the disruption is a much rarer event. The probability of having the correct geometry for this is small, but fortunately not zero. The opportunity to study such an event is expected over the next few years [23]. Comet 73P/Schwassmann-Wachmann was observed suffering progressive disruption between 1995 and 2006, while encounters with these dust trails will occur in 2011, 2017, and 2022. The meteor shower associated with this comet produces weak meteor rates, but fireballs have being frequent in the last few years. The best geometric conditions to observe the recent debris from the 1995 disruption

will occur on May 31, 2022 (Table 6g of [23]). A global campaign to study this shower over the years up to 2022 would provide very important clues on the demise of comets. In particular, a study of the physical properties (bulk density, dynamic strength, etc...), and composition of the fireballs can also provide information regarding the decay products and their subsequent evolution before reaching the Earth [24, 25].

5 Conclusions

CCD and video techniques are providing significant break-throughs in the study of bright fireballs during their interaction with the terrestrial atmosphere. Fireball monitoring can now be achieved in broad daylight as well as during the night. The new techniques can reduce or eliminate some of the biases of data sampling obtained by previous fireball networks. Accurate orbital data can provide valuable information on the physical mechanisms that are producing meter-sized meteoroids in heliocentric orbit. Fireball studies also provide information on the physical properties (bulk density, dynamic strength and porosity), and bulk chemistry of meteoroids. Many questions regarding the origin of meter-sized meteoroids are still open, and are sharing common problems with NEO studies. Further progress in our knowledge on the regions source of meteorites will require a collaborative effort with other researchers from parallel disciplines.

References

[1] J.M. Trigo-Rodríguez J.M., J. Llorca, A. J. Castro-Tirado, J. L. Ortiz , J. A. Docobo and J. Fabregat, "The Spanish Fireball Network," *Astronomy & Geophysics* 47:6, 26-28, 2006.

[2] J.M. Trigo-Rodríguez, A. Castro-Tirado, J. Llorca, J. Fabregat, V. J. Martínez, V. Reglero, M. Jelínek, P. Kubánek, T. Mateo and A. de Ugarte Postigo, "The development of the Spanish Fireball Network using a new all-sky CCD system," *Earth, Moon Planets* 95, 553-567, 2004.

[3] A.J. Castro-Tirado, M. Jelínek, S. Vítek, P. Kubánek, J.M. Trigo-Rodríguez, A. de Ugarte Postigo, T.J. Mateo Sanguino, and I. Gomboš., "A very sensitive all-sky CCD camera for continuous recording of the night sky," in *Advanced Software and Control for Astronomy II.* A. Bridger, N.M. Radziwill, Proceedings of the SPIE, Volume 7019, pp. 70191V-70191V-9, 2008.

[4] J.M. Madiedo, and J.M. Trigo-Rodríguez, "Multi-station video orbits of minor meteor showers," *Earth Moon and Planets* 102, 133-139, 2008.

[5] J.M. Trigo-Rodríguez, J. Borovička, P. Spurný, J.L. Ortiz, J.A. Docobo, A.J. Castro-Tirado, and J. Llorca, "The Villalbeto de la Peña meteorite fall: II. Determination of the atmospheric trajectory and orbit," *Meteoritics & Planetary Science* 41, 505-517, 2006.

[6] J.M. Trigo-Rodríguez, E. Lyytinen, D.C. Jones, J. M. Madiedo, A. Castro-Tirado, I. Williams, J. Llorca, S. Vítek, M. Jelínek, B. Troughton and F. Gálvez, "Asteroid 2002NY40 as source of meteorite-dropping bolides", *Monthly Notices of the Royal Astronomical Society* 382, 1933-1939, 2007.

[7] J.M. Trigo-Rodríguez, J. M. Madiedo, I. Williams, J. Llorca, S. Vítek, and M. Jelínek, "Observations of a very bright fireball and its likely link with comet C 1919 Q2 Metcalf," *Monthly Notices of the Royal Astronomical Society* 394, 569-576, 2009.

[8] J. Llorca, J.M. Trigo-Rodríguez, J.L. Ortiz, J.A. Docobo, J. Garcia-Guinea, A.J. Castro-Tirado, A.E. Rubin, O. Eugster, W. Edwards, M. Laubenstein and I. Casanova, "The Villalbeto de la Peña meteorite fall: I. Fireball energy, meteorite recovery, strewn field and petrography" *Meteoritics & Planetary Science* 40, 795-804, 2005.

[9] J.M. Trigo-Rodríguez, J. Borovička, J. Llorca, J.M. Madiedo, J. Zamorano, and J. Izquierdo, "Puerto Lápice eucrite fall: Strewn field, physical description, probable fireball trajectory, and orbit" *Meteoritics & Planetary Science* 44, 175-186, 2009.

[10] P. Jenniskens, M.H. Shaddad, D. Numan, S. Elsir, A.M. Kudoda, M.E. Zolensky, L. Le, G.A. Robinson, J.M. Friedrich, D. Rumble, A. Steele, S.R. Chesley, A. Fitzsimmons, S. Duddy, H.H. Hsieh, G. Ramsay, P.G. Brown, W.N. Edwards, E. Tagliaferri, M.B. Boslough, R.E. Spalding, R. Dantowitz, M. Kozubal, P. Pravec, J. Borovička,Z. Charvat, J. Vaubaillon, J. Kuiper, J. Albers, J.L. Bishop, R.L. Mancinelli, S.A. Sandford, S.N. Milam, M. Nuevo, and S.P. Worden, "The impact and recovery of asteroid 2008 TC_3" *Nature* 458, 485-488, 2009.

[11] I. Halliday, A.A. Griffin and A.T. Blackwell, "Detailed data for 259 fireballs from the Canadian camera network and inferences concerning the influx of large meteoroids," *Meteoritics & Planetary Science* 31, 185-217, 1996.

[12] P. Spurný, J. Oberst, D. Heinlein, "Photographic observations of Neuschwanstein, a second meteorite from the orbit of the Příbram chondrite", *Nature* 423, 151-153, 2003.

[13] A. Pauls and B. Gladman, "Decoherence time scales for meteoroid streams" *Meteoritics & Planetary Science* 40, 1241-1256, 2005.

[14] D.C. Jones and I.P.Williams, "High inclination meteorite streams can exist, *Earth Moon and Planets*, 102, 35-46, 2008.

[15] J.E. Chambers, "A hybrid symplectic integrator that permits close encounters between massive bodies" *Monthly Notices of the Royal Astronomical Society* 304, 793-799, 1999.

[16] Trigo-Rodriguez, J.M.; Bottke, W.F.; Campo Bagatin, A.; Tanga, P.; Llorca, J.; Jones, D.C.; Williams, I.; Madiedo, J.M.; Lyytinen, E., "Is Asteroid 2002NY40 a Rubble Pile Gravitationally Disrupted?", *Lunar Planet. Sci.* 39, abstract #1692, Lunar and Planetary Institute, Houston, 2008.

[17] H.A. Weaver, Z. Sekanina, I. Toth., C.E. Delahodde, O.R. Hainaut, P.L. Lamy, J.M. Bauer, M.F. A'Hearn, C. Arpigny, M.R. Combi, J.K. Davies, P.D. Feldman, M.C. Festou, R. Hook, L. Jorda, M.S.W. Keesey, C.M. Lisse, B.G. Marsden, K.J. Meech, G.P. Tozzi, and R. West, "HST and VLT Investigations of the Fragments of Comet C/1999 S4 (LINEAR)" *Science* 292, 1329-1334, 2001.

[18] Y. Ma, I.P. Williams, W. Chen, "On the ejection velocity of meteoroids from comets" *Monthly Notices of the Royal Astronomical Society* 337, 1081-1086, 2002.

[19] M. Gounelle, A. Morbidelli, P.A. Bland, P. Spurný, E.D. Young, and M. Sephton, "Meteorites from the Outer Solar System?," in *The Solar System Beyond Neptune*, M.A. Barucci, H. Boehnhardt, D.P. Cruikshank, and A. Morbidelli, Eds., Tucson, Arizona, pp. 525-541, 2008.

[20] M. Gounelle, P. Spurný, P.A. Bland, "The atmospheric trajectory and orbit of the Orgueil meteorite," *Meteoritics & Planetary Science* 41, 135-150, 2006.

[21] T. Hiroi T., Zolensky M.E., Pieters C.E., "The Tagish Lake Meteorite: A Possible Sample from a D-Type Asteroid" *Science* 293, 2234-2236, 2001.

[22] H. Hsieh and D. Jewitt, "A population of comets in the main asteroid belt," *Science* 312, 561-563, 2006.

[23] L. Johnson, "Near Earth Object Observations Program", online presentation available at: `http://www.oosa.unvienna.org/pdf/pres/stsc2009/tech-25.pdf`, 2009.

[24] J.M. Trigo-Rodríguez J.M., J. Llorca, J. Borovička and J. Fabregat, "Chemical abundances determined from meteor spectra: I. Ratios of the main chemical elements," *Meteoritics & Planetary Science* 38, 1283-1294, 2003.

[25] J.M. Trigo-Rodriguez, J. M. Madiedo, I. P. Williams, and A. J. Castro-Tirado, "The outburst of the Kappa Cygnids in 2007: clues about the catastrophic break up of a comet to produce an Earth-crossing meteoroid stream", *Monthly Notices of the Royal Astronomical Society* 392, 367-375, 2008.

Monografías de la Real Academia de Ciencias de Zaragoza **35**, 145–152, (2011).

Remembering Ramón María Aller in the International Year of the Astronomy 2009

José Ángel Docobo

Astronomical Observatory R.M. Aller

Universidade de Santiago de Compostela

15782 Santiago de Compostela, Spain

Ramón María Aller Ulloa was born in Pazo de Filguieroa (Lalín, Galicia-Spain) on 3 February 1878, in an ancestral house in Lalín. He studied secondary school at the Jesuit school in A Guarda and joined the Seminary in Lugo where, at the age of 20 and before becoming the Subdeacon, he graduated with a bachelor's and doctor's degree in Theology.

Upon finishing his priestly studies he promised himself that he would not assume any religious position or receive any type of monetary compensation for his ministry. At that time he decided to take on a second vocation and enroll in his first year of studies in the Exact Sciences at the University of Oviedo (1899-1900 academic year). He would later continue his degree at the University of Madrid and would graduate in 1904.

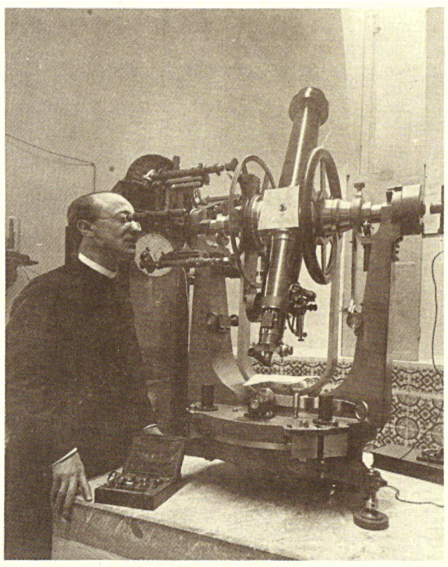

Figure 1.— R.M. Aller working at the Ocharan Observatory

While studying at the seminary, Aller already had a 67mm telescope, a present from his maternal grandmother, Camila Ulloa. This would be the first instrument with which he would practice his love of astronomy. Years late, Miss María Lajosa Sánchez, also from Lalín, would present Aller with a magnificent theodolite made in London. It was with these instruments, located on a balcony in his house, that he would begin to systematically carry out astronomical observations, high-quality observations despite the limited resources at his disposal. His paper: "Observations of the Johannesburg Comet 1910a" was published

in the Observatory of Madrid's 1912 annual, Spain. It was with this publication that he would begin to make a name for himself in astronomy circles in Spain.

Figure 2.— The Observatory of Lalín in 1924

Between 1911 and 1920, he spent long summer periods in the Observatory that Luis Ocharan built in Castro Urdiales, and it was because of this experience that he came up with the idea to build his own observatory in Lalín. And so it was. In 1917, in the garden adjoining his house, he built what is usually referred to as his second observatory. This consisted of two wooden sheds, one of which housed the theodolite and the other the telescope. Other auxiliary instruments and a marine chronometer were also kept in the sheds.

With these new facilities, his observations reached admirable precision. He also carried out detailed theoretical studies on instruments. Many of his works appeared in the "Revista de la Sociedad Astronómica de España y América" (Journal of the American and Spanish Astronomical Society).

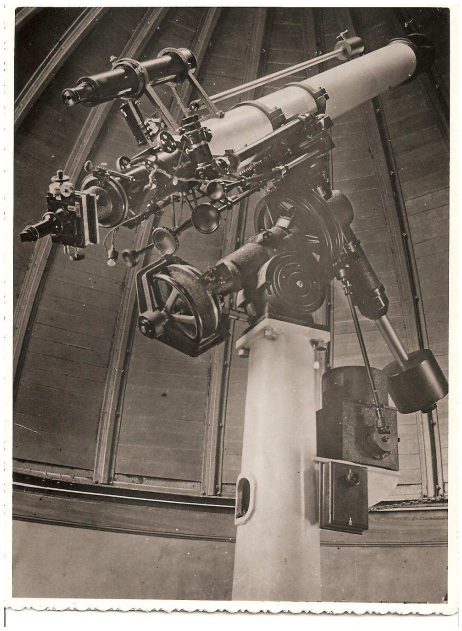

Figure 3.— The refractor Steinheil

It is curious, however, that his first book would be on Mathematics and not on Astronomy: "ALGORITMIA", which he dedicated to Saturnino Aller, his uncle and the book's sponsor, was published in 1918. It was precisely with Saturnino's death that Aller would have the usufruct of his uncle's assets for many years. With the money this provided him, he decided to enlarge his collection of observation instruments with the addition of a 120mm refractor with a focal length of 1800mm.

Housing such an instrument required modifying the observatory's structure and building a dome. Aller himself supervised the changes and new construction, which were completed in 1924. He received the new instrument a year later. Hardly had the new refractor been installed when Aller meticulously chose the scientific programme he would follow, the discussion of which can be found in his article

"Programme of the Observatory of Lalín" published in 1932 in the "Arquivos do Seminario de Estudos Galegos" (Archives of the Galician Studies Seminar). The main aspects of the programme were 1) measurements of double stars, 2) the study of planetary surfaces, and 3) chance observations, including occultations, the position of comets, falling stars, and so on.

Aller first published his micrometric measurements of visual double stars in 1930, in the German journal "ASTRONOMISCHE NACHRICHTEN", which was the main European astronomical journal at the time. Years later in the same publication, he would make the orbit of the double star STT77 known. Others would subsequently follow. One can safely say that it was Aller who introduced the study of double stars in Spain, a subject which would later enjoy an impressive school of followers in Santiago.

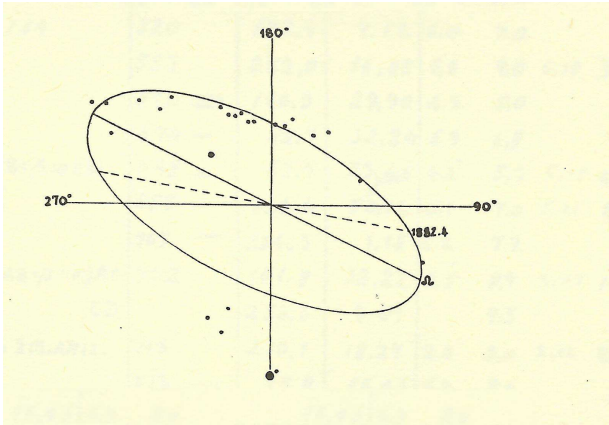

Figure 4.— The orbit of the system STT 77 obtained by Aller was the first double star orbit calculated in Spain

Before 1939, Aller published 43 works in Spanish and foreign journals, besides "ALGORITMIA". He also wrote an exceptional manuscript on Astronomy which he had been working on since his youth. To these achievements, one must also add the study and design of scientific instruments which peaked the interest of German builders. All of this gave the Observatory of Lalín international fame despite its modest resources and one-man staff. What especially stood out was how Aller made full use of his instruments and the meticulousness with which he performed his calculations and observations. Apart from all of this, he dedicated his time to many other things like designing blueprints for houses and churches and even giving classes to young students in Geography, Mathematics, Latin, and so on. And all of this free of charge. He even authored the first biography

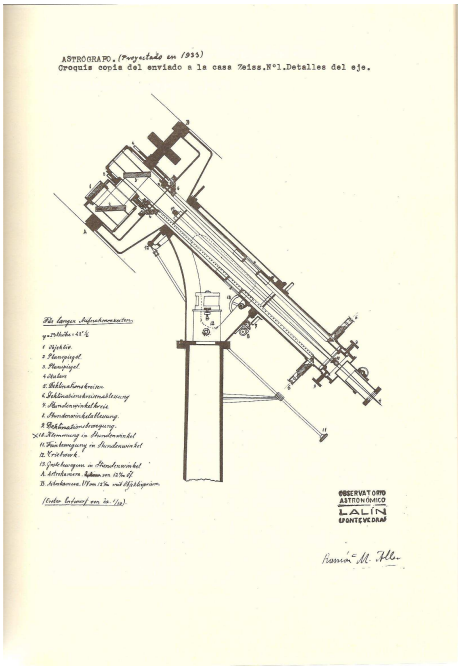

Figure 5.— The astrograph designed by Aller in 1933

of Pedro Rodriguez González, which was published under the title of "El matemático de Bermés" ("The Mathematician from Bermés").

At the end of the Spanish Civil War, the University of Santiago was low on teachers, and someone suggested to Chancellor Carlos Ruiz del Castillo that Aller would make a valuable addition to the teaching staff. They convinced Aller to move to Santiago to teach Mathematical Analysis and Analytical Geometry in the Faculty of Sciences. Although the idea to move the Observatory in Lalín to Santiago had already been raised by professors Luis Iglesias and Isidro Parga before 1936, it was now with Aller in Santiago when the project took shape. It was undoubtedly Enrique Vidal-Abascal's defence of the project before the Higher Council on Scientific Research (Consejo Superior de Investigaciones Científicas: the CSIC) that prompted the Chancellor's Office to give its approval with the sponsorship of the CSIC.

The Astronomical Observatory of the University was built during 1943 and consisted of a single small building with domes in which the instruments from Lalín were installed, obviously with the hopes of enlarging its facilities and scientific observation materials in the future. The Observatory's initial years in Santiago were particularly active ones. On 30 June 1943,Aller defended his doctoral thesis at the University of Madrid. The subject was another one of his favourites: "Some Experiences that are Worthwhile Carrying Out in Observations of Transits Across Vertical Circles." That same year, he was named director of the Observatory and the first edition of his book INTRODUCCIÓN A LA ASTRONOMÍA (INTRODUCTION TO ASTRONOMY) was published, a magnificent book which includes the printed version of the entire manuscript mentioned previously.

The Observatory saw the addition of a transit telescope thanks to a donation by the CSIC who honoured Aller's request for one to be able to continue his research on Positional Astronomy. In subsequent years the Observatory became a centre of excellent academic atmosphere around which astronomy and mathematics scholars converged. Aller was content being surrounded by such enthusiastic youth, especially keeping in mind the many years he spent in scientific solitude in Lalín. The Durán Loriga Theoretical and Mathematical Astronomy section was created within the Observatory in 1945, and included members like professors Enrique Vidal Abascal (its first director) and Eduardo García-Rodeja Fernández. It would serve as the seeds of the Mathematics Department in the Faculty of Sciences, today the Faculty of Mathematics.

Despite the limited observation resources available, practically the same ones that Aller had at his disposal in Lalín, the work carried out in the Observatory was intense, reaching its height in the 1940s and 50s. Some of the most remarkable events that took place at this time include the following:

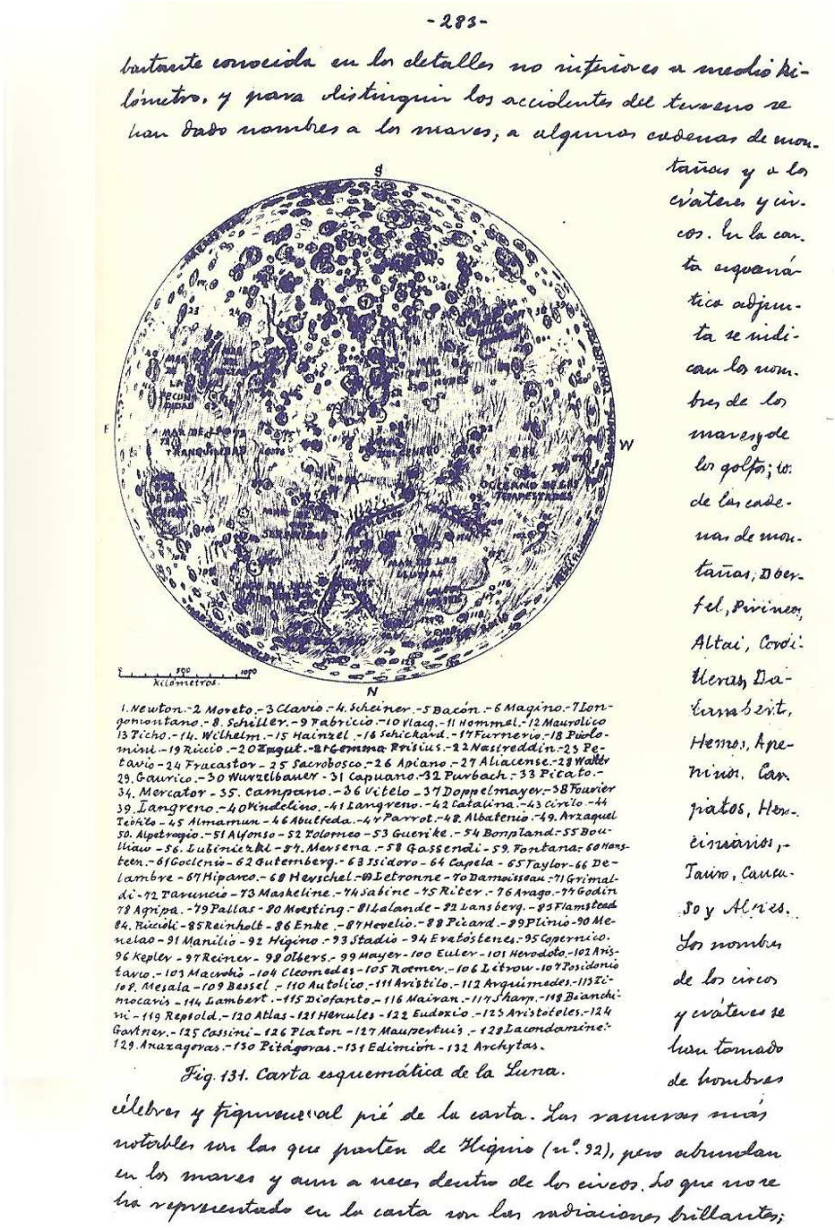

Figure 6.— A page of his hand written book *Introducción a la Astronomía*

— The defence of Enrique Vidal Abascal's doctoral thesis entitled "The Problem with the Apparent Orbit of Visual Double Stars" and directed by Aller (Madrid, 1944).

— The construction of a special base, following Aller's own design, for the transit telescope to carry out observations of transits across vertical circles $\pm 45°$ along with the construction of a sidereal time watch.

— The inauguration of the "Publications of the Observatory of Santiago" series where many of the scientific works carried out in the Centre are gathered, especially those dealing with micrometric measurements of visual double stars, occultations, obser-

vations of transits, as well as other theoretical works.

— The creation of the Astronomy Chair in the Faculty of Sciences in 1944, held by Aller until 1949, the year in which he was named Outstanding Astronomy Professor.

— The appointment of Aller as a member of the "International Astronomical Union Commission 26 (double stars)" in 1948 (Zurich). The following year he was named a member of the National Commission on Astronomy.

— The publication of the book "ASTRONOMÍA A SIMPLE VISTA" (ASTRONOMY AT A GLANCE) in 1948.

— The expansion of the Observatory's facilities with the addition of the Meridian room, the library, research offices and caretaker's quarters.

— The incorporation of various grant holders and contributors among whom were José Pensado Iglesias (who would later become the director of the Observatory of Madrid); Rafael Cid Palacios (Astronomy Chair at the University of Zaragoza); Ángel Docobo Fernández (uncle to José Ángel Docobo Durántez, the Observatory's current director); Antonia Ferrín Moreiras; Jesús Manuel Costa Seoane; Juan Antonio Zaera de Toledo; and many more. One cannot forget Aller's faithful assistant and the Observatory's caretaker, Venancio Froiz Gómez.

— Cid Palacios's doctoral thesis directed by Aller entitled " Contribución al estudio de estrellas dobles visuales" (A Contribution to the Study of Visual Double Stars).

— The publication of the 2nd edition of "INTRODUCCIÓN A LA ASTRONOMÍA" sponsored by the CSIC (1957).

Figure 7.— R.M.Aller at the Astronomical Observatory of the University of Santiago de Compostela

Between 1960 and 1963, in spite of being 83 years old, Aller still directed three more theses: Múgica Buhigas's "ber die Anwendung des Theodolits in der Geodtischen Astronomia" (Munich, 1960); Zaera de Toledo's "On determining the Orbits of Visual Double Stars. A Study of Various Methods. Applications" (Zaragoza, 1962); and Ferrín Moreiras' "Observations of Transits Across Two Vertical Circles" (Santiago, 1963). It was during this time that Aller would begin to receive the first of many tributes, all of which he tried to avoid. The main one, without a doubt, was the homage paid to him by his neighbours in Lalín on 4 September 1960, on the occasion of his being

granted the Great Cross of the Civil Order of Alfonso X, the Wise. Several streets in Madrid, Santiago, A Coruña, Vigo, and Lalín would later carry his name.

Aller preferred two principal lines of investigation: 1) the methods to determine coordinates based on observations of transits across two vertical circles and 2) visual double stars. But in the 53 years that transpired between his first and last articles, Aller also wrote with masterful precision on many other subjects, such as the observation of comets, planetary surfaces, instrumentation, watch making, aurora borealis, shooting stars, eclipses, transits, the description of his observatories, and so forth. In addition, between 1947 and 1949, he wrote a critical bibliography on astronomical treatises in the "Journal of Geophysics," and honouring a request by the Seminar of Galician Studies, he authored the first biography on his fellow countryman Pedro Joseph Rodríguez González, an excellent geodetic scholar in the last century and former director of the Observatory of Madrid. He also made important contributions to the field of Mathematics through his articles on the parabolic theory of errors, sets and the principles of set theory, undefined finite and transfinite numbers, and so on.

Figure 8.— The Astronomical Observatory of the USC

His sensitivity and didactic refinement are immortalized in the books that he left behind. In "ALGORITMIA. Principios fundamentales de la Ciencia de los números" (ALGORITMIA. Basic Principles of the Science of Numbers), he discusses with clear precision the main subjects of mathematical analysis from the notion of whole numbers to differential equations. "INTRODUCCIÓN A LA ASTRONOMÍA" was a significant contribution. Both in its first edition (1943) as well as in the second (1957), he gives a detailed account of the different aspects of Astronomy in order to provide an overall vision of this branch of science. Both editions, which include numerous theoretical concepts,

practical examples and original drawings, were textbooks and reference books in the Faculty of Sciences for years. "ASTRONOMÍA A SIMPLE VISTA" is an interesting book aimed mainly at those who, lacking the necessary means, are equally interested in knowing the wonderful science of the stars. It is a well-documented book that filled an existing void at the time it was written. Now in its 50th anniversary, it has been reproduced jointly by the City Council of Lalín and the University of Santiago de Compostela.

From 1931-34 many of his essays written in Galician appeared in the magazine LOGOS. In 1989, these essays were republished by the Provincial Council of Pontevedra with a prologue by Xosé Filguiera Valverde. After falling ill in 1964, Aller returned to Lalín, where he died on 28 March 1966 at the age of 88. After his death he left his observation instruments as well as the majority of his library collection to the Astronomical Observatory of the University of Santiago.

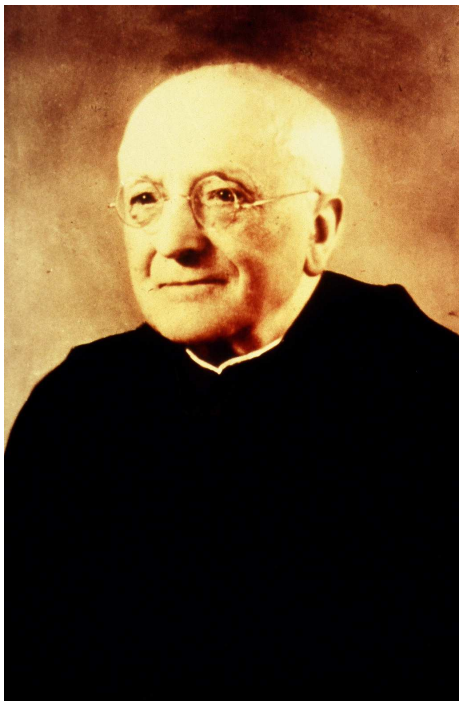

Figure 9.— R.M. Aller, Full Professor at the USC

This man who dedicated his long and productive life to Science and to serving his fellow man, did not dispose of the necessary means of observation to expand his research. On repeated occasions he requested what he always promised himself, that is, to one day have at least a 30cm refractor, a tool which he considered the most basic yet indispensable observation instrument. However, his requests were never honoured by the official bodies to whom he appealed.

Considering the modest resources at his disposal, and the times and places in which his research was carried out, Aller's scientific production was extraordinary: 78 publications (articles, notes, bibliographic comments, ...), 4 books, 5 directed doctoral theses, 4 discoveries of double stars, numerous designs of scientific instruments, and an endless number of unpublished observations, calculations, notes and stellar catalogues. It is because of all of this that he is considered one of the principal Spanish authorities on Astronomy.

Nevertheless, his real legacy was, without a doubt, that which cannot be quantified: his generosity, modesty, humbleness, scientific rigor and dedication to others, which was always manifest. As Vidal Abascal so rightly stated, *Ramón María Aller's true chef-d'oeuvre was his life.*